Thermal excitations of optical nanofibers measured with a fiber-integrated Fabry-Pérot cavity

DISSERTATION

Doctor rerum naturalium

to the Faculty of Physics
at the Johannes Gutenberg Unversität Mainz

by

Christian Wuttke
from Wiesbaden

Mainz, 2014

Advisor:
Second Advisor:

Date of the defense: 29th of April 2014

Declaration of Authorship

I hereby declare that I wrote the dissertation submitted without any unauthorized external assistance and used only sources acknowledged in the work. All textual passages which are appropriated verbatim or para-phrased from published and unpublished texts as well as all information obtained from oral sources are duly indicated and listed in accordance with bibliographical rules. In carrying out this research, I complied with the rules of standard scientific practice as formulated in the statutes of Johannes Gutenberg-University Mainz to insure standard scientific practice.

_____

Christian Wuttke

Abstract

Efficient coupling of light to quantum emitters, such as atoms, molecules or quantum dots, is one of the great challenges in current research. The interaction can be strongly enhanced by coupling the emitter to the evanescent field of subwavelength dielectric waveguides that offer strong lateral confinement of the guided light. In this context subwavelength diameter optical nanofibers as part of a tapered optical fiber (TOF) have proven to be a powerful tool which also provide an efficient transfer of the light from the interaction region to an optical bus, that is to say, from the nanofiber to an optical fiber.

Another approach towards enhancing light–matter interaction is to employ an optical resonator in which the light is circulating and thus passes the emitters many times. Here, both approaches are combined by experimentally realizing a microresonator with an integrated nanofiber waist. This is achieved by building a fiber-integrated Fabry-Pérot type resonator from two fiber Bragg grating mirrors with a stop-band near the cesium D2-line wavelength. The characteristics of this resonator fulfill the requirements of nonlinear optics, optical sensing, and cavity quantum electrodynamics in the strong-coupling regime. Together with its advantageous features, such as a constant high coupling strength over a large volume, tunability, high transmission outside the mirror stop band, and a monolithic design, this resonator is a promising tool for experiments with nanofiber-coupled atomic ensembles in the strong-coupling regime.

The resonator's high sensitivity to the optical properties of the nanofiber provides a probe for changes of physical parameters that affect the guided optical mode, e.g., the temperature via the thermo-optic effect of silica. Utilizing this detection scheme, the thermalization dynamics due to far-field heat radiation of a nanofiber is studied over a large temperature range. This investigation provides, for the first time, a measurement of the total radiated power of an object with a diameter smaller than all absorption lengths in the thermal spectrum at the level of a single object of deterministic shape and material. The results show excellent agreement with an ab initio thermodynamic model that considers heat radiation as a volumetric effect and that takes the emitter shape and size relative to the emission wavelength into account. Modeling and investigating the thermalization of microscopic objects with arbitrary shape from first principles is of fundamental interest and has important applications, such as heat management in nano-devices or radiative forcing of aerosols in Earth's climate system.

Using a similar method, the effect of the TOF's mechanical modes on the polarization and phase of the fiber-guided light is studied. The measurement results show that in typical TOFs these quantities exhibit high-frequency thermal fluctuations. They originate from high-Q torsional oscillations that couple to the nanofiber-guided light via the strain-optic effect. An ab-initio opto-mechanical model of the TOF is developed that provides an accurate quantitative prediction for the mode spectrum and the mechanically induced polarization and phase fluctuations. These high-frequency fluctuations may limit the ultimate ideality of fiber-coupling into photonic structures. Furthermore, first estimations show that they may currently limit the storage time of nanofiber-based atom traps. The model provides a method to design TOFs with tailored mechanical properties in order to meet experimental requirements.

Zusammenfassung

Die effiziente Kopplung von Licht an Materie, wie z.B. Atome, Moleküle oder Quantenpunkte, ist eine der großen Herausforderungen der aktuellen Forschung. Ein Ansatz besteht darin, den Emitter in das evaneszente Feld eines Lichtleiters mit einem Durchmesser, der kleiner ist als die Wellenlänge des Lichtes ist, einzubringen. Durch solche Wellenleiter wird das Lichtfeld auf eine extrem kleine Querschnittsfläche konzentriert. In diesem Zusammenhang haben sich optische Nanofasern mit Durchmessern, die kleiner sind als die optische Wellenlänge, bewährt. Diese können als Teil einer verjüngten Glasfaser realisiert werden, in denen gleichzeitig des Lichts vollständig von der Glasfaser in die Nanofaser geleitet wird.

Ein weiterer Ansatz zur Verbesserung der Wechselwirkung von Licht und Materie besteht darin, einen Resonator zu verwenden in dem das Licht den Emitter mehrfach passiert. Diese beiden Ansätze werden in der vorliegenden Arbeit durch einen Resonator mit integrierter Nanofaser vereint. Dazu werden zwei Bragg-Spiegel mit einem Sperrband nahe der Wellenlänge der Cäsium D2-Linie in die Faser integriert, so dass sie einen Fabry-Pérot Resonator ergeben. Die Eigenschaften dieses Resonators erfüllen die Anforderungen für Experimente der nichtlinearen Optik und der Resonator-Quantenelektrodynamik im Regime starker Wechselwirkung. Seine einfache Handhabung in Kombination mit vorteilhaften Eigenschaften, z.B. eine konstant hohe Wechselwirkungseffizienz entlang der Nanofaser, Verstimmbarkeit, monolithischer Aufbau und hohe Transmission im Durchlassbereich der Spiegel, machen diesen Resonator zu einem vielversprechenden Werkzeug, für Experimente mit stark an das Licht gekoppelten Atomwolken.

Die hohe Empfindlichkeit des Resonators auf Änderungen der optischen Eigenschaften der Nanofaser ermöglicht die Bestimmung von physikalischen Parametern, welche die Lichtmode beeinflussen, so z.B. die Temperatur mittels des thermooptischen Effekts. Dieses Detektionsschema wird hier dazu verwendet, die Dynamik der Thermalisierung durch Wärmestrahlung einer Nanofaser in einem großen Temperaturbereich zu vermessen. Diese Messung bestimmt zum ersten Mal die absolute in das Fernfeld abgestrahlte Wärmestrahlungsleistung eines einzelnen Objekts mit einem Durchmesser, der kleiner ist als alle Absorptionslängen im Wärmestrahlungsspektrum, und dessen Morphologie und Material bekannt sind. Die Messungen lassen sich hervorragend durch ein ab initio thermodynamisches Modell beschreiben, in dem die Wärmestrahlung unter Berücksichtigung der Geometrie und Größe des Strahlers relativ zur Wellenlänge der Strahlung berechnet wird. Das Studium der Wärmestrahlung von mikroskopischen Objekten und deren Modellierungen ausgehend von den Grundprinzipien der Physik, fördert das fundamentale Verständnis und hat wichtige Anwendungen, z.B. das Wärmemanagement in Nanostrukturen oder der Einfluss von Aerosolen auf das Weltklima.

Anhand einer ähnlichen Methode lässt sich der Effekt von mechanischen Moden der verjüngten Faser auf die Phase und Polarisation des geführten Licht studieren. Es zeigt sich, dass diese Größen in Fasern mit dem gängigen exponentiellen Radiusprofil, hochfrequente Modulation aufweisen. Diese stammen von thermisch angeregten Torsionsmoden mit hoher mechanischer Güte, die durch den mechano-optischen Effekt an die optische Mode koppeln. Mittels eines eigens entwickelten optomechanischen Modells, lassen

sich genaue quantitative Vorhersagen über das mechanische Spektrum und die optischen Polarisations- und Phasenfluktuationen erstellen. Diese Resultate haben wichtige Folgen für Anwendungen von Nanofasern im Ultrahochvakuum. Die hier gemessenen Fluktuationen limitieren höchstwahrscheinlich die Lebensdauer von faserbasierten Atomfallen und könnten die ultimative Lichtkopplungseffizienz in photonische Strukturen begrenzen. Andererseits lassen sich nun mittels des Modells Faserprofile mit vorbestimmten mechanischen Eigenschaften realisieren, die den experimentellen Anforderungen angepasst sind.

Publications

Parts of this thesis have been published in the following peer-reviewed journal articles:

- C. Wuttke, M. Becker, S. Brückner, M. Rothhardt, and A. Rauschenbeutel, 'Nanofiber Fabry–Pérot microresonator for nonlinear optics and cavity quantum electrodynamics', Opt. Lett. **37**, 1949–1951 (2012), e-print: arXiv:1202.1730 [quant-ph]

- C. Wuttke and A. Rauschenbeutel, 'Thermalization via Heat Radiation of an Individual Object Thinner than the Thermal Wavelength', Phys. Rev. Lett. **111**, 024301 (2013), e-print: arXiv:1209.0536 [quant-ph]

- C. Wuttke, G.D. Cole, A. Rauschenbeutel, 'Optically active mechanical modes of tapered optical fibers', Phys. Rev. A **88**, 061801(R) (2013), e-print: arXiv:1311.0916 [physics.optics] .

Contents

Introduction **1**

1 Tapered optical fibers **5**
1.1 The electromagnetic wave equation 6
1.2 Optical modes in step-index optical fibers 8
1.3 The fundamental mode of a silica nanofiber 14
1.3.1 Standing waves in an optical nanofiber 16
1.4 Tapered optical fibers (TOFs) 18
1.4.1 TOF fabrication using a flame brushing technique 18

2 Nanofiber resonators **23**
2.1 Fabry-Pérot resonators 24
2.1.1 Fabry-Pérot resonators from plain mirrors 24
2.1.2 Dispersive cavity media 26
2.1.3 Photonic stack mirrors – Transfer matrix formalism 27
2.1.4 Atom–cavity interaction 29
2.2 Nanofiber Bragg grating resonators 33
2.2.1 Fabrication 33
2.2.2 Spatial characterization 38
2.2.3 Optical setup 41
2.2.4 Vacuum system 42
2.2.5 Optical characterization 43
2.2.6 Transmission degradation during the fabrication 48
2.2.7 The effect of gallium on the optical properties of a NFBG 50
2.3 Resonator with an integrated tapered optical fiber (TOF-microresonator) . 53
2.3.1 Resonator fabrication 53
2.3.2 Optical characterization 54
2.3.3 TOF transmission loss 57
2.3.4 Intracavity polarization measurement 58
2.4 Summary 60

3 Thermalization of a nanofiber via thermal radiation **63**
3.1 Thermal radiation theory 65
3.1.1 Thermal radiation according to Planck's law 65
3.1.2 Emissivity of a silica–vacuum interface 67

3.1.3 Fluctuational Electrodynamics (FED) . . . 68
3.1.4 Far-field heat radiation of a silica nanofiber . . . 70
3.1.5 Modification of thermal radiation by surface pollutants . . . 74
3.2 Thermodynamical model of a TOF in vacuum . . . 77
3.2.1 Heat transfer equation . . . 77
3.2.2 Heating of the nanofiber by absorption . . . 78
3.2.3 Simulation of the temperature dynamics of a TOF in vacuum . . . 79
3.3 Relating the temperature change to optical path length changes . . . 80
3.3.1 Thermo-optic coefficient of fused silica . . . 80
3.3.2 Optical path length change of a nanofiber . . . 83
3.4 Measurement results . . . 85
3.4.1 Optical setup . . . 85
3.4.2 Signal . . . 86
3.4.3 Initialization procedure . . . 88
3.4.4 Maximum temperature change as function of the heating power . 90
3.4.5 Pressure dependence of the thermalization behavior . . . 92
3.4.6 Thermalization time constant . . . 93
3.5 Mechanical stability at high temperatures – Fusing temperature . . . 96
3.6 Summary . . . 98

4 Optically active mechanical modes of tapered optical fibers 99
4.1 Theory of elasticity . . . 100
4.2 Waves in tapered optical fibers . . . 104
4.2.1 Torsional waves . . . 105
4.2.2 Compressional waves . . . 111
4.2.3 Transversal waves . . . 113
4.3 Finite element modeling . . . 114
4.3.1 Resonance frequency prediction by the FEM and analytical model 116
4.4 Thermal motion of a fiber . . . 118
4.4.1 Displacement fluctuations of a tapered optical fiber . . . 120
4.5 Influence of mechanical vibrations on the optical nanofiber mode . . . 121
4.5.1 Strain-optic effect . . . 121
4.5.2 Birefringence caused by the mechanical modes of the fiber . . . 122
4.5.3 Effect on the fundamental optical nanofiber mode . . . 125
4.6 Measurement results . . . 129
4.6.1 Experimental setup . . . 129
4.6.2 Spectrum of the optically active mechanical modes . . . 130
4.6.3 Signal as function of the excitation amplitude . . . 134
4.6.4 Variations related to the probe laser polarization . . . 136
4.6.5 Modal amplitude profile . . . 138
4.6.6 Mechanical quality factor . . . 140
4.6.7 Q-factor depending on the background gas pressure . . . 141
4.7 Summary . . . 143

Summary & Outlook 145

A Appendix **149**
A.1 Bessel's little helper 149
A.2 Propagation constant of a mode in a medium with weakly anisotropic permittivity 150
A.3 Transfer matrix of a slit in a fiber 152
A.4 Refractive index of fused silica 154
A.5 Specific heat and heat conductivity of fused silica 156
A.6 Thermal expansion coefficient of fused silica 156
A.7 Thermalization via heat radiation assuming volume heating 158
A.8 Thermalization via heat radiation at cryogenic temperatures in a vacuum environment 161
A.9 Blue print of the vacuum chamber 167

Bibliography **169**

Introduction

Physicists across history have struggled to understand the nature of light. This is reflected in the various models that we have at our disposal which have been developed in the course of this process: An early model of light propagation, the ray theory, was already established in the ancient world. Then, during the 17th century, two rivaling models of waves and corpuscles have been established. With the field theory developed by Maxwell in the 19th century, the foundation for todays view of light as electromagnetic waves has been laid. This approach was very successful because it accurately described the experiments at that time and provided a consistent framework to describe all electromagnetic waves by one theory including optical but also, e.g., radio and radar radiation.

Some phenomena, however, could not be fully explained by Maxwell's famous equations like, e.g., the black-body radiation, and motivated physicists to devise new theoretical frameworks. By assuming that matter emits light in discrete energy portions (quanta), Max Planck derived the first correct description of the black-body radiation in 1901 [1], and thus paved the way for quantum mechanics. This has revolutionized the understanding of matter, light and their interaction and triggered a wealth of novel applications without which our lifestyle would be unthinkable.

Quantum mechanics has been refined ever since and by the discretization of the electromagnetic field in the framework of quantum electrodynamics (QED) a photon description was found. A branch of physics has tried to improve the efficiency and control of light–matter interactions. This has been perfected up to the level of individual atoms that interact with a single photon or even the vacuum state of an optical cavity. The importance of experiments with this extreme level of control is reflected in the recent Nobel price for Serge Haroche and David Wineland in 2012 [2]. In recent years, the availability of nanoscale structures of high optical quality enabled the development of subwavelength-sized waveguides that confine the light to areas on the scale of the optical wavelength. They exhibit a high evanescent field that provides an efficient coupling to emitters that are brought close to the surface of the waveguide. In this context, tapered optical fibers with subwavelength diameter waists were developed which provide an intrinsic and efficient coupling mechanism from the nanofiber to a bus that is suitable for long-range communication, i.e. a standard optical fiber [3]. Today, tapered optical fibers are widely used due to their ease of use and their wealth of applications in optical sensing [4–7], spectroscopy [8, 9], non-linear optics [10–13], cold atom physics [14–20], and for coupling light into photonic devices [21–28]. In order to ensure well-controlled light–matter coupling with such fibers, the phase and polarization of the nanofiber guided light field have to be stable. In Ch. 4 of this thesis the stability of these properties is investigated and it is shown

that in typical tapered optical fibers these quantities can exhibit high-frequency thermal fluctuations with narrow band-widths. These originate from thermally excited mechanical vibrations that influence the optical modes via the strain introduced in the material. These measurements can be accurately modeled which enables one to design the radius profile of the tapered optical fibers according to experimental needs.

The sensitivity of nanoscale waveguides can be further enhanced when confining the light simultaneously in its propagation direction to a small volume in a microresonator [29, 30]. When built with a high optical quality factor, these resonators profit from the extremely small volume in which a photon can be trapped, thereby providing high intensities for small numbers of photons. However, in order to trap a photon long enough to measure the dynamics of the photon–emitter interaction requires extremely small losses and is experimentally challenging. Nevertheless, several such resonators exist which can reach this so-called strong-coupling regime of cavity quantum electrodynamics [28, 31–40]. In Ch. 2 of this work a tapered optical fiber microresonator (TOF microresonator) will be presented with a performance that is comparable to state-of-the-art cavities. It provides advantageous features, such as tunability, a monolithic design for alignment-free operation, and a high coupling strength over a large volume. Furthermore, its high transmission properties make it compatible with the requirements for nanofiber-based atom traps. It, thereby, provides a system that allows to trap a large number of atoms at deterministic positions in the resonator volume while, simultaneously, allowing to perform experiments on them in the single-atom strong-coupling regime of cavity quantum electrodynamics.

The study of thermal radiation has also stayed an active field of physics in which Planck's theory and its bounds are tested. As Planck already stated himself, his law is limited to far-field heat radiation of objects with large sizes and curvatures compared to the wavelength of the thermal radiation [1]. At the time it was already known that the heat radiation of thin filaments is partly polarized and depends on the emission angle [41, 42]. Such phenomena can still be explained by Planck's theory when using Kirchhoff's law which relates a body's thermal emission properties (emissivity) to its optical absorption properties (absorptivity), thereby making them theoretically accessible by electromagnetic theory [43]. This, however, is not the case when, e.g., two bodies are placed at separations that are comparable to the radiation wavelength. Here, the near-field contributes to or even dominates the radiative heat transfer [44, 45] and a new theoretical approach is needed. This has been given by Rytov in the form of fluctuational electrodynamics (FED) [46] in which the electromagnetic field fluctuations are derived from the quantum fluctuations of the materials constituents. Beyond the applications to thermal radiation theory, this approach allows one to predict the Casimir forces acting on to bodies in close proximity [46].

The heat radiation at small scales is of particular interest in the scope of modeling heat exchange in the Earth's climate system where nanoscale aerosoles contribute to the absorption properties of our atmosphere. Therefore, a great effort has been made in order to measure the emissivity of different aerosols. These measurement were performed for different particle classes concerning their size, material, and origin, i.e. natural sources abundant such as airborne silica dust from the Sahara or are man-made such as soot from combustion engines [47–49]. Today's advances in nanofabrication allow to probe the heat

radiation at small scales with extreme control over the shape of the body. This enabled experiments which could show that the heat radiation can be coherent [50] or its spectrum can even be tailored by using metamaterials [51] or controlling the morphology of the emitter [52]. The results presented in Chapter 3 contribute to this field by measuring, for the first time, the total radiated power of an individual object with predetermined shape which is thinner than all absorption lengths of the relevant part of the thermal spectrum.

Beyond this fundamental interest, knowledge of the nanofiber's heat radiation properties is essential for experiments with nanofibers that are carried out under high vacuum conditions. Up to now, little information is available about the nanofiber's temperature in such experiments which is mainly due to the lack of measurement methods to access the temperature. In this work the thermo-optic effect of fused silica is utilized in order to measure the temperature changes via an optical path-length measurement. By using an interferometric technique, i.e., a resonator, the temperature change can be observed by a simple transmission measurement. This method solely requires a thermo-optic effect in the material and is applicable to many similar systems, e.g., optically levitated nanospheres.

CHAPTER 1

Tapered optical fibers

Optical fibers have become the back-bone of our long-range communication infrastructure which is reflected in the recent Nobel prize in 2009 for Charles Kuen Kao, one of the pioneers in optical fiber technology [53]. This is due to their low transmission loss over long distances that is rendered possible by the combination of the extremely high transparency of silica glasses and the fiber structure that shields the light from external influences. Optical fibers typically consist of a core–cladding structure which is shown for the simplest form, the step-index fiber, in Fig. 1.1. In such a fiber, the light is guided by total internal reflection at the interface between the core and the cladding. This is achieved by doping the core so that it exhibits a slightly higher refractive index than the cladding, which is made from pure synthetic fused silica. This simple scheme has been adapted to suit the requirements of a wealth of applications by changing the fiber geometry, materials or devising new transverse light confinements methods, e.g. photonic structures in the cross-section of the fiber.

The optical mode of fibers can be made accessible by tapering the fiber to subwavelength diameters at which point a considerable power fraction of the guided mode propagates outside the fiber medium in the form of an evanescent wave, see Fig. 1.2. Due to the strong mode confinement and the resulting high intensities in the evanescent field, nanofibers have become a widely used tool to efficiently couple emitters to the opti-

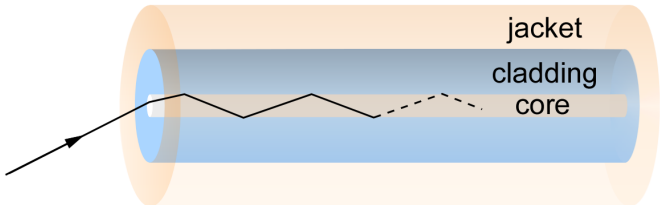

Figure 1.1: *Sketch of a step-index silica fiber. The core (white) exhibits a higher refractive index than the cladding (blue). The black arrow sketches the trace of a light beam that is guided by the fiber via total internal reflection. A polymer jacket is typically added for mechanical protection.*

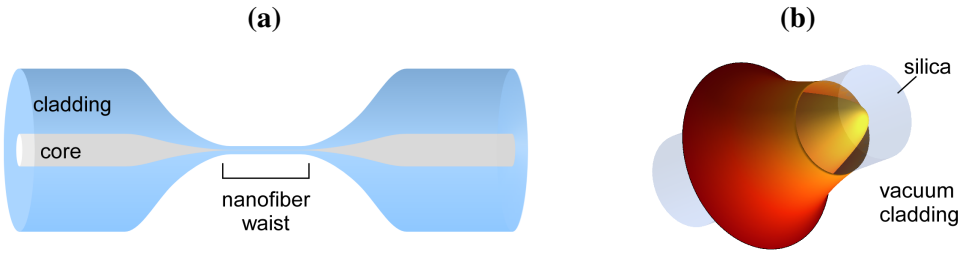

Figure 1.2: *Sketch of a tapered optical fiber (a) and intensity distribution of the optical mode in a subwavelength diameter optical nanofiber (b).*

cal nanofiber mode or to couple light into photonic structures [15, 18–20, 28, 54–58]. Nanofibers can be realized as part of a tapered optical fiber (TOF), see Fig. 1.2, and are typically fabricated from standard optical fibers in a heat and pull process [59, 60]. The radius profile of the TOFs employed in this work is composed of two taper sections that connect the untapered fiber to the nanofiber waist and convert the fiber mode into the nanofiber mode. By carefully designing the radius profile of the TOF nearly the full optical power can be transferred into the nanofiber and back into the fiber on the other end of the tapered section.

In this chapter, the theory of light propagation in optical fibers is presented. Starting from the electromagnetic wave equation, the fiber modes of a step-index optical fiber are derived and discussed in the first two sections. In the third section, the results are applied to a subwavelength diameter nanofiber where propagating modes and standing wave configurations are presented. The last section is concerned with the light guiding in tapered optical fibers and their fabrication method.

1.1 The electromagnetic wave equation

In this section, the electromagnetic wave equation is presented and solved for a homogeneous medium in cylindrical coordinates. These results will be used to derive the fiber modes by applying the boundary conditions at the core–cladding interface to the solution in the next chapter. The fiber modes have been extensively studied in the literature, see e.g. the excellent books by A. Yariv [61] and Snyder & Love for further reading [62]. The derivation given here closely follows that given by Yariv.

The electromagnetic wave equation for the electric field $\boldsymbol{E}$ reads

$$\triangle\, \boldsymbol{E}(\boldsymbol{r},t) - \mu_0\,\epsilon_0\,\mu(\boldsymbol{r})\,\epsilon(\boldsymbol{r})\,\frac{\partial^2 \boldsymbol{E}(\boldsymbol{r},t)}{\partial t^2} = -\nabla\left(\epsilon^{-1}(\boldsymbol{r})\cdot\boldsymbol{E}(\boldsymbol{r},t)\cdot\nabla\epsilon(\boldsymbol{r})\right)\,, \qquad (1.1)$$

where $\triangle$ is the Laplace operator, ∇ is the Nabla operator, t denotes the time variable, μ (μ_0) is the permeability of the material (vacuum), and ϵ (ϵ_0) is the permittivity of the material (vacuum).

Due to the cylindrical symmetry of step-index optical fibers it is convenient to solve the wave equation in cylindrical coordinates with the z-axis oriented along the fiber axis.

Then, the solution in the core and cladding is that of a homogeneous medium and the full fields can be obtained by applying boundary conditions. In an homogeneous medium, the right side of the wave equation Eq. (1.1) vanishes and it takes the same form as that of the magnetic field, where $\boldsymbol{E}$ is replaced by $\boldsymbol{H}$. The Laplace operator in cylindrical coordinates reads

$$\triangle = \partial_r^2 + \frac{1}{r}\partial_r + \frac{1}{r^2}\partial_\phi^2 + \partial_z^2 \,, \tag{1.2}$$

where the short notation $\partial_r = \partial/\partial r$ is used and for the other variables accordingly.

An optical wave that propagates in a fiber can be expressed in the form

$$\boldsymbol{E}(\boldsymbol{r},t) = \boldsymbol{E}(r,\phi)\exp(\mathbb{i}[\omega t - \beta z]) \,, \quad \boldsymbol{H}(\boldsymbol{r},t) = \boldsymbol{H}(r,\phi)\exp(\mathbb{i}[\omega t - \beta z]) \,, \tag{1.3}$$

where β is the propagation constant, $\omega = 2\pi\, f$ is the angular frequency and f is the frequency of the light-field. The electric and magnetic fields are interconnected by Maxwell's equations and the field components that are oriented transversally to the fiber axis, E_r, E_ϕ, H_r, and H_ϕ, can be expressed via the axial components, E_z and H_z, using

$$\begin{aligned} E_r &= \frac{-\mathbb{i}\beta}{\omega^2\mu\epsilon - \beta^2}\left(\partial_r E_z + \frac{\omega\mu}{\beta}\frac{\partial_\phi}{r}H_z\right) \quad E_\phi = \frac{-\mathbb{i}\beta}{\omega^2\mu\epsilon - \beta^2}\left(\frac{1}{r}\partial_\phi E_z - \frac{\omega\mu}{\beta}\partial_r H_z\right) \\ H_r &= \frac{-\mathbb{i}\beta}{\omega^2\mu\epsilon - \beta^2}\left(\partial_r H_z - \frac{\omega\epsilon}{\beta}\frac{\partial_\phi}{r}E_z\right) \quad H_\phi = \frac{-\mathbb{i}\beta}{\omega^2\mu\epsilon - \beta^2}\left(\frac{1}{r}\partial_\phi H_z + \frac{\omega\epsilon}{\beta}\partial_r E_z\right) \end{aligned} \tag{1.4}$$

As a consequence, it is sufficient to solve the wave equation for the z-components of the magnetic and electric field. Using the ansatz Eq. (1.3), the corresponding wave equations read

$$\left[\partial_r^2 + \frac{1}{r}\partial_r + \frac{1}{r^2}\partial_\phi^2 + (k^2 - \beta^2)\right]\begin{bmatrix} E_z \\ H_z \end{bmatrix} = 0 \,, \tag{1.5}$$

where $k = \omega\, n/c_0$ is the propagation constant in the medium with refractive index n and $c_0 = 1/\sqrt{\epsilon_0\mu_0}$ is the speed of light in vacuum. This equation is separable in a radial and angular variable, where the corresponding equation for the angular part is solved by the ansatz

$$E_z(r,\phi) = E_0\, e_z(r)\, \exp(\pm\mathbb{i}\, l\phi) \,, \tag{1.6}$$

where $l \in \mathbb{N}_0$ is a positive integer number and $\boldsymbol{e}(r)$ is the radial field distribution. The sign in the exponential term determines the polarization state of the wave, where + and - correspond to clockwise and counter-clockwise circular polarization, respectively. The remaining differential equation in the radial variable reads

$$\left[\partial_r^2 + \frac{1}{r}\partial_r + (k^2 - \beta^2 - \frac{l^2}{r^2})\right]\begin{bmatrix} e_z \\ h_z \end{bmatrix} = 0 \,. \tag{1.7}$$

This is the Bessel differential equation which has the Bessel functions as solutions. Two sets of solutions for both fields, $\Psi(r) = e_z, h_z$, exist depending on whether $k^2 - \beta^2$ is positive or negative. For the positive case, $h^2 = k^2 - \beta^2 > 0$, one finds

$$\Psi(r) = c_1\, J_l(hr) + c_2\, Y_l(hr) \,, \quad c_1, c_2 \in \mathbb{C} \tag{1.8}$$

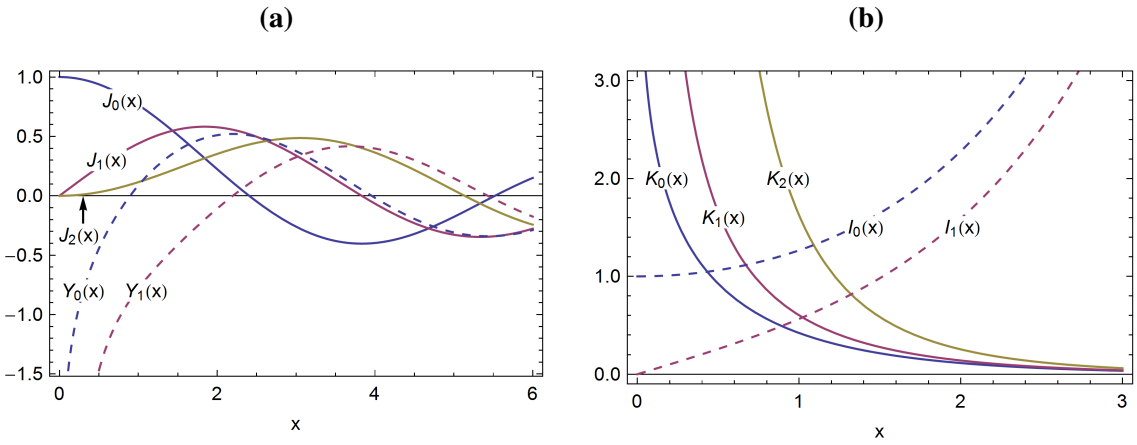

Figure 1.3: *Plot of the Bessel functions of the first and second kind (a) and the modified Bessel functions of the first and second kind (b).*

where c_1 and c_2 are constants that are determined by the boundary conditions and J_l and Y_l are the Bessel functions of order l of the first and second kind, respectively. For the other case $q^2 = \beta^2 - k^2 > 0$ one finds

$$\Psi(r) = c_1\, I_l(qr) + c_2\, K_l(qr)\,, \quad c_1, c_2 \in \mathbb{C} \tag{1.9}$$

where I_l and K_l are the modified Bessel functions of the first and second kind of the order l, respectively. The Bessel functions are plotted for selected parameters in Fig. 1.3.

1.2 Optical modes in step-index optical fibers

The step-index fiber is a circular waveguide that is composed of two cylinders, the core with a radius a that is embedded in the cladding with a much larger radius b. The core exhibits a higher refractive index n_1 than the cladding n_2, see Fig. 1.4, so that the light is guided by total internal reflection at the core–cladding transition. From the solution of the wave equation in cylindrical coordinates it is now possible to directly find the fields of the fiber-guided modes by applying the boundary conditions for the electric and magnetic fields at the core–cladding transition. Typically, the radius of the cladding is very large compared to that of the core and the wavelength of the light, so that we can set $b = \infty$ without loss of generality. Note that the derivation given here is known as the strongly-guiding fiber. For small refractive index contrasts $n_1 - n_2 \ll 1$, e.g. standard optical fibers, a simpler approximation exists which is known as the weakly guiding fiber and is discussed in the literature [61].

For transversely confined guided modes, the propagation constant is required to be between those of a plane wave that is propagating through the cladding material and the core material, respectively: $n_1\, k_0 > \beta > n_2\, k_0$. With that, the mode in the core fulfills $h^2 = n_1^2\, k_0^2 - \beta^2 > 0$ and is given by the first solution Eq. (1.8) with $c_2 = 0$ because Y_l diverges for $r \to 0$:

$$r < a: \qquad e_z(r) = A\, J_l(h\, r)\,, \quad \text{and} \quad h_z(r) = B\, J_l(h\, r)\,, \tag{1.10}$$

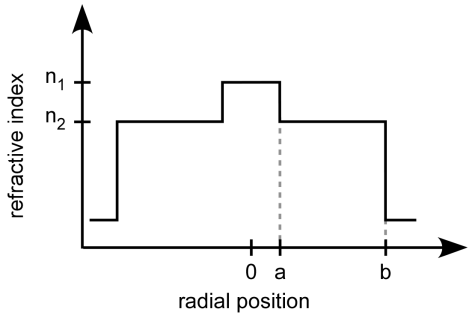

Figure 1.4: *Schematic refractive index profile of a step-index fiber. The radius of the core and cladding are denoted by a and b, respectively, and their corresponding refractive indices by n_1 and n_2, respectively.*

where $A, B \in \mathbb{C}$ are complex constants. In the cladding, the opposite situation is the case, $q^2 = \beta^2 - n_2^2\, k_0^2 > 0$, so that the second solution Eq. (1.9) applies. By requiring the field to be confined in a finite volume one finds $c_1 = 0$ because $I_l(r)$ diverges for $r \to \infty$ so that the field reads

$$r > a: \qquad e_z(r) = C\, K_l(qr)\,, \quad \text{and} \quad h_z(r) = D\, K_l(qr)\,, \tag{1.11}$$

where $C, D \in \mathbb{C}$ are complex constants. The relative amplitudes $A \ldots D$ of the field components are determined from the boundary conditions of the fields at the interface between the two media, i.e. the components parallel to the boundary E_ϕ, E_z, H_ϕ and H_z are required to be continuous at $r = a$.

The remaining field components can now be determined using Eq. (1.4). Since the polarization state of the mode is solely determined by the angular dependence of the fields it is convenient to express it via its angular and radial dependence separately. Then, the fields of the quasi-circularly polarized mode read

$$\boldsymbol{E}^{(\pm)}(r,\phi) = A\, \mathrm{e}^{\pm \mathrm{i}\, l\phi} \begin{pmatrix} e_r(r) \\ \pm e_\phi(r) \\ e_z(r) \end{pmatrix}\,, \quad \boldsymbol{H}^{(\pm)}(r,\phi) = A\, \mathrm{e}^{\pm \mathrm{i}\, l\phi} \begin{pmatrix} \pm h_r(r) \\ h_\phi(r) \\ \pm h_z(r) \end{pmatrix}\,, \tag{1.12}$$

where the sign indicates clockwise (+) and counter-clockwise (-) sense of rotation. The quasi-linearly polarized fields result from a linear combination of the quasi-circularly polarized fields. The two polarization states with the polarization axis oriented along the x- and y-axis can be written as

$$\boldsymbol{E}^{(x)}(r,\phi) = A \begin{pmatrix} e_r(r)\, \cos(l\,\phi) \\ e_\phi(r)\, \mathrm{i}\, \sin(l\,\phi) \\ e_z(r)\, \cos(l\,\phi) \end{pmatrix} \quad \boldsymbol{H}^{(x)}(r,\phi) = A \begin{pmatrix} h_r(r)\, \mathrm{i}\, \sin(l\,\phi) \\ h_\phi(r)\, \cos(l\,\phi) \\ h_z(r)\, \mathrm{i}\, \sin(l\,\phi) \end{pmatrix}\,, \tag{1.13a}$$

$$\boldsymbol{E}^{(y)}(r,\phi) = A \begin{pmatrix} e_r(r)\, \mathrm{i}\, \sin(l\,\phi) \\ e_\phi(r)\, \cos(l\,\phi) \\ e_z(r)\, \mathrm{i}\, \sin(l\,\phi) \end{pmatrix} \quad \boldsymbol{H}^{(y)}(r,\phi) = A \begin{pmatrix} h_r(r)\, \cos(l\,\phi) \\ h_\phi(r)\, \mathrm{i}\, \sin(l\,\phi) \\ h_z(r)\, \cos(l\,\phi) \end{pmatrix}\,. \tag{1.13b}$$

Here, the prefix "quasi" is added due to the non-vanishing axial field components which prevent a direct analogy to free-space polarization states. The radial field distributions in the core region $r < a$ are

$$\begin{aligned}
e_r(r) &= \frac{-\mathbb{i}\beta}{2h}\left[(1-s\,l)\,J_{l-1}(h\,r) - (1+s\,l)\,J_{l+1}(h\,r)\right] \\
e_\phi(r) &= \frac{\beta}{2h}\left[(1-s\,l)\,J_{l-1}(h\,r) + (1+s\,l)\,J_{l+1}(h\,r)\right] \\
e_z(r) &= J_l(h\,r) \\
h_r(r) &= -\frac{\omega\,\epsilon_0\,n_1^2}{2h}\left[(1-s_1\,l)\,J_{l-1}(h\,r) + (1+s_1\,l)\,J_{l+1}(h\,r)\right] \\
h_\phi(r) &= -\frac{\mathbb{i}\omega\,\epsilon_0\,n_1^2}{2h}\left[(1-s_1\,l)\,J_{l-1}(h\,r) - (1+s_1\,l)\,J_{l+1}(h\,r)\right] \\
h_z(r) &= \frac{\mathbb{i}\,s\,\beta\,l}{\omega\,\mu}\,J_l(h\,r)
\end{aligned} \tag{1.14}$$

and in the cladding region $r > a$

$$\begin{aligned}
e_r(r) &= \frac{-\mathbb{i}\,\beta\,v}{2q}\left[(1-s\,l)\,K_{l-1}(q\,r) + (1+s\,l)\,K_{l+1}(q\,r)\right] \\
e_\phi(r) &= \frac{\beta\,v}{2q}\left[(1-s\,l)\,K_{l-1}(q\,r) - (1+s\,l)\,K_{l+1}(q\,r)\right] \\
e_z(r) &= t\,K_l(q\,r) \\
h_r(r) &= -\frac{\omega\,\epsilon_0\,n_2^2\,v}{2q}\left[(1-s_2\,l)\,K_{l-1}(q\,r) - (1+s_2\,l)\,K_{l+1}(q\,r)\right] \\
h_\phi(r) &= -\frac{\mathbb{i}\,\omega\,\epsilon_0\,n_2^2\,v}{2q}\left[(1-s_2\,l)\,K_{l-1}(q\,r) + (1+s_2\,l)\,K_{l+1}(q\,r)\right] \\
h_z(r) &= \frac{\mathbb{i}\,\beta\,l\,s\,v}{\omega\,\mu}K_l(q\,r)
\end{aligned} \tag{1.15}$$

where

$$\begin{aligned}
s &= \left[\frac{1}{(q\,a)^2} + \frac{1}{(h\,a)^2}\right]\left[\frac{J_l'(h\,a)}{h\,a\,J_l(h\,a)} + \frac{K_l'(q\,a)}{q\,a\,K_l(q\,a)}\right]^{-1}, \\
s_1 &= \frac{\beta^2}{k_0^2\,n_1^2}\,s\,, \qquad s_2 = \frac{\beta^2}{k_0^2\,n_2^2}\,s\,, \qquad v = \frac{J_l(h\,a)}{K_l(q\,a)}\,.
\end{aligned}$$

Here, $J'(x) = \partial J(x)/\partial x$ and $K'(x) = \partial K(x)/\partial x$ denote the derivative with respect to the argument. From the field equations it can be already seen that the optical fields of a nanofiber are not necessarily purely transversal, meaning that they exhibit a non-vanishing field component along the propagation direction (z-direction).

The propagation constant β can be determined from the boundary condition which

yields:

$$\left[\frac{J_l'(h\,a)}{h\,a\,J_l(h\,a)}+\frac{K_l'(q\,a)}{q\,a\,K_l(q\,a)}\right]\left[\frac{n_1^2\,J_l'(h\,a)}{h\,a\,J_l(h\,a)}+\frac{n_2^2\,K_l'(q\,a)}{q\,a\,K_l(q\,a)}\right]= \left[\frac{1}{(q\,a)^2}+\frac{1}{(h\,a)^2}\right]^2\left[\frac{l\,\beta}{k_0}\right]^2 . \quad (1.16)$$

This condition is quadratic in $J_l'(h\,a)/h\,a\,J_l(h\,a)$ and can be reformulated via two equations which represent the characteristic equations of two classes of modes that are distinguished by convention. These are called EH-modes with the characteristic equation

$$\frac{J_{l+1}(h\,a)}{h\,a\,J_l(h\,a)}=\frac{n_1^2+n_2^2}{2\,n_1^2}\,\frac{K_l'(q\,a)}{q\,a\,K_l(q\,a)}+\left(\frac{l}{(h\,a)^2}-R\right), \qquad \text{(EH)} \quad (1.17)$$

or HE-modes with the corresponding characteristic equation

$$\frac{J_{l-1}(h\,a)}{h\,a\,J_l(h\,a)}=-\frac{n_1^2+n_2^2}{2\,n_1^2}\,\frac{K_l'(q\,a)}{q\,a\,K_l(q\,a)}+\left(\frac{l}{(h\,a)^2}-R\right), \qquad \text{(HE)} \quad (1.18)$$

where

$$R=\sqrt{\left[\frac{n_1^2-n_2^2}{2\,n_1^2}\right]^2\left[\frac{K_l'(q\,a)}{qa\,K_l(q\,a)}\right]^2+\left[\frac{l\,\beta}{n_1\,k_0}\right]^2\left[\frac{1}{(q\,a)^2}+\frac{1}{(h\,a)^2}\right]^2},$$

and the relations for the Bessel functions in Ch. A.1 were used.

Consider the special case $l=0$ where the fields are independent of the angular variable. It can be shown that two classes of modes exist in which either the electric field or the magnetic field is transversal, meaning that for one of the (E- or H-) fields the axial field component vanishes. They are called the transversal electric modes (TE-modes) for which the only non-vanishing field components are the H_r, H_z, and E_ϕ components and the characteristic equation simplifies to:

$$\frac{J_1(h\,a)}{h\,a\,J_0(h\,a)}=-\frac{K_1(q\,a)}{q\,a\,K_0(q\,a)}\,. \qquad \text{(TE)} \quad (1.19)$$

The other mode class is called transversal magnetic modes (TM-modes) with the corresponding field components being E_r, E_ϕ and H_ϕ and the characteristic equation reads

$$\frac{J_1(h\,a)}{h\,a\,J_0(h\,a)}=-\frac{n_2^2}{n_1^2}\,\frac{K_1(q\,a)}{q\,a\,K_0(q\,a)}\,. \qquad \text{(TM)} \quad (1.20)$$

The characteristic equations are transcendental and can only be solved numerically or graphically. Therefore, the equations are expressed in terms of $h\,a$ using

$$(q\,a)^2=V^2-(h\,a)^2\,, \quad \text{where} \quad V=k_0\,a\,\sqrt{n_1^2-n_2^2}\,. \quad (1.21)$$

Here, the V-parameter was introduced which is proportional to the ratio of the fiber radius and the optical wavelength. Figure 1.5 illustrates the scheme employed to compute the

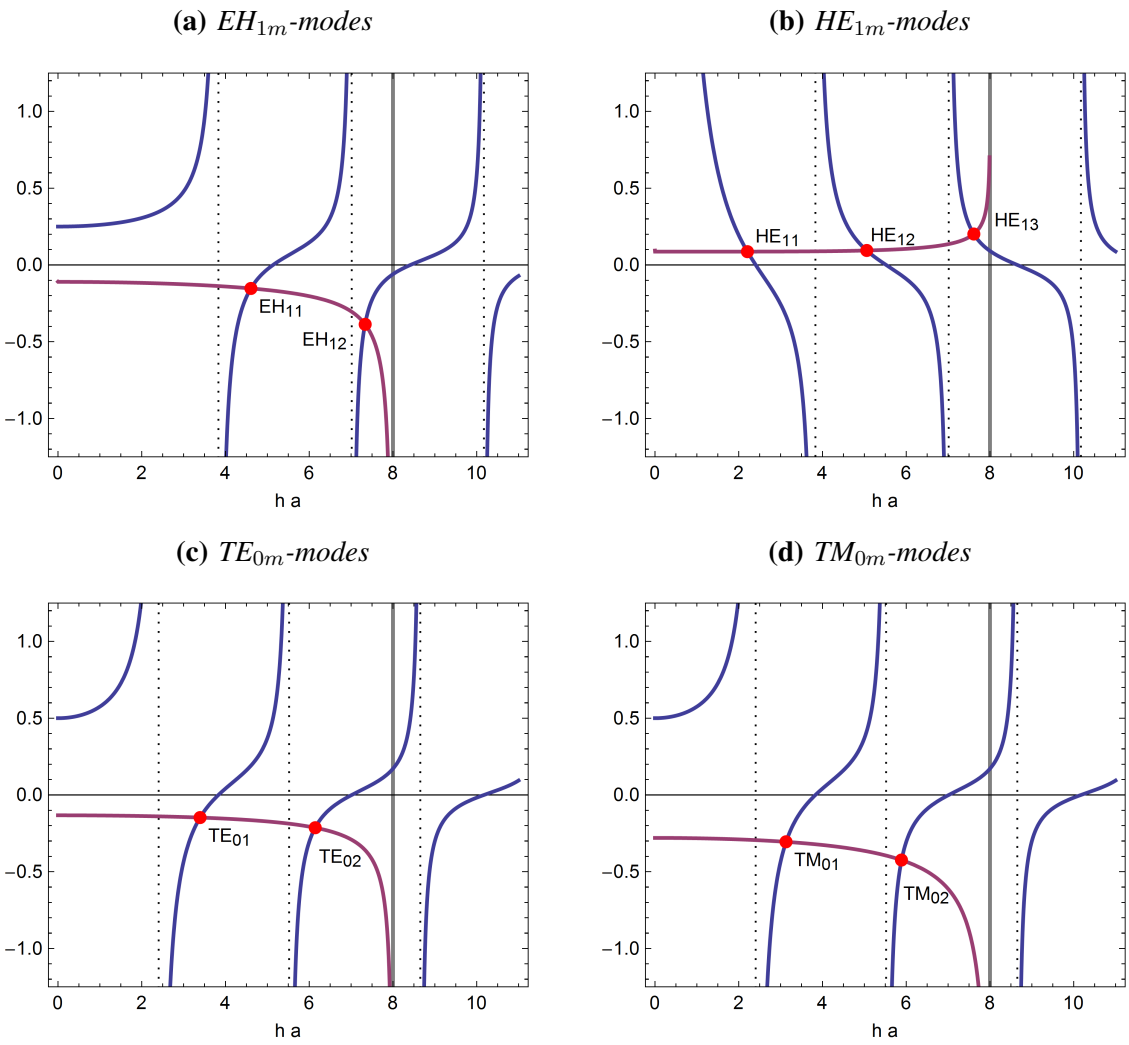

Figure 1.5: *Plot of the left hand side (blue) and right hand side (purple) of the characteristic equations of the modes, Eqns. (1.17–1.20), where the V-parameter is set to $V = 8$ (gray line) and the mode names are given in the subtitles. The intersections are marked with red points with the corresponding mode names.*

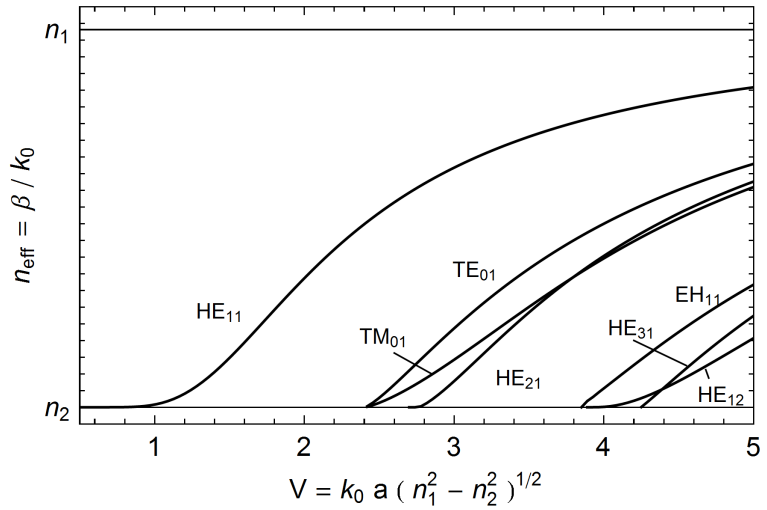

Figure 1.6: *Example plot of the effective refractive index of the fiber mode as function of the V-parameter. Parameters:* $\lambda_0 = 852$ *nm, core* $n_1 = 1.45247$ *(fused silica), and cladding* $n_2 = 1$ *(vacuum).*

graphical solution, in which the left and right side of the characteristic equations are plotted separately and the solution is found at their intersection points. The modes are named after their family and two indices, e.g. $\mathrm{HE}_{\mathrm{lm}}$, where the first index denotes the mode number (l) and the second index m counts the solution number with increasing $h\,a$ values. It can be seen from the plot, that the left side of the characteristic equations diverges at $h\,a = V$. As a consequence, the V-parameter determines the number of modes in a fiber. One mode, the HE_{11}-mode, is distinguished from all other modes by the fact that it always exists, independent of the fiber parameters and optical wavelength. This mode is called the fundamental mode of the fiber. One can formulate a single-mode condition of the fiber, which is given by the minimum V-parameter at which at least one higher order mode exists. The first higher order modes are the TE- and TM-modes for which the first asymptote is given by the first root of $J_0(h\,a) = 0$ at $h\,a = 2.405$, compare Fig. 1.5, so that the single-mode condition of a fiber reads $V < 2.405$.

Using the characteristic equations of the modes, the propagation constant of each mode can be computed for a given V-parameter. This is done for the first 7 modes of a fiber for an exemplary refractive index configuration in Fig. 1.6. The propagation constant is normalized to the free space propagation constant, thereby introducing the more intuitive effective refractive index of the mode $n_{\mathrm{eff}} = \beta/k_0$. The effective refractive index depends strongly on the V-parameter and approaches n_2 for core radii that are small compared to the wavelength, $a/\lambda \to 0$, and n_1 for the opposite case $a/\lambda \to \infty$. This is not surprising since in these two extreme cases either only the core or the cladding remains and the result must match the wave propagation in an homogeneous medium with the refractive index of the remaining material. Note that the propagation constant only depends on the ratio a/λ so that the V-parameter can be tuned equivalently by reducing (increasing) the radius or increasing (reducing) the wavelength by the same relative amount. This also shows that

the modes of a fiber exhibit a strong dispersion, i.e. n_{eff} depends on the wavelength, when the wavelength and the core radius are comparable. The cut-off behavior of the higher order modes can be observed by the fact that no solution for their propagation constants exists below certain V-parameters.

Field distribution in Cartesian coordinates

For some applications it is convenient to use the fields in Cartesian coordinates. The fields directly follow from their cylindrical representation by using the following relation for vector fields

$$\begin{pmatrix} E_x \\ E_y \\ E_z \end{pmatrix} = \begin{pmatrix} \cos(\phi) & -\sin(\phi) & 0 \\ \sin(\phi) & \cos(\phi) & 0 \\ 0 & 0 & 1 \end{pmatrix} \begin{pmatrix} E_r \\ E_\phi \\ E_z \end{pmatrix} , \tag{1.22}$$

and for the magnetic field accordingly. Using the definitions of the electric field Eqns. (1.12-1.13), the corresponding fields in Cartesian coordinates can be computed.

Energy and power stored in an optical mode

Here, the formulas for the electromagnetic energy and intensity are summarized. The electro-magnetic energy density of an optical wave $\mathcal{W}_{\text{em}}$ is given by the sum of the electric energy density $\mathcal{W}_{\text{e}}$ and the magnetic energy density $\mathcal{W}_{\text{m}}$. These contribute equally $\mathcal{W}_{\text{e}} = \mathcal{W}_{\text{m}}$ such that the total energy density can be computed via [62, ch. 11-6ff and 31-4]

$$\mathcal{W}_{\text{em}}(\boldsymbol{r}) = \epsilon_0 \, \boldsymbol{E}(\boldsymbol{r}) \cdot \boldsymbol{\epsilon}(\boldsymbol{r}) \cdot \boldsymbol{E}^*(\boldsymbol{r}) \, . \tag{1.23}$$

For isotropic media this simplifies to

$$\mathcal{W}_{\text{em}}(\boldsymbol{r}) = \epsilon_0 \, \epsilon(\boldsymbol{r}) \, |\boldsymbol{E}(\boldsymbol{r})|^2 \, . \tag{1.24}$$

The intensity of the mode is given by the time averaged Poynting vector component along the propagation direction which reads

$$P_z(\boldsymbol{r}) = \frac{1}{2} \operatorname{Re} \left[\boldsymbol{E}(\boldsymbol{r}) \times \boldsymbol{H}^*(\boldsymbol{r}) \right] \cdot \hat{\boldsymbol{z}} = \frac{1}{2} \operatorname{Re} \left[E_x(\boldsymbol{r}) \, H_y^*(\boldsymbol{r}) - E_y(\boldsymbol{r}) \, H_x^*(\boldsymbol{r}) \right] , \tag{1.25}$$

where $\hat{\boldsymbol{z}}$ is the unit vector along the z-axis. The power that is stored in the optical mode follows from integration over a cross-section perpendicular to the z-axis of the fiber.

1.3 The fundamental mode of a silica nanofiber

Now the light propagation in "vacuum-cladded" optical nanofibers with subwavelength diameter is discussed. Such nanofibers can be produced from standard optical fibers by tapering the latter to a subwavelength diameter. Then, the light is guided by the interface of the former silica cladding and the surrounding medium, e.g. air or vacuum. The fiber core is then small compared to the wavelength so that it does not contribute to the light-guiding. In fact, the nanofiber can now be treated again like a step-index fiber where

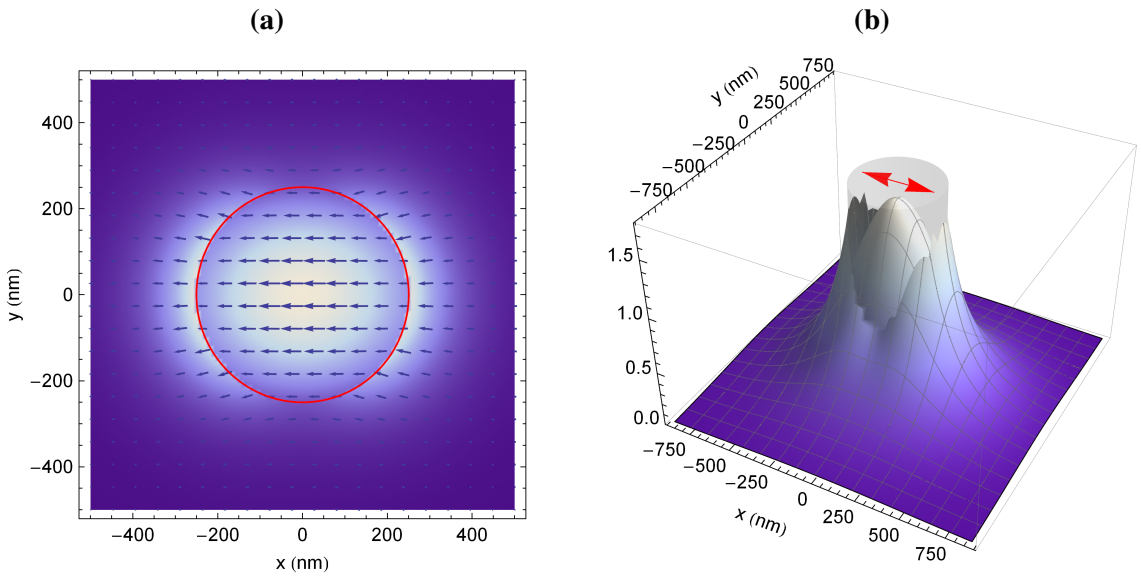

Figure 1.7: *(a) Electric field vector in the plane transverse to the fiber axis (arrows) of the quasi-linearly polarized fundamental nanofiber mode at a position and time of maximum field strength in the transverse direction. The intensity distribution is indicated by the color code, where bright corresponds to high intensities. (b) Absolute of the E-field amplitude $|E|$ at the same time. The red arrow indicates the polarization axis and the translucent cylinder and red circle indicate the nanofiber dimensions and the wavelength and radius were set to $\lambda_0 = 852$ nm and $a = 250$ nm.*

the former cladding plays the role of the core and the surrounding medium that of the cladding. Thus, deriving the solution for the nanofiber guided fields is straightforward using the results from the previous section. This can be achieved by using the radius of the nanofiber as the core radius a, the refractive index of fused silica as n_1, and the refractive index of the surrounding medium as n_2.

In the following experiments, a nanofiber with a diameter of 500 nm is used at wavelengths near the Cs D2-line wavelength of $\lambda_0 = 852$ nm. The E-field and intensity distribution of a nanofiber mode is shown in Fig. 1.7. Here, the polarization is chosen quasi-linearly and its polarization axis is oriented along the x-axis (red arrows). Considering the actual field orientations shown in Fig. 1.7(a), it can be seen that the field polarization of the mode, in fact, exhibits essentially no E_y-component. In Fig. 1.7(b) we observe that the E-field distribution inside the nanofiber resembles the profile of a Gaussian beam. Outside the nanofiber, the mode exhibits a strong evanescent field which extents several 100 nm beyond the nanofiber surface. Its peak magnitude is comparable to that of the part of the field that propagates inside the nanofiber. The mode shows a discontinuity at the surface of the nanofiber which is strongest pronounced along the polarization axis. From Fig. 1.7(a) it becomes clear that this stems form the discontinuity of the E-field component that is perpendicular to the silica–vacuum interface.

This illustrates that a subwavelength diameter optical nanofiber can confine the guided light field to an area that is approximately given by the wavelength squared $\sim \lambda^2$. This is comparable to what is achievable with a tightly focused laser beam. From Gaussian beam

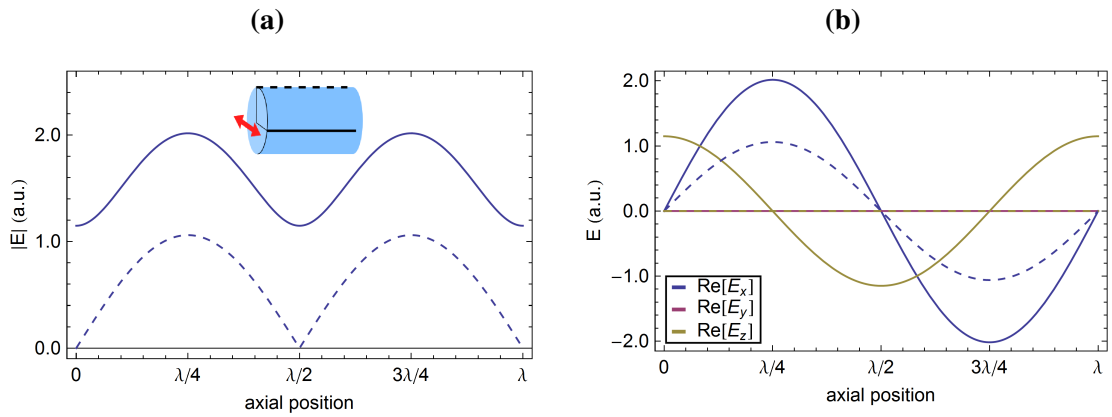

Figure 1.8: *Axial field distribution on the nanofibers surface of the absolute E-field (a) and the individual E-field components (b) of a standing quasi-linearly polarized mode at a time of maximum field strength. These are shown for two polar positions $\phi = 0°$ (solid lines) and $\phi = 90°$ (dashed lines) where the polarization direction is along $\phi = 0°$. This is illustrated by the inset in (a) where the two paths are shown in the corresponding line-type, solid or dashed, and the polarization direction is shown as a red arrow. Here, the wavelength and radius are set to $\lambda_0 = 852$ nm and $a = 250$ nm, respectively.*

optics it is known that when a beam is focused to a waist radius that is on the order of the wavelength $w_0 \sim \lambda$, its Rayleigh length $z_0 = \pi\, w_0^2/\lambda \sim \lambda$ is also on the order of the wavelength [63]. This means that the high divergence of the beam limits the axial length of the region with high intensity. In the case of the nanofiber, however, the region of strong lateral mode confinement is given along its full length. As a consequence, the number of emitters that can be coupled to its light field is greatly enhanced when compared to a free-space beam.

1.3.1 Standing waves in an optical nanofiber

The light–matter interaction capabilities of a nanofiber can be further enhanced by integrating it into a resonator such that the light field passes an emitter that is coupled to the fiber many times [64]. When using a Fabry-Pérot type configuration with two opposing mirrors that are integrated in the fiber, the two counter-propagating waves form a standing wave pattern. Unlike in free space modes, the E-field does not necessarily vanish along the fiber axis. This is due to axial field component which oscillates out of phase with respect to the transverse field components.

Figure 1.8(a) illustrates this feature by showing the absolute E-field strength of a standing wave as function of the axial position at two positions on the surface of the nanofiber with the two polar angles $\phi = 0°$ and $\phi = 90°$. The absolute field strength along the polarization direction ($\phi = 0°$) shows a minimum at $\lambda/2$ which is a factor of two lower than the maximum field strength. Along the other direction, $\phi = 90°$, the full contrast between no field and maximal field can be found. The individual field components are shown in Fig. 1.8(b). Comparing the distributions of the E_x- and E_z-field it

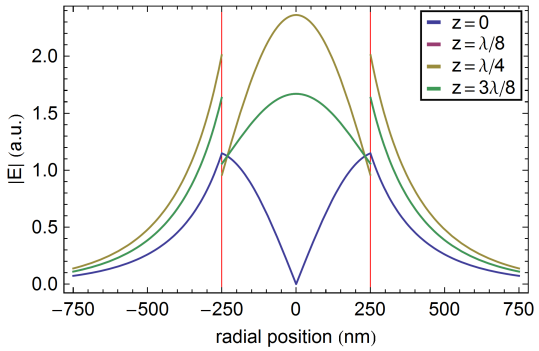

Figure 1.9: *Radial absolute E-field distribution of a quasi-linearly polarized mode at selected axial positions (see legend) for $\phi = 0°$. The time is again chosen such that one obtains the maximum field strength. The nanofiber surface is indicated by red lines.*

becomes clear that this results from the phase relation of these, resulting in a relative axial position shift of their anti-nodes by $\lambda/4$. This results in a rotation of the E-field orientation in the xz-plane from the z-direction at $z = m\,\lambda/2$ to the x-direction at $z = (2m + 1)\lambda/4$, where $m \in \mathbb{Z}$.

Now consider the radial field distribution which is shown in Fig. 1.9 for selected axial positions and $\phi = 0°$ (along polarization axis). It can be seen that the evanescent field changes its absolute value by a factor of two along the fiber axis while the shape of the distribution is essentially constant. This situation is different within the nanofiber where a field node occurs at the center of the fiber and $z = 3\lambda/8$. Here, only the E_z-component contributes so that the E-field points in the two opposite axial directions on the two sides of the nanofiber. However, the E_x-component features no node as can be seen from the trace at $z = \lambda/4$ where $E_z = 0$. This means that it points in the same direction on both sides of the nanofiber. Combining this result with the previous finding that the polarization rotates in the xz-plane, it follows that this rotation exhibits opposite sense of rotation on both sides of the nanofiber.

The fact that the field strength at specific polar angles changes only by a factor two or, alternatively, by the full contrast distinguishes nanofiber-based resonators from free-space resonators. In free space resonators, the interaction region with high light–matter coupling efficiency is restricted to the antinodes of the standing wave, whereas in nanofiber resonators it extents over the full length of the nanofiber. By keeping the emitter position constant and exciting the nanofiber mode with the other polarization ($\phi = 90°$) one can switch to a standing wave pattern with full contrast similar to free-space cavities. This offers the possibility to choose between two field configurations by tuning the polarization axis according to experimental requirements.

1.4 Tapered optical fibers (TOFs)

The properties of the optical modes in optical nanofibers have been discussed in the previous chapter. Such fibers can be realized as the waist of a tapered optical fiber (TOF) that converts the mode of the standard optical fiber efficiently into that of the nanofiber [65].

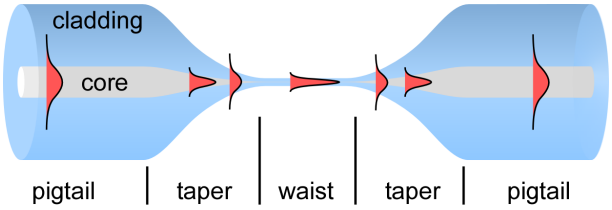

Figure 1.10: *Schematical view of a tapered optical fiber (TOF) in which the optical mode is sketched in red at several axial positions.*

Such a TOF is shown schematically in Fig. 1.10. It is composed of three different parts: The subwavelength diameter nanofiber (waist) is connected on both sides to the unmodified part of the fiber (pigtail) by two regions in which the radius is tapered (taper). The taper part serves two purposes: It mechanically supports the nanofiber waist so that it is part of a monolithic structure and it transports the light efficiently in and out of the nanofiber waist. In a standard optical fiber, the light is guided by the core–cladding transition that exhibits a small refractive index contrast. Here, the optical mode can be described by the weakly guided fundamental LP_{01}-mode [61]. In the nanofiber section, however, the light is guided by the fundamental HE_{11}-mode of the strongly guiding silica–vacuum interface. In addition the nanofiber exhibits a much smaller diameter than the core of the standard optical fiber. In the taper region the radius of the fiber decreases towards the nanofiber, thereby causing a compression of the guided mode. At small V-parameters, the fundamental LP_{01}-mode transforms into the modes that are guided by cladding–vacuum system, thereby expanding into the cladding region. By choosing a sufficiently small taper angle, the mode can be transformed adiabatically into the fundamental HE_{11}-mode of the silica–vacuum system, meaning that nearly the full optical power is transfered into this mode. By further decreasing the radius, it is further compressed. This mode transfer is studied in detail in [66].

By carefully designing the radius profile of the tapered optical fibers and taking great care to maintain a clean environment during and after the tapering process the TOFs can reach high transmission values of $\geq 98\ \%$, see Ch. 2.3.3. As recently reported, it is also possible to guide higher order modes with high transmission value through the TOF [67, 68].

1.4.1 TOF fabrication using a flame brushing technique

The TOFs that are used in this work are produced via the so-called flame-brushing technique in a computer-controlled home-built fiber pulling rig, designed by F. Warken [60, 65]. For the experiments in this thesis, a single-mode optical fiber is tapered to a diameter of 500 nm. Therefore a SM800 manufactured from Fibercore is used, that is made

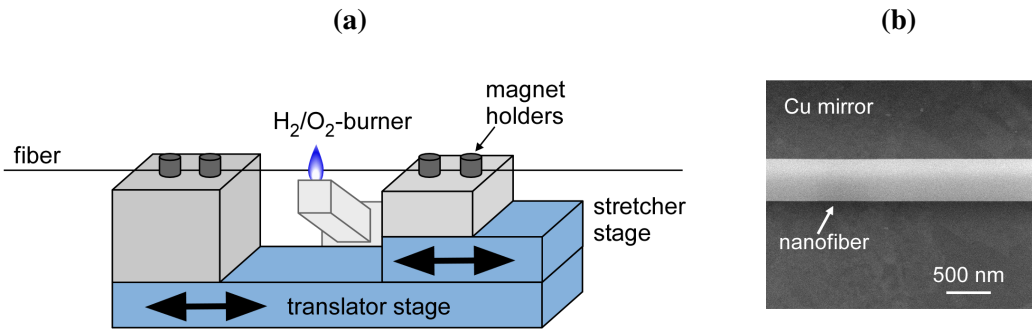

Figure 1.11: *Schematical picture of the fiber pulling rig (a) and electron micrograph of a nanofiber (b).*

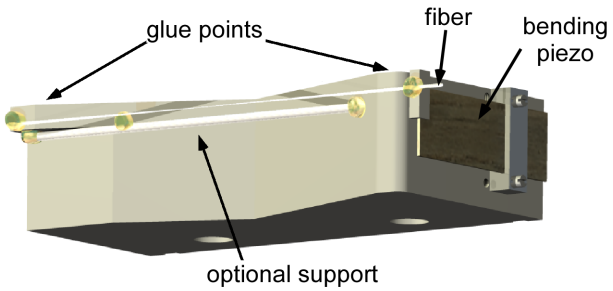

Figure 1.12: *Drawing of the fiber mount. The fiber is fixed to the aluminum holder (left side) and a bending piezo (right side).*

from synthetic fused silica with a germanium doped core. Its cladding and a mode-field diameter are 125 µm and 5.6 µm, respectively. The basic steps for the tapering process are presented in the following.

First, the polymer coating (jacket) of fiber is removed mechanically and the resulting bare fiber is cleaned scrupulously using highly purified aceton from the jacket remainders and a possible pollution caused by the fiber handling. Then the fiber is fixed by magnets to V-groove fiber holders that are attached to the two motorized translation stages of the fiber pulling rig which feature a sub-micron positioning accuracy, see Fig. 1.11(a). Before fixing the second end of the fiber, possible twists in the fiber are removed by laying it out straight and stroking it several times towards the loose end. The translation stages are situated inside a clean box that employs high-efficiency particle (HEPA) filters to ensure a dust-free environment. In the following tapering process, the fiber is heated beyond its softening point by an electronically controlled hydrogen–oxygen burner with a laminar gas-flow in the 1 mm wide heating region. The fiber is moved back and forth relative to the burner using the translator stage while it is simultaneously elongated by the stretcher stage. Thereby, the fiber radius is reduced due to volume conservation. The high surface tension of the silica glass ensures here a smooth fiber surface, see Fig. 1.11(b), and facilitates low scattering losses.

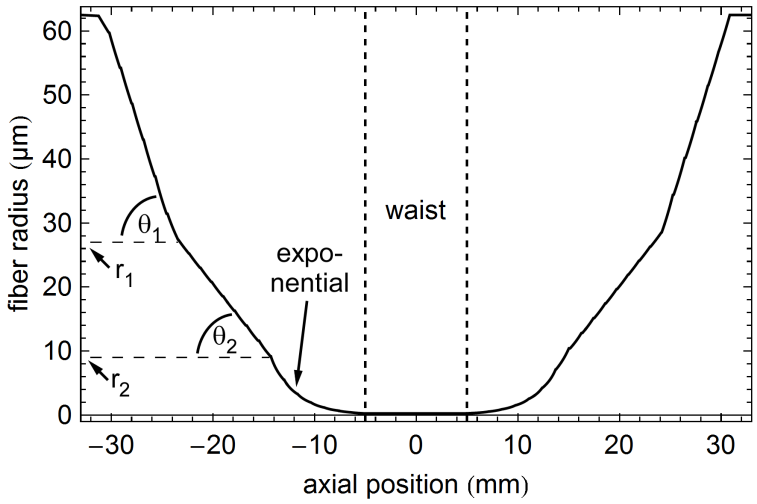

Figure 1.13: *Typical radius profile of a tapered optical fiber. The symmetric profile consisists of r, starting from the untapered fiber, two linear sections with angles θ_1 and θ_2 that decrease to the limiting radii r_1 and r_2. This is followed by a section with a exponentially decreasing radius profile and the cylindrical waist.*

After the pulling process, the fiber is glued to a fiber mount using a UV-curing glue. One of the fiber mounts that is used in the following experiments is shown in Fig. 1.12. It is composed of an aluminum holder with a bending piezo (Piezomechanik BM 120/36/350) attached to one side via a teflon mount. The fiber is fixed on one side to the aluminum holder and to the piezo on the other side using UV-curing glue. This way, the piezo allows to strain the TOF by axially displacing one fiber end by ± 350 µm with a maximum drag force of 0.25 mN in a controlled way. For a further mechanical stabilization enhancement a metal tube can be added parallel to the fiber which is then used to fixate the fiber with additional glue dots.

The flame-brushing technique allows to fabricate nearly arbitrary radius profiles by simulating the tapering process and computing the stage movement trajectories from the design-profile in advance. In this work a symmetrical radius profile is used where each half is composed of two sections with linearly decreasing radius and a section with an exponentially decreasing radius, see Fig. 1.13. Thereby, the mode can be adiabatically transformed in the critical region where the fiber mode leaves the core and is transfered into the nanofiber mode by choosing θ_2 sufficiently small to ensure low losses. Simultaneously, the taper length can be reduced by using a large angle θ_1 in the taper region, where the mode is guided by the fiber core. Measurements of the radius profile carried out in the context of this work with a scanning electron microscope (SEM) have shown that the actual radius profile agree with the simulated radius profile within the measurement accuracy of ± 10 % [69]. Furthermore, the radius homogeneity in the waist region has been determined in previous experiments and shows a very small relative radius variation of ~ 1 % [13].

Modifications of the fused silica caused by the flame brushing technique

Four types of fused silica are commercially available: Type I is produced by electric melting of quartz crystals, type II by flame fusion of natural quartz powder, type III is a synthetic glass that is produced by hydrolization of $SiCl_4$ when sprayed on an OH-flame, and type IV is synthetically produced from $SiCl_4$ in a water vapor-free plasma flame [70]. The glass used for optical fibers is a high quality synthetic fused silica to ensure the high transmission values that are necessary for long range optical communication in the telecom wavelength bands (≈ 1.3 µm and ≈ 1.5 µm). Therefore, it is crucial to have a low impurity level and especially a low water content that exhibits resonances at 2.2 µm and 2.7 µm. The flame brushing technique used in our fiber pulling rig uses an hydrogen–oxygen flame for the fiber heating that will raise the water content in the taper and waist section. As a consequence, the nanofiber can be expected to be of a mixture of type III and type IV fused silica.

CHAPTER 2

Nanofiber resonators

The efficient coupling of light to quantum emitters, such as atoms, molecules or quantum dots, with high control over the interaction is a great challenge and attracts considerable attention. The interaction can be strongly enhanced with respect to free-space approaches by coupling the emitters to the transversely tightly confined evanescent field of subwavelength optical fibers, as presented in the previous chapter. Another approach towards enhancing light–matter interaction is to employ optical microresonators in which the light is circulating and thus passes the emitters many times [29]. Here, both approaches are combined by building a microresonator with an integrated nanofiber waist which allows to reach the strong-coupling regime of cavity quantum electrodynamcis. In addition, such resonators are highly sensitive to variations of the optical properties of the nanofiber. This makes them an interesting tool for the study of physical processes via their effect on the nanofiber guided light as will be shown in the following chapters.

Figure 2.1 shows a sketch of the nanofiber resonator which comes in two designs, depending on the resonator length. Both are composed of two fiber-integrated Bragg mirrors that form a Fabry-Pérot type cavity. These mirrors are either realized as photonic structures in the nanofiber waist, the nanofiber Bragg gratings (NFBG), or as fiber-Bragg gratings (FBGs) in the untapered part of the fiber such that the tapered optical fiber is inside the resonator volume.

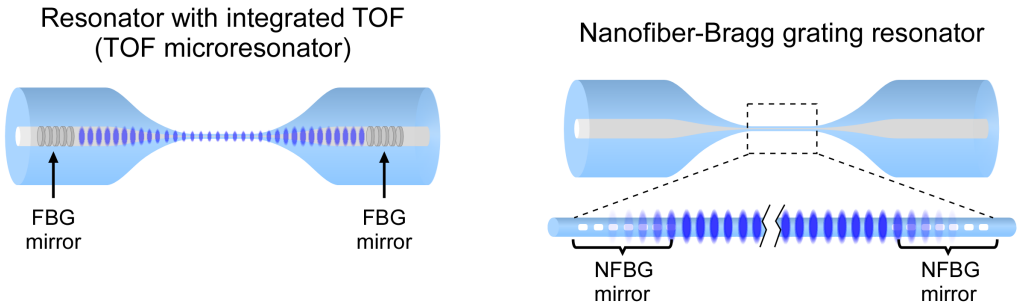

Figure 2.1: *Schematic view of the two designs of the nanofiber resonator.*

A variety of fabrication techniques for FBGs is available. In standard optical fibers, a laser inscription technique is well established [71]. In the case of nanofibers, the small diameter demands high precision techniques for a deterministic fabrication method. Several approaches have been successfully implemented [72, 73], which include focused ion beam milling of grooves or slits in the nanofiber [73–78], chemical thinning of a standard optical fiber with an integrated FBG [79], creating periodic dents in the nanofiber by laser ablation [80, 81], and external gratings brought into the evanescent field of the fiber [82]. Here, the focused ion beam method is employed to fabricate the photonic structures because it provides the highest flexibility in the design of the photonic structures, meaning that the position and shape of each element can be individually chosen.

The first part of this chapter summarizes the theory of Fabry-Pérot type resonators and photonic mirrors. Furthermore, it gives a short introduction to atom–cavity coupling in the framework of cavity quantum electrodynamics and discusses the cavity benchmark parameters. This is followed by the experimental realization of the nanofiber Bragg gratings using a focused ion beam milling technique and their optical characterization. The last part is concerned with fabrication and optical characterization of the resonator with integrated fiber Bragg gratings, the TOF-microresonator.

2.1 Fabry-Pérot resonators

In the following, the theoretical description of Fabry Pérot (FP) resonators is presented. First the simplified model of a FP-resonator made from two mirrors with broad spectral reflectivity is presented. The second part deals with the theory of photonic stacks using the transfer matrix approach that is capable of computing the spectral response of arbitrary photonic structures. The last part gives an introduction to atom–light coupling in the context of cavity quantum electrodynamics. The theory presented here closely follows standard textbooks [63, 83].

2.1.1 Fabry-Pérot resonators from plain mirrors

A Fabry-Pérot etalon consists of two highly reflecting mirrors that are separated by some distance as schematically depicted in Fig. 2.2. Here, the light enters the resonator via the left mirror and is reflected back and forth between the two mirrors. In order to find constructive interference, the phase that is acquired by the field during one round-trip must be an integer multiple of 2π, corresponding to the boundary condition that an integer multiple of half the wavelength of the light fits into the resonator.

Each resonator mirror is described by its complex field amplitude reflection and transmission coefficient $\tilde{r}_i = r_i \exp(\mathbb{i}\,\phi_{r,i})$ and $\tilde{t}_i = t_i \exp(\mathbb{i}\,\phi_{t,i})$ respectively. The resonator volume between both mirrors enters with its transmission value and the phase picked up by the wave while crossing it $t_\mathrm{R} \exp(\mathbb{i}\Delta\phi)$, where $\Delta\phi = k_0\, L_\mathrm{opt}$ is given by the product of the free space propagation constant k_0 and the optical path length $L_\mathrm{opt} = \int_0^L \mathrm{d}z\; n(z)$. The superposition principle allows to sum up the electric field amplitudes at a given point in the volume. This is done for A_ic close behind the left mirror by taking into account that

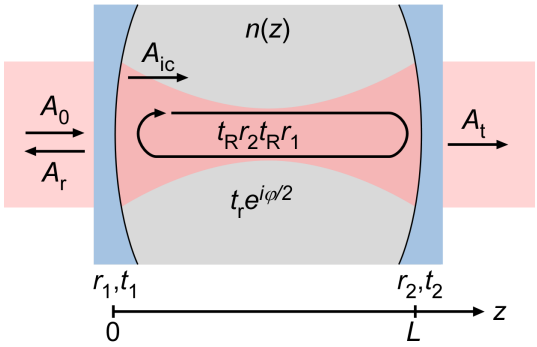

Figure 2.2: *Schematical view of a FP resonator consisting of two mirrors (blue) placed at a distance L from each other and surrounding a medium of refractive index $n(z)$ which may vary as function of the axial position z. The electric field amplitudes of the wave, A, are indicated at different positions in the cavity. The remaining quantities are introduced in the main text.*

the field amplitude is multiplied by $t_\mathrm{R}^2\, r_1\, r_2$ during each round-trip:

$$\begin{aligned} A_\mathrm{ic} &= A_0\, t_1 (1 + r_1\, r_2\, t_\mathrm{R}^2 \exp(2\mathrm{i}\,\Delta\phi) + (r_1\, r_2\, t_\mathrm{R}^2 \exp(2\mathrm{i}\,\Delta\phi))^2 + ...) \\ &= \frac{A_0\, t_1}{1 - r_1\, r_2\, t_\mathrm{R}^2 \exp(2\mathrm{i}\,\Delta\phi)}\,, \end{aligned} \tag{2.1}$$

where the geometrical series $\sum_{n=0}^{\infty} \alpha^n = 1/(1-\alpha)$ for $\alpha < 1$ was used.

Taking the field of the incoming wave into account, the spectral (intensity) transmission T and reflection R of the cavity can be computed from the ratio of the corresponding outgoing intensity to the incoming intensity. Taking into account that the mirrors induce a phase shift of π (only) upon reflection when encountered from outside the cavity (due to energy conservation, see [84]) one obtains:

$$T_{FP} = \frac{|A_{ic}\, t_2\, t_\mathrm{R}|^2}{|A_0|^2} = \underbrace{\left(\frac{t_1\, t_2\, t_\mathrm{R}}{1 - t_\mathrm{R}^2\, r_1\, r_2}\right)^2}_{T_\mathrm{max}} \frac{1}{1 + \left(\frac{2\mathcal{F}}{\pi}\right)^2 \sin^2(\pi f / \Delta f_\mathrm{FSR})}\,, \tag{2.2a}$$

$$\begin{aligned} R_{FP} &= \frac{|-A_0\, r_1 + A_{ic}\, r_2\, t_\mathrm{R}^2 \exp(\mathrm{i}\Delta\phi)\, t_1|^2}{|A_0|^2} \\ &= \frac{r_1^2}{(1 - r_1\, r_2\, t_\mathrm{R}^2)^2} \frac{(1 - [t_1^2 + r_1^2]\, t_\mathrm{R}^2\, r_2/r_1)^2 + 4([t_1^2 + r_1^2]\, t_\mathrm{R}^2\, r_2/r_1)\, \sin^2(\pi f/\Delta f_\mathrm{FSR})}{1 + \left(\frac{2\mathcal{F}}{\pi}\right)^2 \sin^2(\pi f/\Delta f_\mathrm{FSR})}\,, \end{aligned} \tag{2.2b}$$

where the cavity parameters finesse $\mathcal{F}$ and free spectral range Δf_FSR were introduced which are given by the expressions

$$\mathcal{F} = \frac{\pi \sqrt{t_\mathrm{R}^2\, r_1\, r_2}}{1 - t_\mathrm{R}^2\, r_1\, r_2}\,, \quad \Delta f_\mathrm{FSR} = \frac{c}{2\, L_\mathrm{opt}}\,. \tag{2.3}$$

Typical transmission spectra of FP-cavities are shown in Fig. 2.3 for several finesse values. Each features a series of resonances with a frequency spacing of Δf_FSR, corresponding to the roots of the sinus term in Eq. (2.2a). The width of the resonances

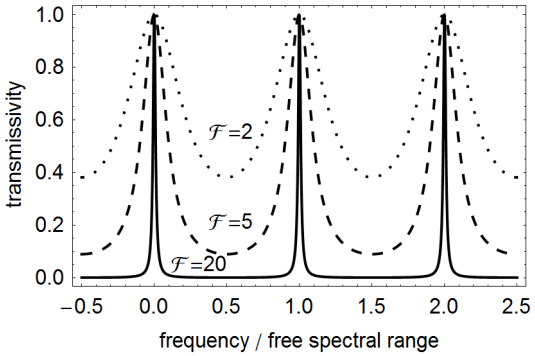

Figure 2.3: *Transmission spectra of symmetric lossless Fabry-Pérot resonators with the finesse values given in the plot.*

decreases with increasing values of $\mathcal{F}$ which can be understood by computing the full width at half maximum (FWHM) of the resonances δf_{res}. For high finesse values $\mathcal{F} \gg 1$ the approximation $\sin(\pi\, f/\Delta f_{\mathrm{FSR}}) \approx \pi\, f/\Delta f_{\mathrm{FSR}}$ holds in the vicinity of the resonance so that the resonance width is given by the expression

$$\delta f_{\mathrm{res}} \approx \Delta f_{\mathrm{FSR}}/\mathcal{F} \tag{2.4}$$

thereby demonstrating that the finesse can be extracted from the spectrum by the ratio of the FSR and the FWHM of the resonance.

In the special case of a cavity that is symmetric ($R = r_1^2 = r_2^2$) with lossless mirrors ($r_i^2 + t_i^2 = 1$) and a intra-cavity transmission $T_R = |t_R|^2$, Equations (2.2a – 2.2b) simplify to

$$T_{FP} = \frac{(1-R)^2\, T_{\mathrm{R}}}{(1-T_{\mathrm{R}}\, R)^2} \frac{1}{1+\left(\frac{2\mathcal{F}}{\pi}\right)^2 \sin^2(\pi f/\Delta f_{\mathrm{FSR}})} \tag{2.5a}$$

$$R_{FP} = \frac{R}{(1-R\, T_{\mathrm{R}})^2} \frac{(1-T_{\mathrm{R}})^2 + 4T_{\mathrm{R}}\, \sin^2(\pi f/\Delta f_{\mathrm{FSR}})}{1+\left(\frac{2\mathcal{F}}{\pi}\right)^2 \sin^2(\pi f/\Delta f_{\mathrm{FSR}})}\,. \tag{2.5b}$$

These equations yield a good approximation for the spectral response of cavities with high quality mirrors.

2.1.2 Dispersive cavity media

When considering nanofiber-based resonators, the dispersion of the nanofiber section has to be taken into account, compare Ch. 1.3. In other words, the change of the phase velocity has to be taken into account when computing the phase that is acquired by the wave when traversing the cavity medium ($\Delta\phi$). It is typically sufficient to replace the optical phase velocity c with the group velocity $c_g = \partial\omega/\partial k$, where k is the propagation constant of the light field. This can be understood by computing the phase change $\Delta\phi(\omega_0) - \Delta\phi(\omega_0 + \Delta\omega)$ that occurs when the light field frequency ω_0 changes by $\Delta\omega$. Then, in

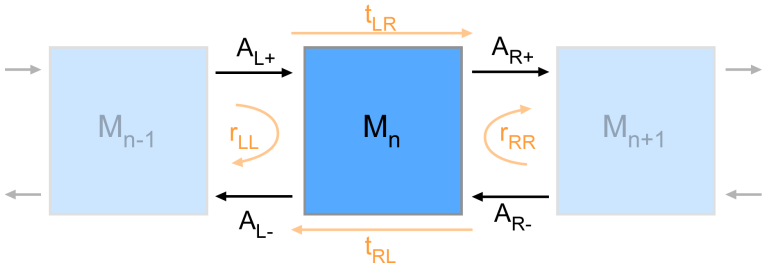

Figure 2.4: *In the transfer matrix formalism, the n-th element of the optical system is described by a matrix that relates the field amplitudes of the incoming and outgoing waves via a matrix M_n. The full system is described by multiplying the matrices.*

linear approximation, the additional phase amounts to

$$\begin{aligned}\Delta\phi(\omega_0) - \Delta\phi(\omega_0 + \Delta\omega) &= L\,k(\omega_0) - L\left[k(\omega_0) + \frac{\partial k}{\partial \omega}(\omega_0)\,\Delta\omega\right] \\ &= L\,\frac{\Delta\omega}{c_g(\omega_0)}\,. \end{aligned} \tag{2.6}$$

Now consider the free spectral range, which corresponds to the frequency spacing for which the relative phase change amounts to π, compare the denominator of Eq. (2.2a). Assuming, without loss of generality, that a resonance occurs at ω_0. Then, Eq. (2.6) yields $L\,\Delta\omega/c_g = \pi$ and the FSR results in

$$\Delta f_{\mathrm{FSR}} = \frac{c_g}{2\,L_{\mathrm{opt}}}\,. \tag{2.7}$$

The expression for the peak width follows in direct analogy.

2.1.3 Photonic stack mirrors – Transfer matrix formalism

The previously used approach of accumulating the reflected and transmitted waves scattered by all interfaces in an optical assembly can quickly become very complex. This applies all the more when treating photonic structures where a high number of elements is involved. This calls for a more versatile approach which is given by the transfer matrix formalism in which each element is treated by its effect on the amplitude and phase of the incoming and outgoing waves. By including all modes that are coupled via an element, this approach gives an exact description. Since this work is concerned with single-mode waveguides, a good approximation of the system is obtained by considering only one mode including the two polarization states and the forward and backward propagating directions. The coupling to other modes is treated as losses.

Consider an optical element with the complex valued amplitudes of the incoming waves A_{L+} and A_{R-} and outgoing waves A_{L-} and A_{R+} at each of its interfaces, see Fig. 2.4. These amplitudes can be related to each other by the matrix equation

$$\begin{pmatrix} A_{R+} \\ A_{R-} \end{pmatrix} = \underbrace{\begin{pmatrix} M_A & M_B \\ M_C & M_D \end{pmatrix}}_{M} \begin{pmatrix} A_{L+} \\ A_{L-} \end{pmatrix}\,, \tag{2.8}$$

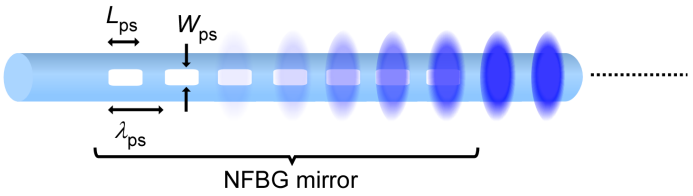

Figure 2.5: *Sketch of a nanofiber Bragg grating, NFBG.*

where the transfer matrix M was introduced. This way, the response of an optical assembly is the product of the matrix representations of its constituent elements

$$M = M_N \cdot M_{N-1} \cdot ... \cdot M_1 \, . \tag{2.9}$$

An equivalent and more intuitive formulation can be gained by using a different combination of the input and output fields

$$\begin{pmatrix} A_{R+} \\ A_{L-} \end{pmatrix} = \underbrace{\begin{pmatrix} t_{LR} & r_{RR} \\ r_{LL} & t_{RL} \end{pmatrix}}_{S} \begin{pmatrix} A_{L+} \\ A_{R-} \end{pmatrix} \, , \tag{2.10}$$

where S is called the scattering matrix. It contains measurable optical properties, i.e. the complex reflection and transmission coefficients. However, it lacks the possibility to compute the response of the assembly by simple multiplication from the scattering matrices of the elements. Since both formulations can be related via

$$M = \frac{1}{t_{RL}} \begin{pmatrix} t_{LR}\, t_{RL} - r_{RR}\, r_{LL} & r_{RR} \\ -r_{LL} & 1 \end{pmatrix} \, , \quad S = \frac{1}{M_D} \begin{pmatrix} M_A\, M_D - M_B\, M_C & M_B \\ -M_C & 1 \end{pmatrix} \, , \tag{2.11}$$

it is advantageous to employ both approaches by first computing the response of the assembly using the transfer matrix and then transforming it to the scattering matrix to obtain the reflection and transmission coefficients.

Nanofiber Bragg gratings

This matrix method is now applied to the case of a photonic structure in an optical nanofiber. The nanofiber Bragg gratings (NFBGs) consists of a stack of alternating nanofiber segments in which the guided mode exhibits different propagations constants. This is experimentally realized by milling slits with a fixed length and spacing into the nanofiber waist, see Fig. 2.5. In the slit sections a larger power fraction of the mode propagates outside the silica compared to the unmodified nanofiber sections, so that the effective refractive index of the mode is lowered. Thereby, the propagation constant of the optical mode is modified periodically leading to the desired reflection properties.

In the transfer matrix formalism, an NFBG with N periods can be described by the matrix that results from multiplication of the two matrices that describe the fiber M_{fiber} and the slit M_{slit}:

$$M_{\text{NFBG}} = M_{\text{slit}} \left(M_{\text{fiber}}\, M_{\text{slit}} \right)^{N-1} \, . \tag{2.12}$$

The unprocessed fiber does not modify the fiber mode and can be treated in analogy to the free propagation of a beam with propagation constant β:

$$M_{\text{fiber}} = \begin{pmatrix} \exp(-\mathbb{i}\,\beta\, D_{\text{ps}}) & 0 \\ 0 & \exp(\mathbb{i}\,\beta\, D_{\text{ps}}) \end{pmatrix} , \tag{2.13}$$

where $D_{\text{ps}} = \lambda_{\text{ps}} - L_{\text{ps}}$ is the separation of the sections with a slit. The transfer matrix of a slit can be computed from coupled mode theory and the corresponding derivation can be found in the literature [78]. A summary of the derivation and the results are given in Ch. A.3.

2.1.4 Atom–cavity interaction

A goal in atom physics is to design and fabricate optical cavities that facilitate the study of the coherent interaction of few atoms with few photons. The challenge here is to enhance the coupling of the atom with the cavity field up to the point where a single photon stored in the cavity interacts multiple times with the atom before it leaves the cavity or is lost from spontaneous decay of the atom into free space. This interaction of few photons and atoms is described in the framework of cavity quantum electrodynamics (CQED) and the regime described above is called the strong coupling regime. Several standard text books give a comprehensive treatment of the theory and experiments [83, 85, 86] and I will only give a brief introduction to the basic concepts and focus on the benchmark parameters for nanofiber-based cavities.

The electric field of a propagating photon with frequency ω_p is known from quantum electrodynamics and can be written as

$$\boldsymbol{E}(\boldsymbol{r}) = \mathcal{E}_0\, f(\boldsymbol{r})\, \left[a\, \boldsymbol{e}^*(\boldsymbol{r}) + a^\dagger\, \boldsymbol{e}(\boldsymbol{r})\right] \tag{2.14}$$

where a and $a^\dagger$ are the photon annihilation and creation operators, $\boldsymbol{e}(\boldsymbol{r})$ denotes the normalized polarization vector, and $f(\boldsymbol{r})$ the cavity mode profile. Furthermore, $\mathcal{E}_0$ denotes the electric field per photon which is derived by assuming that the energy of one photon $\hbar\omega_p$ is stored in the cavity mode:

$$\mathcal{E}_0 = \sqrt{\frac{\hbar\,\omega_p}{\epsilon_0\,\mathcal{V}}} , \qquad \mathcal{V} = \int_V \mathrm{d}V\; \epsilon(\boldsymbol{r})\, |f(\boldsymbol{r})|^2 , \tag{2.15}$$

where the mode volume $\mathcal{V}$ was introduced, $\epsilon(\boldsymbol{r})$ is the permittivity and V is the physical cavity volume.

An atom is treated here as a two-level system that interacts with the photon field via its dipole moment (dipole approximation). The two levels are denoted as the ground state $|g\rangle$ and the excited state $|e\rangle$ which are separated by the energy difference $\hbar\,\omega_a$. The interaction of a cavity photon with an atom in the rotating wave approximation is described by the Hamilton operator

$$H_a = -\mathcal{E}_0\, f(\boldsymbol{r})\, \left[\boldsymbol{d}\cdot\boldsymbol{e}^*(\boldsymbol{r})\, a\, \sigma_+ + \boldsymbol{d}^*\cdot\boldsymbol{e}(\boldsymbol{r})\, a^\dagger\, \sigma_-\right] \tag{2.16}$$

where $\boldsymbol{d}$ is the atomic dipole and $\sigma_- = |g\rangle\langle e|$ and $\sigma_+ = |e\rangle\langle g|$ are the atomic raising and lowering operators, respectively.

The Hamilton operator of the atom–cavity system takes the photon field, the atom and their interaction into account. It is often called the Jaynes-Cummings Hamiltonian, giving credit to the two scientists who devised it [87], and it takes the form

$$H_{\mathrm{tot}} = \frac{\hbar\,\omega_a}{2}\,\sigma_z + \hbar\,\omega_p\,\left[a^\dagger\,a + \frac{1}{2}\right] + \hbar\,\left[g(\boldsymbol{r})\,a\,\sigma_+ + g^*(\boldsymbol{r})\,a^\dagger\,\sigma_-\right]\,, \tag{2.17}$$

where the light–atom coupling is defined by the vacuum Rabi frequency

$$g(\boldsymbol{r}) = -\frac{\mathcal{E}_0}{\hbar}\,\boldsymbol{d}\cdot\boldsymbol{e}^*(\boldsymbol{r})\,f(\boldsymbol{r})\,. \tag{2.18}$$

and the $\sigma_z = |e\rangle\langle e| - |g\rangle\langle g|$ is the atomic inversion operator. Note that, when only one atom is present in the cavity, the phase between the light field and the atomic dipole moment can be chosen such that $\boldsymbol{d}\cdot\boldsymbol{e}^* = \boldsymbol{d}^*\cdot\boldsymbol{e}$ is real. The dynamic of the atom–cavity interaction competes with the loss mechanisms in the system, i.e. the photon emission of the atom into free-space or the loss of the photon from the cavity mode. These two processes are typically characterized by the atomic decay rate $2\gamma_a$ and the cavity mode decay rate 2κ. Note that the rates without the factor 2 refer to the amplitude decay rate. The strong coupling condition for the observation of coherent interaction can then be formulated as

$$g(\boldsymbol{r}) \gg \kappa, \gamma_a\,, \tag{2.19}$$

stating that the evolution of the system must happen much faster than the dissipative processes. These two requirements are often combined in one single, weaker, condition:

$$C = \frac{g^2(\boldsymbol{r})}{2\,\kappa\,\gamma_a} \gg 1\,, \tag{2.20}$$

where C is called the cooperativity parameter per atom [83, Ch. 5]. In other terms its inverse value $N_0 = C^{-1}$ defines a critical atom number for which the dynamics evolves on the same time scale as the (averaged) dissipative processes. The nomenclature for these requirements are not homogeneous throughout the literature. Throughout this work, the following convention will be used: The condition $C \gg 1$ will be referred to as strong coupling regime and the additional requirements $g(\boldsymbol{r}) \gg \kappa, \gamma_a$ as the regime of coherent dynamics and $\kappa > g(\boldsymbol{r}) \gg \gamma_a$ as the fast cavity regime.

The cooperativity is a pure cavity parameter and can be expressed in terms of the mode volume and the quality factor of the resonator mode (Q). By using the expressions for the cavity decay rate and free space atomic transition rate [63, 88]

$$\kappa = \frac{\omega_p}{2\,Q}\,, \quad \text{and} \quad \gamma_a = \frac{|\boldsymbol{d}|^2\,k_0^3}{6\,\pi\,\hbar\,\epsilon_0}\,, \tag{2.21}$$

one obtains

$$C = \frac{3}{4\,\pi^2}\,\frac{Q}{\tilde{\mathcal{V}}}\,|f(\boldsymbol{r})|^2 \tag{2.22}$$

where the mode volume is normalized to the optical wavelength $\tilde{\mathcal{V}} = \mathcal{V}/\lambda_p^3$. This result can be intuitively understood by considering that the photon field at the position of the atom increases for a decreasing mode volume so that the interaction is stronger. Furthermore, a higher Q-factor of the resonator increases the time the photon stays in the cavity and thus results in a higher interaction probability with the atom. As a result of this finding, one typically aims to minimize the mode volume of the resonator, i.e. miniaturize the resonator, and simultaneously reach a high Q factor by minimizing the intra-cavity loss.

CQED parameters of nanofiber-based FP-type resonators

For resonators that incorporate (parts of) a TOF the computation of the mode volume can become highly complex. This is due to the position dependence of the optical propagation constant in the TOF. For efficient light–matter interaction though, only the field in the ultrathin section of the resonator is relevant. As a consequence, the remaining parts of the resonator act as a delay line for the photon and their exact realization plays no role for the CQED performance. This motivates to model such a cavity as a FP-type resonator consisting of a nanofiber with the diameter corresponding to the TOF waist diameter, terminated by two mirrors. The (effective) geometrical length of the resonator in this model, L_{eff}, is then chosen such that the round-trip time t_{RT} of the light field is the same as in the resonator while the effective refractive index is that in the nanofiber waist n_{w}. The light passes the resonator volume two times during a round-trip, so that the effective length is given by

$$L_{\mathrm{eff}} = \frac{c_0}{n_{\mathrm{w}}} \frac{t_{\mathrm{RT}}}{2} = \frac{c_0}{2\, n_{\mathrm{w}}\, \Delta f_{\mathrm{FSR}}} \,. \tag{2.23}$$

In fact, L_{eff} is now determined by measurable cavity parameters. The field per photon results then from the energy integral, where the integration over the cavity length $\int_0^L \mathrm{d}z$ simplifies to that over one wavelength which is multiplied by the number of wavelengths $L_{\mathrm{eff}}/\lambda \int_0^\lambda \mathrm{d}z$ which then results in

$$\hbar\omega = \mathcal{E}_0^2 \epsilon_0 \frac{L_{\mathrm{eff}}}{\lambda} \int_0^\lambda dz \int_A \mathrm{d}A \;\; \epsilon(\boldsymbol{r}) \;\; |f(\boldsymbol{r})|^2 \;\; , \tag{2.24}$$

where A denotes the plane perpendicular to the fiber axis and λ the optical wavelength in the nanofiber, compare Eq. (1.23).

Typically, FP-type resonators are characterized by their free spectral range and finesse, so that it is desirable to find expressions that are based on these quantities. From Eqns. (2.20-2.21) and using the relation $Q = \omega_p \mathcal{F}/(2\pi\, \Delta f_{\mathrm{FSR}})$ one obtains

$$C = \frac{3\epsilon_0\, \mathcal{E}_0^2\, \mathcal{F}}{\hbar\, k_0^3\, \Delta f_{\mathrm{FSR}}} \, |f(\boldsymbol{r})|^2 \tag{2.25}$$

$$\kappa = \frac{\pi\, \Delta f_{\mathrm{FSR}}}{\mathcal{F}} \,. \tag{2.26}$$

Consider the scaling of the CQED parameters with the cavity length L_{opt} in the case where the intracavity loss $(1 - t_{\mathrm{R}}^2)$ or equivalently $\mathcal{F}$, is largely independent of L_{opt} (see also [64]). This assumption is justified in the case of a resonator containing a TOF, where

the major losses originate from the transmission losses of the taper, as well as for resonators made from such photonic structures with high scatter losses. In this case, g depends on L_{opt} via the single photon field according to $g \propto 1/\sqrt{L_{opt}}$ while κ decreases with the cavity length as $\kappa \propto 1/L_{opt}$. Given that γ_a is independent of L_{opt}, this yields

$$g/\kappa \propto \sqrt{L_{opt}} \tag{2.27a}$$

$$g/\gamma_a \propto 1/\sqrt{L_{opt}} \tag{2.27b}$$

$$C = \text{const.} \tag{2.27c}$$

Interestingly, the cooperativity parameter is independent of L_{opt}. This is because the change of the single photon field is compensated by that of the cavity decay rate. However, the two conditions in Eq. (2.19) result in two contradicting requirements: g/κ is maximized when maximizing L_{opt} while g/γ is maximized when minimizing L_{opt}. If $C \gg 1$ is fulfilled, the CQED regime that will be realized (e.g., fast cavity regime or coherent dynamics) can then be chosen according to the desired application via the cavity length.

As an application, the results obtained above will now be applied to a cesium atom that is coupled to a resonator with a nanofiber waist. The maximum coupling between the atom and the nanofiber mode can be reached when the atom is placed at the point of the maximum field intensity, i.e., on the surface of the nanofiber at an antinode of the mode. I choose the quasi-linearly mode because it features a higher maximum field intensity along its polarization axis compared to the quasi-circularly polarized mode. The vacuum Rabi oscillation frequency at the interaction with the π-polarized Cs D2 transition $|F = 4, m_F = 0\rangle \rightarrow |F' = 5, m_{F'} = 0\rangle$, where ($|\boldsymbol{d}| = \sqrt{5/18} \cdot 3.7971 \cdot 10^{-29}\,\mathrm{C\,m}$) results in

$$\frac{g(r=a)}{\sqrt{\Delta f_{\mathrm{FSR}}}} = 2\pi \cdot 978\,|f(\boldsymbol{r})|^2\,\frac{\mathrm{Hz}}{\sqrt{\mathrm{Hz}}} \tag{2.28}$$

$$\gamma_a = 2\pi \cdot 2.6\ \mathrm{Mhz}\ . \tag{2.29}$$

This in particular means that the condition $g \gg \kappa$ is fulfilled for cavities with a FSR larger than $\Delta f_{\mathrm{FSR}} \gg 2.2$ MHz or $L_{\mathrm{opt}} \ll 70$ m which is easily achievable.

2.2 Nanofiber Bragg grating resonators

In the following, a realization of a resonator that is integrated in the nanofiber waist of a TOF is presented. In this resonator, the mirrors are implemented as two nanofiber Bragg grating (NFBG) within the nanofiber. These NFBGs are fabricated using a focused ion beam (FIB) milling machine. Each of them consists of a series of equidistant slits which cause a periodic modulation of the effective refractive index of the mode along the propagation direction of the mode. This can be intuitively understood by comparing the fraction of the mode that propagates in fused silica in a nanofiber section with a slit to that without a slit: In a nanofiber section including a slit, a larger fraction of the mode propagates outside of the fiber so that the effective refractive index is smaller than in a plain nanofiber.

First, the fabrication method of the NFBGs is presented which is complemented by a spatial (3D) characterization scheme similar to the tomographic method. The spatial geometry is used to predict the optical response by the transfer matrix technique. In the next section, the setup for the optical characterization is presented and the optical response of the NFBG resonators is measured. Based on these measurements, the effect of individual fabrication steps on the optical properties of the resonator is studied and a possible annealing procedure of the NFBGs is discussed.

2.2.1 Fabrication

The nanofiber Bragg gratings that constitute the mirrors of the Fabry-Pérot type resonator are realized as a series of slits that are milled in the nanofiber waist of the TOF. For this purpose, commercial focused ion beam milling (FIB) machines are used. They employ a tightly focused gallium ion beam to remove small amounts of material from a surface under vacuum conditions ($p \sim 10^{-6}$ mbar). As schematically shown in Fig. 2.6(a), a primary gallium ion beam with high kinetic energy per particle of $(5 - 30)$ keV impinges on the material where it deposits its energy by collisions. It thereby removes material as secondary ions (a^+), their electrons (e^-), neutral atoms (a), and secondary electrons (e^-). The beam is scanned line-wise over the area that is to be removed (orange area). The small beam width of few nanometers in combination with the raster scanning scheme allows to produce complex structures of very small sizes with high accuracy.

The FIB is realized as an additional module attached to a scanning electron microscope (SEM) in a confocal configuration, see Fig. 2.6(b), in which the two beams intersect with a relative angle of 52 $^\circ$ on the sample. The sample is mounted to a high precision six axis positioning stage which allows one to position and to align the sample in an almost arbitrary way. In particular, the stage is used to bring the sample to the intersection point of the two beams so that the electron beam can be used for the pre-alignment. Only the fine adjustment is done using the FIB-beam, thereby minimizing the damage to the sample outside the areas to be milled.

From our experiments with different FIB machines, it became apparent that it is essential that the machine is situated in a clean laboratory environment. This has two reasons: First the fiber needs to be handled in the environmental atmosphere for several minutes and, second, any pollutants that also enter the vacuum chamber while loading are dis-

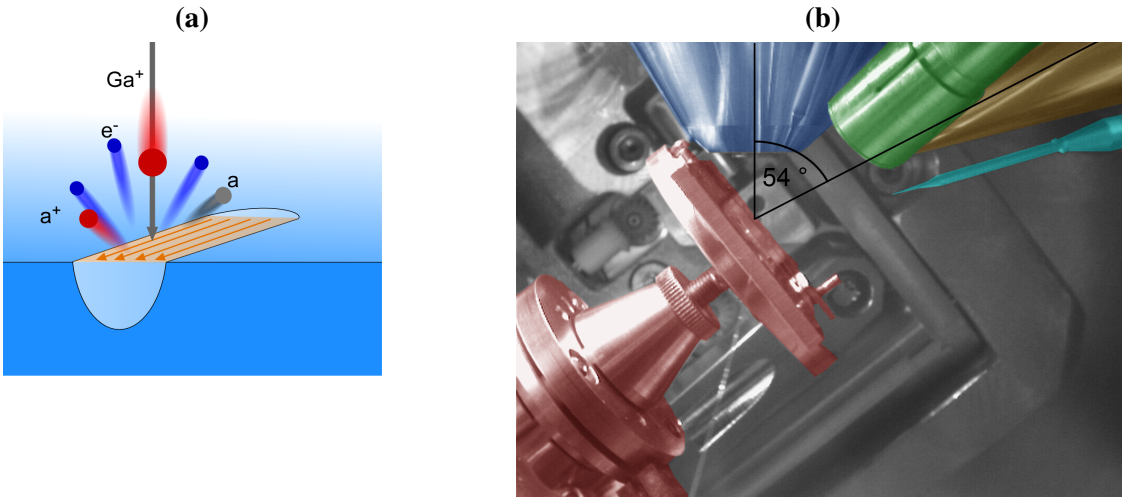

Figure 2.6: *(a) Sketch of the FIB milling process. The primary gallium ion beam knocks out material by collisions in the form of ions, electrons and neutral atoms. (b) Image of the setup in the vacuum chamber of the FIB with retroactively tinted parts. The scanning electron microscope is shown in dark blue, the secondary electron detector in green, the FIB in yellow, the sample and holder in red and the manipulator in light blue.*

tributed during the evacuation process because the latter leads to turbulent flows in the chamber.

Sample preparation

Due to the insulating property of the silica glass, the nanofiber charges up during the milling process. As a consequence, the nanofiber and the ion beam eventually repell each other. When using a free standing fiber, the repulsion induces a transversal vibration of the fiber with amplitudes that are much larger than the fiber diameter so that no precision machining is possible [65]. Several strategies can be employed to avoid the charging or the movement of the fiber, such as metal coating the fiber during the milling process which is removed afterwards [77]. Here, I use a different approach. The fiber is placed on a polished copper mirror where it is fixed by the van der Waals force and can discharge through the metal, see Fig. 2.7. The mirror is structured with grooves to prevent redeposition of the copper that is unintentionally removed when milling through the fiber. The mirrors were structured either from laser ablation or photo-lithography and successive etching. It is essential to produce a smooth surface in order to ensure that the fiber lies flat on the mirror. Surface roughness from dirt or production imperfections severely lower the force that attaches the fiber to the surface. The mirror is cleaned before each FIB fabrication with hydrochloric acid which also removes the oxygen layer on the copper surface and is stored in a dry box with silica gel to prevent oxidation.

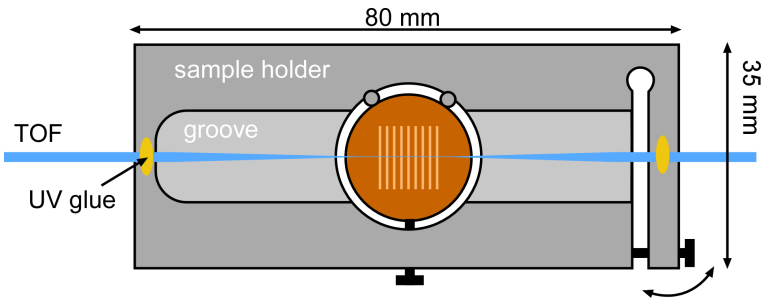

Figure 2.7: *Schematical view of the fiber holder for FIB processing. The fiber is fixed to the holder by UV curing glue and can be strained and relaxed via a cantilever (right fixation point) to deposit or lift off the fiber from the mirror surface (orange).*

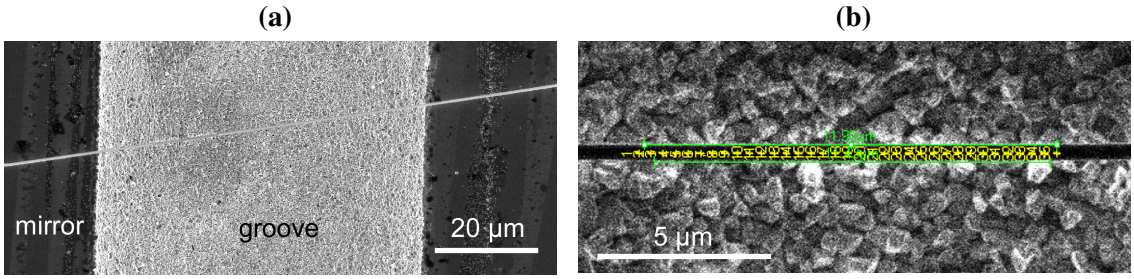

Figure 2.8: *(a) Electron micrograph of the nanofiber (bright diagonal line) placed over a grove (grainy bright area) in a copper mirror with a flat surface (dark areas). (b) Ion micrograph of the nanofiber (dark rectangle) with an software overlay of the milling pattern in yellow (numbers are solely for identification). The two horizontal green lines are used for alignment.*

Sample Alignment

The microfabrication process consists of several steps: First, the fiber is deposited on the copper mirror surface and the mount is inserted into the vacuum chamber. Then, the FIB and SEM are focused onto the mirror surface. Then the mirror is moved into the confocal point of the FIB and SEM beam. This is followed by refocusing the beam which is done sufficiently far away from the nanofiber to minimize the damage to the fiber. In the next, step the mirror is tilted to an angle of $54°$ so that the ion beam is oriented perpendicular to the fiber surface, see Fig. 2.6(b), and the fine adjustment of the fiber alignment can be performed . For this purpose, a position at which the fiber spans a groove is searched, see Fig. 2.8(a), and the mount is rotated to align the fiber along the horizontal scan direction of the beam (horizontal in the image). This is followed by a settling time of a few minutes to avoid mechanical drifts during the milling. Alternatively, the beam scan directions can be rotated, if the machine offers the option. This has the advantage that the mechanical drift can be minimized. The fine adjustment is done using ion beam for imaging. For this purpose, two horizontal reference lines with a spacing of the nanofiber diameter are superimposed to the image, see Fig. 2.8(b). Here, short imaging times with low resolution have to be used in order to avoid unnecessary damage to the sample. The alignment should be checked again after another settling time that is comparable to the machining time to

sample	L_{ps}	W_{ps}	λ_{ps}	periods	mirror distance	facility
TOF-FIB-1	138 nm	51 nm	361 nm	25	(3.0 ± 0.3) mm	ZMNS
TOF-FIB-2	136 nm	51 nm	355 nm	30	(2.39 ± 0.1) mm	MPIP
TOF-FIB-3	136 nm	70 nm	361 nm	25	1 mirror	ZMNS
TOF-FIB-4	136 nm	51 nm	355 nm	25	1 mirror	ZMNS

Table 2.1: *Geometry parameters of the photonic structures, where L_{ps} (W_{ps}) is the slit length (width), λ_{ps} is the periodicity of the structure, see also Fig. 2.5. Furthermore, the number of periods, the mirror separation and the production facility is given for each sample.*

ensure that no further drifts will occur in the system.

Milling procedure

After this preparation routine, the photonic structure can be milled. The exact implementation of the milling routine depends strongly on the operating software of the machine. Two FIB machines were used in the course of my experiments, namely Zeiss NEON 40 EsB in combination with a RAITH system at the Center for Micro- and Nanostructures in Vienna (ZMNS) and a FEI Nova 600 Nanolab at the Max Planck Institute for Polymer Research Mainz (MPIP). In each of them, different strategies were employed but certain aspects are common to all machines and are discussed now.

The milling pattern consists of a series of rectangles (or slits) that are transversely centered on the nanofiber. The slits are periodically arranged along the nanofiber axis with a period of λ_{ps}. This design was chosen because the central slits do not break the symmetry of the quasi-linearly polarized nanofiber modes. Furthermore, they lower the refractive index at a position where the mode exhibits a high intensity, thereby providing a high propagation constant contrast of the nanofiber sections with a slit to those without a slit. By designing the structure elements as slits, the resulting photonic structure resembles a photonic stack composed of two media with different refractive indices. By designing the lengths of the sections such that the waves that are reflected at the beginning and end of the slit constructively interfere, the reflectivity per element can be increased compared to, e.g., a small circular hole. The combination of these properties enables one to produce photonic structures with a high reflectivity even for a low number of periods. The length L_{ps} and width W_{ps} of the slits that were manufactured in the different samples are listed in Table 2.1. The milling depth is chosen much larger than the fiber diameter to ensure that the slits reach through the full fiber.

A major challenge when milling photonic structures in a nanofiber is the charging of the latter. When employing a serial milling scheme, i.e., milling successive individual slits, each slit contains strongly localized charges which interact with the ion beam. The resulting force deflects the fiber during the structuring process. A photonic structure produced by this technique is shown in Fig. 2.9. The fiber is visible as a brighter band oriented horizontally in the image and the groove in the copper mirror as a grainy structure in the remaining part of the image. The photonic structure is visible as spots on the fiber. Note that the slits on the left side of the image that were milled first are positioned

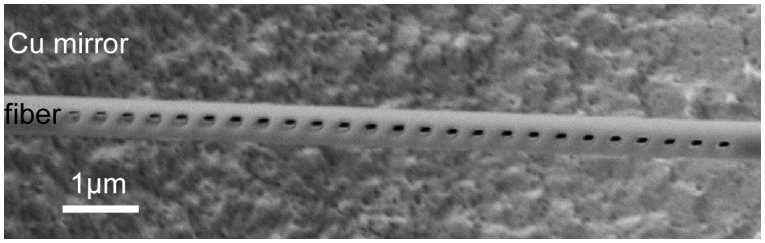

Figure 2.9: *Electron micrograph of a photonic structures produced by serial milling of individual slits. The fiber appears as a bright rectangle and the structures as dark spots. (TOF-FIB-4)*

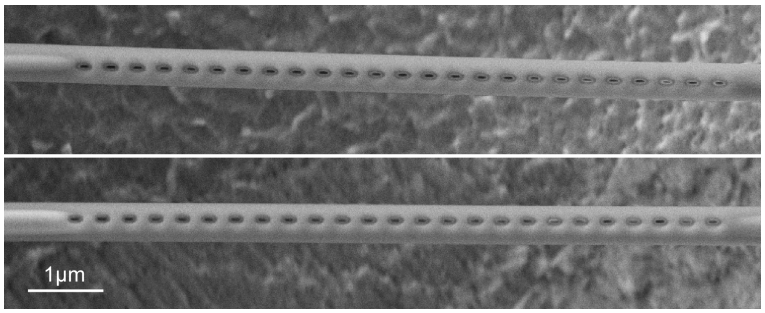

Figure 2.10: *Photonic structures in a nanofiber (TOF-FIB-1). The fiber has been placed on a copper mirror and is suspended free standing above a groove (grainy brackground). SEM voltage: 5 kV, aperture size: 30* µm.

centrally on the fiber while the subsequently milled slits show an increasing deviation from the initial transverse position. Comparing the positions of the slit with that of the holes that were milled in the copper mirror below the slits (dark spots within the holes) one finds that they coincide on the right side of the structures but differ on the left side. This means that the fiber was deflected during the milling process. Such a deflection can be caused by the electrostatic force that the ion beam exerts on the charges in the nanofiber.

It was empirically found, that these localized charges in the serial milling scheme can be avoided by employing a parallel milling strategy in which the full structure is simultaneously milled and the fiber is homogeneously charged. Some FIB operating systems offer this feature directly, in the other case it can be realized by successively milling each slit to a small fraction of the fiber diameter and repeating this structure sufficiently often. In addition, the electron beam of the SEM can be used to charge the fiber negatively during the milling process by imaging a region much larger than the milling area with higher current and repetition rate, i.e. small dwell time and low resolution. Figure 2.10 shows a photonic structure that was milled following this scheme. When using this method, the photonic structure is centered on the nanofiber and shows a homogeneous period and slit geometry.

The FIB as well as the SEM offer a large variety of parameters to control the beam properties. For this application it is essential to optimize the FIB for high resolution, i.e., small beam spot sizes. This can be achieved with high beam energies in combination with

type	energy	current	dwell time	dose ($\mu C/cm^2$)	magnification
FIB	30 keV	$(1-10)$ pA	9 µs	$(3.9-5)\cdot 10^5$	15k
SEM	20 keV	30 µm	short	-	$\approx$10k
FIB-img	30 keV	$(1-10)$ pA	$\ll 9\mu$s	-	15k
SEM-img	$(10-20)$ keV	pA - nA	variable	-	-

Table 2.2: *Typical parameters of the electron and ion beams during the fabrication process. The current is either given in Amperes or characterized by the aperture size used.*

small currents. The latter comes at the expense of the etching rate which, however, need not be high for the small structures considered here. The results presented below have been obtained using the beam parameters for milling and imaging (img) given in Tab. 2.2. Note that the ion beam currents, and therefore the doses, are typically not rigorously calibrated in FIB milling machines since their exact value is not critical for most other FIB applications. Therefore, it is highly recommended to make a calibration run in advance with several milling depths.

2.2.2 Spatial characterization

The geometrical 3D characterization of the NFBGs is performed via a scheme that is similar to a tomographic method. To this end, the FIB is used to remove slices of predetermined width from the nanofiber. The remaining cross-section is now accessible for imaging with the SEM. This measurement can be carried out either parallel or perpendicular to the nanofiber axis and makes a full tomography of the fiber possible. It is, however, a destructive process.

Cross-section method

The cross-section method consists of two basic steps: First, the sample is coated with a conductive layer consisting of a platinum–carbon mixture to prevent charging. Then, a thin slice is removed from the sample and an image is taken. The latter process is repeated several times in order to determine the geometry of the structure. These individual steps are illustrated in Fig. 2.11. The platinum layer is deposited using the ion/electron assisted gas deposition option of the FIB machine which delivers a small amount of material to the area of interest: A metal-organic precursor gas molecules are injected near the sample surface via a thin nozzle. The precursor gas is then cracked by the ion or electron beam, thereby depositing platinum and some residual carbon in the scan area of the beam (deposition area). This layer is conductive, prevents charging of the fiber, and shields it against unwanted ablation.

Now, the ion beam is used to remove thin slices of material, sketched as horizontal lines in the yellow rectangle in Fig. 2.11(b). This way, the structure becomes accessible for SEM imaging. The SEM image is taken under an angle of 52° so that the cross-sections are visible. An exemplary image is shown in Fig. 2.11(c). Each material can be identified by its relative brightness which depends on the individual scattering cross-sections for secondary electron production. The latter depends on the atomic number and

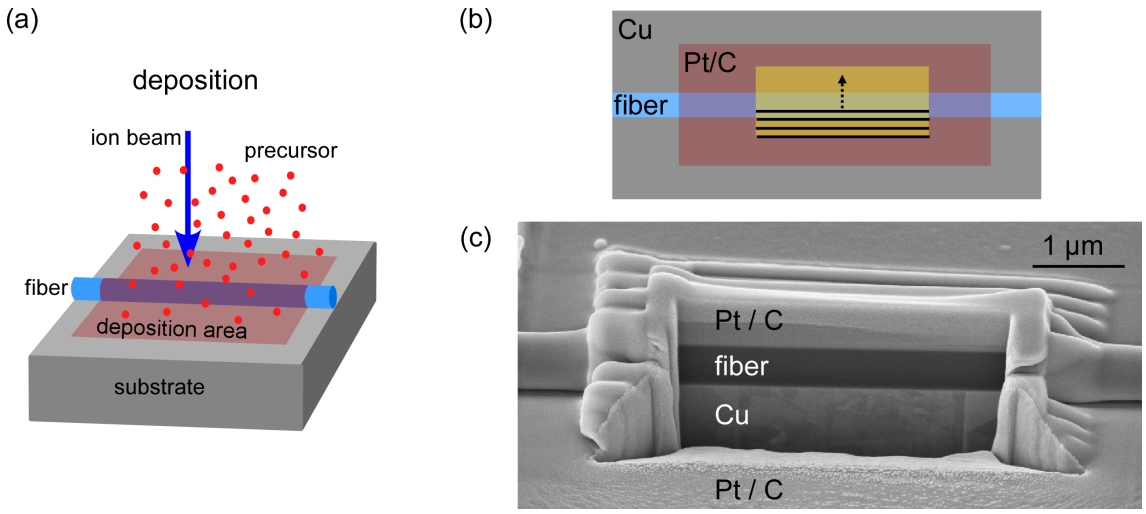

Figure 2.11: *Schematical view of the spatial characterization process. (a) Ion beam assisted platinum deposition process on the fiber. (b) Scheme for cross-section imaging. The yellow area is milled line-wise. After milling of each line, an image is taken with the SEM. (c) Cross-section image of a nanofiber with a diameter of 500 nm near the center.*

density of the material. Thus, the copper and the Pt-rich layer appear brighter compared to the fused silica of the nanofiber [89].

Cross-sections of a NFBG

Figure 2.12 shows the cross sections of a NFBG. The axial cross section shows a series of regularly shaped and spaced slits. These slits that constitute the photonic structure are typically only partially filled with the Pt/C-layer. The resulting voids form when the layer that builds up on the opposing upper sides of the holes merge before the cavity below is filled. While the image gives the impression that the slits do not fully penetrate the fiber, it can be seen from the transverse cross-section that this stems from a small rotation of the fiber with respect to the milling direction. Furthermore, the transverse cross section shows that the slits taper with an angle of $(8 \pm 1)^\circ$ towards the lower side of the fiber. As a consequence, the cross-section reduces by a factor of 4. This feature is typical for FIB milling and originates from the fact that ions which penetrate a surface under a shallow angle have a high probability of leaving the material after a few scattering events. As a consequence, they sputter only small amounts of material and carry their momentum with a tilted trajectory to deeper parts of the structure. This effect is even enhanced by the redeposition of the sputtered material on the sides of the slit.

The fiber cross-section is slightly elliptic with a diameter of $a = (525 \pm 5)$ nm and an ellipticity of $(a - b)/a = (8.5 \pm 0.5)$ % where the long axis (a) is oriented along the slit, see red ellipse in Fig. 2.12(b). For comparison, a circular profile is plotted as dashed lines in the same graph. This elliptical profile results from the redeposition of the sputtered material during the milling process. This effect is clearly visible as a bump at the upper right side of the slit which does not appear for unprocessed fibers, see Fig. 2.12(c).

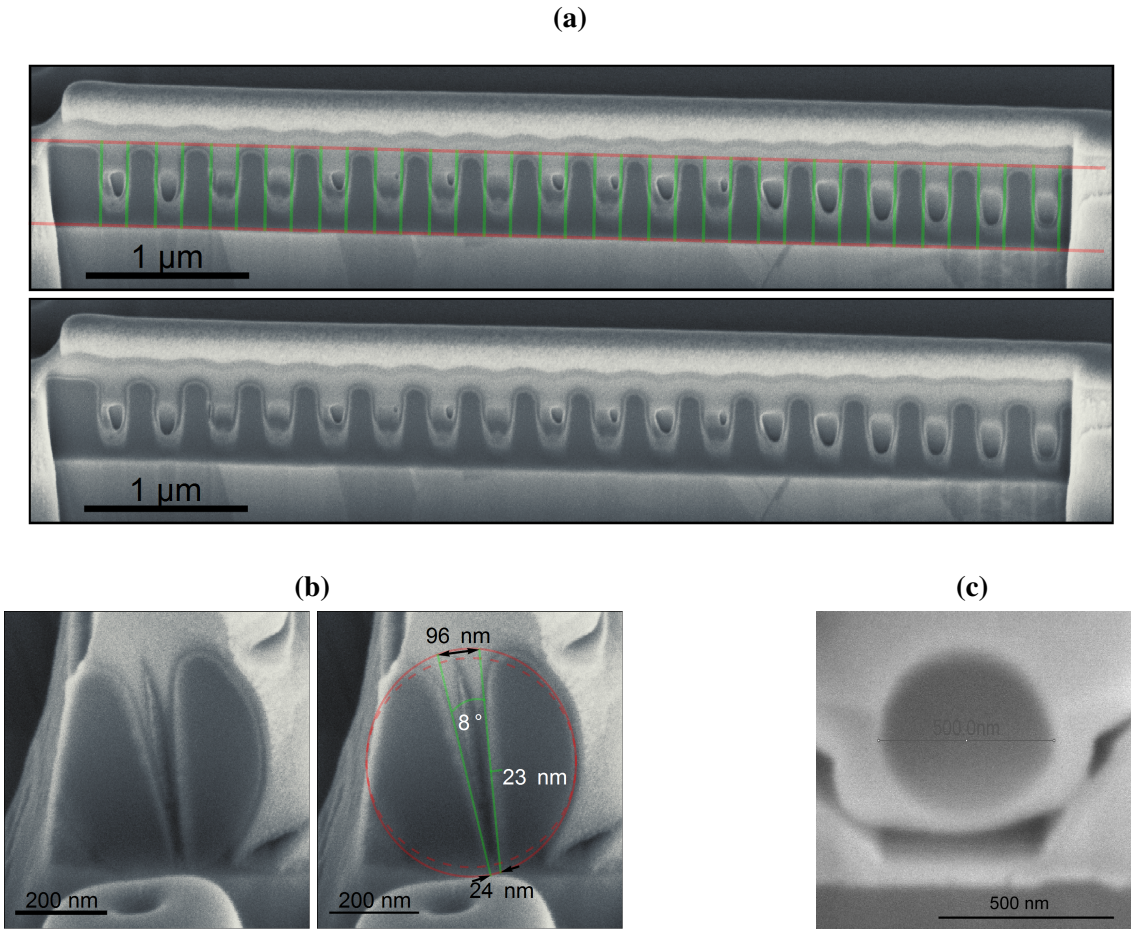

Figure 2.12: *Cross sections of a NFBG in TOF-FIB-1 where the cut-planes are oriented parallel (a) and perpendicular (b) to the fiber axis. The red and green lines indicate the boundaries of the fiber and photonic structure that have been determined from the image. Note that the left side of the fiber in (b) was thinned by the previous measurement and was not taken into account when determining the fiber diameter (red circle). An unmodified version of each image and a transverse cross-section of an unstructured fiber (c) are given for comparison.*

In the images a thin brighter layer is visible on the upper side of the fiber and the edges of the slits which is not present in unprocessed fibers, cf. Fig. 2.12(c). Note that this layer is not observed at the bottom side of the fiber. The fact that it only occurs near surfaces that were exposed to the ion beam suggests that it corresponds to a gallium rich layer that is deposited within the material during the milling process. This is supported by the higher brightness which, in SEM images, corresponds to a higher atomic number or density [89]. Such gallium rich layers have been observed in other experiments and the predicted width of several 10 nm is in accordance with the thickness observed here [90]. Such a layer is, however, unwanted because it induces absorption and raises the refractive index of the material and thereby possibly compensates the effect of the slit on the optical mode [90–92]. A possible annealing procedure to remove this layer is discussed in Ch. 2.2.7.

The geometry of the photonic structure is determined from the images by measuring the positions of the edges, see green markers in Fig. 2.12. The resulting pattern generated from a structure period of $\lambda_{\mathrm{ps}} = 349.2 \pm 0.1$ nm and a slit length of $L_{\mathrm{ps}} = 175 \pm 7$ nm fits the image very well. This confirms that the photonic structure is fabricated with a high homogeneity. The width of the fiber in the slice is determined from the red lines to be 519 ± 9 nm. Note that this does not necessarily correspond to the fiber diameter because the cut might not be centered on the nanofiber. The corresponding uncertainties are estimated during the fitting by tuning each parameter to the two extremal values that yield a good representation of the structure. The systematic uncertainty of the measurement is, however, higher due to the beam resolution (spot size) which is a few nanometers, the pixel size of the SEM raster which is 3.7 nm and 4.5 nm for the horizontal and axial direction, respectively (different due to the tilted imaging axis) and the long term calibration drift of the SEM which leads to a systematic error. The systematic uncertainty of the absolute values is estimated to be $\approx 10\ \%$ of the measured values.

Comparing the measured values $L_{\mathrm{ps}} \times W_{\mathrm{ps}} = (175 \pm 7) \times (24...96)\ \mathrm{nm}^2$ and $\lambda_{\mathrm{ps}} = 349.2 \pm 0.1$ nm to the design parameters of the structure of $L_{\mathrm{ps}} \times W_{\mathrm{ps}} = 138 \times 51\ \mathrm{nm}^2$ and $\lambda_{\mathrm{ps}} = 361$ nm (see Tab. 2.1) one finds that the slit length is considerably larger than the design value. This is due to the finite size of the ion beam which is typically on the order of 10 nm, where the exact value depends on the alignment skills of the operator. The measured periodicity is $3\ \%$ smaller compared to its design value. Taking the uncertainty of the absolute value into account, however, the measured values are in excellent agreement with the design parameters.

2.2.3 Optical setup

The optical properties of the cavity are characterized by measuring their transmission and reflection spectra. When characterizing resonators composed from Bragg grating mirrors, two scales have to be considered: The reflectivity of the individual Bragg grating is wavelength dependent with a reflection band-width on the order of nanometers. In case of the cavity, however, the spectral resonances, are narrower (~ 10 MHz) and closely spaced ($\sim$GHz). To cover both features, two methods are used. A spectrometer in combination with a white light source (WLS) detects the slowly varying features, while a laser setup is employed to resolve the resonances.

The spectral characterization of the cavity is performed with the optical setup shown in Fig. 2.13(a). The cavity is probed using a laser beam, derived from an external cavity diode laser (New Focus Velocity 6316) with a mode-hop free tuning range of $(838 - 853)$ nm. It is sent through a broadband fiber-based 50/50 beam splitter, to which the fiber that incorporates the TOF microresonator is spliced at port 3. The transmitted and reflected signal is detected by fiber-coupled photodiodes (PD1 & PD2).

A cesium vapor absorption spectrum is used as an absolute frequency reference while an etalon is used for relative calibration of the frequency axis. The free spectral range of the etalon was calibrated using a wavelength meter (High-finesse WS6) to be $\Delta f_{\mathrm{FSR}} = (2.8877 \pm 0.0045)$ GHz . The in-coupling was deliberately misaligned so that higher order spatial modes of the etalon are excited. In the confocal configuration, these occur

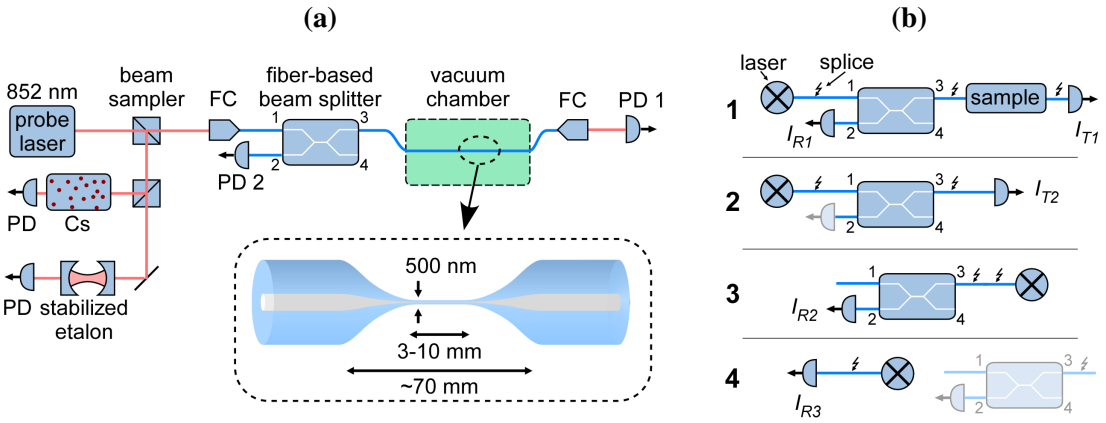

Figure 2.13: *Schematical view of the optical setup (a) and sketch of a TOF (inset), see text for details. (b) Measurement protocol for the transmissivity and reflectivity.*

at frequencies that are shifted by half the free spectral range relative to the fundamental modes, thereby doubling the mode density [63]. The length of the etalon is actively stabilized using the transmission signal of a second, frequency stabilized laser. The TOF integrated resonator can be optionally placed inside a vacuum chamber, see next chapter.

The absolute spectral transmissivity and reflectivity can be measured using the protocol shown in Fig. 2.13(b). It consists of the following steps: First, the reflected and transmitted signals are measured with PD1 & PD2. In the following, the TOF microresonator is removed and PD1 is spliced directly to port 3, and the power at port 3 is measured for normalization. Finally, for calibrating the transmission from port 3 to port 2, the fiber coupler is spliced to port 3 and the signal on PD2 is measured (step 3) and is again normalized by splicing the FC to PD2 (step 4). Finally, one obtains the transmissivity (T_{res}) and reflectivity (R_{res}) of the resonator by using

$$T_{\mathrm{res}} = I_{T1}/I_{T2} \qquad \text{and} \qquad R_{\mathrm{res}} = \frac{I_{R1}}{I_{T2}} \left(\frac{I_{R2}}{I_{R3}}\right)^{-1} . \tag{2.30}$$

For a broadband spectral characterization, a WLS in combination with a spectrometer is used. The spectromter (Avantes Avaspec-2048x14-USB2-FC) covers a spectral range of $600 - 1100$ nm with a resolution of 1.2 nm and the WLS uses a tungsten halogen bulb (AVA Avalight-HAL-S-FC) and covers the spectral range from $(360 - 2000)$ nm. Both, the spectrometer and the WLS are fiber-coupled so that the experimental method follows the same procedure as presented above.

2.2.4 Vacuum system

The cavities can be placed inside an ultra-high vacuum (UHV) chamber. This allows one to test their suitability for cold-atom CQED experiments which are typically performed under UHV conditions. Furthermore, it protects the nanofiber from pollution with dust.

The chamber is schematically shown together with the pump system in Fig. 2.14. The main chamber contains a 30×30 cm^2 breadboard that can be removed through a large

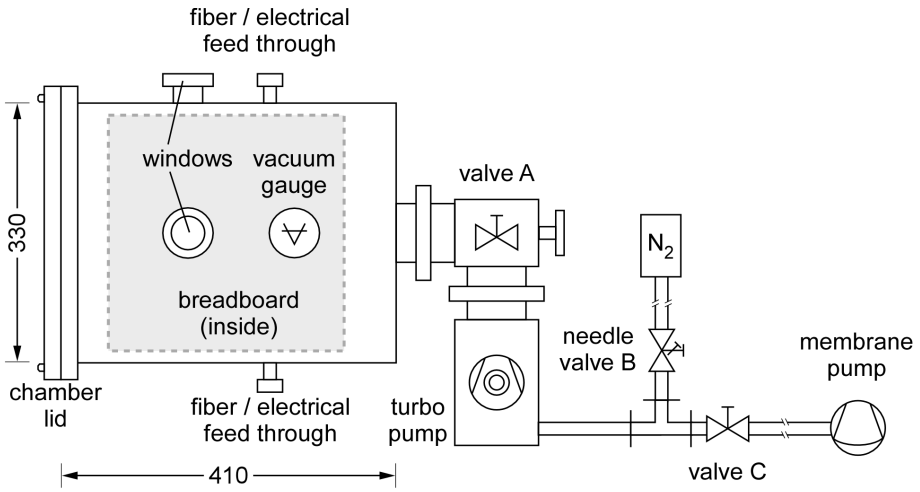

Figure 2.14: *Sketch of the vacuum system viewed from the top. The dimensions are given in mm and the height of the main chamber is 220 mm, see Ch. A.9 for the blueprint of the vacuum chamber.*

opening (lid) and re-equipped for various applications. The TOF is glued to a mount that is fixed on the breadboard. Feedthroughs for several optical fibers and electrical leads are placed on each side of the chamber. For the fibers, a swage-lock feedthrough in combination with a teflon ferule, similar to the technique described in [93], is used.

The pump system is attached via an angled valve (valve A: VAT series 284) to the back-side of the chamber. It consists of a two stage setup including a turbo pump (Pfeiffer HiCube 80) and a membrane pump (Pfeiffer MVP 015). The chamber pressure is measured with full-range pressure gauge (Pfeiffer PKR 251 + TPG 216 Single Gauge) with a relative measurement accuracy of 30 % and a relative precision of 5 %. This system can reach a minimum chamber pressure of 10^{-7} mbar.

A nitrogen gas bottle is connected via a leak valve (valve B) between the two pumps. This allows one to flood the chamber in a controlled way with a small gas flow. This is critical for the transmission properties of the TOF: A high gas flow induces turbulences that raise dust from the inner surfaces of the chamber. Part of this dust settles on the nanofiber waist and can thereby drastically degrade its transmission properties. Great care is taken to minimize this effect. The chamber is placed under a high efficiency particulate air (HEPA) filter and the chamber itself and its surroundings is cleaned thoroughly, first with water to bind the dust and then with isopropanol for oil removal and drying. Furthermore when flooding the chamber, the gas flow is kept low so that the process takes approximately 10 minutes.

2.2.5 Optical characterization

Here, the measurement results concerning the optical response of FIB structured nanofibers are presented. The spectral response is first measured with a WLS and a spectrometer at ambient conditions. The resulting spectra obtained with a NFBG cavity are shown as solid lines in Fig. 2.15(a). A reflection peak with 30 % reflectivity is found at 820 nm

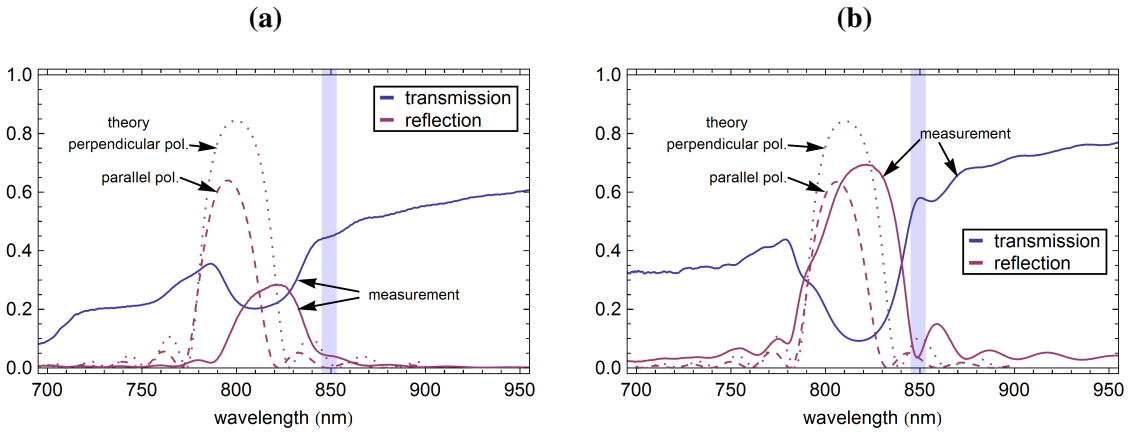

Figure 2.15: *Solid lines: Spectral response of the resonator (a) TOF-FIB-1, and of a single NFBG mirror (b) TOF-FIB-4. The theory prediction for a single NFBG obtained from the transfer matrix method is shown in dashed (dotted) lines for quasi-linear polarization oriented parallel (perpendicular) to the orientation of te slits. The translucent blue region indicates the probe laser scan range. Note that the theory neglects losses so that the transmission and reflection spectrum add up to unity.*

with a full width at half maximum (FWHM) of 38 nm and a corresponding dip in the transmission spectrum.

The spectral shape of the stop-band appears to be broadened which may result from two narrow spectral features (resonances). This may result from a difference in the spectral reflectivity of the NFBG for the two orthogonal polarizations of the fiber mode which are both probed by the unpolarized light of the white light source. This polarization dependence becomes clear when comparing the quasi-linearly polarized nanofiber mode, see Fig. 1.7, with the slit geometry. The electric field distribution of the mode is asymmetric in the transverse plane and exhibits a higher field strength along the polarization axis than along the direction perpendicular to it. As a consequence, at the position of a slit, the power fraction of the mode that propagates inside the silica depends on the polarization direction with respect to the slit orientation. This leads to different effective refractive indices for the two polarization orientations. As a result, the maximum reflectivity, the central wavelength, and the FWHM of the stop-band depend on the incoming polarization. This may explain the asymmetry of the measured reflection band which can arise from two stop bands with slightly different central wavelengths. Furthermore, fabrication imperfections and the effect of the implanted gallium may contribute to the observed effect.

The theory prediction of a single NFBG from the transfer matrix formalism is plotted as dashed and dotted lines in Fig. 2.15(a). The predicted spectral response of the stop-band differs for the two polarization orientations and one finds a FWHM of 30 nm and 37 nm as well as the central wavelengths of 795 nm and 800 nm for the parallel and perpendicular polarization with respect to the slit orientation, respectively. These are in good agreement with the measured values for the wavelength of maximum reflection 828 nm and a FWHM of 38 nm, when taking into account that the effect of gallium on the optical response was

neglected in the model.

The measured maximum reflectivity of the resonator of 28 % is lower than the model predictions of $64\ \%...84\ \%$ for a single mirror. This results from a combination of several effects: The low spectral resolution power of the spectrometer is not capable of resolving the sharp resonances of the cavity so that one finds a lower averaged signal which also depends on the finesse of the cavity. Furthermore, the absorption of pollutants lower the reflection signal by a factor that may also depend on the nanofiber length to the first mirror. In addition, the absorption by gallium and the scattering losses of the mirrors contribute to the loss. The latter can be expected to differ for the two polarization states: When the polarization is oriented perpendicular to the slit, the E-field is also oriented perpendicular to the silica surfaces within the slit and is required to be discontinuous. As a consequence, the field distribution is modified more strongly than for parallel polarization and higher scattering losses occur at the two interfaces at the beginning and end of each slit. Although the theory predicts a higher maximum reflectivity for the perpendicular polarization than for the parallel case, one would expect the opposite situation when including the scattering losses.

The overall transmission does not exceed 60 % and even decreases by a factor of 3 from long towards shorter wavelengths. This low transmission value is most probably caused by scattering losses of the NFBGs, gallium that was implanted in the nanofiber during the fabrication and possibly pollutants on the nanofiber. In particular, the implanted gallium introduces a wavelength dependent absorption that matches the observed spectral absorption [90]. The effect of implanted gallium and pollution during the fabrication will be further investigated in Ch. 2.2.6 and Ch. 2.2.7.

Comparing these results to the spectral response of a single NFBG, see Fig. 2.15(b), one finds a qualitatively similar response. However, the maximum reflectivity is a factor 2 higher in case of the single mirror due to the effects discussed above. In order to make a theory prediction for the optical response of TOF-FIB-4, a parameter set for its geometry had to be generated since no spatial measurement of the structure was performed. For this purpose, the measurement results for TOF-FIB-1 were compared with its design parameters (Tab. 2.1) to extrapolate the geometry of TOF-FIB-4 from its design parameters. The two structures are very similar in their design so that the absolute deviations measured with TOF-FIB-1 can be directly applied to the TOF-FIB-4 resulting in the geometry parameters $L_{\mathrm{ps}} \times W_{\mathrm{ps}} = (173 \times 60)\ \mathrm{nm}^2$ with a transverse taper angle of 8° and $\lambda_{\mathrm{ps}} = 355\ \mathrm{nm}$. The predicted spectral reflectivity features peak at ≈ 795 nm, $3\ \%$ lower than the observed value of 820 nm, while the FWHM of 30 nm is $20\ \%$ smaller than the measured value of 38 nm. The measured maximum reflectivity of $70\ \%$ has to be compared to the predicted values of $64\ \% \ldots 84\ \%$. They are in fact in very good agreement when taking into account that the theory values have to be averaged because the measurement was performed with unpolarized light. Moreover, as pointed out above, the maximum reflectivity for perpendicularly polarized light is overestimated.

High resolution spectrum

The previous samples could not be characterized with high resolution because the probe laser wavelength range has no overlap with the reflection band of the NFBG. The spec-

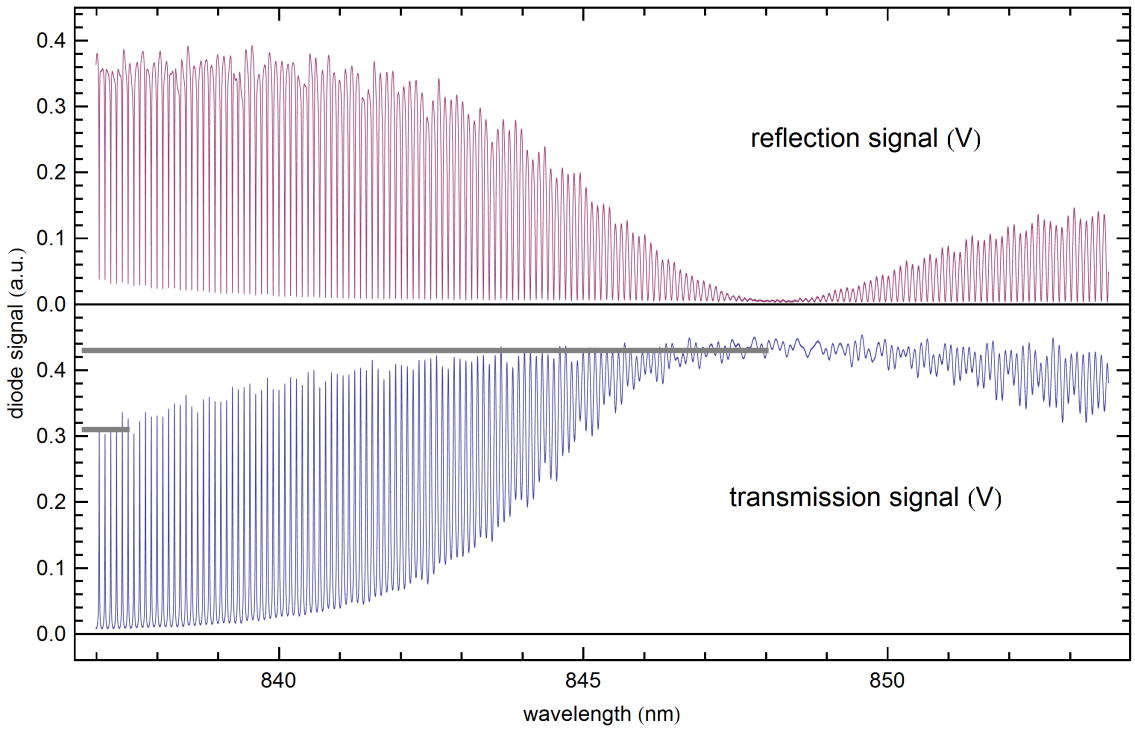

Figure 2.16: *Reflection (blue) and transmission (red) spectra of TOF-FIB-2. The resonances show up as peaks (dips) in the transmission (reflection) spectrum. The short and long gray bar indicate the values that are used to determine the intracavity transmission $T(R_{\max})$ and $T(0)$, respectively.*

trum of one sample where such a scan was possible is shown in Fig. 2.16. It features a series of high finesse resonances at wavelengths around 838 nm which continue towards higher wavelengths with decreasing finesse. The envelopes of the spectra resemble those observed in the previous measurements, compare to Fig. 2.15, but are shifted towards higher wavelengths.

The cavity parameters of the resonator are determined by fitting Airy-functions to sections of the spectrum, each covering one spectral range, see Fig. 2.17(a). The maximum finesse of $\mathcal{F} = 11.1 \pm 0.2$ was measured at a wavelength of 838 nm where the free spectral range is $\Delta f_{\mathrm{FSR}} = 40.70(5)$ GHz. The latter is in very good agreement with the theory prediction of $\Delta f_{\mathrm{FSR}} = 41.1(1)$ GHz obtained from the measured cavity length $L = 2.39(1)$ mm and the group velocity $v_g = 1.9665 \cdot 10^8$ m/s, see Ch. 2.1.2.

From these values, a prediction for the cavity performance in CQED applications can be obtained, see Ch. 2.1.4. Thanks to the strong lateral confinement of the nanofiber mode one obtains a small normalized mode volume of $\tilde{\mathcal{V}} = 995$. The Q-factor of the cavity is $Q = 9.6 \cdot 10^4$ and one obtains a cooperativity of $C = 7.3 \pm 0.1$ which shows that the resonator, despite its moderate finesse, could provide strong coupling between light and matter. Consider now a cavity with the same parameters at the wavelength of the cesium D2-line transition. The corresponding coupling and decay rates take the values

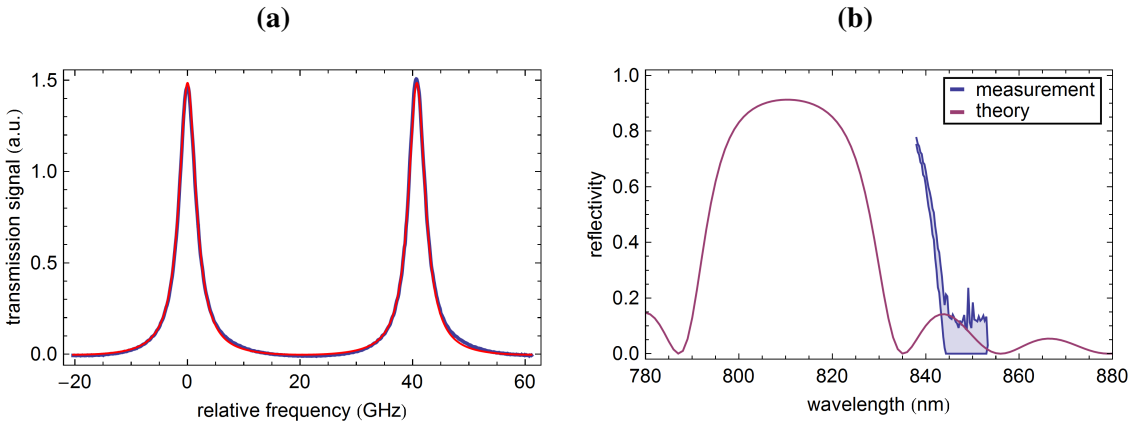

Figure 2.17: *(a) Section of the transmission spectrum from Fig. 2.16 with the highest measured finesse (blue). A fit with an Airy-function to the data is shown in red. (b) Reflectivity spectrum of an NFBG that is determined from the spectral variation of the finesse of TOF-FIB-2, for details see the text. The blue lines surrounding the shaded region indicate the maximum and minimum reflectivity spectrum extracted from the measurement results. The purple curve indicates the theory prediction obtained with the transfer matrix formalism.*

$(g, \kappa, \gamma_a)/(2\pi) = (200, 1830, 2.6)$ MHz. Thus, the resonator operates in the fast cavity regime with parameters that are comparable to state of the art optical resonators [39].

Intracavity losses

The fact that the mirror reflectivity (R) decreases to zero within the measured wavelength range facilitates a measurement of the intra-cavity losses. The method takes advantage of the fact, that the light passes the resonator only once when the mirrors do not reflect but multiple times at high reflectivity. This yields an approximate value using the assumptions of a symmetric cavity and of losses that are dominated by the nanofiber absorption ($1 - T_{\mathrm{R}}$). One obtains for the maximum resonator transmission at maximum mirror reflectivity $T_{\mathrm{FP}}(R_{max}) = (1-R)^2\, T_{\mathrm{R}}/(1-T_{\mathrm{R}}\, R)^2$ and at minimum mirror reflectivity $T_{\mathrm{FP}}(0) = T_{\mathrm{R}}$. Using the maximum transmission values around 838 nm and 848 nm, see gray lines in Fig. 2.16, one obtains the ratio $T_{\mathrm{FP}}(R_{\mathrm{max}})/T_{\mathrm{FP}}(0) = 0.43/0.31$. In combination with the relation of the finesse, Eq. (2.3), one obtains the values of $R = 0.78$ and $T_{\mathrm{R}} = 0.95$, respectively. The losses in the resonator volume amount to $5\ \%$ which is small compared to the transmission losses that were observed in the broad band spectra, cf. Fig. 2.15. This is due to the fact that the total transmission signal of the TOF exhibits additional losses that do not contribute to the intra-cavity losses. Further loss channels can be introduced by, e.g., the nanofiber that is not part of the resonator and which is of comparable length to the resonator length. Furthermore, the photonic structures can exhibit a transmission loss that is not probed upon reflection and does not contribute to the cavity loss.

Reflectivity spectrum

An estimation of the mirror reflectivity can be obtained from the finesse using Eq. (2.3) and assuming a symmetric cavity $R = r_1^2 = r_2^2$. Then the mirror reflectivity takes the form

$$R_{\mathrm{FP}} = \frac{2\,F^2 + \pi^2 - \pi\sqrt{4\,F^2 + \pi^2}}{2\,F^2\,T_{\mathrm{R}}}\,. \tag{2.31}$$

The resulting reflectivity of a single NFBG is shown in Fig. 2.17(b). It reaches a maximum value of (76 ± 1) % within the tuning range of the spectroscopy laser. Note that this high reflectivity is reached with only 30 slits thanks to the high contrast of the propagation constant modulation. Moreover, the spectral shape suggests that the maximum reflectivity is not reached and can be found at smaller wavelength.

A prediction of the reflectivity profile is obtained using the transfer matrix formalism, see Ch. 2.1.3. For this purpose, the geometry parameters were derived from the design structure by taking into account the previously determined modifications caused by the fabrication method (see also Ch. 2.2.2). Using this method, one obtains 30 slits of $L_{\mathrm{ps}} \times W_{\mathrm{ps}} = 173 \times 60\ \mathrm{nm}^2$ with a (design) period of $355\ \mathrm{nm}$ and a slit taper angle of $8°$. The result is shown in Fig. 2.17(b) as a red line. The maximum of the predicted reflectivity is again shifted by $\approx 30\ \mathrm{nm}$ ($3.6\ \%$) towards shorter wavelengths with respect to the measurement. Apart from this shift, it shows a good agreement with the measured values. This shows that even with a comparatively small number of slits a high reflectivity of 90 % is realistic.

2.2.6 Transmission degradation during the fabrication

Some samples that were fabricated with the FIB method show substantial losses. In order to identify the fabrication steps that cause these losses, the transmissivity of a sample was monitored during the fabrication process. In the following, the losses caused by the evacuation process and residual gas deposition during imaging by the electron and ion beam are studied. The latter is a result of residual hydrocarbonous molecules in the chamber from, e.g., grease or finger prints which are cracked by the electron beam so that the residues are deposited onto the imaged areas. The deposition rate scales inversely with the beam energy ($E^{-0.8}$) so that lower beam energies yield higher contamination [89, Ch. 3.5.4].

Two optical fiber feedthroughs were attached to the vacuum chamber of the SEM/FIB machine and the sample was spliced between these two fiber ends. The light of a WLS was launched into one of the fibers from outside of the vacuum chamber and the transmitted signal was recorded by a spectrometer that was connected to the other fiber, similar to the method described in Ch. 2.2.3. For this measurement, the copper substrate was fixed in the mount such that the fiber is not in contact with the surface and maintains its transmission. The measurement was carried out differentially, meaning that two spectra were taken before and after each fabrication step ($S_0(\lambda)$ and $S_1(\lambda)$), respectively. The loss of each step is determined from the ratio of the two corresponding spectra by $L(\lambda) = 1 - S_1(\lambda)/S_0(\lambda)$. The results are shown in Fig. 2.18(a). The data shows that already the evacuation of the FIB chamber introduces substantial losses that can reach values of up to 50 %. This is

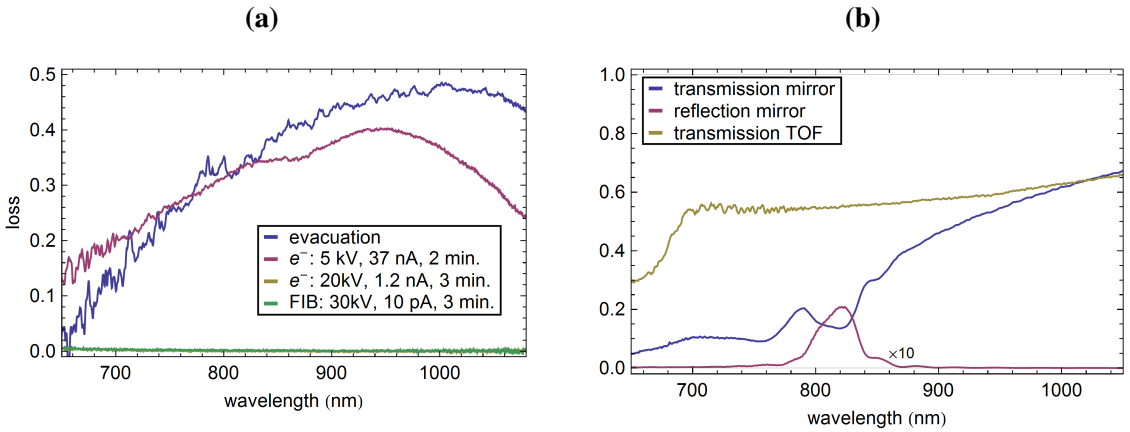

Figure 2.18: *(a) Study of the losses induced by selected fabrication steps where the beam parameters are given in the legend (facitlity: USTEM). (b) Optical response of two samples that were mounted to the same fiber holder. One sample was structured (mirror) and one sample was left unstructured (TOF). The reflectivity was magnified by a factor of* 10 *to improve the visibility. Sample TOF-FIB-3 structured at the ZMNS.*

due to the fact that most FIB machines are optimized for a fast evacuation of the chamber to reduce production times. As high gas flows raise dust, this is not compatible with nanofiber applications. Note, however, that the FIB machine used in this experiment was situated in a laboratory environment where no special care was taken to reduce the pollution (USTEM) by, e.g., filtering the air or cleaning the chamber. The situation is expected to be better in the other machines at the ZMNS and MPIP.

Now, the losses caused by residual gas deposition due to the imaging with the electron or ion beams are characterized. To this end, the nanofiber is imaged with a typical magnification ($5000\times$) over a time span of few minutes. When using the fabrication parameters of 20 kV (30 kV) electron (ion) beam acceleration voltage, no significant transmission degradation is found, see Fig. 2.18(a). To check the sensitivity of the method, the electron beam is also tuned to the worst case setting of low beam energy and high current. The measurement shows losses on the order of $40\ \%$ for this case, thereby demonstrating that high beam energies are essential to minimize the losses caused by residual gas deposition.

In order to determine the accumulated losses that are caused by the ion beam milling process, two samples were fixed to the same mount and only one of them is structured with one NFBG. Thereby, both TOFs undergo the same fabrication steps except for the milling itself. The two transmission spectra are shown Fig. 2.18(b). For the unprocessed fiber (yellow) a nearly constant transmission loss of $40\ \%$ is observed that is caused by the treatment. The structured fiber shows a transmission spectrum that matches that of the unprocessed fiber at high wavelengths but shows increasing losses for smaller wavelengths. The spectral transmission loss of the structured fiber matches the absorption characteristics of gallium-rich layers in fused silica [90–92]. Thereby, it confirms the statement that the bright layers observed in the cross-sections, see Ch. 2.2.2, originate from a gallium implantation.

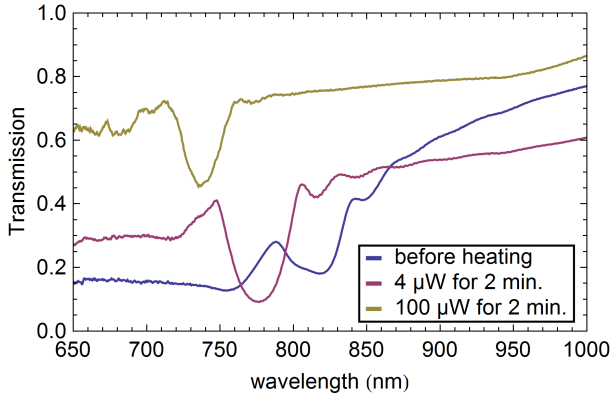

Figure 2.19: *Transmission spectrum before and after heating the fiber via the absorbed power of a light field with a wavelength of* (832 ± 12) *nm propagating through the fiber. The corresponding powers and times are shown in the legend. Sample TOF-FIB-3*

2.2.7 The effect of gallium on the optical properties of a NFBG

The gallium that is implanted into the nanofiber is undesirable due to the losses and the refractive index modification it induces. The dose employed for the milling process of $\sim 10^{18}$ $\mathrm{Ga/cm^2}$ is very high and leads to high gallium concentrations in which even metallic colloids can form [94]. The implanted gallium is bound in different chemical states ranging from those situated in microchannels which are highly mobile to bound configurations in the SiO_2 network which are immobile [95–97].

Two approaches are available in order to minimize the amount of gallium: The ion dose can be lowered by employing gas etching agent that increase the milling rate. After the milling procedure, an annealing procedure can be employed to remove the gallium via diffusion and evaporation. The diffusion of gallium in silica at high temperatures has been studied [95–97] and it was found that a large fraction of the gallium can be removed from the sample by baking at temperatures of $(300 - 1100)$ °C for ~ 30 min, depending on the glass and the implantation technique and the implantation parameters.

The widely used baking procedure that employs an oven is impractical for tapered optical fibers. It poses the risk of pollution by evaporation of residues from previous experiments that redeposit on the nanofiber. Therefore, I chose a different approach in which the fiber is heated via the absorbed power of a laser that is sent through the fiber, compare to the method used in Ch. 3. For this purpose, the TOF is placed in a vacuum environment at pressures below 10^{-5} mbar where no heat transport via gas occurs. In this way, the heating takes place in regions with high concentrations of the absorbing gallium.

The transmission spectra of a NFBG mirror before and after the annealing procedure are shown in Fig. 2.19. They show that even when using small heating powers of few µW, the reflection band shifts by nearly 50 nm towards shorter wavelengths after a short processing times of 2 minutes. Furthermore, the substructures on the transmission dip vanish and the reflection band becomes more pronounced. The transmission increases at short wavelengths but surprisingly decreases at longer wavelengths. From the literature, the former effect is expected because gallium shows a higher absorption at shorter wave-

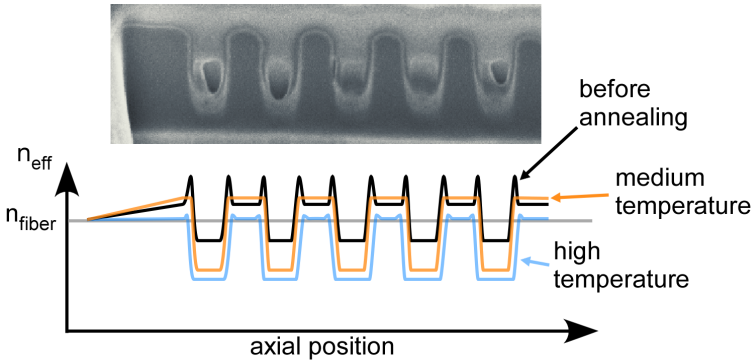

Figure 2.20: *Schematical view of the effective refractive index profile of the optical mode along a NFBG. The inset shows a cross section of a structure that is taken from Fig. 2.12(a)*

lengths [90–92, 94]. The transmission decrease may be a result of higher scattering losses or the formation of metal clusters with absorption bands in the near infrared wavelength range. A further measurement with the same heating power and a longer heating time of 15 min showed no further changes.

When increasing the heating power to 100 µW, the reflection band shifts again by 40 nm towards shorter wavelengths and the overall transmission improves to values of $60\,\%$ to $80\,\%$. This observation of a transmission improvement that reaches an equilibrium at a given temperature and shows only improvement at a higher temperatures can result from two effects: When gallium is removed from the fiber, the temperature decreases due to the smaller absorption so that the evaporation becomes less efficient. Furthermore, the different chemical states of gallium in silica and their corresponding mobility can also cause this effect. First, the highly mobile part evaporates, while the more tightly bound part requires a higher activation energy and therefore does not evaporate until the nanofiber is heated to a higher temperature. The fact, that the transmissivity does not reach 100 % can be attributed to scattering losses, other pollutants or to the fraction of gallium that is bound in the silica.

The spectrum obtained after heating to higher temperatures surprisingly shows a decreasing amplitude of the transmission dip, which is in contrast to the change caused by the previous heating. Such a behavior can be explained by assuming that a fraction of the gallium diffuses through the glass, rather than evaporates: Before the annealing process, the gallium is concentrated at the sides of a slit causing an effective refractive index profile of the mode as sketched in Fig. 2.20. Here the slit sections exhibit a lower effective refractive index contrast with respect to the nanofiber than one would expect from a simple void. The purpose of the slit is to create a section in which the optical mode exhibits a larger power fraction outside the silica glass, thereby resulting in a lower effective refractive index $\Delta n_{\mathrm{eff}} < 0$. The gallium, however, increases the refractive index and can compensate the effect of the void. In an extreme case, this may in principle result in the inverse photonic structure, in which the slit exhibits a higher Δn_{eff} compared to the unprocessed nanofiber.

When heating the sample, the total amount of gallium decreases due to evaporation. Furthermore, the gallium diffusion leads to a more homogeneous distribution of the re-

mainder and resulting in slightly increased and homogeneous refractive index of the glass. This can result in a higher contrast of the propagation constant in the slit sections compared to the unprocessed sections, and thereby enhances the reflectivity. At higher temperatures, more gallium leaves the material, thereby lowering the refractive index and widening the slits due to mass conservation. After this heating step, the refractive index contrast is lower and the length of the slits relative to that of the unmodified part of the fiber is changed. This can result in a smaller transmission dip, corresponding to a lower reflectivity of the photonic structure, and an increase of the overall transmission due to less absorption from gallium.

This measurement shows that the NFBGs can not yet be employed in combination with nanofiber-based atom traps. Even powers on the order of 100 μW are sufficient to heat the fiber to very high temperatures in an UHV environment. For the trap, high laser powers of several 10 mW are required which would most certainly fuse the fiber at the NFBG due to the high absorption. However, when combining the annealing procedure by heating with gas-assisted etching during the FIB milling, the absorption may be sufficiently small to enable high laser powers. In this context, this annealing method could be easily implemented in such an experiment as it can be carried out in the vacuum chamber that is later used for the experiment.

2.3 Resonator with an integrated tapered optical fiber (TOF-microresonator)

In the following a Fabry-Pérot type resonator with an integrated tapered optical fiber (TOF) is presented. It is realized by two fiber-Bragg grating (FBG) mirrors that are placed in the untapered part of the fiber and enclose the TOF, similar to what has been reported in [75]. The resonator is designed to operate at the cesium D2 line wavelength of 852 nm. Such FBG mirrors can be taylor made for a wide range of wavelengths and reflectivities, making this resonator type a versatile instrument that can be designed for a wealth of possible quantum objects.

The section outline is as follows: First, the fabrication procedure of the resonator is described and the taper profiles are given. This is followed by the optical characterization which is performed with the setup that was presented in the previous section. Then, the TOF transmission loss is determined from a finesse measurement before and after the tapering process and the intracavity polarization is measured. Using the optical properties of the resonator, a prediction of the CQED performance is made.

2.3.1 Resonator fabrication

The TOF-microresonator is a Fabry-Pérot type resonator with two laser written fiber Bragg gratings (FBGs) in the untapered part of the fiber acting as cavity mirrors that enclose a tapered optical fiber, see Fig. 2.21(a). This way the light is reflected back and forth between the two FBG-mirrors, passing the TOF including the nanofiber twice per round-trip. The reflection band of the FBGs is designed to exhibit high reflectivity at the cesium D2-line wavelength of 852 nm.

Several techniques for FBG inscription, suited for a wealth of applications such as fully fiber integrated lasers, sensors and telecom filters are available and are comprehensively presented in [71]. In this work, they are fabricated in the group of M. Rothhardt at

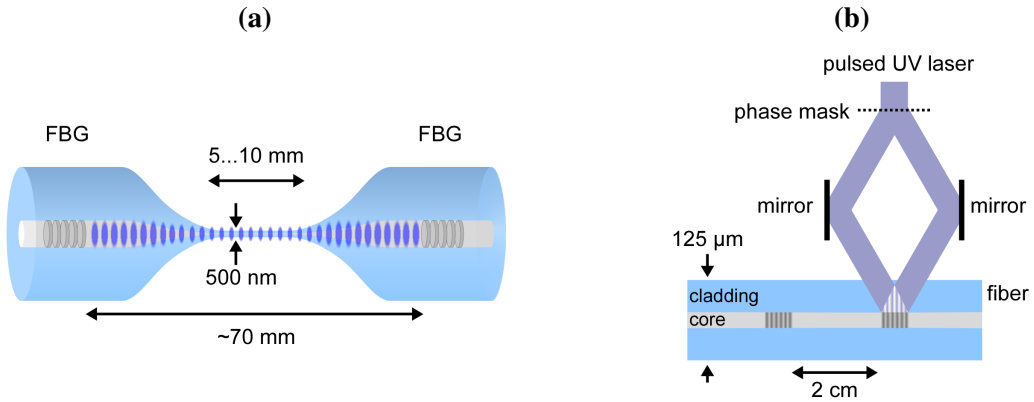

Figure 2.21: *Schematic view of the TOF-microresonator (a) sketch of the FBG inscription process using an interference method (b).*

sample	Θ_1	Θ_2	r_1	r_2	L_{waist}
TOF-resonator 1	5 mrad	2 mrad	30 µm	10 µm	5 mm
TOF-resonator 2	5 mrad	2 mrad	30 µm	10 µm	5 mm
TOF-resonator 3	5 mrad	2 mrad	27 µm	7 µm	10 mm
TOF-resonator 4	5 mrad	2 mrad	30 µm	10 µm	5 mm

Table 2.3: *Radius profile of the individual TOF-microresonators given with the parameters that were introduced in Fig. 1.13.*

the Institute of Photonic technologies in Jena who employ an interferometric laser writing technique that can be used with standard optical fibers [98]. The technique is based on the effect that the refractive index of fused silica is permanently modified when illuminated with sufficiently high optical intensities. This way, a periodic refractive index modulation in the fiber core is induced by exposing the fiber to a pulsed laser with a periodic intensity profile, see Fig. 2.21(b). This intensity profile is created in a Talbot-type interferometer where a laser beam is split and recombined under an angle. To obtain a high index modulation contrast, laser light in the ultraviolet (UV) wavelength range is used and the fiber is loaded with hydrogen prior to the processing. The latter is removed by heating after the FBG inscription.

After the FBG inscription, the fiber section in between the FBGs is tapered using the technique described in Ch. 1.4.1. Here, the TOF radius profile was optimized for high transmission to minimize intra-cavity losses while simultaneously maintaining a short taper profile in order to fit between the mirrors. A waist diameter of 500 nm was chosen because it provides a high coupling properties for quantum optics experiments with cesium atoms. The parameters of the TOF radius profile as defined in Fig. 1.13 are summarized in Tab. 2.3 for the samples used here. The angle of the conical section next to the untapered fiber (Θ_1) is chosen high in order to minimize the taper length, while the angle of the second conical section Θ_2 is chosen small enough to ensure an adiabatic mode transformation and, thereby, to maintain a high TOF transmission. After the tapering process, the TOF microresonator is fixed to the mount shown in Fig. 1.12. It incorporates a bending piezo realized as one of the fixing points that can be used to tune the resonator frequency via strain.

2.3.2 Optical characterization

The optical characterization is performed with the setup that was presented in the previous chapter, see Ch. 2.2.3-2.2.4. High-resolution transmissivity and reflectivity spectra of TOF-resonator 1 are shown in Fig. 2.22. They show a reflection band centered around 852.54 nm with a FWHM of ≈ 0.2 nm in which a series of resonances are visible as peaks (dips) in the reflection (transmission) spectrum. The highest finesse is reached at the central frequency of the reflection band with an on-resonance transmission of $11\ \%$. An excerpt of the transmission spectrum at this wavelength is shown in Fig. 2.23. The two resonances per FSR in the upper trace correspond to two orthogonal quasi-linearly polarized modes which are split due to intrinsic birefringence, see also Ch. 2.3.4 below.

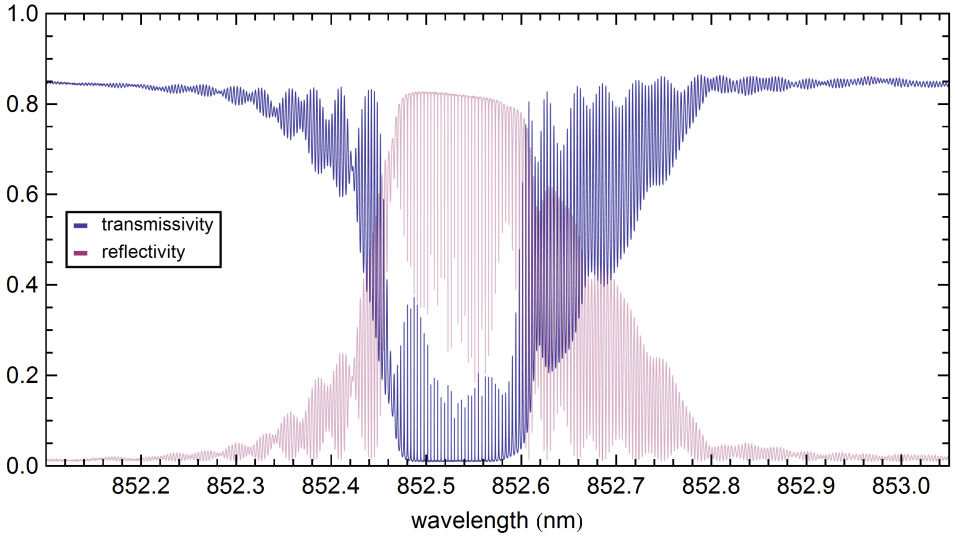

Figure 2.22: *Spectral transmission and reflection of the TOF microresonator. Within the 0.2 nm wide stop band, the TOF microresonator modes show up as peaks (dips) in the transmission (reflection).*

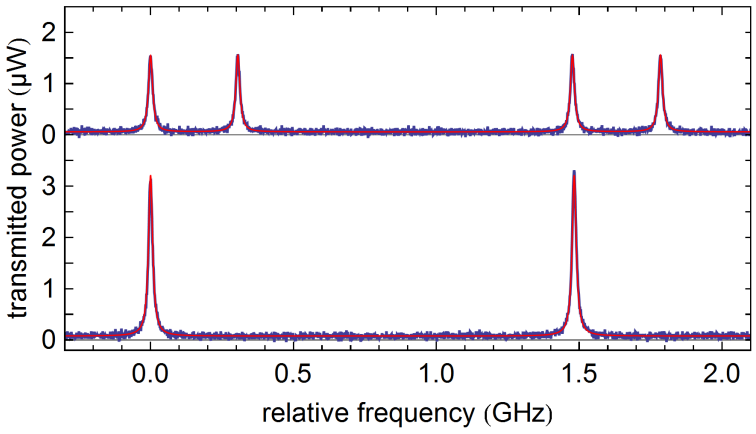

Figure 2.23: *Spectral transmission signal over one FSR for two polarization states. The solid red lines are Airy-function fits.*

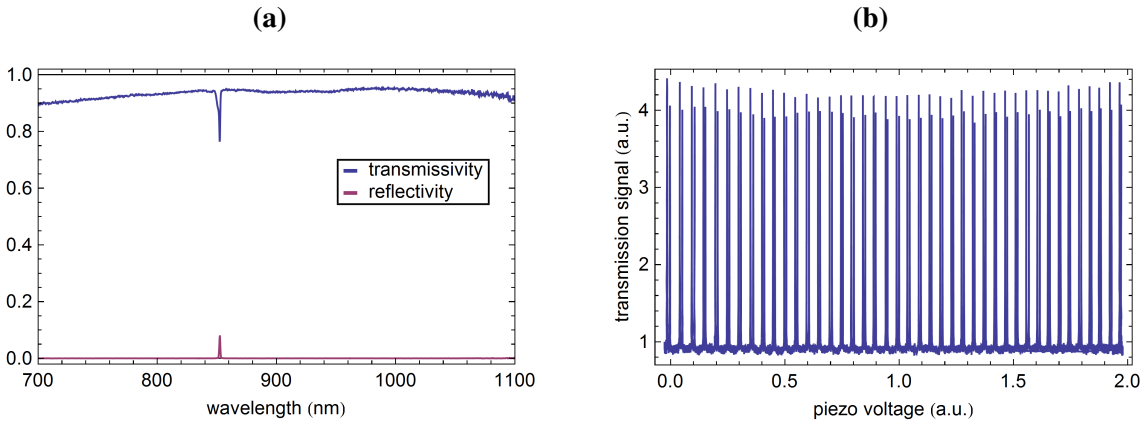

Figure 2.24: *(a) Broadband spectrum of the reflectivity and transmissivity of TOF-resonator 1 measured with a spectrometer and WLS. (b) Transmission signal as function of the mechanical strain induced by the bending piezo of the fiber mount (TOF-resonator 1). Each pair of resonances corresponds to the two polarization states of the resonator.*

For the lower trace, the polarization of the input light was chosen to match one of these modes. The finesse and FSR are determined by fitting a section from the signal covering 1 FSR by an Airy-function Eq. (2.2a) including an offset. It yields $\mathcal{F} = 85.6(3)$ and $\Delta f_{\mathrm{FSR}} = 1.48084(45)$ GHz at a vacuum wavelength of $\lambda = 852.53(5)$ nm. The FSR is in good agreement with the theoretical value of $1.47(8)$ GHz, where the optical path length of $L_{\mathrm{opt}} = 10.2(6)$ cm is computed from the known lengths and propagation constants of the different TOF microresonator sections. Note that the nanofiber section is short compared to the TOF microresonator length so that the cavity medium is non-dispersive in good approximation.

The capacity of the resonator for light–matter enhancement can be determined from the finesse and FSR. Using the results derived in Ch. 2.1.4 one obtains a value for the cooperativity parameter of $C = 56.5 \pm 0.4$ which is nearly an order of magnitude higher compared to the NFBG resonator ($C = 7.3 \pm 0.1$). This resonator is thus very well suited for experiments in the strong-coupling regime, even when the emitter is positioned at distances of few 100 nm above the nanofiber surface. This is due to its high quality factor of $Q = 2 \cdot 10^7$ while the normalized mode volume of $\tilde{\mathcal{V}} = 2.7 \cdot 10^4$ is still small. The latter is rather suprising in view of the macroscopic length of the resonator and is a result of the strong transverse confinement by the nanofiber. For the π-polarized Cs D2 transition $|F = 4, m_{\mathrm{F}} = 0\rangle \rightarrow |F' = 5, m_{\mathrm{F}'} = 0\rangle$, one obtains $(g, \kappa, \gamma)/2\pi = (38,\ 8.6,\ 2.6)$ MHz. The resonator, thereby, is fit for strong coupling in the coherent CQED regime $g \gg \kappa, \gamma_a$.

In order to determine the transmission over a broader spectral range, a measurement was performed using a WLS and a spectrometer, see Fig. 2.24(a). In the ranges from $700 \ldots 850$ nm and $854 \ldots 1100$ nm, the transmission is $T = 90(5)$ %. The resonator, therefore, allows to send light at wavelengths outside the reflections band through the fiber for e.g. addressing emitters coupled to the resonator at other wavelengths. In addition the resonance frequencies of the resonator modes are tunable over more than 62 GHz, or 42 FSRs, by mechanically straining the fiber, see Fig. 2.24(b). Note that this measurement

exploits only a small fraction of the maximum tuning range of the resonator. The latter can be estimated from the optical path length change induced by the maximum possible strain at the rupture point of the nanofiber of $\epsilon_{\max} \approx 14\ \%$ [99]. Consider a resonance at the frequency $f_0 = m\,\Delta f_{\mathrm{FSR}}$ which is an integer multiple of Δf_{FSR}, where the boundary condition of the resonator yields $m = 2\,L_{\mathrm{opt}}/\lambda_0$. With that one obtains a maximum resonance frequency tuning range of

$$\Delta f_0^{\max} = \frac{\partial f_0}{\partial L_{\mathrm{opt}}}\,\Delta L_{\mathrm{opt}} = \frac{-\Delta f_{\mathrm{FSR}}}{\lambda_0}\,(1-\alpha_{\mathrm{so}})\,2\,L_{\mathrm{waist}}\,\Delta\epsilon_{\max} \approx -1.5\cdot 10^3\,\Delta f_{\mathrm{FSR}}\ ,$$

where α_{so} is the strain-optic coefficient, see Ch. 4.5.1. This technique is suitable for actively stabilizing the resonance frequency to an external reference with a high dynamic range [100].

2.3.3 TOF transmission loss

The TOF microresonator allows to precisely determine the TOF transmission loss. For this purpose, the finesse of the FBG resonator is measured before and after tapering the fiber. In both cases, the finesse relates to the mirror reflectivity and the intracavity loss via Eq. (2.3). Due to the nearly lossless fiber transmission of the initial fiber, the intracavity losses can be neglected for the untapered cavity: $t_{\mathrm{R}} = 1$. Therefore, the TOF transmission can be calculated from the finesse of the resonator before the tapering, $\mathcal{F}_0$, combined with the finesse of the TOF microresonator, $\mathcal{F}_1$:

$$t_{\mathrm{R}}^2 = \frac{\mathcal{F}_0^2\left(2\mathcal{F}_1^2+\pi^2-\pi\sqrt{4\mathcal{F}_1^2+\pi^2}\right)}{\mathcal{F}_1^2\left(2\mathcal{F}_0^2+\pi^2-\pi\sqrt{4\mathcal{F}_0^2+\pi^2}\right)}\ , \tag{2.32}$$

see also Eq. (2.31).

The finesse of the untapered resonator is determined by strain-tuning the resonator. Due to the small length of the resonator of 2 cm, its spectral mode spacing of 0.012 nm is comparable to the spectral width of the FBG mirrors. In this case, the FBGs add a wavelength dependent phase such that the free spectral range of the Fabry-Pérot model becomes wavelength dependent and the Airy function Eq. (2.2a) does not correctly describe the spectrum. An intuitive understanding of this situation can be reached by considering how far the wave enters a FBG, the so-called penetration depth: Within the transmission band of the FBG, the full intensity that enters the FBG reaches the far end, meaning that the wave wave fully penetrates the FBG. At the maximum reflectivity, however, the majority of the wave is reflected after a certain number of FBG periods so that the penetration depth takes its minimum value. Taking into account that the length of both FBG mirrors amounts to ≈ 6 mm which is comparable to the length of the resonator it can be seen that the spectral dependence of the penetration depth yields a considerable contribution to L_{opt}.

When fitting the spectrum using the Airy function the finesse and FSR will be overestimated. However, this effect can be minimized by taking advantage of the fact that

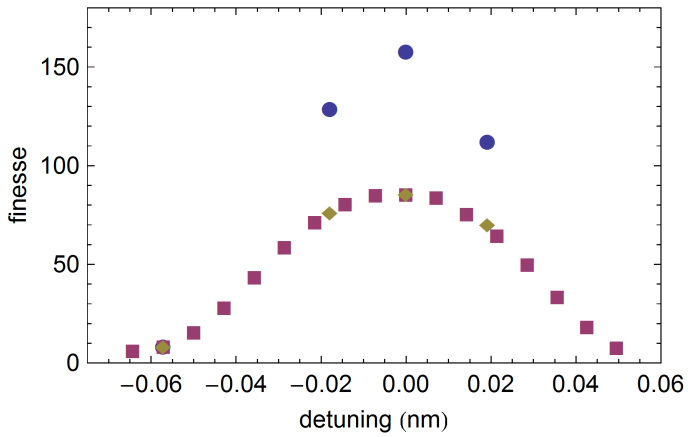

Figure 2.25: *FBG cavity finesses before (circles) and after tapering the fiber (squares) as a function of the laser detuning. Diamonds: see text.*

the penetration depth is symmetric in frequency around the maximum reflectivity. When setting the laser to a frequency such that the two resonances closest to the maximum reflection are arranged symmetrically around the latter, their FBG penetration depths are similar. In this way, the maximum value of $\mathcal{F}_0^{max} = 158(8)$ was measured. Using the maximum finesse of the tapered resonator $\mathcal{F}_1^{max} = 85.6(6)$ the TOF transmission value of $t_R^2 = 0.983(1)$ is obtained. Note that the single-pass intracavity losses $1 - t_R^2$ are smaller than the total off-resonance TOF-microresonator transmission losses $1 - T$, see Fig. 2.24(a): The latter includes additional losses due to, e.g., in- and outcoupling through the FBGs.

In order to check the validity of the value of t_R^2, the finesses was measured for several wavelengths before and after tapering the resonator, see Figure 2.25. The detuning is defined as zero at the wavelength of maximum finesse. A projected finesse value was derived from t_R^2 and the data points of the untapered cavity are displayed in the same graph (diamonds). These projected finesses match the measured values for the TOF microresonator, thereby confirming the consistency of the analysis.

2.3.4 Intracavity polarization measurement

Knowledge of the polarization of the resonator mode is essential for its applications because it determines the exact field configuration and with that the coupling strength to emitters that are brought into its field. The polarization state of the mode in the nanofiber section is determined by analyzing the polarization-dependent emission characteristics of the Rayleigh-scattered light from the nanofiber waist similarly to the method presented in [101]. In essence, the method relies on the analysis of the polarization-dependent emission characteristics of the Rayleigh-scattered light from the nanofiber waist. This light is collected with a CCD camera through a polarization filter, see Fig. 2.26(a). When the nanofiber mode is quasi-linearly polarized one finds a signal variation when rotating the polarization axis of the mode via a half-wave plate. One obtains a signal contrast of

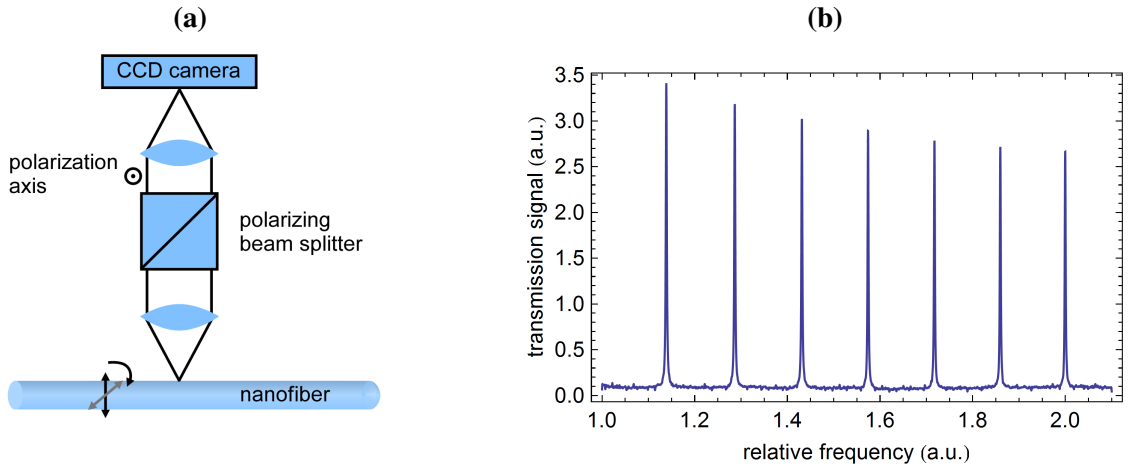

Figure 2.26: *Schematical view of the polarization optimization setup (a) and transmission signal of the TOF microresonator probed with the quasi-linearly polarized mode in the nanofiber (b). Only one set of resonances is visible, thereby proving the quasi-linear polarization of the resonator mode.*

≈ 90 % for the quasi-linearly polarized mode while no intensity variations for the quasi-circularly polarized mode due to the angular symmetry of the latter.

The method to determine the polarization of the resonator mode consists of three steps: First, at a wavelength smaller than the FBG stop-band, the birefringence of the fiber is compensated by polarization compensation optics (PCO) in order to obtain a quasi-linearly polarized mode in the nanofiber section (measured signal contrast 90.3 %). Then, it is checked that the polarization does not change with the wavelength over the spectral range of the FBG stop-band. This was done by measuring the polarization at a wavelength higher than the FBG stop-band without changing the settings of the PCO. This measurement confirmed that the birefringence in the fiber is indeed canceled out and the nanofiber mode is quasi-linearly polarized within the FBG stop-band wavelength range. In the last step, it is checked whether one resonator mode can be selectively excited by rotating the linear polarization. The resulting spectrum is shown in Fig. 2.26(b) and shows that the second can be suppressed by -19 dB, thereby confirming that the modes of the resonator are quasi-linearly polarized in the nanofiber waist.

2.4 Summary

In conclusion, I have experimentally realized a Fabry-Pérot type microresonator with an integrated subwavelength diameter optical nanofiber that is part of a tapered optical fiber (TOF). Its mirrors are realized as fiber-Bragg gratings designed for high reflectivity near the Cs D2 line wavelength. Depending on the desired resonator length, these mirrors are realized as nanofiber Bragg gratings (NFBGs) within the nanofiber waist or as fiber Bragg grating (FBGs) mirrors in the untapered section of the fibers on both sides of the TOF such that the complete TOF including the nanofiber is part of the cavity volume. This allows to fabricate resonators with nearly arbitrary lengths, from half the wavelength in the smallest possible resonator, i.e. a point-defect mode, to the length scale at which absorption in the optical fiber is no longer negligible (~ 100 m) [102].

The NFBGs in the nanofiber waist were realized by 25 to 35 uniform periodically arranged slits along the fiber that are fabricated using a focused ion beam milling machine. In order to measure the spatial form a NFBG, a tomographic method based on successive ion beam milling and scanning electron microscope imaging was employed. Such measurements enable the development of accurate optical models for the NFBGs. The NFBGs fabricated in this work feature high reflectivities of more than 75 % at wavelengths of ≈ 820 nm with a full width of at half maximum of 30 nm. Their spectral response is modeled by using the transfer matrix method in combination with coupled mode theory [78]. It predicts the central wavelength of the stop-band and its spectral width with a relative accuracy of 3 % and 20 %, respectively.

The NFBG resonators reach a maximum finesse of $\mathcal{F} = 11.1 \pm 0.2$ at a vacuum wavelength of 838 nm with a free spectral range of $\Delta f_{\mathrm{FSR}} = 40.70(5)$ GHz and an intracavity intensity loss of 5 %. Its performance is limited by pollutants on the nanofiber that are deposited during the fabrication process as well as gallium that is implanted by the ion beam. I devised an annealing procedure in which a photonic mirror was heated to high temperatures in a vacuum environment by the absorbed light of a laser that is sent through the fiber. From the transmission spectrum of the NFBG, I was able to show that the a large part of the gallium is removed from the nanofiber and the overall transmission can be improved by 30 %.

In order to realize resonators with lengths on the order of centimeters, two fiber Bragg grating mirrors were integrated in the untapered part of the optical fiber such that they enclose the TOF. This so-called TOF microresonator features a finesse of $\mathcal{F} = 85.6 \pm 0.3$ at a vacuum wavelength of $\lambda_0 = 852.53(5)$ nm with a free spectral range of $\Delta f_{\mathrm{FSR}} = 1.48084(45)$ GHz. Its mode is quasi-linearly polarized in the nanofiber section due to birefringence in the resonator. Using this resonator, the taper transmission loss was determined with high precision to be $t_{\mathrm{R}}^2 = 0.983(1)$ from a measurement of the finesse of the resonator before and after the tapering process.

These resonators can operate in the strong coupling regime of cavity quantum electrodynamics (CQED) and fulfill the requirements for non-linear optics applications. In contrast to other nanofiber FBG cavites [75, 77, 78, 81], they allow for observations of coherent effects in cavity quantum electrodynamics, such as quantum Rabi oscillations, and their performance is comparable with or superior to other state-of-the-art fiber-based

cavities [36, 39, 103]. Furthermore, the large tuning range of the resonator length allows to choose the CQED regime of interest, such as fast cavity regime or coherent dynamics.

In addition nanofiber microresonators offer advantageous properties such as tunabilty and a monolithic design enabling alignment-free operation. The TOF microresonator features a constant high cooperativity over the full length of the nanofiber waist. This, in combination with its high transmission outside of the fiber Bragg grating stop band, makes this resonator a promising tool for, e.g., cavity quantum electrodynamics with fiber-coupled atomic ensembles [18, 64] and for the realization of quantum network node functionalities, such as, triggered single photon sources [104], quantum memories based on intra-cavity electromagnetically induced transparency [105], and entangled two photon sources [106]. The nanofiber Bragg grating resonator, however, profits from the high control over the design of the photonic structures provided from the FIB fabrication method which allows to adapt it according to experimental needs in future applications, e.g., cavity optomechanics with photonic structures [107].

Beyond their applications in quantum-optics, nanofiber resonators are highly sensitive to variations of the optical modes propagation constant, which can be used for, e.g., refractive index sensing [7, 79]. In combination with the well-characterized physical properties of the fiber material, the resonators gives also access to physical parameters of a nanofiber which will be exploited in the next chapters to study the thermal radiation and mechanical modes of a tapered optical fiber.

CHAPTER 3

Thermalization of a nanofiber via thermal radiation

Thermalization via heat radiation is an omnipresent process which, e.g., determines the temperature of stars and planets or the functioning of incandescent lamps. For a perfectly black body, the spectral emissive power of far-field thermal radiation was first explained by Planck [1] who used quantized energies for the radiation field, thereby breaking the grounds for quantum theory. The thermal radiation of a real object can then be related to that of a perfectly black body by introducing a correction factor, the so-called spectral emissivity which is treated as a surface property that depends on the specific material and the surface roughness [108]. However, as Planck already stated himself, his theory is designed to describe the far-field heat radiation of macroscopic bodies. Strictly speaking, it can therefore not be applied to objects that have a size or separation comparable to the thermal wavelength:

$$\lambda_T = \frac{\hbar\, c_0}{k_\mathrm{B}\, T} \approx \frac{2.3\ \mathrm{mm}}{T[\mathrm{K}]}\ , \tag{3.1}$$

where $\hbar$ is the reduced Planck's constant, c_0 is the speed of light in vaccum, k_B is Boltzmann's constant and T is the temperature. At room temperature, the thermal wavelength takes the value of $\lambda_T(300\ \mathrm{K}) \approx 8\ \mu\mathrm{m}$. In particular, as soon as the absorption length for the thermal spectrum gets comparable to or larger than the size of the radiating body, thermal radiation becomes a volumetric effect and the spectral emissivity has to take the photonic properties of the object into account. These effects call for a more comprehensive theoretical description. Two established theoretical frameworks in this context are Mie scattering in combination with Kirchhoff's law and fluctuational electrodynamics (FED) [46, 47, 109, 110]. Both approaches give accurate predictions for the far-field thermal radiation [109] which, in case of the infinite cylinder, have been formally been shown to be identical [111]. In addition, the FED-framework has proven to be a versatile tool which also allows one to compute Casimir forces and the radiative heat transfer of arbitrarily shaped bodies in the far- and near-field [112].

The radiative heat exchange of particles smaller than the thermal wavelength has been extensively studied in the past with ensembles of, e.g., soot particles or interstellar dust

in the context of climate physics and astrophysics, respectively [47, 48]. In general, these ensembles are not monodisperse, meaning that only statistical information on their size, shape, and material properties is available. More recently, the progress in nanofabrication led to a new approach using deterministically produced samples of well-defined shape and material. This way, the effect of size and geometrical structure of an object on the spectrum, coherence, and angular distribution of its far-field thermal radiation has been investigated [44, 50–52, 113]. Moreover, it has been shown that the radiative heat transfer rate can be strongly enhanced by near-field effects [45].

The heat radiation of nanofibers is also highly relevant for experiments that employ TOFs with a nanofiber waist in a high vacuum environment. Here, the heat transport is dominated by heat radiation meaning that it determines the temperature of the nanofiber at a given heating rate. In such experiments, even small absorbed optical powers of $\sim 100\ \mu\mathrm{W}$ within the nanofiber can lead to high temperatures due the minuscule heat capacity of the nanofiber of $\sim \mathrm{nJ/K}$. This has posed a major problem in the development of nanofiber-based atom traps because the light absorption had to be reduced to obtain fibers that can sustain the required optical powers. In the fibers with a high enough optical quality are available. However, the only information concerning the temperature that is accessible at the moment is that it is below the fusing temperature of the nanofiber. Even this fusing temperature is, to the best of my knowledge, not determined yet, except for the fact that it is beyond the softening point of fused silica. The measurements and the models presented here were motivated by these pressing questions.

Here, I measure the thermalization dynamics of an tapered optical fiber with a nanofiber waist. This measurement determines, for the first time, the far-field heat radiation of an individual object of predetermined size and shape which is thinner than the thermal wavelength and all absorption lengths of the relevant part of the thermal radiation spectrum. The fiber resides in an ultra high vacuum chamber and due to the low heat conductivity of silica combined with the large ratio of the nanofiber length to its cross-sectional area, the heat transport is dominated by far-field heat radiation. The measurement is based on detecting thermally induced optical path length changes using the TOF-microresonator which are recorded during the heating and cooling process.

The outline of the chapter is as follows: The first section gives an introduction to thermal radiation theory covering Planck's theory and fluctuational electrodynamics (FED). Based on this, an ab-initio thermodynamical model of tapered optical fibers is derived. In order to compare theory and measurement, the optical path-length change of the TOF is derived from the thermo-optic effect and the thermal expansion of the glass. The following sections show the experimental setup and the measurement results.

3.1 Thermal radiation theory

In this chapter the theory of thermal radiation in the far field is presented. In order to compute the thermal radiation of optical nanofibers two theory approaches can be followed: Planck's law for black bodies can be used with the correction by Kirchhoff's law that takes into account that the fiber is not a perfectly black body by its emissivity. The latter is related to the absorption and can be derived from Mie theory. One may alternatively compute the thermal radiation in the framework of fluctuational electrodynamics (FED). Both approaches lead to the same results and provides one a choice of the method.

Here, I choose the approach using fluctuational electrodynamics to compute the radiated power of the nanofiber. Nevertheless, the theory of black-body radiation according to Planck's law has been an important concept which has been taught at universities for the last century. This makes it an important reference point for most physicists and can be used to point out the difference of the black-body radiation emitted by large scale in contrast to nanoscale objects. For this didactic purpose, I will also carry out the analysis using a naïve approach, in which an infinitely large silica block is scaled to match the surface area of the nanofiber without changing its emission characteristics.

The first section is concerned with the thermal radiation according to Planck's law. In the second section the basic concepts of fluctuational electrodynamics (FED) are explained and the third section presents the predictions for a nanofiber extracted from Planck's theory and FED. For a comprehensive theory treatments please refer to the literature: For black-body radiation according Planck's law to [108, 114] and for the FED theory to [109, 110, 115, 116].

3.1.1 Thermal radiation according to Planck's law

In his original work, Planck derived the electromagnetic energy density in a medium consisting of a large number of small oscillators with eigenenergies covering the whole spectrum [1]. His revolutionary idea was that, while there are oscillators in the material for any given frequency, they are only allowed to exchange energy with the optical field in quantized amounts depending on their frequency $\Delta E = h\,\nu$, where h is called Planck's constant and ν is the oscillator frequency. As a consequence, the statistical properties of the energy distribution changes fundamentally compared to the previous, classical, treatment of this problem: The fixed number of oscillators with discrete energy levels gives rise to a countable number of distributions in which the total energy can be dispersed onto these levels. By computing this energy distribution he was able to derive the first correct description of the radiation spectrum of a black body. The formula of the spectral radiance (or spectral intensity) $W(\nu, T)$ is now known as Planck's law and is solely determined by fundamental constants and the temperature of the body T (in Kelvin):

$$W(\nu, T)\,\mathrm{d}\Omega\,\mathrm{d}\nu = \frac{2\nu^2}{c_0^2}\,\frac{h\nu}{\exp\left(\frac{h\nu}{k_\mathrm{B}T}\right) - 1}\,\mathrm{d}\Omega\,\mathrm{d}\nu \tag{3.2}$$

where $k_\mathrm{B} = 1.38065 \cdot 10^{-23}$ J/K Boltzmann's constant, c_0 is the speed of light in vacuum, and $\mathrm{d}\Omega = \int \mathrm{d}\phi \int \mathrm{d}\theta$ is infinitesimal solid angle. The fact that the eigenenergies of the os-

cillators are equally distributed over the whole electro-magnectic spectrum, and therefore, absorb light at any incoming wavelength gives rise to the name black body.

The total radiated power H can be determined by integration the spectral radiance over the surface area of the body, all frequencies and all emission angles in the upper hemisphere. It takes the form of the Stefan-Boltzmann law[1]:

$$H(T) = A\,\sigma_{\mathrm{SB}}\,T^4\ , \tag{3.3}$$

with the Stefan-Boltzmann constant $\sigma_{\mathrm{SB}} = \pi^2 k_{\mathrm{B}}^4/(60\hbar^2 c^2)$. It states that the radiated power scales with the 4th power in temperature.

To reflect the fact that most objects are not perfect absorbers and therefore not ideal black-bodies a correction factor called emissivity $\epsilon(T)$ with values ranging from 0 to 1 has to be added to Eq. (3.2) and Eq. (3.3) which in general can also be temperature dependent:

$$H(T) = \epsilon(T)\,A\,\sigma_{\mathrm{SB}}\,T^4\ . \tag{3.4}$$

The emission characteristics of the body depend on the angle of emission, geometry, surface properties, e.g. reflecting or diffusing, temperature and the spectral properties of the material. For this purpose, it is useful to define the spectral emissivity $\epsilon_\nu(\nu,\theta,\phi)$ which is linked to the total emissivity ($\epsilon(T)$) via the spectral radiance at the specific temperature:

$$\epsilon(T) = \frac{2\int_0^\infty \mathrm{d}\nu \int_0^{2\pi} \mathrm{d}\phi \int_0^{\pi/2} \sin(\theta)\mathrm{d}\theta\ \epsilon_\nu(\nu,\theta,\phi)\,W(\nu,T)\,cos(\theta)}{\sigma T^4}\ . \tag{3.5}$$

A practical concept to determine the spectral emissivity has been given by Kirchhoff, who has proven that a body in thermodynamic equilibrium with its surroundings emits as much energy as it absorbs for each direction and wavelength [43]:

$$\epsilon_\nu(\nu,\theta,\phi,T) = \alpha_{\mathrm{abs}}(\nu,\theta,\phi,T)\ . \tag{3.6}$$

where $\alpha_{\mathrm{abs}}(\nu,\theta,\phi,T)$ is the spectral absorbtivity. This can be understood by considering the opposite case: Let a body in thermodynamic equilibrium absorb more energy than it emits along angle θ_1, while emitting more energy than it absorbs along a different angle θ_2. Then, energy is pumped from angle θ_1 to θ_2 so that any object in direction θ_1 would be cooled without external work. That would lead to a decrease in entropy and is, therefore, in contradiction to the Second Law of Thermodynamics. Similar arguments hold for ν and T.

Kirchhoff's law has proven to be an important and useful tool since it links the thermodynamic properties of a body (emissivity) to its optical properties (absorptivity). It, thereby, allows to determine its thermal radiation characteristics from properties that are optically measurable as well as predictable by the comprehensive theoretical framework of electrodynamics. However, the determination of the spectral absorptivity of an object can be challenging due to its numerous free parameters.

[1]Note, that the surface of the body appears smaller when viewed under an angle. This has to be taken into account when integrating over all angles in the hemisphere by the geometrical visibility factor, $\cos(\theta)$. The integral over the emission angle reads then $\int \mathrm{d}\Omega\ \cos(\theta) = \int_0^{2\pi} \mathrm{d}\phi \int_0^{\pi/2} \mathrm{d}\theta\ \sin(\theta)\ \cos(\theta) = \pi$.

This framework is a powerful tool but limited to large bodies and to far-field radiation as Planck already stated himself [1]. In particular, as soon as the absorption length for the thermal spectrum gets comparable or larger than the size of the radiating body, thermal radiation becomes a volumetric effect and the spectral emissivity has to take the photonic properties of the object into account. In this case, the thermal radiation does not scale with the surface area and has to be evaluated for each geometry individually. Furthermore, as soon as the separation of two objects is comparable or smaller than the thermal radiation wavelength their surrounding evanescent fields overlap and the heat transfer through this channel contributes to or even dominates the radiative heat transfer. However, the far-field thermal radiation of small objects can still be computed individually for each geometry from their photonic properties. This has been solved for various symmetrical geometries, such as, cylinders, spheres and ellipsoids using Mie theory [47]. In particular, the emissivity of a nanofiber can be computed using this approach.

3.1.2 Emissivity of a silica–vacuum interface

In order to compare the prediction from Planck's theory with the measurement results, the emissivity of a polished silica—vacuum interface is derived here. While this approach is artificial and gives a naïve picture of heat radiation, Planck's law is an important reference point for most physicists and is included here for didactic purposes.

The treatment of an object as a silica—vacuum interface of the same surface area neglects the transmission through the body and is thus in principle only valid for structures which are much larger than all absorption lengths in the thermal radiation spectrum. This condition is, however, not fulfilled in the case of silica at high temperatures for which the thermal spectrum significantly extends into the visible range where fused silica is highly transparent. However, in order to be able to compare the FED prediction to Planck's law including a color correction that does not make any assumptions regarding the size of the object, I will follow this approach.

The spectral emissivity is then derived from Kirchhoff's law and energy conservation. The latter means that the optical transmission, reflection and loss add up to unity and since the transmission of an infinite body vanishes one finds $\epsilon_\nu(\nu,\Omega) = 1 - \alpha_{\mathrm{refl}}(\nu,\Omega)$, where $\alpha_{\mathrm{refl}}(\nu,\Omega)$ is the spectral reflectivity. The total hemispherical emissivity follows from Eq. (3.5) and the spectral reflectivity according to Frensel's formula by averaging over both polarizations [117]:

$$\alpha_{\mathrm{refl.}}(\nu,\Omega) = \frac{1}{2}\left(\left|\frac{\tilde{n}_1(\nu)\cos(\theta) - \sqrt{\tilde{n}_2^2(\nu) - \tilde{n}_1^2(\nu)\sin^2(\theta)}}{\tilde{n}_1(\nu)\cos(\theta) + \sqrt{\tilde{n}_2^2(\nu) - \tilde{n}_1^2(\nu)\sin^2(\theta)}}\right|^2 + \left|\frac{\tilde{n}_2^2(\nu)\cos(\theta) - \tilde{n}_1\sqrt{\tilde{n}_2^2(\nu) - \tilde{n}_1^2(\nu)\sin^2(\theta)}}{\tilde{n}_2^2(\nu)\cos(\theta) + \tilde{n}_1\sqrt{\tilde{n}_2^2(\nu) - \tilde{n}_1^2(\nu)\sin^2(\theta)}}\right|^2\right), \quad (3.7)$$

where $\tilde{n}_1 = 1$ and θ are the complex refractive index and the angle of incidence in vacuum, respectively, and $\tilde{n}_2$ is the complex refractive index of silica. The resulting total

hemispherical emissivity is plotted in Fig. 3.1 as a function of temperature for all combinations of the maximum and minimum traces of the real and imaginary part of the refractive index. For the further calculations only the minimum and maximum emissivity

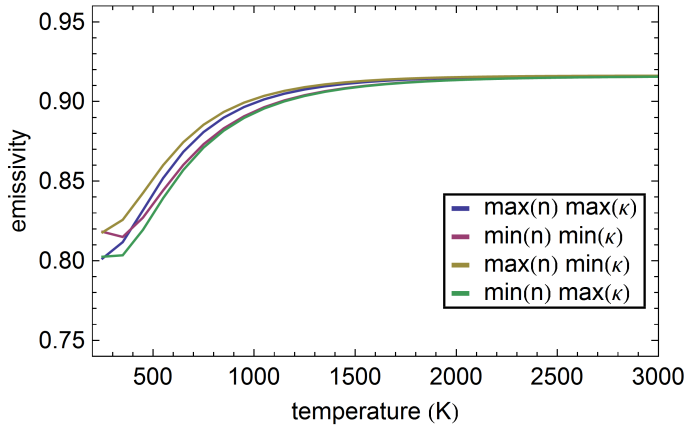

Figure 3.1: *Spectral emissivity of a polished silica—vacuum interface as function of temperature.*

traces (green and yellow lines, respectively) are used.

3.1.3 Fluctuational Electrodynamics (FED)

This chapter introduces the concept of fluctuational electrodynamics (FED), first developed by Rytov [46], that will be used in the following to compute the far-field radiation of the nanofiber. In order to motivate how the general formulation of the thermally excited fields are derived, I will present the key ideas following the derivation in [109] without dwelling on technical details. For comprehensive treatments please refer to [46, 109, 110, 118–121].

The concept of FED is based on the idea that thermal radiation is the electromagnetic radiation that originates from thermal fluctuations of the quantum states in a body. This can be computed from a central theorem of statistical mechanics, the fluctuation dissipation theorem (FDT), that relates the thermal noise power spectral density to the susceptibility of a system. Consider a system where the response Y to an external driving F can be expressed via a susceptibility χ according to $Y(\omega) = \chi(\omega)\, F(\omega)$. The noise power spectral density $\langle Y\, Y^* \rangle$ of the amplitude Y that results from thermal excitation can then be computed from the fluctuation dissipation theorem

$$\langle Y\, Y^* \rangle = \left(\hbar + \frac{2\,\hbar}{\exp(\hbar\,\omega / k_\mathrm{B}\, T) - 1} \right) \mathrm{Im}\,(\chi) \tag{3.8a}$$

$$\xrightarrow[\text{classical}]{\hbar \to 0} \frac{2\, k_\mathrm{B}\, T}{\omega}\, \mathrm{Im}\,(\chi)\ , \tag{3.8b}$$

given here in the quantum mechanical formulation as well as in the classical limit[2] [118,

[2]Note that the zero-point energy has only to be taken into account in quantum measurements and cancels out when computing fluxes.

120]. By relating the imaginary, i.e. the absorptive part, of the susceptibility to the thermal fluctuations it shows that the latter originate from the dissipation in the internal degrees of freedom of the system. This is a very fundamental concept which finds applications in different branches of physics, e.g., thermal radiation as presented here or thermal motion (see next chapter) [118].

In the case of thermal radiation the FDT is formulated in a generalized form for vector quantities with the electric dipole moment $\boldsymbol{p}$ of a body that is exerted by an electric field $\boldsymbol{E}$ so that $\boldsymbol{p} = \epsilon_0 \, \boldsymbol{\chi} \, \boldsymbol{E}$. Thereby, the polarizability $\boldsymbol{\chi}$ plays the role of the objects susceptibility, the electric field represents the external driving and the dipole moment is the fluctuating quantity. With that, one obtains the following expression for the (cross) power spectral density of the dipole moment of the particle in thermodynamic equilibrium:

$$\langle p_k \, p_l^* \rangle = \left(\hbar + \frac{2\,\hbar}{\exp(\hbar\,\omega / k_\mathrm{B}\,T) - 1} \right) \mathrm{Im}\left(\epsilon_0 \, \chi_{kl}\right) \ , \tag{3.9}$$

where k and l are the indices of the polarization vector components. This fluctuating dipole emits electromagnetic radiation which is the heat radiation. The photonic and material properties of the object are accounted for by the polarizability of the object. In practical applications the particles spectral polarizability with respect to a complete basis set of incident electromagnetic waves is required in order to compute the thermal radiation.

In the next step, the polarizability of the object can be expressed using Green's functions and thereby allow for a numerical analysis of an object [112]. For this purpose, the polarizability fluctuations are interpreted as fluctuating currents which can be related via Maxwell's equations via $\boldsymbol{j} = -\mathbb{i}\omega \, \boldsymbol{p}$ for a field with frequency ω, thereby resulting in

$$\langle j_k(\boldsymbol{r}) j_l^*(\boldsymbol{r}) \rangle = \omega^2 \left(\hbar + \frac{2\,\hbar}{\exp(\hbar\,\omega / k_\mathrm{B}\,T) - 1} \right) \mathrm{Im}\left(\epsilon_0 \, \epsilon_{kl}(\boldsymbol{r})\right) \ , \tag{3.10}$$

where the polarizability is replaced by the dielectric constant $\boldsymbol{\epsilon} = \mathbb{1} + \boldsymbol{\chi}$ as their imaginary parts are equal. Now, the electric and magnetic fields can be directly computed using Green's tensor functions $\boldsymbol{G}$ of the system:

$$\boldsymbol{E}(\boldsymbol{r}, \omega) = \mathbb{i} \, \mu_0 \, \omega \int \mathrm{d}^3 \boldsymbol{r}' \, \boldsymbol{G}^{EE}(\boldsymbol{r}, \boldsymbol{r}', \omega) \, \boldsymbol{j}(\boldsymbol{r}', \omega) \tag{3.11a}$$

$$\boldsymbol{H}(\boldsymbol{r}, \omega) = \int \mathrm{d}^3 \boldsymbol{r}' \, \boldsymbol{G}^{HE}(\boldsymbol{r}, \boldsymbol{r}', \omega) \, \boldsymbol{j}(\boldsymbol{r}', \omega) \ , \tag{3.11b}$$

where the definition $\boldsymbol{G}^{EE}$ and $\boldsymbol{G}^{HE}$ is not essential for the basic understanding and can be found in [109, 120]. These results can be employed to compute the cross power spectral density of arbitrary combinations of electric and magnetic field components that arise from the fluctuating currents in an object. Thereby it is possible to compute the energy density, the power flow or forces that arise from thermal fluctuations via Maxwell's stress tensor. The flux of the radiation in the far field is given by the Poynting vector

$$\boldsymbol{S}(\boldsymbol{r}, \omega) = (1/2) \, \mathrm{Re}[\boldsymbol{E}(\boldsymbol{r}, \omega) \times \boldsymbol{H}^*(\boldsymbol{r}, \omega)] \ .$$

which can be computed from cross-spectral densities of the type $\langle E_k(\boldsymbol{r},\omega)H_l^*(\boldsymbol{r},\omega)\rangle$. In the simplest case of an isotropic medium $\boldsymbol{\epsilon}(\boldsymbol{r}) = \mathbb{1}\,\epsilon(\boldsymbol{r})$, the following expression follows

$$\langle E_k(\boldsymbol{r},\omega)\, H_l^*(\boldsymbol{r},\omega)\rangle = \frac{-\mathbb{i}\omega^3}{c_0^2}\int \mathrm{d}^3\boldsymbol{r}_1 \left(\frac{\hbar\,\omega}{2} + \frac{\hbar\,\omega}{\exp(\hbar\,\omega/k_\mathrm{B}\,T)-1}\right) \times \mathrm{Im}[\epsilon(\boldsymbol{r}_1)]\, \boldsymbol{G}_{km}^{EE}(\boldsymbol{r},\boldsymbol{r}_1,\omega)\, \boldsymbol{G}_{lm}^{HE*}(\boldsymbol{r},\boldsymbol{r}_1,\omega)\,. \quad (3.12)$$

While this formulation is more complex, it features similarities to the expressions derived for the dipole moment, see Eq. (3.9) above. The major difference is that geometry and material is now represented by Green's tensors in conjunction with the imaginary part of the dielectric tensor. It is, however, a very general formulation of the fluctuating fields and a powerful concept that allows to make predictions for a wealth of situations beyond that of far-field thermal radiation, such as, e.g., near-field radiative heat transfer, Casimir forces acting between bodies at different temperatures, or coherence effects of the thermal radiation.

3.1.4 Far-field heat radiation of a silica nanofiber

In this section the results for the far field heat radiation of a cylinder obtained from FED calculations are presented, as derived in [111]. The radiated power per unit length, $\partial_z H_\mathrm{rad}$, of an infinite cylinder of radius a at temperature T_c that is composed of an isotropic material with the spectral dielectric function ϵ and spectral magnetic permeability μ can be expressed as

$$\partial_z H_\mathrm{rad} = \frac{4}{c_0}\int_0^\infty \mathrm{d}\nu\, \frac{h\,\nu^2}{\exp\left(h\nu/k_\mathrm{B}T_\mathrm{c}\right)-1} \sum_{P=\parallel,\perp}\sum_{l=-\infty}^{\infty} \times \int_{-1}^{1}\mathrm{d}\xi\, \left(\mathrm{Re}\left(T_{l,\xi}^{PP}\right) + |T_{l,\xi}^{PP}|^2 + |T_{l,\xi}^{P\bar{P}}|^2\right)\,, \quad (3.13)$$

where $P = \{\perp,\parallel\}$ is the polarization of the radiated light with respect to the plane given by the propagation direction of the emitted radiation and the cylinder axis, see Fig. 3.2. Furthermore, $\bar{P}$ denotes the polarization perpendicular to P, l is a mode number similar to the one defined for the fiber modes, $\xi = \sin(\theta)$ is the sine of the polar emission angle $\theta \in [-\pi/2, \pi/2]$ with respect to the fiber axis. The latter can also be expressed by $\xi = k_z/k_0$ the ratio of the axial propagation constant k_z and the vacuum propagation constant $k_0 = 2\pi\,\nu/c_0$.

The T-matrix elements are given by

$$T_{l,\xi}^{\perp\perp} = -\frac{J_l(q\,a)}{H_l^{(1)}(q\,a)}\,\frac{\Delta_1\Delta_4 - K^2}{\Delta_1\Delta_2 - K^2}\,, \qquad T_{l,\xi}^{\parallel\parallel} = -\frac{J_l(q\,a)}{H_l^{(1)}(q\,a)}\,\frac{\Delta_2\Delta_3 - K^2}{\Delta_1\Delta_2 - K^2}\,,$$
$$T_{l,\xi}^{\perp\parallel} = T_{l,\xi}^{\parallel\perp} = \frac{2\mathbb{i}\,K}{\pi\,\sqrt{\epsilon\mu}\,(q\,a\,H_l^{(1)}(q\,a))^2}\,\frac{1}{\Delta_1\Delta_2 - K^2}\,,$$

where $J_l(x)$ is the Bessel function of the first kind of order l and $H_l^{(1)}(x)$ is the Hankel function of the first kind of order l. The variable $q = k_0\sqrt{1-\xi^2}$ denotes the component

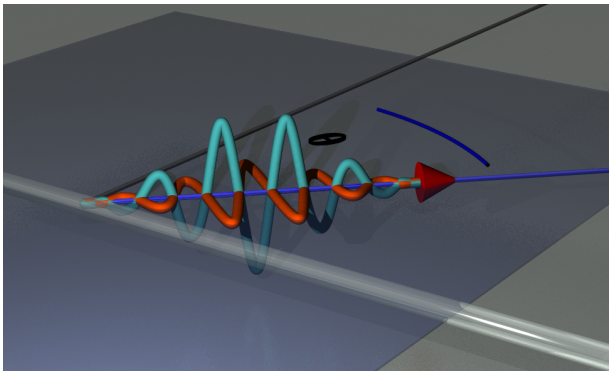

Figure 3.2: *Schematic view of the photons that are radiated from a nanofiber (transparent cylinder). The plane spanned by the fiber axis and the emission direction is shown in transparent blue. A stilized photon with parallel and perpendicular polarization is shown in red and blue, respectively.*

of the propagation constant that is perpendicular to the cylinder axis. Furthermore the following definitions have been used:

$$\Delta_1 = \frac{J_l'(q_1\,a)}{q_1\,a\,J_l(q_1\,a)} - \frac{1}{\epsilon}\frac{H_l^{(1)\prime}(q\,a)}{q\,a\,H_l^{(1)}(q\,a)}\,, \qquad \Delta_2 = \frac{J_l'(q_1\,a)}{q_1\,a\,J_l(q_1\,a)} - \frac{1}{\mu}\frac{H_l^{(1)\prime}(q\,a)}{q\,a\,H_l^{(1)}(q\,a)}\,,$$

$$\Delta_3 = \frac{J_l'(q_1\,a)}{q_1\,a\,J_l(q_1\,a)} - \frac{1}{\epsilon}\frac{J_l'(q\,a)}{q\,a\,J_l(q\,a)}\,, \qquad \Delta_4 = \frac{J_l'(q_1\,a)}{q_1\,a\,J_l(q_1\,a)} - \frac{1}{\mu}\frac{J_l'(q\,a)}{q\,a\,J_l(q\,a)}\,,$$

$$K = \frac{l\,\xi\,k_0\,c_0}{\sqrt{\epsilon\mu}\,R^2\,\omega}\left(\frac{1}{q_1^2} - \frac{1}{q^2}\right)\,, \qquad q_1 = k_0\sqrt{\epsilon\mu - \xi^2}\,,$$

where the prime denotes the derivative with respect to the argument: $f'(x) = \partial f(x)/\partial x$. The material properties enter solely via the dielectric function and permeability which is given above. Note that these results are the same as the ones obtained from Mie theory [47, 111].

The spectral emissivity of a silica cylinder $\epsilon_{\nu,a}(\nu)$ of radius a can now be computed from the ratio of the total radiated power per surface area of the fiber $\partial_x\partial_\nu H_{\mathrm{rad}}/(2\pi a)$ to the spectral emissive power of a black body $P_\nu(\nu,T)\;\mathrm{d}\nu = \int \mathrm{d}\Omega\;\cos(\theta)\,W(\nu,T)$. The latter is obtained from Planck's formula by integrating the spectral radiance $W(\nu,T)$ over all emission angles in the hemisphere. From Eq. (3.13) and Eq. (3.2) the spectral hemispherical emissivity follows and takes the form

$$\epsilon_{\nu,a}(\nu) = \frac{c_0}{\nu\,\pi^2\,a}\sum_{P=\parallel,\perp}\sum_{n=-\infty}^{\infty}\int_{-1}^{1}\mathrm{d}\xi\;\times\left(\mathrm{Re}\left(T_{l,\xi}^{PP}\right) + |T_{l,\xi}^{PP}|^2 + |T_{l,\xi}^{P\bar{P}}|^2\right)\,. \tag{3.14}$$

It should be stressed that this spectral emissivity is only valid for the particular fiber diameter it has been computed for and yields incorrect results when used for different diameters by scaling the surface area, as in standard heat radiation theory (compare Eq. (3.4)). In particular, the heat radiation of very thin cylinders scales with the volume and thereby illustrates that the concept of emissivity as property that is solely determined by material

and the surface of the body cannot be applied to objects with sizes comparable to the thermal wavelength [111]. However, a structure-dependent emissivity is a useful tool for the numerical computation of the radiated power because the costly numerically integration of the T-matrix only needs to be evaluated once for each diameter and then may be used to compute H_{rad} for several temperatures.

The total radiated power of the fiber follows by integrating the product of the emissivity and the spectral emissive power:

$$H_{\mathrm{rad}}(T) = A_{\mathrm{cyl}} \int_0^\infty \mathrm{d}\nu \, P_\nu(\nu, T) \, \epsilon_{\nu,a}(\nu) \, , \tag{3.15}$$

where $A_{\mathrm{cyl}} = 2\pi \, a \, \Delta z$ is the surface area of the cylinder of length Δz. This is illustrated for a fused silica cylinder with a diameter of 500 nm in Fig. 3.3. One finds sharp emission peaks at the wavelengths of the infrared absorption bands of silica. Their emissivity exceeds in some cases a value of 1. This means that the fiber emits a more power than one would expect from a black body with the same surface area. A qualititative understanding of this effect can be gained when considering that the optical path length of a round trip on the surface of the nanofiber in its cross-section amounts to $2\pi \, a \, n \approx 10$ µm (see Fig. A.1 for n). This coincides with the wavelength of the emitted radiation so that intereference effects can change the mode density such that one finds an enhanced emission. The totally emitted power, however, is smaller compared to a black body ($\epsilon(\nu) = 1$) because the fiber exhibits a small emissivity for large parts of the spectrum. Furthermore, the sharp spectral features of the emissivity result in a different temperature scaling of the radiated power. Three regimes can be distinguished: At very low temperatures a black body emits most of the thermal radiation at low frequencies for which the nanofiber is transparent. With increasing temperatures, a growing amount of radiation is emitted at infrared wavelengths for which the nanofiber is highly absorbing. As a consequence, the radiated power of a nanofiber increases more rapidly compared to a black body resulting in a T^6-dependence (see also Ch. A.8 and [111]). At temperatures much larger than room temperature we find the opposite situation. Here, a black body would emit an increasing fraction of the radiated power in the visible wavelength range for which the nanofiber is transparent and its emissivity is low. As a consequence, the increase of the radiated power with temperature is much lower for a nanofiber than for a black body. In the third regime around 300 K the comparatively broad maximum of P_ν is located at the two peaks of the spectral emissivity of the fiber so that the temperature scaling is expected to be comparable to that of the black body.

In the considerations above the temperature effects on the spectral emissivity of the nanofiber have been neglected. These arise from a geometry change caused by the thermal expansion and a change of the dielectric function due to the thermo-optic effect. However, the thermal expansion of the fiber is on the order of 10^{-3} [122] and therefore much smaller than the uncertainty of the radius profile of the fiber. The thermo-optic effect primarily causes a frequency shift of the UV absorption band of ≈ 10 % in the temperature range considered here [123] (see also Ch. 3.3.1 below). The contribution of this absorption band to the thermal radiation is negligible for the temperatures considered here so that they are neglected in the following.

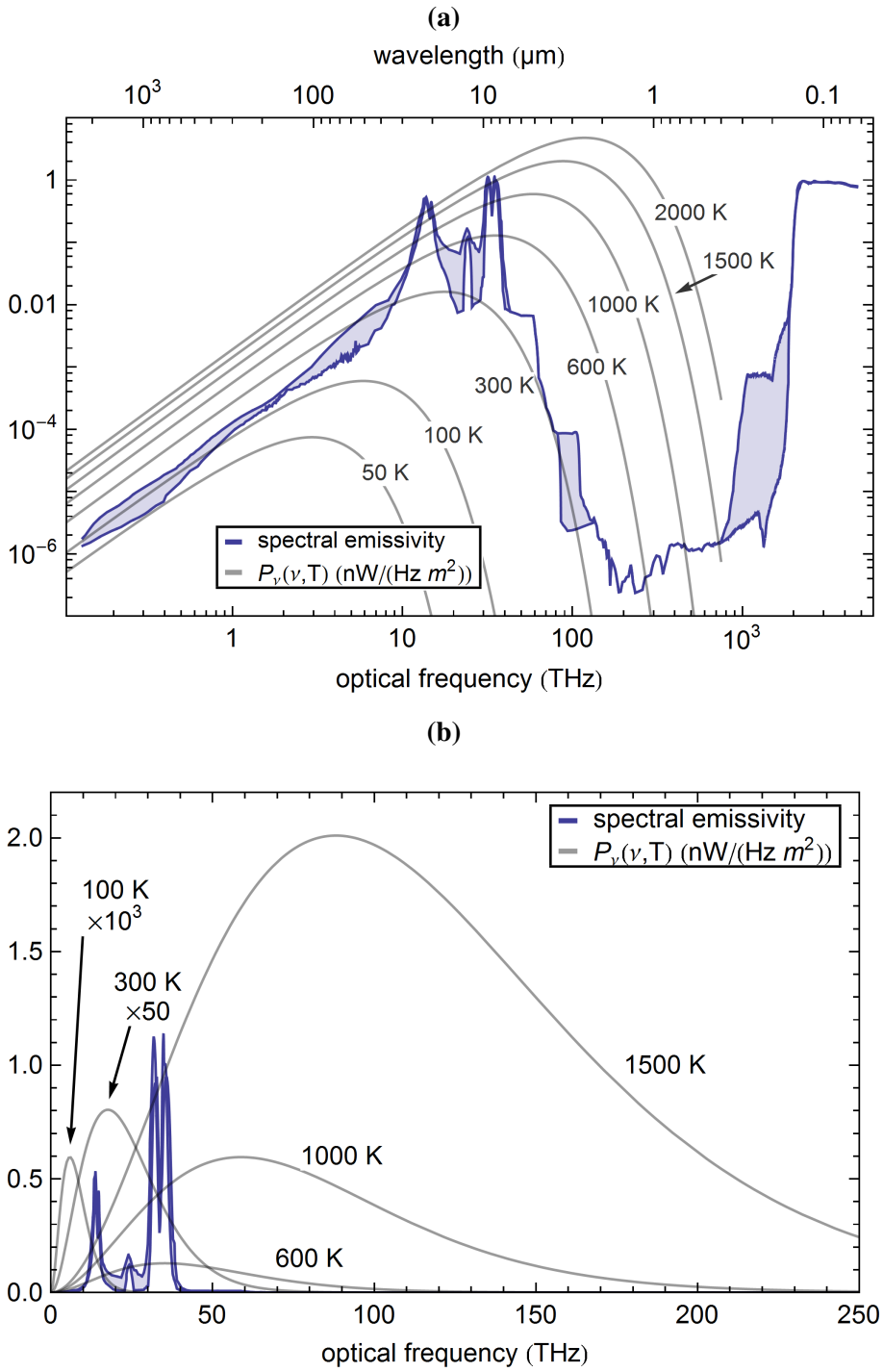

Figure 3.3: *Spectral emissivity ($\epsilon_{\nu,250\ \mathrm{nm}}$) of a nanofiber with $a = 250$ nm radius (blue) and black-body spectral emissive power, $P_\nu(\nu, T)$, for the tempeatures denoted in the plot (grey). The same plotis shown either double-logarithmically (a) or linearly (b). The total emitted power can be obtained by integrating the product of the emissivity and the spectral emissive power for the corresponding temperature. The lines delimiting the blue area are the two extremal traces of $\epsilon_{\nu,a}$ that are obtained from the dielectric function taking the uncertainty of the latter into account.*

3.1.5 Modification of thermal radiation by surface pollutants

A small amount of light-absorbing surface pollution on the nanofiber is unavoidable but can, according to Kirchhoff's law, significantly change the emission characteristics of the latter. In the case where a fiber is highly polluted, the thermal radiation of the pollutants can in principle be comparable or even exceed that emitted by the nanofiber. In order to minimize this bias, it is essential to keep the pollution on the fiber at a low level. To this end, the TOFs are protected by all reasonably possible measures from airborne pollution: The air above the optical tables is filtered using high efficiency particle filters (HEPA), the TOFs are transported in closed dust free boxes and a slow pumping scheme is used during the evacuation process to minimize dust deposition due to turbulent air flow. These methods render the extremely high TOF transmission values exceeding $98\ \%$ possible, see Ch. 2.3.3. However, a point of concern is that the fiber is heated in the following experiments via the light of a heating laser (wavelength 780 nm) that is absorbed by pollutants on the nanofiber surface. Kirchhoff's law implies that heat radiation in the spectral region of the heating laser wavelength is primarily emitted by the pollutants. In the following, I will show that the overall emittance of the fiber is only weakly modified by the presence of the pollutants. It still iswell-described assuming a pure silica fiber meaning that the measurements indeed probe the thermal radiation of the nanofiber and not that emitted by pollutants. First the arguments are briefly summarized which are then presented in detail.

In essence, the absorption of the pollutant in the near infrared (NIR) spectral range ($[0.7 \ldots 2]\mu$m) only dominates because of the extreme transparency of the silica. However, it is still extremely small and, in particular, negligible compared to that of silica in the wavelength range where the latter is opaque, see Fig. A.1. As a result, the emittance of the total structure (silica nanofiber including the pollutants) is dominated by the properties of silica in the relevant spectral regions, i.e., where the vast majority of the heat radiation is emitted.

More in detail, the TOF transmission loss caused by the pollutant can be determined from a measurement of the intracavity loss of a resonator with an integrated TOF at the probe wavelength, see Ch. 2.3.3, and amounts to $A_{\mathrm{polut}}(\lambda_{\mathrm{probe}}) < 2 \cdot 10^{-2}$. Only a fraction of this transmission loss is actually caused by absorption as it also includes scattering losses due to non-adiabatic mode transformation in the taper sections and scattering losses caused by the pollutants. As a conservative estimation of the absorption caused by pollutants, one may still assume that the entire transmission loss through the TOF is due to absorption caused by the pollutants. From $A_{\mathrm{polut}}(\lambda_{\mathrm{probe}})$ an effective extinction coefficient at the probe laser wavelength can be estimated:

$$\kappa_{\mathrm{eff}}(\lambda_{\mathrm{probe}}) = \frac{A_{\mathrm{polut}}(\lambda_{\mathrm{probe}})\,\lambda_{\mathrm{probe}}}{4\pi\,L_{\mathrm{waist}}} < 3 \cdot 10^{-7}\ . \tag{3.16}$$

This is seven orders of magnitude smaller than the peak extinction coefficient of fused silica in the IR range $\kappa_{\mathrm{silica}} \sim 1$, see Fig. A.1. As a consequence, even for temperatures as high as 2000 K, the spectral radiated power of the pollutants in the NIR range is much smaller than the spectral radiated power of silica in the IR range because the correspond-

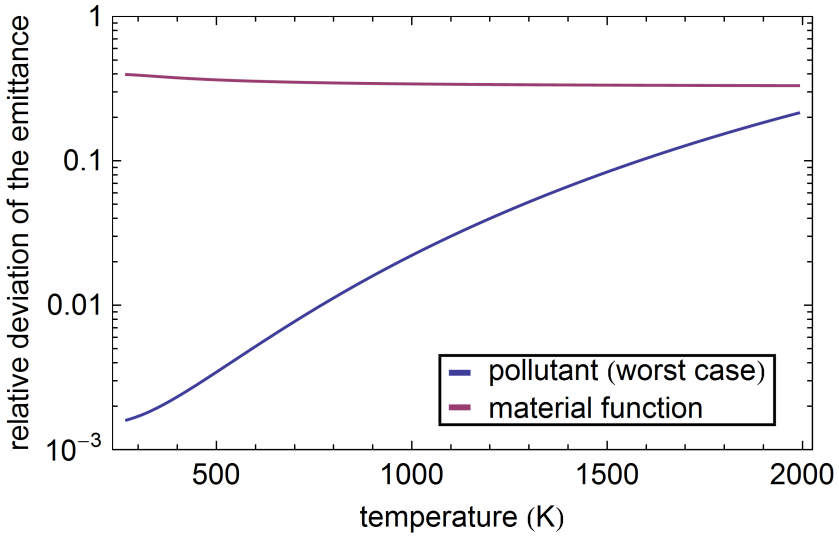

Figure 3.4: *Calculated relative deviation of the radiated power with and without pollutant. The upper estimate of the absolute radiated power with pollutants that enters into this ratio has been obtained by adding $\kappa_{\mathrm{eff}} = 5 \cdot 10^{-4}$ to the spectral extinction coefficient of fused silica and computing the far-field radiation of a 500 nm cylinder composed a material with the resulting dielectric function. The purple line shows the relative uncertainty of the emittance due to the uncertainty of the dielectric function of silica (see above). This shows, that the deviation caused by the pollutants, even in the worst case, is smaller than the uncertainty resulting from the dieletric function.*

ing ratio of spectral radiances given by Planck's formula does by far not overcompensate this factor.

Moreover, from $A_{\mathrm{polut}}(\lambda_{\mathrm{probe}})$, an estimate of the effective layer thickness of the pollutants can be inferred by comparing this value to what is observed in surface absorption spectroscopy of nanofiber-adsorbed dye molecules [8]: If the pollutants were perfectly black molecules with an extinction coefficient κ_{polut} on the order of 1, the absorption of $A_{\mathrm{polut}}(\lambda_{\mathrm{probe}}) = 2\ \%$ in the NIR spectral range would correspond to less than $1\ ‰$ of a closed monolayer of these molecules on the nanofiber surface or, equivalently, an effective layer thickness of less than 1 pm. Even if $\kappa_{\mathrm{polut}}(\lambda_{\mathrm{probe}})$ was two orders of magnitude lower (i.e., slightly more transparent than indium tin oxide) the corresponding effective layer thickness would still be below 0.1 nm. This means that the pollutant would contribute a volume fraction below $f_{\mathrm{V}} = 5 \cdot 10^{-4}$ to the nanofiber which is taken as an upper limit in the following.

From f_{V}, the maximum value that the effective extinction coefficient can possibly reach in any part of the spectrum can now be estimated. It is given by the maximum possible value of the pollutants extinction coefficient (which is on the order of $\kappa_{\mathrm{polut}} \sim 1$) multiplied by the volume fraction, yielding $\kappa_{\mathrm{eff}}(\lambda_{\mathrm{max}}) \sim 5 \cdot 10^{-4}$. This is more than four orders of magnitude smaller than the peak value for fused silica in the IR range.

Assuming this worst-case value for the entire spectrum, a maximum relative deviation of the radiated power of $20\ \%$ at 2000 K compared to the case without can be found, see

Fig. 3.4. Note that several worst-case estimations entered this value: The absorption of the pollutants is overestimated by assuming it to be solely responsible for the entire TOF transmission losses. By assuming that the pollutants have a low extinction coefficient at the probe laser wavelength one obtains a large layer thickness of pollutants and thus a large volume fraction. And finally, it was assumed that the pollutants are totally opaque ($\kappa_{\mathrm{polut}} \sim 1$) at all wavelengths except for the probe laser wavelength. In conclusion the effect of the pollutants on the heat radiation properties of the nanofiber is negligible. Even in the worst case their contribution is covered by the uncertainty of the other parameters.

3.2 Thermodynamical model of a TOF in vacuum

In order to gain a quantitative understanding of the temperature dynamics of the nanofiber under the influence of heating, here an ab initio thermodynamical model of the TOF is developed that includes heat transport via thermal radiation, heat conduction along the TOF, and heat diffusion through the surrounding background gas. The model includes the radius profile of the TOF as well as material constants of fused silica and the total radiated power per unit length of the TOF. The latter is computed using FED predictions for an infinite cylinder (see above). For comparison, the model is also evaluated using naïve approach given by Planck's law including the spectral emissivity of a silica surface with equal area. The heating of the fiber is experimentally realized by the absorption of a heating laser which corresponds to the typical heat source which occurs in most fiber experiments.

3.2.1 Heat transfer equation

From energy conservation, one finds the following differential equation of the heat transfer as function of the (local) temperature T [124]:

$$c_\mathrm{p}\,\rho\,\partial_t T\,\mathrm{d}V = \nabla(q_\mathrm{hc}\nabla T)\,\mathrm{d}V - \sqrt{\frac{k_\mathrm{B}\,f^2}{8\pi\,M_{N2}\,T_0}}p\,(T-T_0)\,\mathrm{d}A \\ - [\mathrm{d}H_\mathrm{rad}(T) - \mathrm{d}H_\mathrm{rad}(T_0)] + \mathrm{d}P_\mathrm{abs}\,, \quad (3.17)$$

taking into account the following heat transfer processes given in order of appearance: heat conduction, heat transport in the surrounding gas at pressure p, thermal radiation and a heating source $\mathrm{d}P_\mathrm{abs}$. The quantities are given in Tab. 3.1, and the dependencies on temperature, space and time are omitted for clarity.

symbol	constant	value range from T_0 to the highest T covered in Ref.	temperature range convered in Ref.	Ref.
T_0	room temperature	(294 ± 0.5) K	-	-
q_hc	heat conductivity	$(1.3 - 2.1)$ W/(K·m)	$(0.1 - 1650)$ K	[125]
c_p	specific heat (silica)	$(700 - 1500)$ J/(kg·K)	$(0 - 2000)$ K	[126]
ρ	density (silica)	2200 kg/m^3	-	[125]
f	degrees of freedom of N_2	6	-	-
M_{N2}	molecular mass of N_2	$4.653 \cdot 10^{-26}$ kg	-	-

Table 3.1: *Model parameters with values in the range from room temperature to the maximum temperature available in literature. For temperature dependencies see Appendix.*

In this model, temperature gradients in the background gas were neglected. This is valid for mean free path lengths of the molecules, Λ, that are much larger than the distance to the heat sink, such as, e.g., the fiber mount or the vacuum chamber wall. The pressure up to which this condition is fulfilled can be estimated by assuming a typical

distance to the heat sink which is here 10 cm. The mean free path length scales inversely proportional to the gas density and therefore also the pressure $\Lambda \propto n^{-1} \propto p^{-1}$ where $\Lambda(10^3\ \mathrm{mbar}) = 70$ nm for nitrogen [124]. A mean free path length of $\Lambda = 10$ cm can be found for a nitrogen gas pressure of $p \approx 10^{-3}$ mbar. For higher pressures, the model may overestimate the effect of heat diffusion. Note, however, that the transition to the regime in which the background gas exhibits a temperature gradient can take place in a pressure range that covers several orders of magnitude. For this reason, the validity of this assumption was experimentally checked (see below).

3.2.2 Heating of the nanofiber by absorption

The heating of the nanofiber section is achieved by the absorbed power of a laser field. It has been shown that the transmission loss of silica nanofibers is primarily governed by surface pollution [127]. In the model, it is therefore assumed that the heating of the TOF is caused by surface absorption. Note that, there is no means to determine where the laser is absorbed, the other extreme case of heating by pure volume absorption is studied in Ch. A.7 and yields essentially the same results.

The power that is absorbed by surface polutants is proportional to the surface intensity of the fundamental fiber mode integrated over the circumference of the fiber:

$$\partial_z P_{\mathrm{abs}}(z) \propto a(z) \int_0^{2\pi} \mathrm{d}\phi\, |\boldsymbol{E}(a(z), \phi, z)|^2 \,. \tag{3.18}$$

This heating power distribution $\partial_z P_{\mathrm{abs}}(z)$ is normalized to the total absorbed power P_{abs} which is given by the integral of the heating power distribution along the fiber axis. Figure 3.5 shows an exemplary profile of $\partial_z P_{\mathrm{abs}}$ which is computed for the radius profile of TOF-resonator #3.

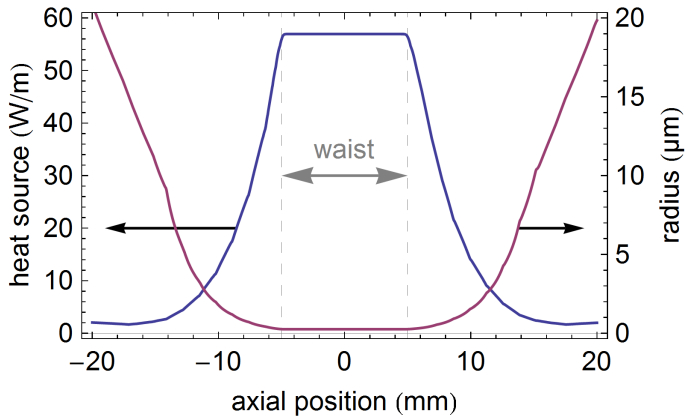

Figure 3.5: *Heating power distribution of the surface source (blue) and TOF radius (red) as function of the position along the fiber axis.*

3.2.3 Simulation of the temperature dynamics of a TOF in vacuum

Starting from the heat transfer equation Eq. (3.17), a model of the TOF heat exchange in vacuum is now developed. The fiber exchanges an extremely small amount of heat energy with the vacuum chamber which, therefore, stays at room temperature during the experiment. Furthermore, due to the small diameter of the nanofiber, it can be assumed that it exhibits a constant temperature across its diameter. This allows to reduce the model to one dimension in space along the fiber axis (z-axis). After differentiating the resulting equation with respect to z, one finds the following differential equation (in units of W/m):

$$\pi a^2 \, c_\mathrm{p} \, \rho \, \partial_t T = \pi a^2 \partial_z \left(q_\mathrm{hc} \, \partial_z T \right) - \sqrt{\frac{k_b \, f^2}{8\pi \, M_{N2} \, T_0}} \, p \, (T - T_0) \, 2\pi a \\ - \left[\partial_z H_\mathrm{rad}(T) - \partial_z H_\mathrm{rad}(T_0) \right] + \partial_z P_\mathrm{abs} \quad (3.19)$$

where $\partial_z H_\mathrm{rad}$ describes the radiated power per unit length. This equation is solved numerically for a given radius profile using the so-called method of lines implemented in Mathematica. Here a spatial discretization of 0.1 mm along the fiber axis is used and the simulated axial range covers the nanofiber and a taper section that extends at least 1 cm beyond either side of the waist: $L_\mathrm{sim} = L_\mathrm{waist} + 2$ cm. At these points, the fiber diameter has increased to ~ 10 µm and is thus a factor of 20 larger than the waist diameter. As a consequence, the evanescent field and hence the heating power vanishes and the heat capacity per unit length increases by a factor of 400. The boundary conditions are chosen such that the fiber is thermalized to ambient temperature at the beginning of the simulation $T(t = 0, z) = T_0$ and no heat flow occurs at the boundary of the simulation cell: $\partial_z T(t, \pm L_\mathrm{sim}/2) = 0$.

By solving Eq. (3.19), one obtains a temperature profile as a function of time and position along the fiber, $T(t, z)$. An exemplary temperature profile is shown in Fig. 3.6 for a TOF with 10 mm waist length which was heated for 1 s with a heating power of $P_\mathrm{abs} = 50$ µ. The model predicts a thermalization dynamics that happens on a time-scale of 100 ms. The temperature profile reaches its maximum at the fiber waist and decays within a few millimeters in the taper-region to room temperature.

In the low pressure regime, the largest uncertainties that enter into the model are the radius profile, which is known with a relative error of ± 10 % [13, 69], and the wavelength-dependent complex refractive index of fused silica, $\tilde{n}$. The latter is the sole material property that is used in the calculation of the radiated power. It was extracted from various literature sources for wavelengths ranging from ≈ 3 nm to ≈ 3 mm (see Section A.4 in the Appendix). The thermalization dynamics is modeled for the maximum and minimum values of the complex refractive index values for type III and IV fused silica available in literature with the radius profile scaled by 90 % and 110 %, compare Fig. 3.4. In order to compare the model predictions to the measured data, the thermalization dynamics for all combinatations of maximum and minimum radius profiles and complex refractive indices spectra is simulated to account for their uncertainties.

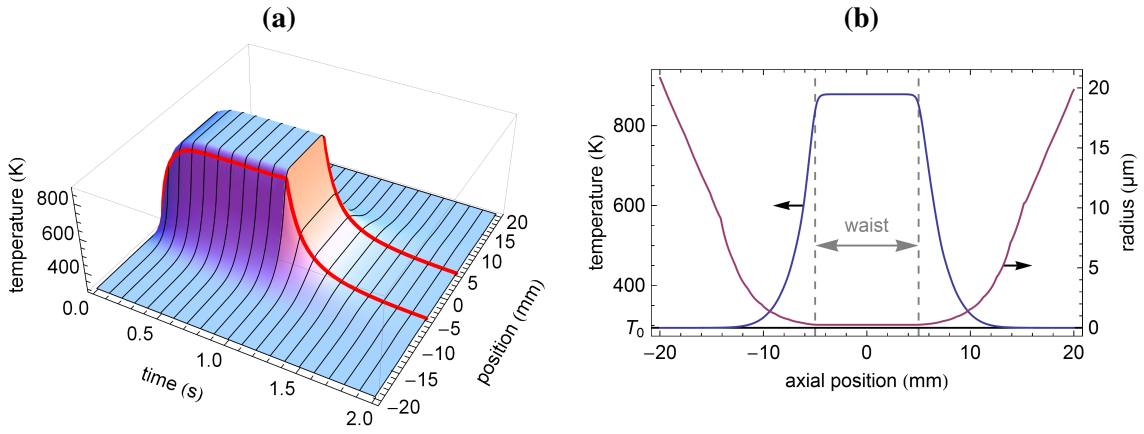

Figure 3.6: *(a) Temperature as function of time and position along the fiber axis, where the heating is switched on (off) at $t = 0$ s ($t = 1$ s). The red lines indicate the limits of the waist region. (b) Equilibrium temperature profile at $t = 1$ s (blue) and radius profile (red). The dashed line indicate the waist region. Simulation parameters: $L_{\mathrm{waist}} = 10$ mm, $a = 250$ nm, and $P_{\mathrm{abs}} = 50$ μW.*

3.3 Relating the temperature change to optical path length changes

The measurement method is based on detecting optical path length changes that are induced by the temperature change of the fiber material. In order to compare the predictions of the model with the measurement results, the temperature change has to be related to the optical path length change. This thermally induced optical path length change has its origin in two basic effects: The thermo-optic and the strain-optic effect of silica, i.e., the temperature- and strain-dependence of its refractive index as well as the radial thermal expansion of the fiber. All effects lead to a change of the V-parameter of the vacuum-clad fiber waist, either via a change of the refractive index or via a change of the fiber radius. This results in a change of the effective refractive index of the fundamental fiber mode. In the following, first the thermo-optic coefficient of fused silica is extracted from various literature sources for a large temperature range. Then, the thermally induced optical path length change of a nanofiber is derived as a function of temperature.

3.3.1 Thermo-optic coefficient of fused silica

The thermo-optic coefficient of fused silica has been extensively studied in literature[123, 128–130]. However, few studies have been carried out for temperatures exceeding $\sim$ 800 K. To my knowledge, the widest temperature range, $(300 - 1570)$ K, has been characterized using the thermally induced wavelength change of a FBG-mirror stop-band $\Delta\lambda_{\mathrm{B}}$ at a wavelength of $\approx$1570 nm [131]. Based on this literature source the thermo-optic coefficient for silica at a wavelength of 1570 nm is extracted and compared to the value from different sources. The result is then related to the thermo-optic coefficient of silica at the wavelength of 852 nm that is employed for the measurement in this work using a

theoretical model.

It can be shown that the center wavelength of the FBG stop band λ_B exhibits the following temperature dependence [132]

$$\frac{1}{\lambda_\mathrm{B}}\frac{\partial\lambda_\mathrm{B}}{\partial T} = \left[(1-\alpha_\mathrm{so})\alpha_\mathrm{te}(T) + \frac{1}{n}\frac{\partial n(T)}{\partial T}\right] , \tag{3.20}$$

where $\alpha_\mathrm{so} = (\Delta n/n)/(\Delta L_\mathrm{strain}/L_0) = -0.206$ is the strain-optic coefficient of silica for light that is perpendicularly polarized to the strain direction [133], $\mu_\mathrm{P} = -0.168$ is Poisson's ratio for silica [133] and $\alpha_\mathrm{te} = (\partial L)/(L_0\,\partial T) = (4\ldots7)\cdot10^{-7}/\mathrm{K}$ is the thermal expansion coefficient [122, 134–136] (details see Ch. A.6 below). The temperature dependence of the stop-band wavelength is weak ($\lambda_\mathrm{B}^{-1}\,\partial_T\,\lambda_\mathrm{B} \sim 10^{-5}$ 1/K) so that one can approximate the relative refractive index change $\Delta n/n$ for a temperature change from T_0 to T_1 by

$$\frac{\Delta n(T_1)}{n(T_0)} = \frac{\Delta\lambda_\mathrm{B}(T_1)}{\lambda_\mathrm{B}(T_0)} - \int_{T_0}^{T_1}(1-\alpha_\mathrm{so})\alpha_\mathrm{te}(T)\,\mathrm{d}T , \tag{3.21}$$

where $\Delta\lambda = \lambda(T_1) - \lambda(T_0)$. Note that, the stress-optic coefficient exhibits also a temperature dependency $\partial\alpha_\mathrm{so}/(\alpha_\mathrm{so}\,\partial T) = 1.34\cdot10^{-4}$, determined in the temperature range (300-450) K [137]. However, due to the small temperature range for which this literature value is determined and the fact that this yields only a minor relative correction to the total refractive index change of smaller than 10^{-3}, this effect is neglected for the purpose of this analysis. Furthermore, to the best of my knowledge, the thermal expansion coefficient of silica is measured to a maximum temperature of 1000 K [122]. For higher temperatures a linear extrapolation of the two highest temperature values is employed.

Using Eq. (3.21) the refractive index change is computed from [131] at 1550 nm and is shown as a black curve in Fig. 3.7 together with literature values that employ various methods [98, 123, 128–130]. It shows a good agreement within a relative uncertainty of $\Delta(\partial n/\partial T)/(\partial n/\partial T) \approx 10\,\%$ that is indicated by the limits of the grey area.

From the previous considerations, the refractive index change at a wavelength of 1550 nm is determined as function of the temperature. Now a model is applied in order to derive $\Delta n(T)$ for the wavelength used in the experiment of 852 nm. In order to do so, an established model that predicts the dispersion of the thermo-optic coefficient [123] is used. According to this theory the thermo-optic effect is due to a temperature dependence of the excitonic absorption band of fused silica. The latter is the electronic band with the lowest transition energy to the valence band of $\Delta E_\mathrm{eg} = 10.2$ eV and is therefore the absorption band with the highest wavelength of $\lambda_\mathrm{eg} = 122$ nm in the UV-range. It can be shown that the temperature dependence of the refractive index follows as

$$\frac{\partial n(\lambda,T)}{\partial T} = \frac{n_\infty^2-1}{2n}\left(-3\alpha_\mathrm{te}(T)\,R(\lambda) - \frac{R(\lambda)^2}{E_\mathrm{eg}}\frac{\partial E_\mathrm{eg}(T)}{\partial T}\right) , \tag{3.22}$$

where $R(\lambda) = \lambda^2/(\lambda^2-\lambda_\mathrm{ig}^2)$, $\lambda_\mathrm{ig} = 117$ nm is the wavelength transition to the isentropic band, and $n_\infty = 1.43$ is the low-frequency refractive index in the IR-region [123].

In order to obtain a wavelength independent expression for the thermo-optic effect, the relative variation of the excitonic transition energy is computed. This is done for the

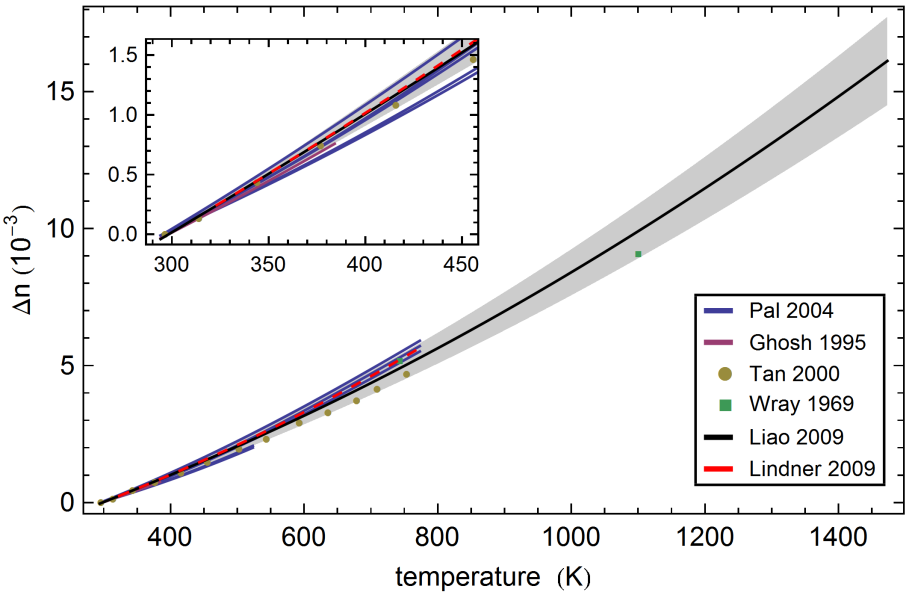

Figure 3.7: *Refractive index change as function of temperature for a wavelength of* $\lambda_0 = 1550(20)$ *nm extracted from [131] (black line) and from various literature sources (see legend). The grey area indicates an error estimate for the refractive index change that is used in the following. It is given by* ± 10 % *of the values of the black curve. Inset: magnified view of the smaller temperatures.*

integral expression $\int_{T_0}^{T} \partial T \; E_{\mathrm{eg}} \, (\partial_T E_{\mathrm{eg}})$ which is approximated in the temperature range $(300 - 1000)$ K by an empirical fit of the form :

$$\int_{T_0}^{T} \mathrm{d}T \; \frac{1}{E_{\mathrm{eg}}} \frac{\partial E_{\mathrm{eg}}}{\partial T} = 7.34(6) \cdot 10^{-3} - 2.221(3) \cdot 10^{-5} \, T[\mathrm{K}] - 9.26(3) \cdot 10^{-9} \, (T[\mathrm{K}])^2 \, , \tag{3.23}$$

where the coefficient of determination is $(1 - R^2 < 10^{-5})$. Note that, the temperature range is limited by the thermal expansion coefficient which, however yields only a small contribution to the temperature dependence. The fit yields still excellent results for the full temperature range up to 1570 K. This result is now used to compute $n(T)$ for $\lambda_0 = 852$ nm via Eq. (3.22).

The resulting refractive index change for the laser wavelength in the experiment (852 nm) is shown in Fig. 3.8 together with the two literature values that are closest to this wavelength and cover the highest temperature range. By fitting the temperature-dependent refractive index change with a 2nd-order polynomial function (coefficient of determination: $R^2 = 1 - 6 \cdot 10^{-6}$) and by differentiating the latter with respect to the temperature, one obtains the following analytic approximations for the temperature dependent thermo-optic coefficient:

$$\frac{\partial n(T)}{\partial T} = 9.627(9) \cdot 10^{-6} + 7.74(1) \cdot 10^{-9} \, (T - 299 \text{ K}) \, , \tag{3.24}$$

which will be used in the following.

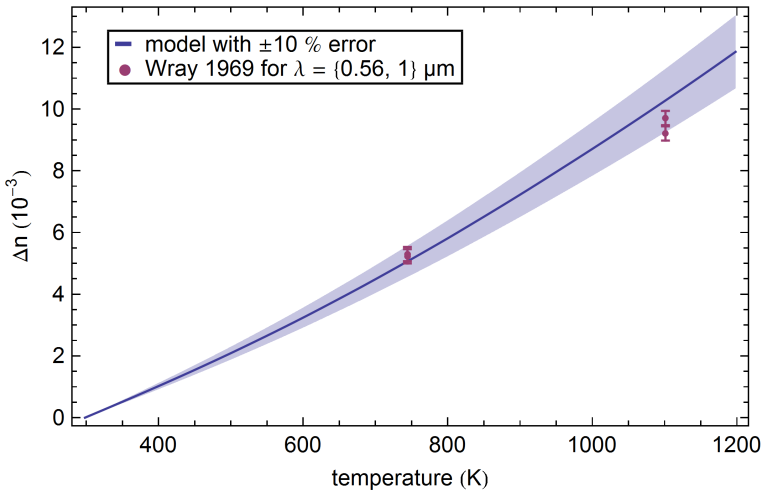

Figure 3.8: *Model prediction of the refractive index change due to the thermo-optic effect for* $\lambda_0 = 852$ *nm (blue) together with a 10 % error margin (shaded area). The red points are two measured values at the two nearby wavelengths of 560 nm and* 1 µm *from [130].*

3.3.2 Optical path length change of a nanofiber

When the refractive index of silica is changed, the V-parameter of the fiber is affected and thereby the effective refractive index of the mode, compare Ch. 1.3. However, depending on the V-parameter of the fiber, a variable fraction of the power of the mode propagates outside the fiber. This is taken into account by a radius dependent factor $\partial_n n_{\text{eff}}(a) \leq 1$ when computing the optical path length change.

Following the heat-and-pull process, the TOF is pre-strained by $\Delta L_{\text{strain}}/L_{\text{waist}} \approx 4\,\%$ before fixing it to the mount. When heated, the thermal expansion results in a strain reduction and thereby in an increase of the radius due to the reduced transversal contraction and an increase of the refractive index of silica by the strain-optic effect. Note that, the fiber reaches very high temperatures beyond the glass transition temperature during the experimental cycle so that the fiber yields and the strain is lowered. However, the short experiment cycles prevent a full relaxation so that a fraction of the initial stress remains (see also Ch. 3.5 below).

Taking these effects into account, the thermally-induced change of the effective refractive index for a given fiber radius can be expressed by

$$\begin{aligned}\frac{\partial n_{\text{eff}}(a,T)}{\partial T} &= \frac{\partial n_{\text{eff}}(a)}{\partial n}\left(\frac{\partial n(T)}{\partial T} + \frac{\partial n}{\partial \sigma}\frac{\partial \sigma(T)}{\partial T}\right) + \frac{\partial n_{\text{eff}}}{\partial a}\left(\frac{\partial a(T)}{\partial T} + \frac{\partial a}{\partial \sigma}\frac{\partial \sigma}{\partial T}\right) \\ &= \frac{\partial n_{\text{eff}}(a)}{\partial n}\left(\frac{\partial n(T)}{\partial T} - n\,\alpha_{\text{te}}(T)\,\alpha_{\text{so}}\right) + \frac{\partial n_{\text{eff}}(a)}{\partial a}(1+\mu_{\text{P}})\alpha_{\text{te}}(T)\,a\,,\end{aligned}$$

where σ denotes the axial stress.

Note that, the strain-optic effect on the longitudinal field components of the fiber mode is neglected which is justified due to their comparatively small contribution to the E-field

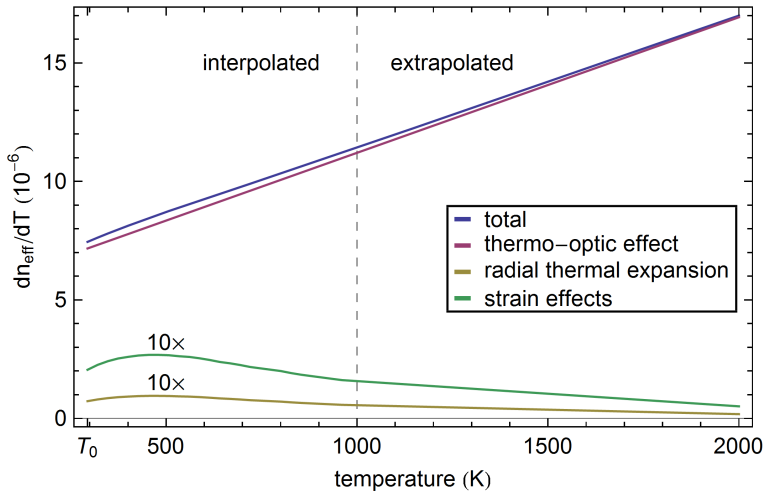

Figure 3.9: *Thermal change of the effective refractive index of a 500 nm diameter nanofiber as function of temperature. The three contributions are plotted separately as marked in the legend.*

of the fiber mode (see Ch. 1.3). The resulting thermal change of the effective refractive index is plotted as function of temperature in Fig. 3.9. The major contribution to the refractive index results from the thermo-optic effect of the silica, whereas the other effects yield a relative contribution smaller than 5 %. The thermal expansion coefficient limits the temperature range in which literature values are available so and has to be extrapolated for temperatures above 1000 K.

In all the above considerations, the effect of the fiber core has been neglected. This is justified because the core constitutes a negligible fraction (< 0.5 %) of the fiber material which contributes to the guiding of the light in the nanofiber section and, in addition, has similar optical properties as the cladding material.

3.4 Measurement results

In this section the results of the thermalization measurements are presented. First, the optical setup is presented which is followed by the evaluation scheme that extracts the optical path length change from the transmission signal of the resonator. Then a pre-thermalization routine is described that is employed before each measurement in order to establish a reproducible thermal situation. In the following sections, the thermalization via heat radiation is investigated by performing experiments with different heating powers and analyzing the equilibrium situation as well as the thermalization dynamics. The influence of the heat transport via gas is investigated by a measurement with constant heating parameters that was repeated at different gas pressures.

3.4.1 Optical setup

The thermalization dynamics of the nanofiber is measured via the thermally induced optical path length change ΔL_{opt} using the TOF-microresonator presented in Ch. 2.3. For this purpose, the transmission signal of the resonator is probed with a laser at a fixed frequency while heating the nanofiber waist by the absorbed light of a second laser.

The optical setup is similar to the one used for the resonator characterization in the previous section, compare Ch. 2.2.3 and is schematically shown in Fig. 3.10. The probe laser is frequency stabilized by means of the transmission signal of an etalon which again is length-stabilized to a cesium spectroscopy via a transfer laser. The nanofiber waist is

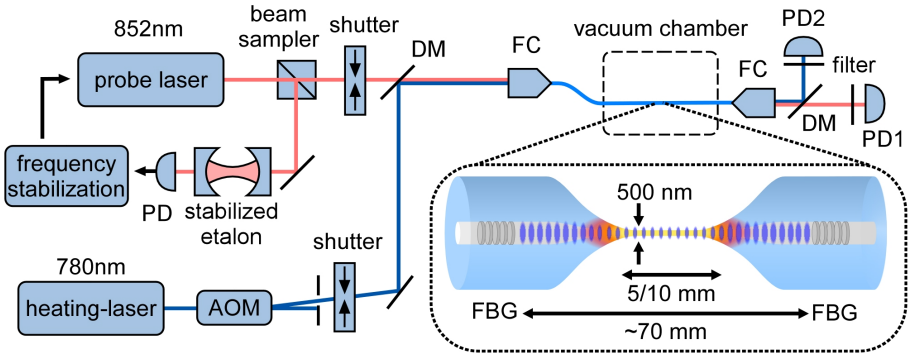

Figure 3.10: *Schematical view of the optical setup: The inset schematically shows the TOF-microresonator including the nanofiber. For details see text*

heated by sending a second laser field (heating laser) through the TOF. For this purpose, a titanium-sapphire laser which is stabilized to a wavelength of $\lambda_{\mathrm{heat}} \approx 780$ nm within the transmission band of the FBGs is used. Its power is adjustable by means of an acousto-optic modulator (AOM) setup in single-pass configuration using the first diffraction order. The AOM is manufactured by Crystal Technologies model 3080-125 1W and powered by the driver module AODR 1080F-AENO-2.0 at 80 MHz. A small fraction of the heating laser power is absorbed along the nanofiber, thereby heating the latter.

Both lasers are combined on a dichroic mirror (DM) before they enter the fiber. After exiting the TOF, the transmitted probe and heating laser fields are separated by a second

DM and spectral filters such that their respective powers can be measured independently using photodiodes (PD1 & PD2). The heat source can be turned on and off, thereby allowing to measure the heating and cooling dynamics of the nanofiber. For this purpose, home-made mechanical shutters that are adapted from digital cameras are used to switch the laser beams. Their switching times were measured by the rise- and fall-time of the laser transmission signal measured between 10 % to 90 % of the maximum signal to be 500 µs and 200 µs respectively. This is two orders of magnitude faster than the thermalization times in the experiment (see below) and can be considered instantaneous. Note that one could in principle also use the AOM for this purpose but the additional shutters allow the AOM to thermalize, thereby increasing the stability of the intensity.

3.4.2 Signal

The signal obtained from the measurements consists of two time traces of the transmitted probe and heating laser power. Based on this signal, the optical path length change in the tapered optical fiber is extracted and compared to the theory prediction.

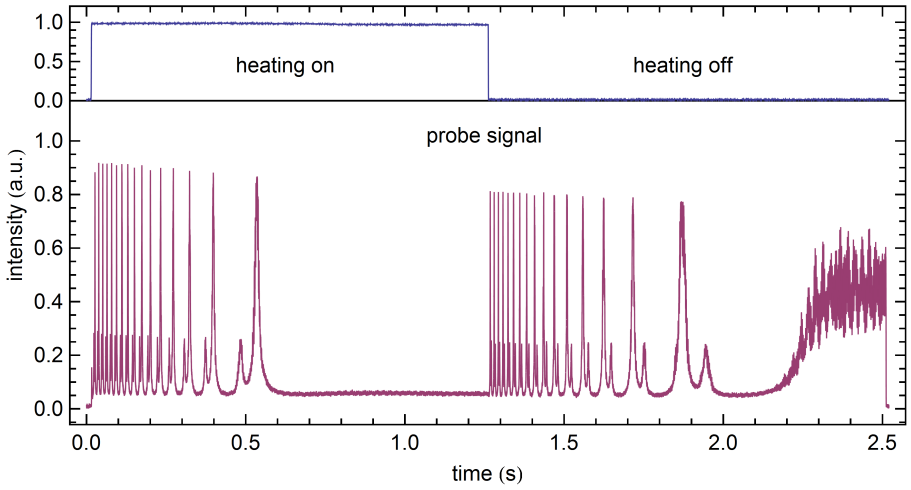

Figure 3.11: *Exemplary transmission traces of the heating laser (blue) and probe laser (red) during one measurement cycle obtained at the lowest heating power measured in the experiment. In the probe laser transmission signal pairs of peaks occur which correspond to the two perpendicularly polarized modes of the birefringent resonator.*

An exemplary time trace is shown in Fig. 3.11, where the transmission signal of the heating laser is shown as the blue upper trace and that of the probe laser in the purple lower trace. During the first half of a measurement cycle the heating laser is switched on, thereby heating the nanofiber. After the TOF reaches an equilibrium thermal situation it is switched off in order to also measure the cooling dynamics. The time trace of the resonator shows a sequence of Fabry-Pérot transmission peaks that first arrive in quick succession and later with larger time separations. It, thereby, shows the expected behavior of a thermalization dynamics that progresses with a quick temperature change in the beginning which slows down when approaching the equilibrium situation.

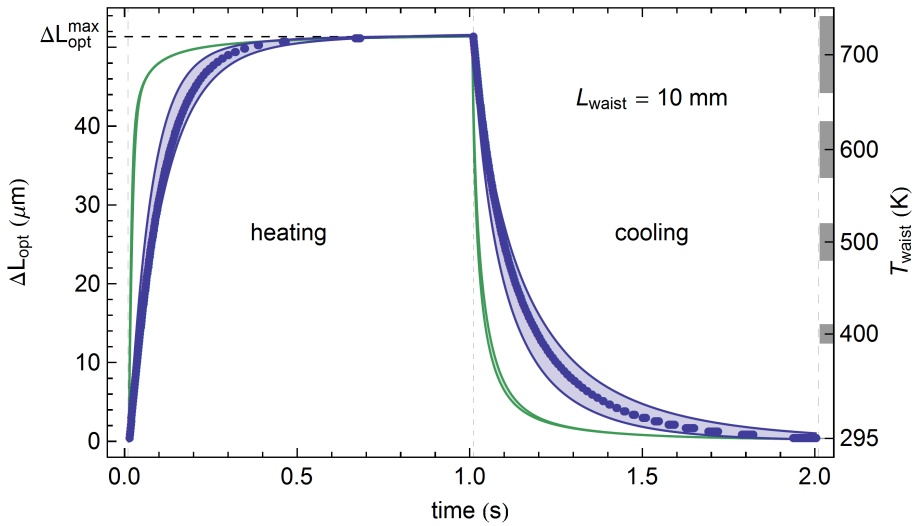

Figure 3.12: *Thermally induced optical path length change of the silica nanofiber. Circles: Experimental data; blue bands: FED predictions; green bands: predictions using Planck's law. Sample: TOF microresonator #3 at* $p \approx 10^{-6}$ *mbar.*

The arrangement of the resonance pairs that correspond to the two perpendicularly polarized modes of the resonator confirms that the nanofiber shows the inverse dynamics during the heating and cooling process. However, the absolute sign is unknown when solely using this method but can be determined by comparing the ordering of the spectral features to a spectrum of the resonator. Using this method, we find that ΔL_{opt} increases with increasing temperature, verifying the theory prediction.

The transmission peak intensities of the resonator also show a $\approx 10\ \%$ variation during the measurement. This is due to a variation of the laser to fiber coupling efficiency caused by thermal lensing in the fiber coupling optics. This effect occurs at high optical intensities, when the laser beam heats the material and thereby induces an intensity dependent refractive index profile that, in turn, acts as a lens. By optimizing the coupling of the heating laser this effect was minimized so that the peak to peak variation does not exceed 6 % at the maximum variation that occurs for high powers within the first 50 ms and on average is considerably lower (compare Fig. 3.11).

By counting the transmission peaks of one resonator mode detected on PD1 and measuring the time at which they appear one can infer a time dependent change of the optical path length ΔL_{opt}. The optical path length change that occurs between two consecutive peaks follows directly from the boundary condition of Fabry-Pérot resonators and is given by half the probe laser wavelength $\lambda_0/2 = 426$ nm. Due to the discrete nature of the data which relies on counting peaks, an additional data point is added at the end of each, the heating and cooling part of the cycle, to reflect the fact that no further peak has been observed. Its value is chosen to be $\lambda_0/4$ higher (lower) than the last measurement point with an uncertainty of $\pm\lambda_0/4$, thereby accounting for the fact that the optical path length has changed by less than $\lambda_0/2$. Figure 3.12 shows an exemplary trace of the optical path length change in which the heating laser power was set to $P_{\mathrm{heat}} = 32.7(1)$ mW and the

background gas pressure is $p = 10^{-6}$ mbar.

In order to compare these results with theory predictions, ΔL_{opt} is computed from the theoretical temperature profiles via the temperature-dependent effective refractive index which is integrated along the TOF-resonator. The theory bands in Fig. 3.12 are delimited by the two extremal theory time traces of ΔL_{opt} that reproduce the maximum observed optical path length change $\Delta L_{\mathrm{opt}}^{\mathrm{max}}$ (solid lines). The temperature axis was produced by relating ΔL_{opt} to the waist temperature via the model prediction, where the limits of the gray bars represent the maximum and minimum prediction of ΔL_{opt} for a given temperature at the center of the nanofiber T_{waist}, compare Ch. 3.4.4 below. Note that the temperature scale in Fig. 3.12 refers to the cooling process. The corresponding scale for the heating process differs from the latter due to the different temperature profiles and the non-linear thermo-optic effect, and is not shown for clarity. The time dependence of ΔL_{opt} predicted by FED and the experimental data are in excellent agreement while the prediction for Planck's law predicts a considerably faster thermalization.

3.4.3 Initialization procedure

The heating laser power is not only absorbed by the nanofiber but also by the FBGs and the unprocessed parts of the fiber. Their temperature change influences the optical path-length in the same way as the nanofiber so that they can not be distinguished. However, the nanofiber and the untapered optical fiber thermalize on different time scales. By exploiting this difference, an initialization procedure can be developed that establishes a well defined reproducible initial thermal condition of the fiber.

In order to determine the thermalization dynamics of the FBGs in the untapered part of the fiber, a thermalization measurement is carried out in which their transmission spectrum is recorded during heating and cooling. For this purpose, the heating laser is switched on and off while simultaneously scanning the probe laser over a large fraction of the spectrum and recording the transmission signal, see Fig. 3.13(a). Then, the wavelength of a spectral feature is tracked (gray bars in each spectrum) and the resulting wavelength shift, $\Delta\lambda^{\mathrm{feat.}}$, is plotted as function of time in Fig. 3.13(b). The thermalization time constant is determined by exponential fits which yield values of $\tau_{\mathrm{heat}} = (6.7 \pm 0.3)$ s for the heating dynamics and of $\tau_{\mathrm{cool}} = (11.5 \pm 0.8)$ s for the cooling dynamics.

Based on this measurement the following initializing pulse sequence of the heating laser was devised: First the heating laser power is set to a high value ($80-160$ mW) and is sent through the TOF for 30 s. This heating time is significantly longer than the thermalization time constant of the unprocessed fiber parts. Then, the heating laser is switched off for 2 s. This cooling time is ten times longer than the thermalization time constant of the nanofiber, see above. This ensures that the nanofiber is thermalized at ambient temperature while the unprocessed fiber exhibits a constant initial condition.

To check the performance of this initialization sequence, $\Delta L_{\mathrm{opt}}^{\mathrm{max}}$ was measured in two subsequent measurement series, first with increasing and then decreasing heating power, see Fig. 3.14. The measurement results obtained without the initialization sequence are not reproducible in the upwards and downwards sweep and yield higher values compared to the measurement with the initialization sequence. Both effects can be explained to a

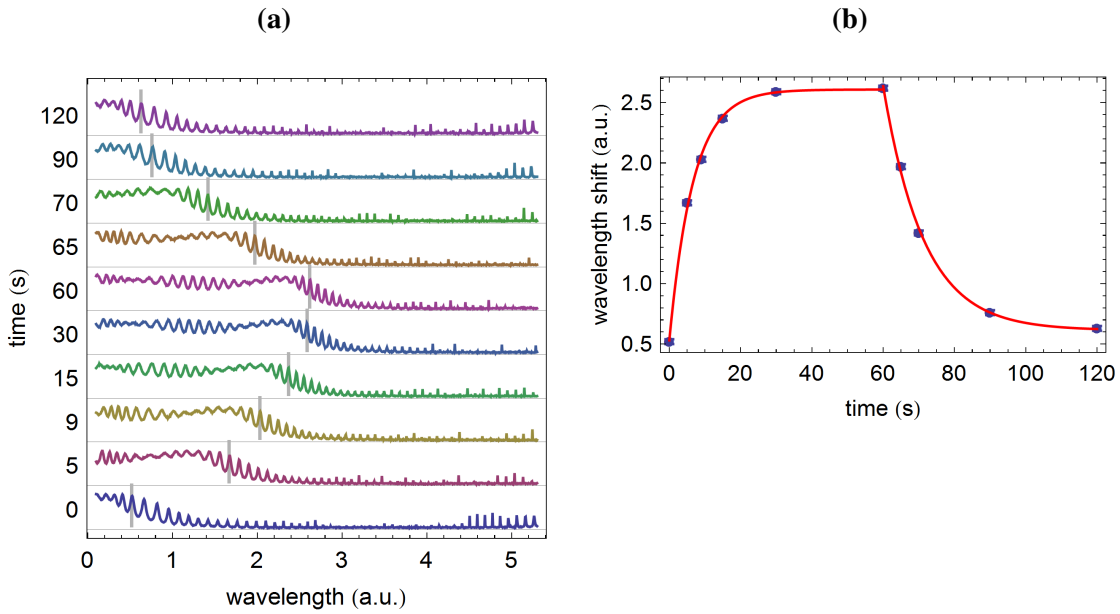

Figure 3.13: *(a) Waterfall plot of individual TOF-microresonator transmission spectra that were taken at the time indicated at the axis. (b) Wavelength of the spectral feature indicated by the gray lines in (a) as function of time (points) and exponential fits (red line). Sample: TOF microresonator #2 at* $p \approx 10^{-6}$ *mbar.*

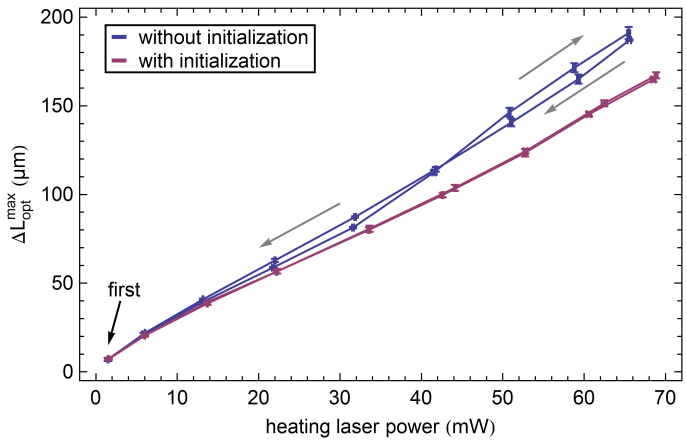

Figure 3.14: *Investigation of the effect of the initialization sequence on the reproducibility of the measurements by two subsequent measurement series of* $\Delta L_{\mathrm{opt}}^{\mathrm{max}}$ *first with increasing heating power then with decreasing heating power. The arrows indicate the ordering in which the points were measured. Sample: TOF-microresonator #2 at* $p \approx 10^{-6}$ *mbar.*

heating of the unprocessed fiber and FBGs: The increasing temperature yields an additional contribution to the optical path length change, thereby explaining the higher values. Furthermore their longer thermalization times generate a memory effect that influences subsequent measurements so that the results are not reproducible. The measurements including the initialization sequence, however, show none of these effects and yield reproducible results.

3.4.4 Maximum temperature change as function of the heating power

The equilibrium situation, i.e. the maximum temperature reached by the fiber, is quantified by the maximum optical path length change. This is measured as function of the heating power and reveals the temperature scaling of the radiated power because it probes at which temperature the heating power is balanced by the radiated power in the equilibrium situation.

The following measurements are performed with two resonators, TOF-resonators 2 and 3, with different waist lengths of 5 mm and 10 mm, respectively. The results for $\Delta L_{\mathrm{opt}}^{\mathrm{max}}$ as function of the heating laser power transmitted through the TOF, P_{heat}, are shown in Fig. 3.15. Both samples, show a nearly linear increase of $\Delta L_{\mathrm{opt}}^{\mathrm{max}}$ as function of the heating power within the observed power range.

In order to compare these results with theory predictions, the theoretical time trace of ΔL_{opt} is computed from the temperature profiles via the temperature-dependent effective refractive index which is integrated along the TOF-resonator. Furthermore, the ratio η between the measured heating laser power (P_{heat}) and the model parameter of the total absorbed heating power (P_{abs}) has to be determined. For this purpose, the two powers are related via $P_{\mathrm{abs}} = \eta\, P_{\mathrm{heat}}$ and η is determined by fitting the data with the extremal theory predictions that result from the uncertainties of the TOF radius profile and the refractive index of silica. This is done individually for the predictions concerning the radiated power from Planck's law and FED, by using the same scheme: First, η is determined by fitting the predictions independently to the data using the four parameter sets concerning the radius and the complex refractive index each with the minimum and maximum curve. Then, the mean of the minimum and maximum resulting η-value is computed $\bar{\eta} = (\eta_{\mathrm{max}} + \eta_{\mathrm{min}})/2$, see Tab. 3.2. Note that the value of $\bar{\eta}$ for the longer resonator is smaller than that for the shorter resonator. This substantiates the assumption that the heating is due to surface absorption by pollutants because in material (volume) absorption η scales with the nanofiber length. Now that $\bar{\eta}$ is determined, the absorbed power and heating laser power can be related via $P_{\mathrm{abs}} = \bar{\eta}\, P_{\mathrm{heat}}$. The two extremal theory predictions, that correspond to η_{max} and η_{min}, are plotted as solid lines bounding the colored bands in Fig. 3.15. For both resonators, the FED predictions are in excellent agreement with the experimental data while Planck's law predicts a sub-linear increase of the equilibrium temperature, and therefore of $\Delta L_{\mathrm{opt}}^{\mathrm{max}}$. This qualitative deviation stems from the different scaling of the radiated power with temperature for the two models: T^4 assuming Stefan-Boltzmann law and $< T^3$ in the case of the FED prediction, compare to Ch. 3.1.4.

The equilibrium waist temperature T_{waist} can now be determined from the theory

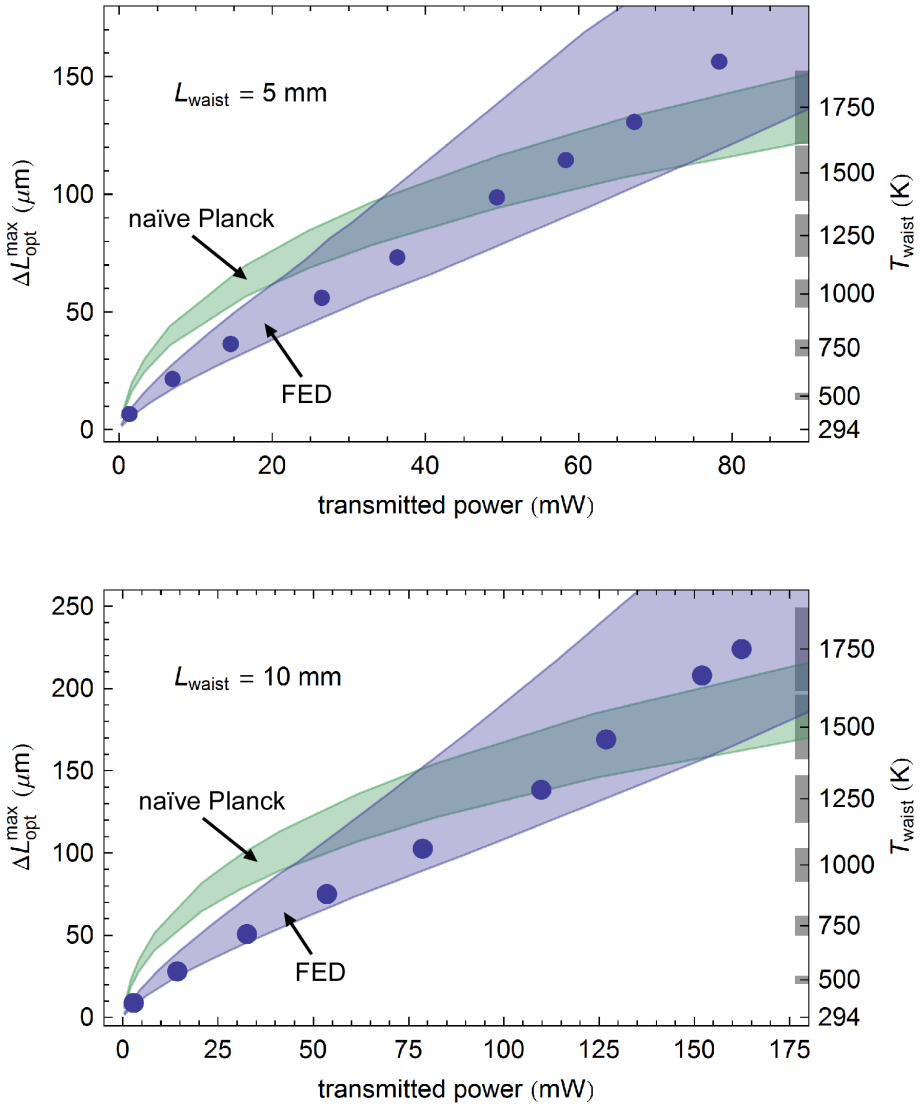

Figure 3.15: *Maximum optical path length change as a function of the heating laser power transmitted through the TOF (points) for the two samples TOF-microresonator #2 ($L_{\mathrm{waist}} = 5$ mm) and TOF-microresonator #3 ($L_{\mathrm{waist}} = 10$ mm)*

sample	$\bar{\eta}_{\mathrm{FED}}$	$\bar{\eta}_{\mathrm{Planck}}$	TOF loss	L_{w}
TOF-resonator 2	$2.0(6) \cdot 10^{-3}$	$3.0(7) \cdot 10^{-2}$	$1.38(9)\,10^{-1}$	5 mm
TOF-resonator 3	$1.3(4) \cdot 10^{-3}$	$2.4(7) \cdot 10^{-2}$	$1.1(2)\,10^{-2}$	10 mm

Table 3.2: *Values of the absorption coefficient η for both samples. The last row shows the values of the TOF transmission loss, that were obtained using the method described in Ch. 2.3.3*

which relates T_{waist} to $\Delta L_{\mathrm{opt}}^{\mathrm{max}}$. To this end, I again use the two extremal predictions of $\Delta L_{\mathrm{opt}}^{\mathrm{max}}$ to determine the two corresponding extremal predictions for the temperature at the center of the waist, $T_{\mathrm{waist}}^{\mathrm{max}}$ and $T_{\mathrm{waist}}^{\mathrm{min}}$, respectively. The resulting non-linear temperature scale, $\bar{T}_{\mathrm{waist}} = (T_{\mathrm{waist}}^{\mathrm{max}} + T_{\mathrm{waist}}^{\mathrm{min}})/2$, where $\Delta\bar{T}_{\mathrm{waist}} = (T_{\mathrm{waist}}^{\mathrm{max}} - T_{\mathrm{waist}}^{\mathrm{min}})/2$, is shown on the right axes of all panels of Fig. 3.2, with the ticks and the gray bars indicating $\bar{T}_{\mathrm{waist}}$ and $\Delta\bar{T}_{\mathrm{waist}}$, respectively. It covers a temperature range from room temperature to almost 2000 K. Note that the temperature scale in Fig. 3.15 again refers to the cooling process. Note also, that the upper temperature limits exceed the glass transition temperature of fused silica of 1450 K and no fusing of the TOF was observed in the experiment. The fusing point of the nanofiber is investigated in theory and measurement in Ch. 3.5, below.

3.4.5 Pressure dependence of the thermalization behavior

In order to measure the contribution of the heat transport via the background gas, a measurement of $\Delta L_{\mathrm{opt}}^{\mathrm{max}}$ with a constant heating power is repeated for different gas pressures. The results for TOF-resonator 3 and $P_{\mathrm{heat}} = 13.2(4)$ mW are shown in Fig. 3.16. The data shows that $\Delta L_{\mathrm{opt}}^{\mathrm{max}}$ is constant for pressures lower than 10^{-4} mbar. This confirms that the heat diffusion through the background gas is negligible for all other measurements presented here, which were performed at pressures below 10^{-6} mbar.

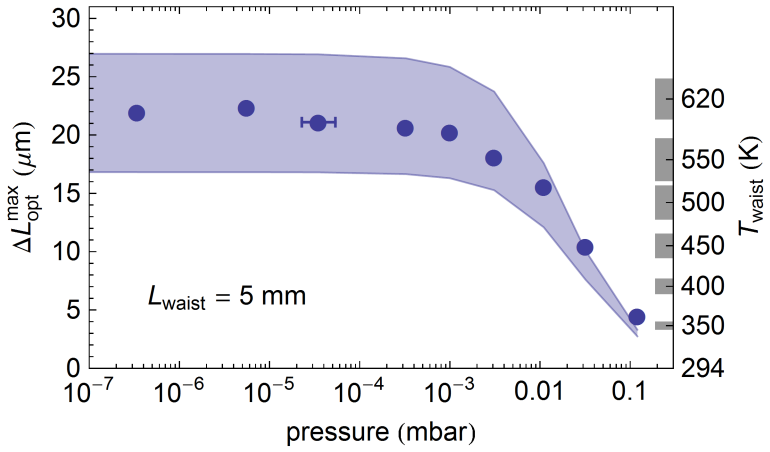

Figure 3.16: *Maximum optical path length change measured as function of pressure, measured with TOF-microresonator #2 at* $P_{\mathrm{heat}} = 13.2(4)$ *mW.*

Beyond 10^{-4} mbar, the maximum optical path length decreases with increasing pressure. Here, the increasing gas density facilitates a more efficient cooling which first becomes comparable to the radiative cooling and, at higher pressures, dominates the heat transport. The theory prediction is in good agreement with the measured data. Nevertheless, the model underestimates $\Delta L_{\mathrm{opt}}^{\mathrm{max}}$ with increasing pressure. This is a consequence of the fact, that the model neglects temperature gradients in the background gas and therefore overestimates the gas heat transport, see Ch. 3.2 above. However, this comparatively simple model which requires no information on the details of the setup in the vacuum

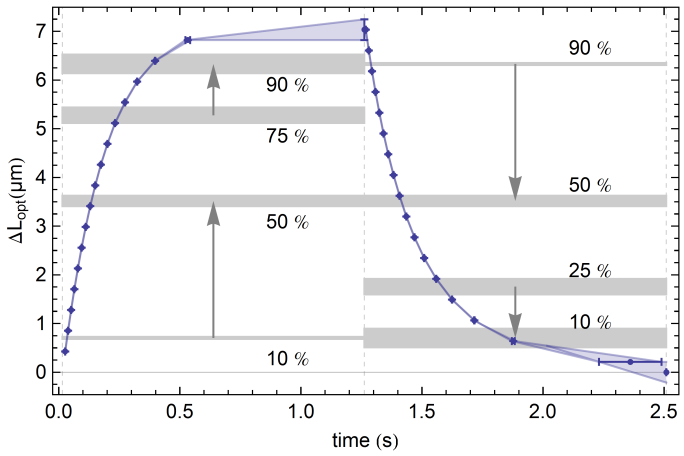

Figure 3.17: *Measured optical path length change as function of time for an exemplary measurement. The two blue shaded areas at the measurement points indicate the envelope of the data points including their uncertainty. Gray horizontal bars: fraction of the maximum optical path length change including the uncertainty of* $\Delta L_{\mathrm{opt}}^{\mathrm{max}}$*. Sample: TOF microresonator #2 at* $p \approx 10^{-6}$ *mbar.*

chamber, and in particular no laborious 3D modelling, yields a good approximation even at pressures for which the typical distances to the heat sink exceed the mean free path length of the gas particles by two orders of magnitude.

3.4.6 Thermalization time constant

The time scale at which the thermalization dynamics takes place is determined by the heat capacity of the material and the heat exchange rate with the surroundings, compare the heat transfer equation Eq. (3.17). A measurement of the thermalization dynamics, therefore, carries information about the total power transfer at any temperature that the system exhibits during the process. Due to the fact, that the heat conduction transport of the material and that via gas at low pressures yield negligible contributions to the total heat transfer, this measurement is highly sensitive to the total radiated power of the nanofiber.

Here, the thermalization dynamics is analyzed for varying heating powers and thus for varying $\Delta L_{\mathrm{opt}}^{\mathrm{max}}$. For this purpose the rise and fall time of ΔL_{opt} is determined. For the latter a model independent method is employed which is illustrated in Fig. 3.17. In order to quantify the initial and the final dynamical behavior, two time spans are extracted in which the signal changes between $10\ \% - 50\ \%$ and $75\ \% - 90\ \%$ of $\Delta L_{\mathrm{opt}}^{\mathrm{max}}$ in case of the heating cycle and $90\ \% - 50\ \%$ and $25\ \% - 10\ \%$ in case of the cooling cycle. Here, the uncertainty of the measured data is taken into account by using the maximum and minimum value of $\Delta L_{\mathrm{opt}}^{\mathrm{max}}$ when computing the thresholds (upper and lower bound of the gray bars in Fig. 3.12. Then, for each threshold pair, a minimum and maximum time is determined that the envelope of the measured data stays within the two thresholds under consideration of the finite threshold width. The rise/fall times and their uncertainty are then defined by the mean value of each pair of minimum and maximum time spans and half their difference, respectively.

The measurement results are shown in Fig. 3.18 as a function of $\Delta L_{\mathrm{opt}}^{\mathrm{max}}$. The thermalization time constants are on the order of 100 ms and decrease with increasing $\Delta L_{\mathrm{opt}}^{\mathrm{max}}$. Such a decrease can be explained by a superlinear increase of the radiated power as function of temperature: Here, the heat transport becomes disproportionately higher with increasing temperature, thereby resulting in the faster dynamics. Despite their different nanofiber waist lengths, both samples show the same thermalization time constants, thereby confirming that the heat conduction along the material yields only a minor contribution to the heat exchange rate.

For the purpose of comparing the measurements to the model, I derive the same quantities by means of the same method from the model predictions and plot them as bands in the same graphs. Note, that all theory predictions in this figure are ab initio results without any adjustable parameters. The agreement between the experimental data and the FED predictions is excellent, whereas the naïve approach using Planck's law predicts up to one order of magnitude shorter time constants and, therefore, highly overestimates the radiated power from the nanofiber. In case of the final time constants of the heating cycle the theory prediction underestimates the time constants. This can be explained by small fluctuations of the heating power (see Ch. 3.4.2 above) which cause a large uncertainty of the final thermalization time due to the shallow increase of ΔL_{opt} near the equilibrium situation. However, this power fluctuation affects the initial thermalization time only weakly since the dynamics of ΔL_{opt} happens much faster here. In both cases, i.e. the initial heating and cooling dynamics, the agreement between theory and data is excellent.

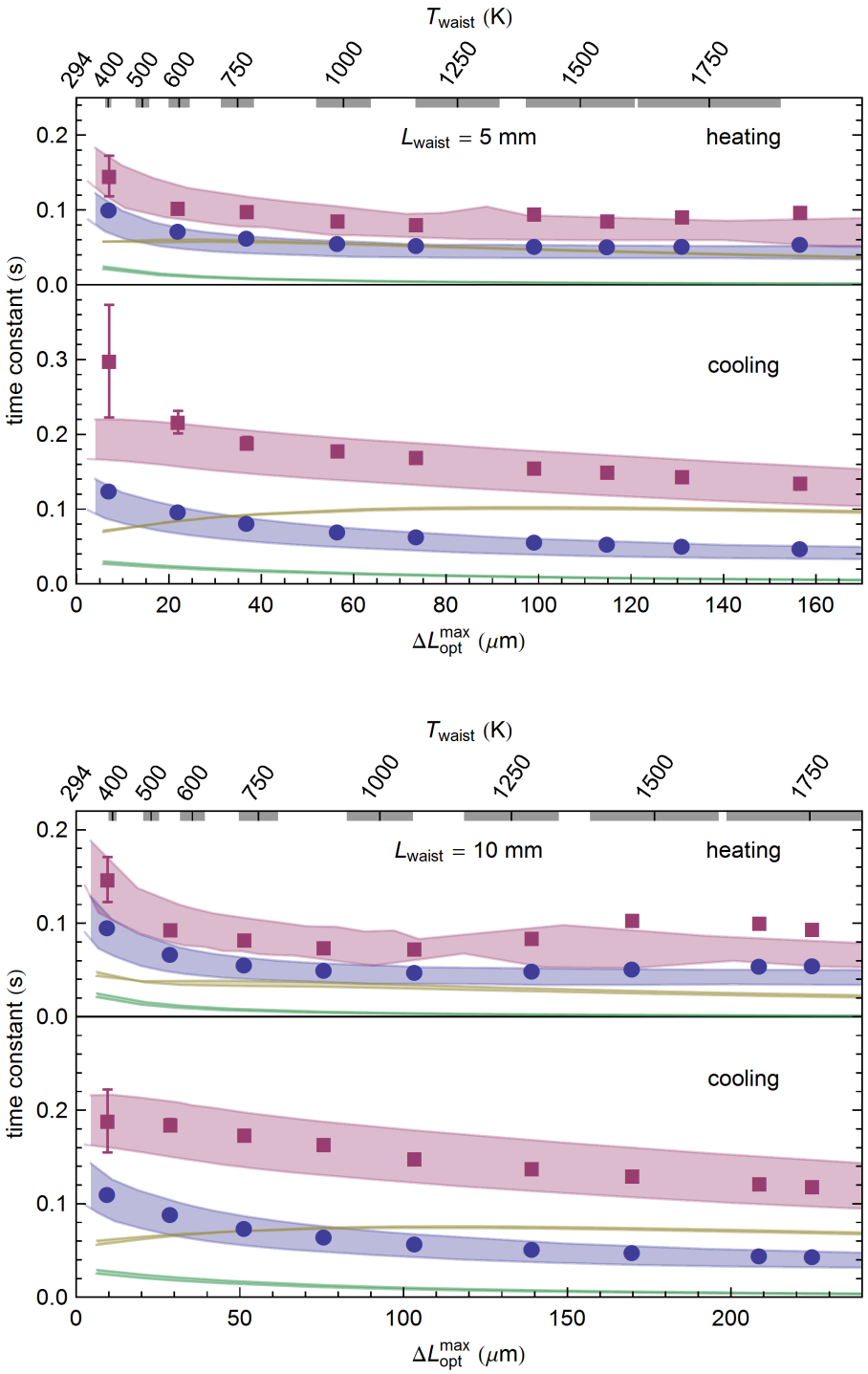

Figure 3.18: *Thermalization time constants of the silica nanofiber as a function of the maximum optical path length change for the two TOF resonators. Blue circles: measured initial time constants; red squares: final time constants; blue (red) bands: FED predictions for initial (final) time constants; green (yellow) bands: predictions for initial (final) time constants using Planck's law.*

3.5 Mechanical stability at high temperatures – Fusing temperature

While temperatures that exceed the glass transition temperature of fused silica of about 1450 K [138] are observed in the experiment, no breaking due to melting is observed. To investigate this further, TOF-resonator 2 was heated to its breaking point by increasing the heating power step-wise. The findings are compared by a theory prediction that is obtained by considering the fiber as a viscous catenary.

Let us first theoretically examine the mechanical stability of the fiber at high temperatures by treating it as a thin viscous filament with a temperature dependent viscosity $\eta(T)$. For this purpose, we compute the characteristic time of the viscous dynamic in dependence of the temperature and compare it to the measurement cycles. As the fiber is pre-strained, two different characteristic time constants have to be considered: The relaxation from the initial strain in the fiber σ_i by elongation which happens on the timescale of

$$\tau_s = \frac{3\,\eta(T)}{\sigma_i} \tag{3.25}$$

and the fusing at which the initial strain is already released and gravity causes the deformation

$$\tau_v = \frac{\eta(T)}{3\,\rho\,g\,L_{\text{waist}}}\,, \tag{3.26}$$

where g is the gravitational acceleration [139]. The latter formula can intuitively understood by estimating the strain caused by the weight-force of the nanofiber across its cross-section $\sigma \sim g\,\rho\,\pi a^2 L_{\text{waist}}/(\pi a^2)$ which reproduces Eq. (3.26), save the prefactor. It has been shown, that the viscosity of silica can be described by the Arrhenius-model $\eta(T) = \eta_\infty \exp\left(E_{\text{a}}/(RT)\right)$, where $R = 8.314510$ J/mol K is the molar gas constant, η_∞ high temperature limit of the viscosity and E_a is the activation energy which was experimentally determined to be [138]

$$\eta(T)[\text{Pa s}] = \begin{cases} 3.8\cdot 10^{-14}\,\exp\left(\frac{712\text{ kJ/mol}}{RT}\right) & 1000\text{ K} < T < 1400\text{K} \\ 5.8\cdot 10^{-8}\,\exp\left(\frac{515.4\text{ kJ/mol}}{RT}\right) & 1400\text{ K} < T < 2500\text{K} \end{cases}. \tag{3.27}$$

The resulting characteristic times are shown for the cases in which the fiber only experiences gravity and that of axial strain in Fig. 3.19. The characteristic times rapidly decrease with increasing temperature thereby changing their values over many orders of magnitude. When the fiber is heated, the strain is released due to viscous elongation of the fiber up to the point at which the strain is too small for a significant change on the time scale of one measurement cycle $\tau_s > 60$ s. With that, the remaining stress after heating to a temperature of $T \approx 1800$ K can be estimated from Fig. 3.19 to be $\sigma > 100$ kPa. As this is the stress at the maximum temperature and, thereby, maximum thermal elongation, it is ensured that the fiber stays stressed during the measurements. The temperature at which the fiber fuses should occur when the characteristic time $\tau_v \approx (0.5 \ldots 5)$ s becomes comparable to the measurement cycle ($\tau \approx 1\ s$). Using this condition, the fusing temperature is determined to be $T = (2710 \pm 140)$ K.

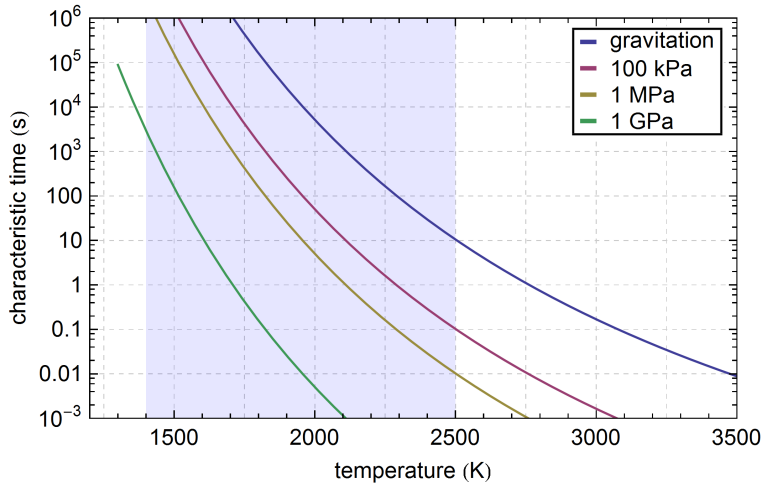

Figure 3.19: *Characteristic time scales of the viscous deformation dynamics caused by gravitation and different axial strains. The interpolated range is marked blue.*

Note that the viscous elongation leads to a radius reduction which, however, is negligibly small. The maximum change of the waist length is on the order of $1\ \%$ of the initial waist length so that we estimate a radius change by considering volume conservation to be $\Delta r/r = -\sqrt{L}/2 \cdot \Delta L/L \approx O(10^{-3})$. This value is much smaller compared to the uncertainty of the TOF radius profile.

The fusing point of the fiber is determined experimentally by increasing the heating power step-wise up to the point at which the fiber transmission breaks down during the measurement cycle. Here, the initialization procedure is omitted to prevent it from damaging the fiber. The maximum transmitted power the fiber could sustain for a complete cycle is $192(10)$ mW with $\Delta L_{\mathrm{opt}}^{\mathrm{max}} = 235(5)$ µm which corresponds to a predicted equilibrium waist temperature of $T_{\mathrm{waist}} = (2515 \pm 255)$ K. Note, that the uncertainty of the latter only takes the uncertainty of the heat exchange rates into account and is actually higher due to the extrapolation used for the thermo-optic coefficient. The measured value is in excellent agreement with the theory prediction, thereby demonstrating the consistency of the analysis.

3.6 Summary

In this work, I have studied the thermalization via heat radiation of an individual nanoscopic object by means of a silica nanofiber of predetermined shape with a diameter of 500 nm, smaller than the thermal wavelength. My method is based on the interferometrical detection of thermally induced path length changes that can be related to the nanofiber temperature via the well-known material properties of fused silica. For this purpose, I employed a fiber-integrated Fabry-Pérot type resonator with an integrated TOF (TOF microresonator) which was heated in the nanofiber region by the absorbed light of a heating laser sent through the fiber.

The dynamics of the thermalization is extracted via rise and fall time time constants of the signal, which were on the order of 100 ms. The equilibrium situation is characterized by the maximum optical path length change as function of the heating power. Thereby, the temperature scaling of the radiated power is probed via the equilibrium situation, where the heating power is balanced by the radiated power. The thermalization dynamics, carries information about the total radiated power at any temperature that the system exhibits until reaching equilibrium. By using samples of different lengths and performing measurements at different pressures, I confirmed that the heat conduction of silica and the heat transport via gas play essentially no role in the thermalization process. As a consequence, the heat transfer is governed by thermal radiation.

I developed an ab-initio thermodynamical model of a tapered optical fiber that is based on its geometry and material constants and includes heat transport via heat radiation, heat conduction and heat diffusion in gas. In order to compare the temperature predictions from the model to the optical path length changes that were observed in the experiment, I gathered extracted material properties of silica from various literature sources and combined them such that they essentially cover a temperatures range from ambient conditions up to its glass transition temperature. My analysis confirms over a large temperature range that the total thermally radiated power in the far-field is accurately predicted by fluctuational electrodynamics which is based on first principles using only the optical properties and shape and size of the emitter.

While the heat exchange rate via thermal radiation of particles smaller than the thermal wavelength has been studied extensively before [47, 48], the samples employed in previous measurements have not been monodisperse, meaning that only statistical information of their morphology, size and material was available. In contrast to that, here a single object of predetermined shape and material has been studied, thereby enabling the direct comparison to an ab-initio model.

Modeling the thermalization of microscopic particles with arbitrary shape from first principles has important applications in the framework of, e.g., heat management in nanodevices, radiative forcing of aerosoles in the earth's atmosphere [49], or cavity optomechanics experiments [140]. Furthermore, the interferometric detection scheme that was devised in this work may prove to be useful for thermalization measurements in other experiments, such trapping and cooling of optical microspheres [140–142]. Beyond that, a direct verification of the FED model implies that other predictions derived from the same principles apply at the corresponding size scale, e.g. repulsive Casimir forces [143].

CHAPTER 4

Optically active mechanical modes of tapered optical fibers

Nanoscale photonic structures are becoming increasingly interesting due to their various applications in the fields of sensing [144] quantum optics [18, 19, 54, 145], and quantum information processing [146]. This is due to their capability to efficiently couple light to matter via their highly confined evanescent light field in combination with their flexibility concerning shape, material and dispersion relation. The applications of nanoscale photonic structures rely on the stability of the phase and polarization of the guided light field as well as on the position of the structures. Achieving this stability is all the more challenging in a high vacuum environment where the mechanical damping due to the surrounding gas is negligible. Moreover, due to the small scales involved, even the thermal motion can lead to significant displacements.

Here, I investigate mechanical modes of a tapered optical fiber (TOF) that influence the fiber guided light. I experimentally demonstrate that torsional mechanical modes exhibit surprisingly high quality factors and lead to resonantly enhanced vibrations that modulate the phase and polarization of the optical mode via the strain-optic effect. Based on an analytic model as well as on experimental measurements, I will show that the commonly used exponential radius profile of TOFs confines a subset of the torsional mechanical modes to the nanofiber section, leading to the high Q-factors.

In the first section of the chapter, a model is developed that describes the mechanical modes of a TOF and their effect on the polarization of the fiber guided optical modes. This is achieved in three steps: First the mechanical modes of the TOF are computed from the wave equation as well as from a finite element method (FEM) model. Then, the thermally excited displacement of the modes is derived. In the last step, the effect of the mechanical strain on the optical modes via the strain-optic effect is computed. The second section is concerned with the experimental method and the measurement results.

4.1 Theory of elasticity

A body that is subject to forces undergoes a deformation in which its constituents (atoms, molecules, ...) are deflected from their equilibrium position in their bound state. This gives rise to internal forces which counteract the external forces. When both forces match, the body reaches a new, deformed equilibrium configuration. The theory of elasticity provides the theoretical framework to describe such phenomena in the static as well as in the dynamic case. Here, the basic concepts and notations are introduced that are necessary to understand the mechanical properties of tapered optical fibers. A comprehensive treatment is given in standard literature [147–150].

The continuous nature of the body under study makes it convenient to formulate the theory in terms of density, so that the forces are expressed by force densities $\boldsymbol{F}(\boldsymbol{r})$ in units of N/m^3. Then the total force acting on a volume element V is then given by the volume integral $\int_V \boldsymbol{F}(\boldsymbol{r})\,\mathrm{d}\boldsymbol{r}$ which, according to Newton's third law, must be matched by the forces exerted on the surfaces of the volume. This motivates the introduction of the stress tensor $\boldsymbol{\sigma}$ that is evaluated on the elements surface and which relates to the force via

$$\int_V \boldsymbol{F}\,\mathrm{d}V = \oint_S \boldsymbol{\sigma}\cdot\boldsymbol{n}_S\,\mathrm{d}S\;, \tag{4.1}$$

where S is the surface of the volume and $\boldsymbol{n}_S$ is the vector normal to the surface. Using the divergence theorem from vector analysis, the force density can be identified as the source of stress and, therefore, expressed via the divergence of the stress:

$$\boldsymbol{F}_i = \partial_{\boldsymbol{x}_k}\boldsymbol{\sigma}_{ik}\;, \tag{4.2}$$

where Einstein's notation was used. Following this equation, the stress tensor can be intuitively understood by considering its components on the surface of a volume element in a body, as illustrated in Fig. 4.1(a). Here, the simple case of a volume element in which the edges are oriented along the Cartesian basis is chosen. Then, the last index of $\boldsymbol{s}$ is the same as the index of the axis that is perpendicular to the plane. Those stress components oriented perpendicularly to the surfaces are labeled with equal indices, corresponding to forces perpendicular to the surface plane. Those stress components with unequal indices yield tangential forces and are called shear stresses.

The stress causes a displacement of the material points $\boldsymbol{u}(\boldsymbol{r})$, e.g., the position of the atoms or lattice sites. The theory distinguishes between a bulk displacement, in which the full body is shifted and which does not give rise to strain, and rotation which is given by the antisymmetric part of the strain tensor and a deformation which is described by the symmetric part of the strain tensor:

$$\boldsymbol{s}_{mn} = \frac{1}{2}\left(\frac{\partial\boldsymbol{u}_m}{\partial\boldsymbol{x}_n} + \frac{\partial\boldsymbol{u}_n}{\partial\boldsymbol{x}_m}\right)\;. \tag{4.3}$$

Figure 4.1 (b) illustrates the relationship between strain and displacement in the simplified case of an infinitesimal square. The blue square is stressed and deforms to result in the transparent blue figure. In this case, the variation of the displacement at the points A or B is computed by multiplying the strain tensor with the corresponding coordinate vector that starts at the fixed point O: $\overline{OA} = (0, \Delta x_2)$ and $\overline{OB} = (\Delta x_1, 0)$ respectively.

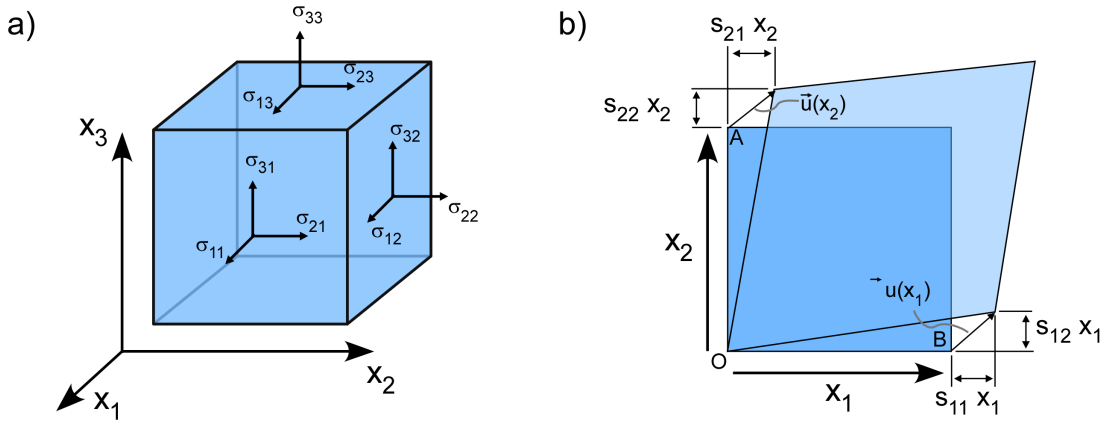

Figure 4.1: *a) Illustration of the stress tensor components on the surface of a volume element. b) Illustration of relation between strain and displacement in two dimensions. The blue square depicts the body in its equilibrium state without stress and the transparent figure that with stress applied. For simplicity, the point O is fixed.*

Stress $\boldsymbol{\sigma}$ and strain $\boldsymbol{s}$ are coupled by a generalized form of Hooke's law [147, §5]

$$\boldsymbol{\sigma} = \boldsymbol{c} : \boldsymbol{s} \text{ , and} \tag{4.4a}$$

$$\boldsymbol{s} = \boldsymbol{c}' : \boldsymbol{\sigma} \text{ ,} \tag{4.4b}$$

where $\boldsymbol{c}$ and $\boldsymbol{c}'$ are the elasticity and compliance tensor, respectively, and the double dot operator sums over the two neighboring index pairs, e.g. $(\boldsymbol{a} : \boldsymbol{b})_{mn} = \boldsymbol{a}_{mnij}\, \boldsymbol{b}_{ij}$ or $\boldsymbol{a} : \boldsymbol{b} = \boldsymbol{a}_{ij}\, \boldsymbol{b}_{ij}$, depending on the rank of the tensors. Both the stress and the strain tensor are symmetric, $\boldsymbol{s}_{mn} = \boldsymbol{s}_{nm}$ and $\boldsymbol{\sigma}_{mn} = \boldsymbol{\sigma}_{nm}$, such that $\boldsymbol{c}$ and $\boldsymbol{c}'$ are also symmetric in each index pair. This, strongly reduces the number of free parameters and facilitates a contracted notation in which rank 2 tensors simplify to vectors and rank 4 tensors to square matrices. Then, the corresponding equations reduce to matrix equations and the strain and stress tensors are written as vectors using the rule [1]

$$\boldsymbol{\sigma} \;=\; \begin{bmatrix} \boldsymbol{\sigma}_{xx} & \boldsymbol{\sigma}_{yy} & \boldsymbol{\sigma}_{zz} & \boldsymbol{\sigma}_{xy} & \boldsymbol{\sigma}_{xz} & \boldsymbol{\sigma}_{yz} \end{bmatrix} \text{ ,} \tag{4.5}$$

where the square brackets are used to distinguish the contracted notation from the standard notation (round brackets). Then, the elasticity and elasticity tensors can be written as the matrices:

$$\boldsymbol{c} = \frac{E_Y}{(1+\nu)(1-2\nu)} \begin{bmatrix} 1-\nu & \nu & \nu & & & \\ \nu & 1-\nu & \nu & & \boldsymbol{0}_{3\times 3} & \\ \nu & \nu & 1-\nu & & & \\ & & & 1-2\nu & 0 & 0 \\ & \boldsymbol{0}_{3\times 3} & & 0 & 1-2\nu & 0 \\ & & & 0 & 0 & 1-2\nu \end{bmatrix} \tag{4.6a}$$

[1] Note that other notations can be found in the literature in which the ordering of the mixed terms (xy, xz, yz) is different. These, however, couple via a diagonal matrix so that $\boldsymbol{c}$ and $\boldsymbol{c}'$ are not affected. In the Voigt notation (only) the mixed strain components are additionally scaled by a factor 2, i.e. $2s_{xy}$, so that the lower right square matrix of $\boldsymbol{c}$ and $\boldsymbol{c}'$ have to be scaled accordingly.

$$\boldsymbol{c}' = \frac{1}{E_Y}\begin{bmatrix} 1 & -\nu & -\nu & & & \\ -\nu & 1 & -\nu & & \mathbf{0}_{3\times3} & \\ -\nu & -\nu & 1 & & & \\ & & & 1+\nu & 0 & 0 \\ & \mathbf{0}_{3\times3} & & 0 & 1+\nu & 0 \\ & & & 0 & 0 & 1+\nu \end{bmatrix}, \tag{4.6b}$$

where $\nu = 0.168$ is Poisson's ratio and $E_Y = (70 \pm 4)$ GPa is Young's modulus with the corresponding values for bulk fused silica [133, 151, 152]. Note that when considering nanoscale structures, surface effects can alter the elastic properties [153, 154]. This effect, however, contributes at sizes far below 100 nm so that the bulk values can be used in the case of 500 nm diameter fibers used here.

When evaluating Eq. (4.4)(b) for a stress along one axis caused by a force (F) applied to a certain area (A), e.g. $\boldsymbol{\sigma}_{11} = F/A$, the well-known form of Hooke's law is found

$$\begin{aligned} \boldsymbol{s}_{11} &= \boldsymbol{\sigma}_{11}/E_Y \\ \boldsymbol{s}_{22} = \boldsymbol{s}_{33} &= -\nu\,\boldsymbol{\sigma}_{11}/E_Y \end{aligned}$$

where the second expression describes the transversal contraction perpendicular to the stress direction.

The energy stored in an elastic medium is composed of the kinetic part (E_{kin}) that stems from the motion of the mass segments and the potential energy (E_{pot}) which is the energy that has been invested to deform the body to its current configuration. It can be computed using

$$E_{\text{kin}} = \int \mathrm{d}r^3\, \frac{1}{2}\,\rho\,(\partial_t \boldsymbol{u}) \cdot (\partial_t \boldsymbol{u}) \tag{4.7a}$$

$$\begin{aligned} E_{\text{pot}} &= \int \mathrm{d}r^3 \left[\frac{\lambda_{\text{Lamé}}}{2}\,(\boldsymbol{s} : \mathbb{1})^2 + \mu_{\text{Lamé}}\,\boldsymbol{s} : \boldsymbol{s}\right] \\ &= \int \mathrm{d}r^3 \left[\frac{\lambda_{\text{Lamé}}}{2}(\boldsymbol{s}_{11} + \boldsymbol{s}_{22} + \boldsymbol{s}_{33})^2 \right. \\ &\qquad \left. + \mu_{\text{Lamé}}(\boldsymbol{s}_{11}^2 + \boldsymbol{s}_{22}^2 + \boldsymbol{s}_{33}^2 + 2\,[\boldsymbol{s}_{12}^2 + \boldsymbol{s}_{13}^2 + \boldsymbol{s}_{23}^2])\right], \end{aligned} \tag{4.7b}$$

where ρ is the mass density and the material constants are expressed in the more convenient form of the first and second Lamé constants $\lambda_{\text{Lamé}} = E_Y\nu/[(1+\nu)(1-2\nu)]$ and $\mu_{\text{Lamé}} = E_Y/(2+2\nu)$, respectively. The latter is also known as the shear modulus $G = \mu_{\text{Lamé}}$.

Up to now, the displacements were assumed to be inifinitesimal. For finite displacements, the material coordinate system differs from the spatial coordinate system which has to be taken into account when computing the strain. This is known as the geometric nonlinearity and can be accounted for by replacing the strain with

$$\boldsymbol{s}_{mn} = \frac{1}{2}\left(\frac{\partial \boldsymbol{u}_m}{\partial \boldsymbol{x}_n} + \frac{\partial \boldsymbol{u}_n}{\partial \boldsymbol{x}_m} + \frac{\partial \boldsymbol{u}_l}{\partial \boldsymbol{x}_m} \cdot \frac{\partial \boldsymbol{u}_l}{\partial \boldsymbol{x}_n}\right). \tag{4.8}$$

This nonlinearity is in general very small and can be neglected in most cases, like compression or flexion of the material. However, in the case of torsion, its contribution can

be sufficiently large so that it has to be taken into account. Possible modifications of the torsional wave equation will be discussed in the corresponding section. Furthermore, the geometric non-linearity will be taken into account in the finite element model and when computing the strain for the strain-optic effect.

4.2 Waves in tapered optical fibers

When an elastic body is displaced from its equilibrium state, a restoring force occurs that counteracts the displacement. Such a restoring force causes periodic motion of a volume element which interacts with the adjacent elements such that the displacement propagates through the material in the form of a mechanical wave until encountering a boundary, e.g., a free or fixed surface. Here, the wave equation of the theory of elasticity is presented together with its solutions for three special cases: Torsional waves in which an angular displacement (rotation) of a cross section with respect to its neighbors propagates through the fiber, string-like and flexural waves which are defined by a displacement in the transversal (radial) direction and finally compressional waves in which a displacement in the axial direction propagates along the fiber. The following section is based on [147, 148, 150, 155] and a helpful summary of the solutions for a circular rod can be found in [156]. At the beginning of the respective sections, literature references will be given for the corresponding, more specialized, treatments.

The wave equation can be derived by writing Newton's second law for the internal forces in terms of force and acceleration densities. Writing the force as the divergence of the stress, c.f. Eq. (4.2), one finds

$$\rho\, \partial_t^2\, \boldsymbol{u}_i = \boldsymbol{F}_i = \partial_{\boldsymbol{x}_k}\, \boldsymbol{s}_{ik}\ . \tag{4.9}$$

Expressing the strain by the displacements according to Eq. (4.3), the wave equation of the linear elastic theory follows:

$$\rho\, \partial_t^2 \boldsymbol{u} = \frac{E_Y}{2(1+\nu)(1-2\nu)}\, \nabla \cdot \mathrm{div}(\boldsymbol{u}) + \frac{E_Y}{2(1+\nu)}\ \triangle\, \boldsymbol{u}\ . \tag{4.10}$$

In the case of nanofibers, the wavelengths are on the order of the nanofiber length which is much larger than the thickness of the fiber. This allows to assume plane wavefronts in the fiber cross-section, $\boldsymbol{u}(t, \boldsymbol{x}) = \boldsymbol{u}(t, z)$, which is known as the long-wavelength or slender rod approximation. As a consequence, modes with higher transversal orders can be neglected where, e.g., the inner part exhibits an opposite displacement compared to the outer part of the fiber.

For all three kinds of waves, the wave equation simplifies to one spatial dimension and will be presented in the following together with their solutions for tapered optical fibers. The radius profile $a(z)$ of one half of a TOF is shown in Fig. 4.2 in which the zero point is set to the symmetry point of the fiber such that $z_1 = L_w/2$ is half the waist length. The corresponding geometry parameters are given in Tab. 4.1. The profile is composed of three basic shapes: Cylinders in the waist and the unprocessed parts of the fiber, truncated cones in section 3 and 4 and an exponentially increasing profile in section 2. The wave equation is solved for each of these shapes individually and then the amplitude and force is matched at each boundary to find the solution for the TOF.

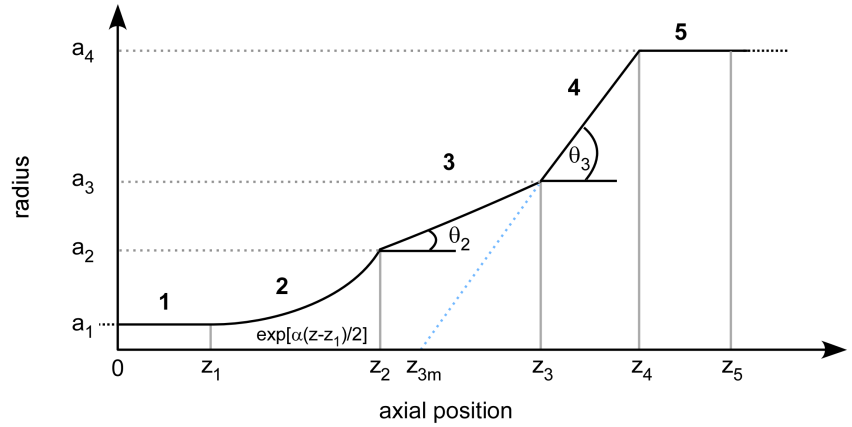

Figure 4.2: *Schematical view of half of a TOF radius profile, with the origin set to the center of the waist. The TOF radius profile is symmetric by rotation around the fiber axis and mirror symmetric around the axial zero point. The sections are numbered as indicated on top of the profile.*

sample	L_{waist} mm	ΔL mm	α 1/m	θ_2 mrad	θ_3 mrad	a_2 µm	a_3 µm	z_2 mm	z_3 mm	z_4 mm
TOF-M1	10	0.25	380	2	5	8.97	28.6	14.4	24.1	30.8
TOF-M2	10.4	≈ 0	380	2	5	8.97	28.6	14.6	24.3	31.0
TOF-M3	10	0.25	380	2	5	8.97	28.6	14.4	24.1	30.8
TOF-M4	5	0.1	383	2	5	11.3	29.9	12.5	22.0	28.7
TOF-M5	3	0.25	379	2	5	9.25	28.5	11.0	20.6	27.3

Table 4.1: *Geometry parameters (as introduced in Fig. 4.2) of the TOFs used in the measurements. TOF-M2 corresponds to TOF-resonator 3 used for the thermalization measurements, compare Ch. 3.*

4.2.1 Torsional waves

A torsional motion is a motion where the cross-sectional planes of a body rotate with respect to each other but exhibit no radial or axial displacement [157]:

$$\boldsymbol{u}_r = \boldsymbol{u}_z = 0 \;\text{ and }\; \partial_\phi \boldsymbol{u}_\phi = 0 \,.$$

In the slender rod approximation all points in the cross-section rotate in phase so that the displacement vector is given by:

$$\boldsymbol{u}(t,\boldsymbol{r}) = \phi(t,z)\, r\, \hat{\boldsymbol{\phi}} = \phi(t,z)\,(-y\,\hat{\boldsymbol{x}} + x\,\hat{\boldsymbol{y}}) \tag{4.11}$$

in cylindrical and cartesian coordinates, respectively. The corresponding wave equation for a cylinder with varying cross-section is known as a Webster-type equation and takes the form [157]

$$c_t^{-2}\,\partial_t^2\,\phi(t,z) - \partial_z^2\,\phi(t,z) - \left(\frac{\partial_z I_p(z)}{I_p(z)}\right)\partial_z\phi(t,z) = 0\,, \tag{4.12}$$

where $I_p(z) = \int_A r^2 \mathrm{d}A = \pi a^4/2$ is the polar moment of inertia at the cross section $A(z)$, for fused silica $c_t = \sqrt{G/\rho} = (3680 \pm 130)\ \mathrm{m/s}$ is the phase velocity of the torsional wave and $G = E_Y/(2+2\nu) = (30 \pm 2)$ GPa is the shear modulus [133, 151, 152]. Note that torsional waves are dispersion free, i.e., their phase velocity is independent of the oscillation frequency.

To solve the wave equation, it is convenient to first separate it in time and space and construct solutions of the form

$$\phi(t, z) = \phi(z) \cos(\omega\, t) \tag{4.13}$$

so that only the differential equation in the axial coordinate remains. Here, the real valued functions and coefficients are chosen. In the following, the wave equation for each section of the TOF is solved individually.

Cylinder

In the simplest case of a homogeneous cylinder, in which $\partial_z I_p(z) = 0$, the wave equation Eq. (4.12) reduces to its simplest form

$$\partial_z^2\, \phi(t, z) + k_0^2\, \phi(t, z) = 0\ , \tag{4.14}$$

with the well-known solutions:

$$\phi_\mathrm{a}(z) = \sin(k_0\, z)\ , \quad \phi_\mathrm{b}(z) = \cos(k_0\, z)\ , \quad \text{where } \ k_0 = \omega/c_t\ . \tag{4.15}$$

Exponential Horn

An object with an exponentially increasing radius profile, $a(z) = a_0 \exp(\alpha\, z/2)$, is commonly denominated exponential horn. Here, Eq. (4.12) takes the form

$$\partial_z^2\, \phi(t, z) + 2\alpha\, \partial_z \phi(t, z) + k_0^2\, \phi(t, z) = 0\ . \tag{4.16}$$

It corresponds to the differential equation of the one-dimensional damped harmonic oscillator (DHO), where the spatial evolution of the torsional wave corresponds to the time evolution of the DHO. In this analogy, the damping term is frequency dependent $\zeta = \alpha/k_0 = \alpha\, c_t/\omega$. Thus, the frequency determines the damping regime: For frequencies below a cut-off frequency $\omega_t^{co} = \alpha\, c_t$ (corresponding to critical damping) no solution of propagating waves exists, meaning that the complete body moves with the same phase (no nodes) and the amplitude decreases exponentially with z. The corresponding two solutions are given by

$$\phi_\mathrm{a}(z) = \exp(-\alpha\,[z - z_1]) \times \begin{cases} \exp(\beta\,[z - z_1]) & \beta = \sqrt{\alpha^2 - k_0^2} > 0 \\ z & \alpha^2 = k_0^2 \\ \cos(\beta\,[z - z_1]) & \beta = \sqrt{k_0^2 - \alpha^2} > 0 \end{cases}\ , \tag{4.17a}$$

$$\phi_\mathrm{b}(z) = \exp(-\alpha\,[z - z_1]) \times \begin{cases} \exp(-\beta\,[z - z_1]) & \beta = \sqrt{\alpha^2 - k_0^2} > 0 \\ 1 & \alpha^2 = k_0^2 \\ \sin(\beta\,[z - z_1]) & \beta = \sqrt{k_0^2 - \alpha^2} > 0 \end{cases}\ , \tag{4.17b}$$

compare e.g. [124].

The cut-off behavior of the exponential horn is of great importance for the mechanical eigenmodes of the TOF. Below the cut-off frequency, the modes are restricted to amplitude profiles which decay to zero amplitude along the exponential taper section. Taking the solutions of the cylindrical section into account, this requirement can only be met by amplitude profiles for which the nanofiber length is approximately a multiple of the wavelength ($n\,\lambda/2 \approx L_w$). As a result, the modal shape and the frequency spectrum can be expected to be similar to that of a nanofiber which is fixed at both ends. This restriction is gradually released for increasing frequencies beyond ω_t^{co}. Here, the increasing values of k_0 results in higher β values and, therefore, shorter oscillation periods along the exponential section. As a consequence, the restriction of the slope at the boundary to negative values (below ω_t^{co}) is gradually released. Furthermore, the mode can exhibit nodes within the exponential section, thereby, allowing for a larger variety of modal shapes.

Cone

Cones have a linearly increasing radius profile of the form $a(z) = \theta\, z$, for which the wave equation takes the form of a Bessel-type equation

$$\partial_z^2\,\phi(t,z) + \frac{4}{z}\,\partial_z\phi(t,z) + k_0^2\,\phi(t,z) = 0\;.$$

For a cylinder with its tip at z_m the solutions are given by

$$\phi_{\mathrm{a}}(z) = \frac{\cos(k_0\,[z-z_m])}{k_0^2(z-z_m)^2} - \frac{\sin(k_0\,[z-z_m])}{k_0^3\,(z-z_m)^3} = -\sqrt{\frac{\pi}{2}}\,\frac{J_{3/2}(k_0\,[z-z_m])}{(k_0\,[z-z_m])^{3/2}} \tag{4.18a}$$

$$\phi_{\mathrm{b}}(z) = \frac{\cos(k_0\,[z-z_m])}{k_0^3\,(z-z_m)^3} + \frac{\sin(k_0\,[z-z_m])}{k_0^2\,(z-z_m)^2} = -\sqrt{\frac{\pi}{2}}\,\frac{J_{-3/2}(k_0\,[z-z_m])}{(k_0\,[z-z_m])^{3/2}}\;. \tag{4.18b}$$

In the case of the TOF, the values of z_m can be determined from the opening angles θ together with the axial position and the radius of the small end of the cone: $z_{2m} = z_2 - a_2/\tan(\theta_2) \approx z_2 - a_2/\theta_2$ for section 3 and $z_{3m} \approx z_3 - a_3/\theta_3$ for section 4.

Boundary conditions

The full solution of the wave equation is constructed from the piecewise solutions by matching the amplitude as well as the torque $M(z_n) = G\,I_p(z_n)\,\partial_z\phi(z_n)$ at the boundaries:

$$A_n\,\phi_{n,a}(z_n) + B_n\,\phi_{n,b}(z_n) = A_{n+1}\,\phi_{n+1,a}(z_n) + B_{n+1}\,\phi_{n+1,b}(z_n)\;, \tag{4.19a}$$

$$A_n\,\phi'_{n,a}(z_n) + B_n\,\phi'_{n,b}(z_n) = A_{n+1}\,\phi'_{n+1,a}(z_n) + B_{n+1}\,\phi'_{n+1,b}(z_n)\;, \tag{4.19b}$$

where n is the index of the boundary at z_n and $\phi_{n,a}$ and $\phi_{n,b}$ as well as $\phi_{n+1,a}$ and $\phi_{n+1,b}$ are the two adjacent amplitude functions. The wave constant (k_0) is fixed for all sections and the amplitude is required to be zero at the fixing points of the fiber at z_5:

$$A_5\,\phi_{5\mathrm{a}}(z_5) + B_5\,\phi_{5\mathrm{b}}(z_5) = 0\;. \tag{4.20}$$

The symmetry of the TOF-profile motivates to search for symmetric or antisymmetric modes with respect to the $z = 0$ plane. This can be achieved by setting either $A_1 = 0$ or $B_1 = 0$ and solving the boundary conditions for one half of the TOF.

The resulting system of linear equations ca be written as a homogeneous matrix equation of the form

$$\mathbb{M} \cdot V = 0 \,, \tag{4.21}$$

with the coefficients vector $V = \begin{pmatrix} A_1 & A_2 & B_2 & A_3 & B_3 & A_4 & B_4 & A_5 & B_5 \end{pmatrix}^T \in \mathbb{R}^9$. The matrix $\mathbb{M}$ is composed of the amplitude functions as well as their derivatives at the boundaries:

$$\mathbb{M} = \left(\begin{array}{ccccccccc}
\phi_{1\mathrm{a}}(z_1) & -\phi_{2\mathrm{a}}(z_1) & -\phi_{2\mathrm{b}}(z_1) & 0 & 0 & 0 & 0 & 0 & 0 \\
\phi'_{1\mathrm{a}}(z_1) & -\phi'_{2\mathrm{a}}(z_1) & -\phi'_{2\mathrm{b}}(z_1) & 0 & 0 & 0 & 0 & 0 & 0 \\
\hline
0 & \phi_{2\mathrm{a}}(z_2) & \phi_{2\mathrm{b}}(z_2) & -\phi_{3\mathrm{a}}(z_2) & -\phi_{3\mathrm{b}}(z_2) & 0 & 0 & 0 & 0 \\
0 & \phi'_{2\mathrm{a}}(z_2) & \phi'_{2\mathrm{b}}(z_2) & -\phi'_{3\mathrm{a}}(z_2) & -\phi'_{3\mathrm{b}}(z_2) & 0 & 0 & 0 & 0 \\
\hline
0 & 0 & 0 & \phi_{3\mathrm{a}}(z_3) & \phi_{3\mathrm{b}}(z_3) & -\phi_{4\mathrm{a}}(z_3) & -\phi_{4\mathrm{b}}(z_3) & 0 & 0 \\
0 & 0 & 0 & \phi'_{3\mathrm{a}}(z_3) & \phi'_{3\mathrm{b}}(z_3) & -\phi'_{4\mathrm{a}}(z_3) & -\phi'_{4\mathrm{b}}(z_3) & 0 & 0 \\
\hline
0 & 0 & 0 & 0 & 0 & \phi_{4\mathrm{a}}(z_4) & \phi_{4\mathrm{b}}(z_4) & -\phi_{5\mathrm{a}}(z_4) & -\phi_{5\mathrm{b}}(z_4) \\
0 & 0 & 0 & 0 & 0 & \phi'_{4\mathrm{a}}(z_4) & \phi'_{4\mathrm{b}}(z_4) & -\phi'_{5\mathrm{a}}(z_4) & -\phi'_{5\mathrm{b}}(z_4) \\
\hline
0 & 0 & 0 & 0 & 0 & 0 & 0 & \phi_{5\mathrm{a}}(z_5) & \phi_{5\mathrm{b}}(z_5)
\end{array}\right) .$$

Here, each two lines correspond to a boundary (indicated by lines) and the last line to the fixing point at the TOFs end.

Equation (4.21) has non-trivial solutions for V if the matrix $\mathbb{M}$ is singular: $\det(\mathbb{M}) = 0$. This condition is fulfilled for a set of discrete values of the only free parameter of the system, i.e., the oscillation frequency. Each of the solutions corresponds to a resonant torsional mode of the TOF. The coefficient vector is the kernel of $\mathbb{M}$ and is numerically determined for each mode.

Figure 4.3 shows the amplitude profile of several selected modes. Two classes of modes are can be distinguished, one that is essentially restricted to the nanofiber section (nanofiber modes) and another one that exhibits high amplitudes near the fixation points (taper modes). The latter can be understood as the combination of two singly-clamped oscillators, i.e., the two halves of the TOF profile without the nano-fiber, that are weakly coupled by the nano-fiber. These modes come in pairs with small frequency separations corresponding to the odd and even configurations, so that they show a clear signature which can be easily identified. Due to their high amplitude near the fixation points, they are expected to suffer from high clamping losses and thus have a comparatively low mechanical quality factor (Q-factor).

The fundamental torsional nanofiber mode occurs at 163 kHz and the second harmonic at 323 kHz, which is in good approximation twice the value of the frequency of the fundamental mode. Beyond the cut off frequency of the exponential taper profile, the spectral density of the resonances increases, as can be seen from the frequency of two neighboring modes in Fig. 4.3(a). From the comparison of the modal amplitude profile, the effect cut-off behavior of the exponential horn is clearly visible: The mode is confined to the nanofiber section below the cut-off frequency and exhibits an exponential decay in

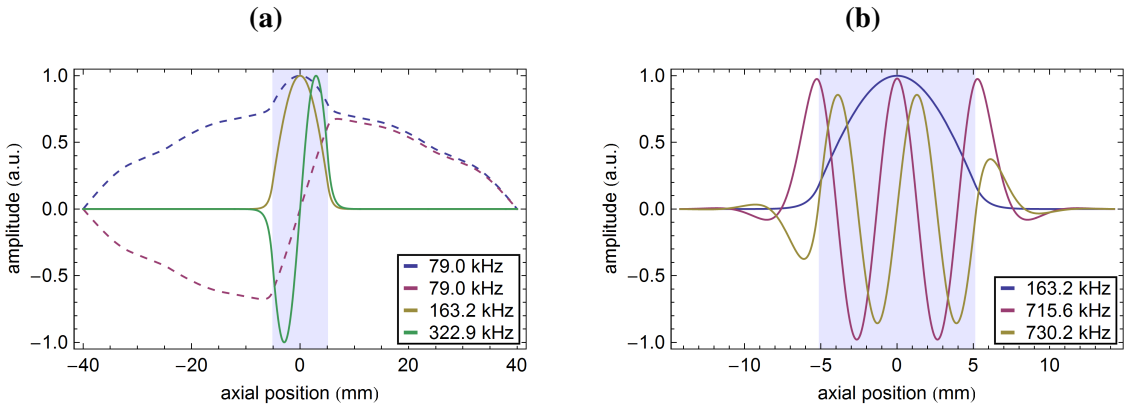

Figure 4.3: *(a) Fundamental and second harmonic of each, the nanofiber mode (solid lines) and the taper modes (dashed lines). The predicted eigenfrequencies of the latter two are* 78985.8305 *Hz and* 78985.8304 *Hz, respectively. (b) Two selected neighboring higher order modes beyond the cut-off frequency and the fundamental mode shown for reference. The waist region is marked blue and the corresponding eigenfrequencies are given in the legend. Fiber profile TOF-M1 where* $\omega_t^{co} = 2\pi \cdot 445$ *kHz.*

sections adjacent to the waist. At higher frequencies the less strict requirements on the slope of the amplitude are visible as well as anti-nodes in the exponential sections.

Mode energy

The energy of a torsional wave is derived by computing the strain from the displacements and inserting the result into the energy relations Eq. (4.7)

$$E_{\text{torsion}} = \frac{1}{2} \int \mathrm{d}z \, I_p(z) \, \left([\partial_t \phi(t,z)]^2 + c_t^2 \, [\partial_z \phi(t,z)]^2 \right) \, , \tag{4.22}$$

where the first and second terms give the kinetic the potential energy contributions, respectively. In the case of a mode with zero displacement at both ends, a form where the potential part is expressed via the wave equation can be found by partial integration:

$$E_{\text{torsion}} = \frac{1}{2} \int \mathrm{d}z \, I_p(z) \, \left([\partial_t \phi(t,z)]^2 - \phi(t,z) \, \frac{c_t^2}{I_p(z)} \, \partial_z [I_p(z) \, \partial_z \phi(t,z)] \right) \, , \tag{4.23a}$$

$$= \omega_0^2 \int \mathrm{d}z \, I_p(z) \, \phi^2(t,z) \, , \tag{4.23b}$$

where the wave equation was used to obtain the latter result.

Geometric nonlinearity

In the case of torsional waves, even small stresses can give finite displacements so that the geometric nonlinearity has to be taken into account and may give rise to modifications of the wave equation. This case has been studied in detail by Erofeev et al., who found that

for the slender rod approximations the resulting wave equation can be expressed as [158]

$$\partial_t^2\phi - c_t^2(1+\eta_{\text{finite}}\,(\partial_z\phi)^2)\,\partial_z^2\phi = 0\,, \tag{4.24}$$
$$\eta_{\text{finite}} = \frac{3\,c_l^2\,I_p^*}{2\,c_t^2\,I_p}\,, \quad I_p^* = \int_0^{2\pi}\mathrm{d}\phi\int_0^a r^4\,r\,\mathrm{d}r = \frac{\pi\,a^6}{3}\,.$$

Note that the additional term scales quadratically with the slope and therefore with the amplitude. In the linear approximation of small amplitudes, the equation reproduces the result of the linear theory.

The magnitude of the modification can be estimated by computing $\eta_{\text{finite}}\,(\partial_z\phi)^2$. The typical wavelength of the modes considered here is on the order of the nanofiber length $L_w \sim 5$ mm such that $\partial_z\phi(z) \approx \phi(z)\,n_m\,\pi/L_w$, where higher order modes are taken into account by the mode number n_m. With that the upper boundary of the nonlinear contribution is given by

$$\eta_{\text{finite}}\,(\partial_z\phi(z))^2 \approx 2(1+\nu)\,a^2\,\pi^2\,\phi^2\,n_m^2/L_w^2 \sim 10^{-7}\,(n_m\,\phi)^2\,.$$

In this work, small mode numbers $n_m < 20$ and small amplitudes excited by thermal fluctuations are considered $\phi \sim 10^{-4}$, see Ch. 4.4. In this case, the geometric nonlinearity yields a negligible modification of the wave equation. As a consequence, it is sufficient to use the linear wave equation to derive the modes while the geometric nonlinearity has to be taken into account when computing the strain that originates from the torsional vibration.

Axial load

The fiber in the experiment is strained before it is attached to its mount. When applying axial stress to the fiber, the wave velocity is changed according to [159]

$$c_t^2 = \frac{G+\sigma_{\text{ax}}(z)}{\rho} = c_t^2\,[1+2(1+\nu)\,s_{\text{ax}}(z)]\,, \tag{4.25}$$

where $\sigma_{\text{ax}}(z)$ is the axial stress, $s_{\text{ax}}(z)$ is the local axial strain. Note, that this is an effect that results from the strain in the material and does not assume a non-linear material response, i.e., a non-linear Young's modulus. The stress is largest at the position of small cross-sectional area, i.e., in the waist region. Due to the quadratic dependency of the stress on the radius and the exponential radius increase in the taper region, the high stress values are localized in and around the waist region. This effect is taken into account by assuming that only the waist is strained, $s_{\text{ax}} = \Delta L/L_w$, for which the higher phase velocity is used. Note that, this introduces a reflection at the edges of the waist due to the rapid change of the phase velocity which occurs not in this way in the TOF due to the smoother axial profile of the phase velocity of the latter. There is no straight-forward way to implement this smooth velocity change in this model. However, it will be treated correctly in the finite element model, see Ch. 4.3.

The scaling behavior of the resonance frequency with axial strain can be computed from the change of the phase velocity and the length. For a cylinder with fixed ends one

obtains:

$$\frac{f(s_{\mathrm{ax}})}{f(0)} = n_m \frac{\sqrt{1+2(1+\nu_P)\,s_{\mathrm{ax}}}}{1+s_{\mathrm{ax}}} \approx n_m\,(1+\nu_P\,s_{\mathrm{ax}})\,, \tag{4.26}$$

where n_m is the mode number and $\nu_P = 0.168$ is Poisson's ratio.

Temperature

In some experiments with nanofibers, the absorbed power from the guided light field can heat the fiber to temperatures up to or even beyond 1000 K. This is in particular valid for the nanofiber atom-trap where light field powers of several 10 mW are used [18, 19, 93].

Higher temperatures have two basic effects on the mechanical properties. First, the material expands at higher temperatures, thereby reducing the axial stress and, second, the Young's modulus and Poisson's ratio change. The latter two increase from room temperature to 1400 K by approximately 11 %. Here, they reach their maximum value and decrease for even higher temperatures [151]. This changes the speed of sound and the cut-off frequency of the torsional horn by up to $+5$ %. The thermal expansion of the nanofiber can be quantified using the thermal expansion coefficient of silica $\alpha_{te} = L^{-1}\Delta L/\Delta T \sim 10^{-7}\,1/\mathrm{K}$ (see Ch. A.6) and amounts to $\Delta L/L \sim 10^{-4}$ for the temperature range considered here. Its effect can, therefore, be neglected with respect to the change in the elastic constants. In the experiments concerned with the investigation of the mechanical modes that are presented here, however, a much smaller power of $\sim 10\mu$W is used so that the measurements are performed at room temperature.

4.2.2 Compressional waves

Compressional waves show a periodic series of expansion and compression along the propagation direction. The wave equation can be derived by balancing the axial force density by the acceleration of a mass segment, $(\partial_z F)\,\Delta z = \rho\,S\,\partial_t^2 u_z\,\Delta z$, where S is the cross-sectional area, to the counteracting forces by the stressed material described by Hooke's law $(\partial_z F)\,\Delta z = \partial_z\,(S\,E_Y\,\partial_z u_z)\,\Delta z$. The resulting equation takes the form of the Webster equation [155, 160]

$$c_c^{-2}\,\partial_t^2\,u_z(t,z) - \partial_z^2\,u_z(t,z) - \left(\frac{\partial_z S_c(z)}{S_c(z)}\right)\,\partial_z u_z(t,z) = 0\,, \tag{4.27}$$

where $S_c = \pi a^2$ is the cross-sectional area and $c_c = \sqrt{E_Y/\rho} = (5630 \pm 170)\ \mathrm{m/s}$ is the compressional wave velocity [133, 151, 152]. This wave equation can be transformed into the torsional wave equation by interchanging the moment of inertia with the cross-sectional area and the corresponding displacement variables. As a result, it can be solved in direct analogy to the previous considerations, taking into account that $2\,[\partial_z S_c(z)]/S_c(z) = [\partial_z I_p(z)]/I_p(z)$.

The solutions for the cone with the radius profile $a(z) = \theta z$ are:

$$u_{z,a}(z) = \frac{\sin(k_n z)}{k_n z} = \sqrt{\frac{\pi}{2\,k_n z}}\,J_{1/2}(k_n z)\,, \quad u_{z,b}(z) = \frac{\cos(k_n z)}{k_n z} = \sqrt{\frac{\pi}{2\,k_n z}}\,J_{-1/2}(k_n z)\,.$$

In case of the exponential horn where $a(z) = a_0 \exp(\alpha z/2)$ one obtains

$$u_{z,a}(z) = \exp(-\alpha\,(z - z_1)/2) \times \begin{cases} \exp(\beta\,[z - z_1]) & \beta^2 = \frac{\alpha^2}{4} - k_0^2 \geq 0 \\ \cos(\beta\,[z - z_1]) & \beta^2 = k_0^2 - \frac{\alpha^2}{4} > 0 \end{cases}, \tag{4.28a}$$

$$u_{z,b}(z) = \exp(-\alpha\,[z - z_1]/2) \times \begin{cases} \exp(-\beta\,[z - z_1]) & \beta^2 = \frac{\alpha^2}{4} - k_0^2 \geq 0 \\ \sin(\beta\,[z - z_1]) & \beta^2 = k_0^2 - \frac{\alpha^2}{4} > 0 \end{cases}. \tag{4.28b}$$

Here, the corresponding cut-off frequency is given by $\omega_c^{co} = \alpha c_c/2$ which differs by a factor of $\omega_c^{co}/\omega_t^{co} = \sqrt{(1+\nu)/2} = 0.764$ from that of the torsional vibration.

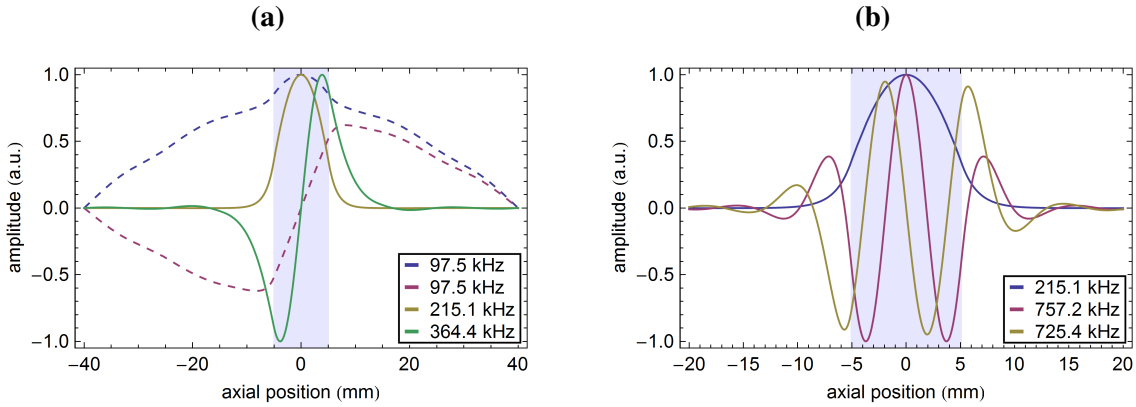

Figure 4.4: *Selected compressional modes of TOF-M1: First and second harmonic of each, the nanofiber mode (solid lines) and the taper mode (dashed lines). (b) Fundamental compressional mode and two selected neighboring higher order modes beyond the compressional cut-off frequency $\omega_c^{co} = 2\pi \cdot 341$ kHz. The waist region is marked blue and the corresponding eigenfrequencies are given in the legend.*

Figure 4.4 shows selected compressional modes. Their similarity to the torsional waves manifests in a similar mode structure and amplitude profile. In direct analogy, the modes can be separated into nanofiber modes and taper modes. Here, the reduced cut-off frequency is already below the resonance frequency of the second harmonic so that the amplitude profile of the latter can extend much further into the taper region compared to the fundamental mode and exhibits nodes within the exponential horn.

Mode energy

In analogy to the derivation given in the section of the torsional mode the energy is given by

$$E_c = \frac{\rho}{2} \int \mathrm{d}z\, S_c(z) \left([\partial_t u_z(t,z)]^2 - u_z(t,z)\, \frac{c_c^2}{S_c(z)}\, \partial_z [S_c(z)\, \partial_z u_z(t,z)] \right), \tag{4.29a}$$

$$= \rho\, \omega_0^2 \int \mathrm{d}z\, S_c(z)\, u_z^2(t,z) \tag{4.29b}$$

where, again, the wave equation was used to obtain the latter expression.

4.2.3 Transversal waves

As their name already suggests, transversal waves have displacements perpendicular to the fiber axis. The restoring force arises either from a bending moment due to material deformations (flexural waves) or a transversal force that arises from axial stress in a curved fiber (string waves). Here, the axial stress determines which of both forces dominates. In case of the TOF, a constant axial force applied at both ends leads to stresses that cover 4 orders of magnitude due to the large radius variations. As a consequence, the analysis must consider both effects simultaneously.

Again, the wave equation is formulated from Newton's second law. The forces arise from the stiffness of the fiber against flexing and those caused by the axial strain in a curved fiber (string-like) :

$$A\,\rho\,\partial_t^2 u(t,z) + \underbrace{\partial_z^2\left[E_Y\,I_a(z)\,\partial_z^2 u(t,z)\right]}_{\text{flexural}} - \underbrace{F_{\text{ax}}\,\partial_z^2 u(t,z)}_{\text{string-like}} = 0 \tag{4.30}$$

where F_{ax} is the axial force, $I_a(z) = \int \mathrm{d}A\, y^2 = \pi\, a^4(z)/4$ is the second moment of inertia with respect to the neutral axis, i.e., $\hat{\boldsymbol{x}}$-axis or $\hat{\boldsymbol{y}}$-axis. In order to estimate the relative magnitude of both contributions, the simplified case of a homogeneous cylinder is considered, such as the waist or the unprocessed part of the fiber. For waves the curvature typically yields $\partial_z^2 u \sim -k_z^2\, u$, so that the ratio of the force densities can be estimated by

$$\iota = \frac{\partial_z\, F_{\text{flex}}}{\partial_z F_{\text{string}}} \sim \frac{E_Y\, I_a\, k_z^4}{F_{\text{ax}}\, k_z^2} \propto \frac{1}{\lambda_m^2}\,.$$

For low order modes, it can be assumed that the wavelength is on the order of the TOF length (7 cm) so that $k_z \sim 2\pi/1\ \mathrm{cm}$. Note that ι scales inversely and quadratically with the wavelength λ_m of the mode. The axial force is constant along the fiber and limited by the ultimate material strength of $\sigma = 12$ GPa [99] at the thinnest point, i.e., the waist. The samples in the experiments are stressed to a large fraction of this ultimate limit, so that the axial force amounts to $F_{\text{ax}} \sim 1$ mN. The extremal values of the ratio are $\iota \sim 10^{-7}$ in the waist and $\iota \sim 10^2$ in the unprocessed part of the fiber. This demonstrates that the transversal waves are string-like in the waist region and undergo a transition to flexural waves with increasing radii in the fiber taper. This complex problem is solved numerically using a model based on the finite element method. The latter is described in the next section.

4.3 Finite element modeling

Finite element models (FEM) offer a higher flexibility when studying complex situations such as complex geometries, the effect of initial strain or non-homogeneous Young's modulus distributions caused by temperature gradients. Furthermore, they are free of assumptions or simplifications in the formulation of the problem. As a trade-off, they are restricted by the computational power which limits the accuracy of the model. By comparison, to the analytical approach is much less demanding in computational power but is restricted to basic geometries. However, analytic expressions are typically easier to interpret since they are not limited to the single simulated geometry. This shows that an FEM model is a useful asset which complements the analytic approach also in the prospect of future applications where more complex situations may be of interest.

The FEM model of the TOF is implemented in the commercial COMSOL software environment. In FEM models, the simulated body is discretized into small adjacent volumes, the so-called mesh, the sum of which constitutes an approximation of the body. The differential equation of the problem is then transformed to finite differences in the points where several elements touch (nodes) and evaluated along the edges of the volume elements, thereby allowing a numerical solution. Here, a two-step process is used to compute the eigenfrequencies: First, the equilibrium situation for the initial strains and stresses is computed. Then, a successive harmonic solver finds the vibrational eigenmodes of this equilibrium situation. The geometric nonlinearity is taken into account in this model.

The geometrical model is implemented as a CAD-drawing of the TOF which is constructed from cylinders, cones and a body with exponentially increasing radius. The latter is implemented as a body of rotation from the corresponding radius profile. As a boundary condition, the mode is restricted to zero displacement at both ends of the taper (z_4 in Fig. 4.2). The initial strain is taken into account by defining a homogeneous strain along the full fiber length. Its magnitude is given by the displacement after the fiber pulling process normalized to the model length. The correct strain profile is then produced after the first simulation step (equilibrium situation). This way, the total elongation of the TOF is neglected which, however, is small compared to the fiber length ≤ 1 %. In particular, the waist region is well-described because the taper sections contract to compensate the initial strain. As a consequence primarily the thinnest part of the TOF, i.e., the waist region, is strained and elongated which gives a good approximation of the experimental situation.

In FEM-modeling, the accuracy of the result strongly depends on the discretization, thereby making the mesh-generation one of the most important steps. Typically, one aims for volume elements with an aspect ratio near unity. This way, the numerical values along each line are similar in their numerical magnitude. Several quality measures can be defined to benchmark the mesh, such as the radius ratio of largest sphere that fits in the element and that of the smallest sphere that encompasses the element. For a high quality mesh these quality measures should be maximized to unity. For practical purposes it is sufficient to reach values of $\sim 10^{-2}$. Furthermore, the growth rate, that is the relative size of two neighboring elements, should be kept small [161]. The number of elements is, however, limited by increasing memory constrains and computation time.

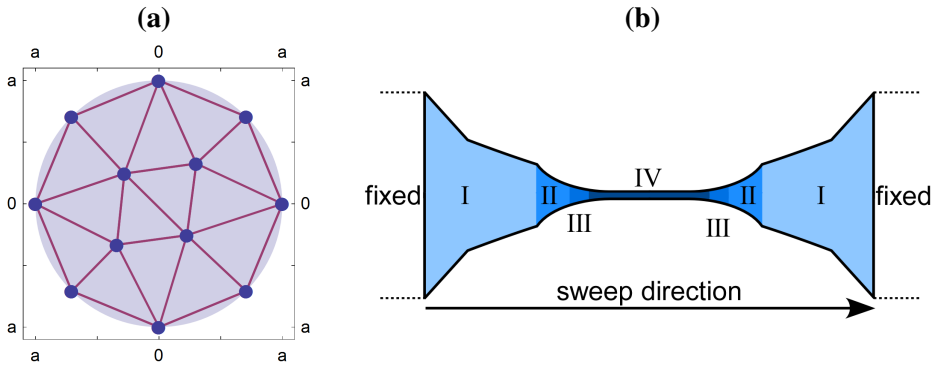

Figure 4.5: *(a) 2D-mesh at the front-face of the fiber (colored disk). (b) Schematical view of the meshing domains, indicated by different colors, used for the sweep rule.*

domain	number of axial copies	length
I	160	to exponential profile $\approx$24 mm
II	150	4.5 mm
III	700	3.2 mm
IV	2500	L_w + 4 mm

Table 4.2: *Parameters of the swept mesh for each meshing domain.*

The TOF's high aspect ratio of its length relative to its diameter complicates the mesh generation. Here, the commonly used automatic strategies yield either poor quality meshes or require a very high number of elements. I therefore employ a meshing strategy that takes the modal shape into account. As previously discussed, modes of the lowest radial and angular order are of interest in which the cross-section of the fiber stays basically undeformed. This is achieved by using a swept mesh for which, in a first step, a low resolution 2D-mesh is automatically generated for one end face of the fiber, see Fig. 4.5(a). This mesh is then copied in equidistant steps along the fiber axis while being scaled to the TOF diameter at the corresponding position. In order to generate a mesh of sufficient quality, the TOF is divided into different domains with individual axial element densities to take the large dynamical diameter range into account, see Fig. 4.5(b). The axial mesh density is strongly enhanced in the region of the exponential profile and the nanofiber waist where a rapid radius change occurs. The corresponding number of axial copies of the transverse mesh are given in Tab. 4.2 where region I ranges from the fixing point at the start/end of the taper to the exponential profile. With these values, a mesh consisting of 63000 elements is generated with an average and minimum quality of 0.04 and 0.003 respectively, and an average and maximum growth rate of 1.3 and 12 respectively. Using a 2x8 core dual XEON (2.4 GHz) computer, the problem can be solved for 500 eigenmodes with a memory consumption of $\approx$14 GB in 1 1/2 hours.

The FEM model does not distinguish between different mode types so that a post-selection scheme is necessary. For this purpose, the resulting displacement vector profiles

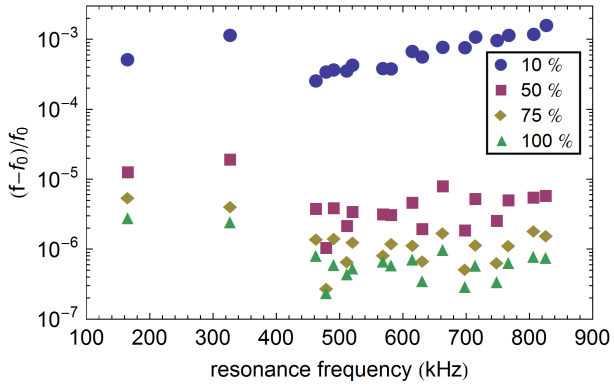

Figure 4.6: *Relative frequency deviation of the torsional modes compared to a simulation with* $\eta_{\mathrm{FEM}} = 1.5$*. The scaling parameter* η_{FEM} *is given in the legend. Radius profile: TOF-M1.*

of all modes are evaluated in a line on the surface of the fiber. The torsional and compressional modes are discriminated from the transversal modes by their vanishing radial displacement component. The torsional wave can then be distinguised from the compressional wave by its vanishing axial displacement component.

To check the modeling accuracy, the simulation is performed with different axial element densities. For this purpose, the number of axial copies in each section, given in Tab. 4.2, is multiplied by a constant factor η_{FEM}. The resonance frequencies obtained from each of these simulations are then compared to a reference simulation with the high axial element density $\eta_{\mathrm{FEM}} = 1.5$ using

$$\frac{f - f_0}{f_0} = \frac{f(\eta_{\mathrm{FEM}} = X) - f(\eta_{\mathrm{FEM}} = 1.5)}{f(\eta_{\mathrm{FEM}} = 1.5)} \,.$$

The result is plotted for the torsional resonance frequencies in Fig. 4.6. Comparing the result obtained with $\eta_{\mathrm{FEM}} = 0.1$ to that with $\eta_{\mathrm{FEM}} = 0.5$, an accuracy improvement of two orders of magnitude can be observed. When comparing the results obtained with $\eta_{\mathrm{FEM}} > 0.5$ the deviations are already smaller than those resulting from the fabrication uncertainties of the TOF profile. With that the model is converged to a relative accuracy of higher than 10^{-5} for $\eta_{\mathrm{FEM}} = 1$ which will be used in the following.

4.3.1 Resonance frequency prediction by the FEM and analytical model

The frequency predictions for the compressional and torsional nanofiber modes of both models are compared in Fig. 4.7. Both theories show resonances with comparatively large frequency spacing below the ω^{co} which are followed by closely spaced resonances beyond ω^{co} as expected from the previous considerations concerning the torsional horn. When comparing both theories one observes that the FEM-model predicts $1.5\ \%$ and $4\ \%$ higher frequencies for two lowest order torsional and compressional modes, respectively. Furthermore, the resonance frequencies beyond ω_{co} differ substantially. These differences

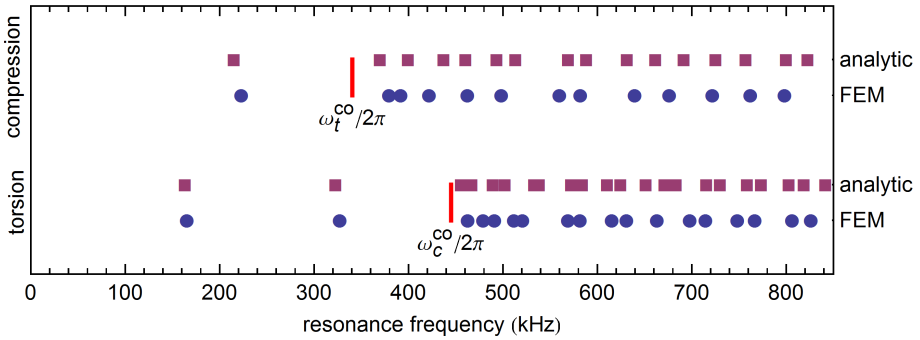

Figure 4.7: *Resonance frequencies of the compressional and torsional nanofiber modes predicted by both models. The resonances are marked by points and the corresponding cut off frequencies of the exponential horn by red lines. For clarity, the taper modes are not displayed. Radius profile: TOF-M1*

can be explained by the fact that the FEM-model takes the axial strains in the taper regions into account which yields an increase of the phase velocity and the transversal contraction. Both effects are only partially considered in the analytic model. Beside that, both theories predict the fundamental modes with good precision and reproduce the features of the spectrum in good qualitative agreement.

4.4 Thermal motion of a fiber

The Brownian motion of the atoms in the material results in fluctuating forces that can excite the mechanical modes of the TOF. The response of the nanofiber to these thermal fluctuations can be calculated from the fluctuation-dissipation theorem (see also Eq. (3.8)) where the spectral response function of the system $\chi(\omega)$ is related to the power spectral density of the displacement. The classical approximation ($\hbar\omega \gg k_{\mathrm{B}}T$) holds at room temperature for the mechanical frequencies considered here. As a consequence, the fluctuation-dissipation theorem can be used in its classical limit

$$S_\phi = \frac{4\,k_{\mathrm{B}}\,T}{\omega}\,\mathrm{Im}\,(\chi)\ . \tag{4.31}$$

Here, the convention of the one-sided power spectral density is used where both the negative and positive frequencies are considered by ω (hence the factor 2 with respect to Eq. (3.8)). Furthermore, the equations in this section are given in complex notation to keep the expressions simple. The real-valued amplitudes are obtained by applying boundary conditions or taking the real part of the wave function. Note that some care has to be taken when computing the energy densities because the formulation given above is only valid for real valued amplitudes.

The spectral acceptance of the TOF to torque is derived from the wave equation Eq. (4.12). For this purpose, the dissipation is included via the loss angle ξ and a torque density $M(t,z)$ is added as a source term [162, 163]:

$$-\partial_t^2\,u_\phi(t,z)+(1+\mathbb{i}\xi)\,c_t^2\left[\,\partial_z^2\,u_\phi(t,z)+\frac{\partial_z I_p(z)}{I_p(z)}\,\partial_z u_\phi(t,z)\,\right]=I_p^{-1}(z)\,M(t,z)\ . \tag{4.32}$$

This equation is separable in time and space and can be solved using the ansatz $u_\phi(t,z) = \sum_n \phi_{0,n}\,\phi_n(z)\,\exp(\mathbb{i}\omega t)$. The differential operator of the spatial differential equation is self-adjoint (proof see below) so that a complete set of orthogonal spatial eigenmodes can be found with respect to the product

$$\int_0^L \mathrm{d}z\,I_p(z)\,\phi_n(z)\phi_m(z)=I_{\mathrm{eff,n}}\,\delta_{mn}\ . \tag{4.33}$$

In the next step, the frequency response function of the system to a driving torque $M(t,z) = M(z)\,\exp(\mathbb{i}\omega t)$ is determined. Fur this purpose, the equation is multiplied from the left side with $I_p(z)\,\phi_n(z)$ and integrated over the length. Taking into account that the spatial part yields the eigenvalue and the modes are orthogonal one obtains:

$$\omega^2\,\phi_{0,n}-(1+\mathbb{i}\xi)\,c_t^2\,k_{0,n}^2\,\phi_{0,n}=I_{\mathrm{eff,n}}^{-1}\int_0^L \mathrm{d}z\,\phi_n(z)\,M(z)\ .$$

Now, the source term is decomposed in the basis of the eigenmodes that are weighed by the normalized (dimensionless) polar moment of inertia $M(z) = \sum_n M_n\,\phi_n(z)\,I_p(z)/I_{\mathrm{eff,n}}$. It follows that

$$\omega^2\,\phi_{0,n}-(1+\mathbb{i}\xi)\,\omega_{0,n}^2\,\phi_{0,n}=I_{\mathrm{eff,n}}^{-1}\,M_n\ ,$$

where $\omega_{0,n}^2 = c_t^2\, k_{0,n}^2$. This shows that the frequency response of the torsional motion of a string can be treated as a that of a torsional pendulum with the amplitude $\phi_{0,n}$ and a (mode dependent) effective moment of inertia $I_{\mathrm{eff,n}}$. The frequency response function of each eigenmode is now extracted by solving for $\phi_{0,n}$ and by dividing by the driving torque:

$$\chi_n = \frac{\phi_{0,n}}{M_n} = \frac{1}{I_{\mathrm{eff,n}}}\,\frac{1}{\omega^2 - \omega_{0,n}^2 - \mathrm{i}\,\omega_{0,n}^2\,\xi} = \frac{1}{I_{\mathrm{eff,n}}}\,\frac{\omega^2 - \omega_{0,n}^2 + \mathrm{i}\,\omega_{0,n}^2\,\xi}{(\omega^2 - \omega_{0,n}^2)^2 + \omega_{0,n}^4\,\xi^2}\,. \tag{4.34}$$

Using this result together with Eq. (4.31) the power spectral density of the displacement is given by

$$S_{\phi(z)}(\omega) = 4\,k_{\mathrm{B}}\,T\,\sum_{n=1}^{\infty}\,\frac{\phi_n^2(z)}{I_{\mathrm{eff,n}}\,\omega}\,\frac{\omega_{0,n}^2\,\xi}{(\omega^2 - \omega_{0,n}^2)^2 + \omega_{0,n}^4\,\xi^2}\,. \tag{4.35}$$

Thus, the power spectrum of each resonance is a Lorentzian multiplied with an additional factor of $1/\omega$. This is a consequence of the constant dissipation term that was included in the differential equation. However, this approximation is only valid for frequencies near the resonance and yields unphysical results when kept constant for the full spectrum. It gives rise to a singularity in the static case so that the frequency integral of $S_\phi(\omega)$ diverges, corresponding to an infinite amount of energy stored in each mode. For high-Q resonators, the approximation is valid for the spectral region in which most of the energy is stored, i.e., near the resonance frequency, and it is sufficient to consider several peak widths in the integration [162]. The variance of the maximum displacement amounts to

$$\left\langle \phi_{0,n}^2 \right\rangle = \frac{k_{\mathrm{B}}T}{\omega_{0,n}^2 I_{\mathrm{eff,n}}}\,. \tag{4.36}$$

This result can also be obtained by computing the modal energy at the resonance frequency, corresponding to the high-Q approximation, and using the equipartition theorem.

Based on these results, the power spectral density can be expressed in terms of the variance and a frequency-dependent term which is valid in the spectral region close to the resonance frequency where ξ is constant:

$$S_{\phi_{0,n}}(\omega) = \frac{4\left\langle \phi_{0,n}^2 \right\rangle}{\omega}\,\frac{\xi}{([\omega/\omega_{0,n}]^2 - 1)^2 + \xi^2}\,, \tag{4.37}$$

where the maximum value is reached at the resonance frequency

$$S_{\phi_{0,n}}(\omega_{0,n}) = \frac{4\,Q}{\omega_{0,n}}\left\langle \phi_{0,n}^2 \right\rangle\,. \tag{4.38}$$

The variance of the displacement amplitude is given by the integral of the power spectral density and is independent of the Q-factor.

Paralleling this derivation, the thermal displacement of the string modes as well as that of the compressional modes can be computed. Both wave equations are formulated in terms of force per unit length with a source term and results in the same relation:

$$\langle \phi_{0,n}^2 \rangle = \frac{k_{\mathrm{B}}T}{\omega_{0,n}^2 M_{\mathrm{eff,n}}}\,, \quad \text{with} \quad M_{\mathrm{eff,n}} = \int_0^L \mathrm{d}z\,\rho\,S_c(z)\,u_{z,n}^2(z)\,, \tag{4.39}$$

where $M_{\mathrm{eff,n}}$ is the effective mass of the mode with index n. Here, the equivalence of the different types of harmonic oscillators manifests: The effective moment of inertia is replaced by an effective mass when the wave equation in terms of torque is replaced by one in terms of force. One may wonder why such different types of vibrations apparently yield the same expression for the thermal displacement. Despite the formal similarities, it becomes clear that the results will differ strongly when taking the sound velocity as well as the modal shapes into account.

4.4.1 Displacement fluctuations of a tapered optical fiber

Combining the results from the previous chapter with the analytic model, supplying resonance frequencies and effective moments of inertia, the thermal displacement of the TOF can be computed. In the case of TOF-M4, the fundamental torsional mode has a frequency of 288.6 kHz with $I_{\mathrm{eff}} = 4.6 \cdot 10^{-26}\,\mathrm{kg\,m^2}$. The modes beyond $\omega_{co} \approx 2\pi \cdot 450$ kHz exhibit a considerably higher $I_{\mathrm{eff}} \sim 4 \cdot 10^{-25}\,\mathrm{kg\,m^2}$ which is due to the fact that an increasing part of the taper section participate in the oscillation and contribute with their higher moment of inertia. With these values the standard deviation of the angular displacement yields $\langle \phi_{0,n}^2 \rangle^{1/2} = 1.7 \cdot 10^{-4}$ for the fundamental mode and $\sim 2 \cdot 10^{-5}$ for the higher order modes at room temperature (300K).

For the compression modes, the effective mass for the fundamental axial mode at 328.6 kHz is $M_{\mathrm{eff}} = 3 \cdot 10^{-12}$ kg. Again, the effective mass yields higher values of $M_{\mathrm{eff}} \sim 2 \cdot 10^{-11}$ kg for the modes with frequencies higher than $\omega_{co} \approx 2\pi \cdot 340$ kHz. The thermal displacements at room temperature is on the order of $\langle u_z^2 \rangle^{1/2} = 10$ pm and $(2 - 10)$ pm for the higher order modes.

Nanofibers are employed in a temperature range from the cryogenic [58] up to near the melting point of the silica [164]. The thermal displacement scales with the square root of the temperature so the thermal amplitude, starting from room temperature, decreases by a factor $\sim 1/10$ towards 4 K and increases by a factor ~ 3 towards temperatures near the melting point of fused silica.

The thermal amplitude coefficients also depend on the length of the nanofiber. Consider the simplified case of a homogeneous cylinder: The effective mass as well as the effective moment of inertia scale linearly with the fiber length $I_{\mathrm{eff,n}}, M_{\mathrm{eff,n}} \propto L$ (see Eqns. (4.33) and (4.39)) while the resonance frequency scales inversely proportional $\omega_{0,n} \propto L^{-1}$ so that the amplitude scales as

$$\sqrt{\left\langle \phi_{0,n}^2 \right\rangle} \propto \sqrt{L}\,. \tag{4.40}$$

Note that the situation is more complex in the case of the TOF but the taper design is typically kept identical for all nanofiber lengths and may be included in good approximation by adding a constant, effective length.

4.5 Influence of mechanical vibrations on the optical nanofiber mode

The mechanical vibrations cause a periodic strain which induces anisotropy in the silica due to the strain-optic effect. This chapter is concerned with the effect on the polarization and propagation constant of the fundamental optical nanofiber mode. First, the refractive index variation due to the strain is computed using Pockel's tensor formalism. These results are used to evaluate the change of the propagation constant of different polarization states of the mode. The theoretical treatment is restricted to the nanofiber section, i.e., a fused silica cylinder. This simplified model yields a good approximation of the mechanical TOF mode since the largest displacements occur in the nanofiber region. Furthermore, it yields a prediction of the order of magnitude of the effect and allows one to gain a qualitative understanding.

4.5.1 Strain-optic effect

When silica is subject to strain, it changes its refractive index and becomes birefringent due to the strain-optic effect. Mathematically, the strain-optic effect is described by relating the change of the impermittivity tensor $\boldsymbol{\delta\eta}$, to the material strain by Pockel's tensor $\boldsymbol{p}$ [63, 165]

$$(\boldsymbol{\delta\eta})_{ij} = \boldsymbol{p}_{ijkl}\boldsymbol{s}_{kl} \ . \tag{4.41}$$

The modified dielectric (permittivity) tensor follows from $\boldsymbol{\epsilon} = (\boldsymbol{\epsilon}^{-1}+\boldsymbol{\delta\eta})^{-1}$. The material response to strain depends on its structure which may be amorphous or crystalline. In the case of an amorphous solid, it can be expressed in contracted notation as [166]

$$\boldsymbol{p} = \begin{bmatrix} p_{11} & p_{12} & p_{12} & & & \\ p_{12} & p_{11} & p_{12} & & 0_{3\times 3} & \\ p_{12} & p_{12} & p_{11} & & & \\ & & & p_{44} & 0 & 0 \\ & 0_{3\times 3} & & 0 & p_{44} & 0 \\ & & & 0 & 0 & p_{44} \end{bmatrix} \tag{4.42}$$

where $p_{11} = 0.12$, $p_{12} = 0.27$ and $p_{44} = (p_{11} - p_{12})/2 = -0.073$ are photoelastic constants of fused silica [167].

The resulting symmetric and real valued impermittivity tensor can be diagonalized and the corresponding eigenvectors remain unchanged when inverting this tensor. This in particular means, that waves with their (electric) field amplitude oriented along these vectors encounter a single refractive index which is derived from the corresponding eigenvalue. In other terms, the electric field is proportional to the electric displacement field $\boldsymbol{E} \propto \boldsymbol{D}$ where the proportionality constant is given by the eigenvalue (squared in case of the refractive index).

Example: Stress along one axis

It is instructive to evaluate the material response to a stress along one axis, say the z-axis: $\boldsymbol{\sigma} = \begin{bmatrix} 0 & 0 & \sigma_z & 0 & 0 & 0 \end{bmatrix}$. After computing the strain according to Eq. (4.8) and applying Eq. (4.41), the change of the impermettivity tensor results to

$$\delta\eta = \sigma_z / E_Y \begin{bmatrix} -2\nu(p_{11}+p_{12}) + p_{12} & -2\nu(p_{11}+p_{12}) + p_{12} & p_{11} - 2\nu\, p_{12} & 0 & 0 & 0 \end{bmatrix} ,$$

and thereby remains diagonal, i.e., the last three components are zero. Two different values are found for the direction parallel to the strain and those perpendicular to it. One can compute the refractive index change using the relation for diagonal impermittivity tensors and small changes $\delta n_{ll} = -n_{ll}^3\, \delta\eta_{ll}/2$, yielding

$$\Delta n_{\parallel} = \delta n_{33} = -\frac{\sigma_z}{E_Y}\, \frac{n_0^3}{2} (p_{12} - \nu\,(p_{11} + p_{12})) \tag{4.43a}$$

$$\Delta n_{\perp} = \delta n_{11} = \delta n_{22} = -\frac{\sigma_z}{E_Y}\, \frac{n_0^3}{2} (p_{11} - 2\,\nu\, p_{12}) \,. \tag{4.43b}$$

The material becomes birefringent with the two principal directions oriented parallel and perpendicular to the stress direction, respectively. This result should be kept in mind because it often allows one to gain an intuitive understanding when analyzing the strain-optic effect.

Due to the pre-tensioning of the fiber, an initial axial stress of a few percent of the Young's modulus $\sigma_z \approx 1\ \%\ E_Y$ is present during the experiment. This modifies the refractive index of the fiber by $\Delta n_{\parallel} = 9.3 \cdot 10^{-3}$ and $\Delta n_{\perp} = 5.8 \cdot 10^{-3}$. This anisotropy results in an optical path length change which is independent of the polarization state of the guided mode.

4.5.2 Birefringence caused by the mechanical modes of the fiber

In the following, the material response in form of refractive index changes to torsional and compression waves in a fiber is derived. For this purpose, first the strain caused by a mode with a sinusoidal amplitude profile is computed which is then used in the Pockel's formalism (compare Eq. (4.41)) to predict the modification of the impermittivity tensor of the nanofiber.

Torsional wave

Assuming a standing torsional wave in a homogeneous cylinder of length L, the amplitude profile takes the form

$$\boldsymbol{u} = \underbrace{\phi_{0,n}\, \cos(\omega_n\, t)}_{\phi_{0,\omega,n}} \sin(k_n\, z) \begin{pmatrix} -y & x & 0 \end{pmatrix} , \tag{4.44}$$

where $z \in [0, L]$ is the axial position, $k_n = n\pi/L$ is the mechanical wave number, n is the mode index, and $\omega_n = c_t\, k_n$ is the eigenfrequency of the mode. The strain tensor

including the geometric nonlinearity is computed according to Eq. (4.3) :

$$\boldsymbol{s} = \frac{1}{2}\begin{bmatrix} \phi_{0,\omega,n}^2\,\sin^2(k_n\,z) \\ \phi_{0,\omega,n}^2\,\sin^2(k_n\,z) \\ \phi_{0,\omega,n}^2\,k_n^2\,(x^2+y^2)\cos^2(k_n\,z) \\ 0 \\ \phi_{0,\omega,n}\,k_n\,\cos(k_n\,z)\,[-y + x\,\phi_{0,\omega,n}\sin(k_n\,z)] \\ \phi_{0,\omega,n}\,k_n\,\cos(k_n\,z)\,[x + y\,\phi_{0,\omega,n}\sin(k_n\,z)] \end{bmatrix} \tag{4.45a}$$

$$\approx \frac{1}{2}\begin{bmatrix} \phi_{0,\omega,n}^2\,\sin^2(k_n\,z) \\ \phi_{0,\omega,n}^2\,\sin^2(k_n\,z) \\ 0 \\ 0 \\ \phi_{0,\omega,n}\,k_n\cos(k_n\,z)\,[-y + x\,\phi_{0,\omega,n}\sin(k_n\,z)] \\ \phi_{0,\omega,n}\,k_n\cos(k_n\,z)\,[x + y\,\phi_{0,\omega,n}\sin(k_n\,z)] \end{bmatrix} \tag{4.45b}$$

where the 3rd term (33-component) is neglected because it is a factor $(k_n\,r)^2 \lesssim 10^{-8}$ smaller than the remaining strains. Note that all terms proportional to $\phi_{0,\omega,n}^2$ oscillate with twice the frequency of the mechanical motion. The strain caused by thermal excitation of the fundamental torsional mode in a 5 mm long fiber ($\phi_0 \approx 1.7 \cdot 10^{-4}$) is on the order of $s \sim 10^{-8}$. From Eq. (4.41) the change of the impermittivity follows

$$\boldsymbol{\delta\eta} = \frac{1}{2}\begin{bmatrix} \phi_{0,\omega,n}^2\,(p_{11}+p_{12})\,\sin^2(k_n\,z) \\ \phi_{0,\omega,n}^2\,(p_{11}+p_{12})\,\sin^2(k_n\,z) \\ \phi_{0,\omega,n}^2\,2\,p_{12}\,\sin^2(k_n\,z) \\ 0 \\ -p_{44}\,\phi_{0,\omega,n}\,k_n\cos(k_n\,z)[y - x\,\phi_{0,\omega,n}\sin(k_n\,z)] \\ p_{44}\,\phi_{0,\omega,n}\,k_n\cos(k_n\,z)[x + y\,\phi_{0,\omega,n}\sin(k_n\,z)] \end{bmatrix}. \tag{4.46}$$

Based on this result, a birefringence of the axial with respect to both transversal directions ($\boldsymbol{\eta}_{11} = \boldsymbol{\eta}_{22} \neq \boldsymbol{\eta}_{33}$) is found. The mixed impermittivity contributions, $\boldsymbol{\eta}_{13}$ and $\boldsymbol{\eta}_{23}$, are approximately one order of magnitude smaller than the first three components: $(p_{11} + p_{12})\,\phi_{0,\omega,n} \sim 10^{-4}$ and $p_{44}\,\{k_n\,x, k_n\,y\} \sim 10^{-5}$. They are, therefore, not negligible. Furthermore, the sinusoidal terms in components $\boldsymbol{\eta}_{13}$ and $\boldsymbol{\eta}_{23}$ are much smaller than the first term in the same bracket due to the very small amplitude $\phi_{0,\omega,n} \sim 10^{-4}$. Nevertheless, they cannot be neglected because the two terms contribute at different spatial positions.

This rather complex situation is analyzed by plotting the eigenvectors of the permittivity tensor ($\boldsymbol{\epsilon} = (\boldsymbol{\eta}_{SiO_2} + \boldsymbol{\delta\eta})^{-1}$) in Fig. 4.8. A wave with the electric field oriented along each of these directions experiences the corresponding refractive but is unmodfied otherwise. In other words, the E-field along each of the principal directions is proportioal to the D-field along the same direction. The torsion gives rise to a helical anisotropy that vanishes at the node of the mechanical mode. The remaining principal direction is oriented in the radial direction. Comparing this result with Eq. (4.46) it becomes apparent that the last two components of $\boldsymbol{\delta\eta}$ result in the helical orientation of the principal permittivities, because they mix the transversal field components with the axial component. The helical anisotropy of the contorted fiber has the two quasi-circularly polarized optical modes as eigenmodes. They exhibit a different propagation constant which will be computed in Ch. 4.5.3.

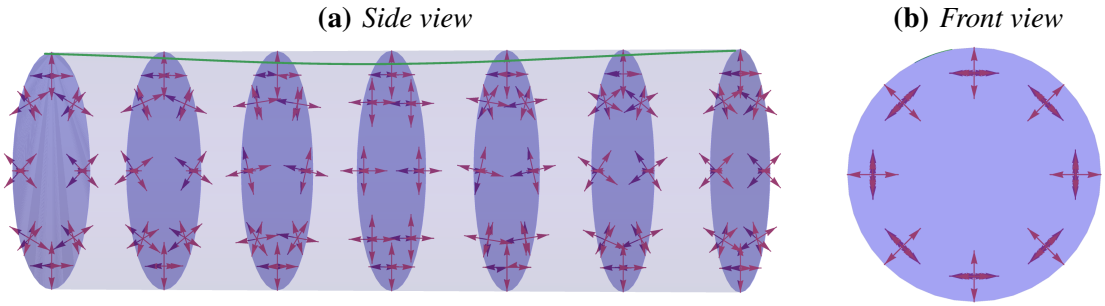

Figure 4.8: *Principal permittivity directions caused by a thermally excited torsional mode at the time of maximum displacement which is evaluated at several positions along the fiber axis. An exaggerated displacement profile is indicated by a green line on the surface of the fiber. The length of the fiber is $L = 5$ mm.*

Compressional wave

Up to now, only the axial displacement of the compressional waves is known from the wave equation, see Eq. (4.27). In order to compute the strain, the transversal displacements have to be derived from Hooke's law. The latter relates the transverse to the axial strains: $s_\perp = -\nu\,\sigma_\parallel/E_Y = -\nu\,s_\parallel$. The displacements caused by the thermal excitation of few picometers are sufficiently small to use the linear strain theory so that $\boldsymbol{u}_x = x\,\boldsymbol{s}_x = -x\,\nu\,\partial_z \boldsymbol{u}_z$ and for the y-component accordingly. Consider, again, a standing wave in a homogeneous cylinder of length L which has a sinusoidal amplitude profile of the form $\boldsymbol{u}_z = u_0\,\cos(\omega\,t)\,\sin(k_n\,z)$ so that the full displacement vector is given by

$$\boldsymbol{u} = \underbrace{u_0\,\cos(\omega\,t)}_{u_{0,\omega}} \begin{pmatrix} -x\,\nu\,\cos(k_n\,z) & -y\,\nu\,k_n\,\cos(k_n\,z) & \sin(k_n\,z) \end{pmatrix}, \tag{4.47}$$

causing strains of the form

$$\boldsymbol{s} = \frac{1}{2}\begin{bmatrix} -2\nu\,u_{0,\omega}\,k_n\,\cos(k_n\,z) \\ -2\nu\,u_{0,\omega}\,k_n\,\cos(k_n\,z) \\ 2u_{0,\omega}\,k_n\,\cos(k_n\,z) \\ 0 \\ x\,u_{0,\omega}\,\nu\,k_n^2\,\sin(k_n\,z) \\ y\,u_{0,\omega}\,\nu\,k_n^2\,\sin(k_n\,z) \end{bmatrix}. \tag{4.48}$$

The strain is antisymmetric in z with respect to the fiber center at $z = L/2$, corresponding to the cosine terms. When thermally excited, the magnitude of the strain is on the order of $s \sim 4 \cdot 10^{-9}$ for the fundamental mode ($u_z \sim 10$ pm) . The resulting impermittivity change is

$$\boldsymbol{\delta\eta} = u_{0,\omega}\,k_n \begin{bmatrix} (p_{12} - \nu[p_{11} + p_{12}])\,\cos(k_n\,z) \\ (p_{12} - \nu[p_{11} + p_{12}])\,\cos(k_n\,z) \\ (p_{11} - 2\nu\,p_{12})\,\cos(k_n\,z) \\ 0 \\ x\,p_{44}\,\nu\,k_n\,\sin(k_n\,z)\,/2 \\ y\,p_{44}\,\nu\,k_n\,\sin(k_n\,z)\,/2 \end{bmatrix}. \tag{4.49}$$

In contrast to the torsional waves, the last two terms (13- and 23-component) are much smaller than the first three terms due to the additional factors $k_n\, x \sim k_n\, y \sim 10^{-4}$. As a direct consequence, the principal axes of the refractive index are given by the fiber axis and two directions in the fiber cross section, the latter having equal refractive indices. This finding shows that the compressional waves will have no effect on the polarization of the guided light.

4.5.3 Effect on the fundamental optical nanofiber mode

Here, the effect of the mechanical modes on the fundamental optical nanofiber mode is derived. This is achieved by evaluating the change of the propagation constants of two optical polarization states as function of the axial position along the nanofiber. The small permittivity changes caused by the thermally excited mechanical modes leave the field distribution of the fiber mode essentially unmodified. As a consequence, a perturbative treatment can be used as derived in Ch. A.2.

In this approximation of small permittivity changes, the propagation constant change of the optical mode is given by

$$\Delta\beta = k_0 \sqrt{\frac{\epsilon_0}{\mu_0}}\, \frac{\int_{A_\infty} \boldsymbol{E} \cdot \Delta\boldsymbol{\epsilon} \cdot \boldsymbol{E}^* \,\mathrm{d}A}{2 \int_{A_\infty} Re\left[\boldsymbol{E} \times \boldsymbol{H}^*\right] \cdot \hat{\boldsymbol{z}} \,\mathrm{d}A} \,, \tag{4.50}$$

compare Eq. (A.18). From the impermittivity changes derived above, the permittivity of the fiber can be computed as function the position via $\boldsymbol{\epsilon}(\boldsymbol{r}) = [\boldsymbol{\eta}_0(\boldsymbol{r}) + \boldsymbol{\delta\eta}(\boldsymbol{r})]^{-1}$, where $\boldsymbol{\eta}_0(\boldsymbol{r})$ is the permittivity of the unstrained nanofiber. For the following calculations, the two quasi-circularly polarized fields HE_{11}-modes are chosen because of the helical birefringence induced by the torsional mode. The compressional mode induces no helical anisotropy but also none that could induce an asymmetry concerning the quasi-linearly polarized mode so that one is free to choose the polarization basis for the analysis. Then the propagation constant change $\Delta\beta_\pm(z)$ is numerically computed as function of the axial position using the field distribution of the clockwise (+) and counter-clockwise (-) quasi-circularly polarized HE_{11}-mode.

Torsional mode

The result for a thermally excited torsional vibration of a 5 mm long silica cylinder is shown in Fig. 4.9(a) in the form of the effective refractive index change $\Delta n_{\mathrm{eff},\pm} = \Delta\beta_\pm / k_0$. The change is on the order of $\Delta n_{\mathrm{eff},\pm} \sim 10^{-8}$ and basically scales with $\phi^2_{0,\omega,n}$ so that it is essentially positive and oscillates with twice the mechanical frequency. The variation of $\Delta n_{\mathrm{eff},\pm}$ becomes maximal at the two ends of the fiber. This is a result of the zero displacement boundary condition which allows high strains that are compensated by the supports. Note that in case of the TOF, most amplitude profiles decrease towards the fixing points so that $\Delta n_{\mathrm{eff},\pm}$ approaches zero.

Comparing the results for the two polarization states, a difference on the order of 10 % of the full signal can be observed which is plotted in Fig. 4.9(b). This difference results from the contributions that scale linearly with the mechanical amplitude. Furthermore,

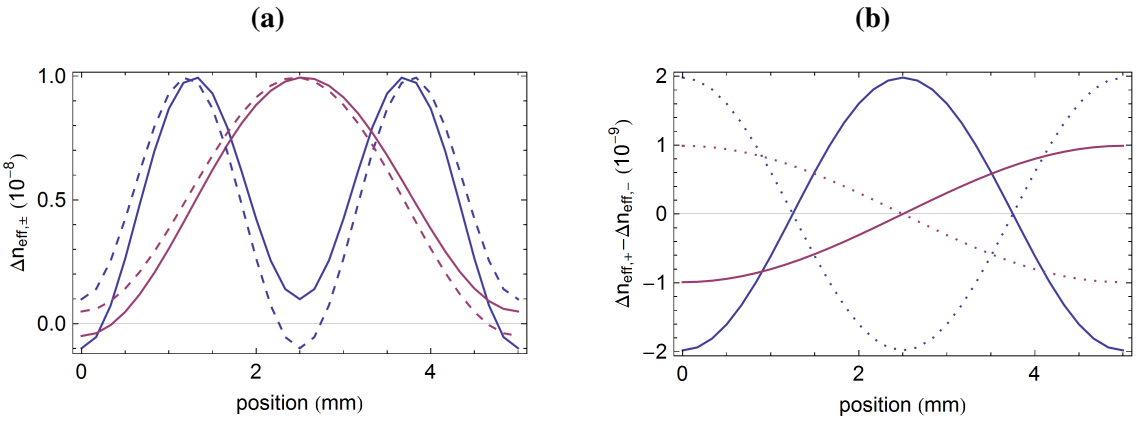

Figure 4.9: *(a) Effective refractive index variation as function of the axial position caused by the thermally excited fundamental (purple) and second harmonic (blue) torsional mode at the time of maximum positive deflection. The two quasi-circularly polarized modes are shown as solid and dashed lines, respectively. When using the negative amplitude, the two modes interchange their role (dashed and solid lines interchange). (b) Difference of the effective refractive index variation of the two circularly polarized modes (solid and dashed lines in (a)) at the time of maximum positive (solid lines) and maximum negative deflection (dotted lines). Maximum thermal displacement* $1.7 \cdot 10^{-4}$ *rad.*

$\Delta n_{\mathrm{eff},+} - \Delta n_{\mathrm{eff},-}$ is, when considering the individual sections between two nodes, an antisymmetric function in the axial position with respect to the position of the antinode. This can be intuitively understood by comparing the sense of rotation about the fiber axis of the quasi-circulary polarized mode to that of the principal strains along the fiber. The optical mode is approximately constant along the fiber while the strain follows the slope of the displacement and changes its sense of rotation at each antinode. Consider two arbitrary points of both sides of and with equal distance to an antinode. The strains at both points are of same magnitude but are oriented mirror symmetrically with respect to the antinode. Since the two polarization states have opposite sense of rotation they interchange their role at both points. Note that the anisotropy is created between the direction of the strain and perpendicular to it.

From these considerations, one finds that both polarization states experience the same change in their propagation constant on mirror symmetric points around an antinode. As a consequence, the net relative phase shift of the two modes is zero when integrated over the length of the fiber waist so that no signal occurs in an ideal system. However, small fabrication imperfections can cause asymmetries that give rise to a polarization signal. Measurements of the radius profile that were carried out using the fibers from the pulling rig in our group have shown that small radius variations occur along the fiber axis with a relative magnitude of $\approx 1\ \%$ [13]. I will brielfy present one of the mechanism that cause these variations. For this purpose, consider the last step of the tapering process (cf. Ch. 1.4.1): After the fiber is tapered to its final radius profile, the translations stages stop and a short time passes until the flame is retracted. During that time, the fiber glass is still malleable subject to gravitation so that the fiber sags. This results in a small radius

deformation with a width that is on the order of the flame width (≈ 1 mm) occurs.

Now, the additional phase accumulated by the optical mode is quantified. For this purpose, first the maximum phase difference between the two circularly polarized modes is computed that is caused by the fundamental torsional mode. It occurs at the antinode (fiber center) and can be obtained by integrating the propagation constant. This is done as function of the maximum amplitude ($\phi_{0,\omega,n}$) which yields the linear relation

$$\Delta\gamma_{\mathrm{tor,rel}} = \int_0^{L/2} (\Delta\beta_+ - \Delta\beta_-)\,\mathrm{d}z = 6.8 \cdot 10^{-2}\,\phi_{0,\omega,n} =: \chi_{\mathrm{tor,rel}}\,\phi_{0,\omega,n}\ . \tag{4.51}$$

A non-vanishing difference between propagation constant of the two (quasi-) circular polarizations $\Delta\beta_+ - \Delta\beta_- \neq 0$ corresponds to chiral birefringence. When a linearly polarized mode encounters such a medium the polarization axis rotates by an angle

$$\Delta\theta_{\mathrm{tor,pol}} = \frac{1}{2}\int \mathrm{d}z\,(\Delta\beta_+ - \Delta\beta_-)\ . \tag{4.52}$$

As a direct consequence, the quasi-linearly polarized light field rotates it polarization axis forth and back along the contorted fiber with maximum rotation angles at the antinodes. After traversing the full length of the fiber, the polarization axis returns to its initial direction. The standard deviation of $\Delta\theta_{\mathrm{tor,pol}}$ at the center of a TOF with a 5 mm long nanofiber waist due to the thermal motion of the fundamental torsional motion, see Ch. 4.4.1, is

$$\langle \Delta\theta^2_{\mathrm{tor,pol}} \rangle^{1/2} = 5.8 \cdot 10^{-6}\ . \tag{4.53}$$

The total phase variation of the modes amounts to:

$$\Delta\gamma_{\mathrm{tor,abs}} = \int_0^{L/2} \Delta\beta_\pm\,\mathrm{d}z \approx 3.17 \cdot 10^3\,\phi^2_{0,\omega,n} =: \chi_{\mathrm{tor,abs}}\,\phi^2_{0,\omega,n}\ . \tag{4.54}$$

which is nearly independent of the polarization state. Note that after passing the full length of the fiber, the total phase acquired amounts to twice this value.

In standing wave patterns produced by counter propagating light beams, this effect results in variations of the axial node and antinode positions. This is a consequence of the position-dependent refractive index and yields different values depending on the axial position. In particular, it vanishes at the fiber center because both beams acquire the same phase while traversing half the fiber.

The additional phase can also be expressed as a change of the optical path length:

$$\Delta L_{\mathrm{opt}} = \Delta\gamma_{\mathrm{tor,abs}}/k_0 \tag{4.55}$$

Such an optical path length change can be detected using a resonator where the optical path length variation changes the free spectral range and the resonance frequencies, accordingly.

Compressional mode

The corresponding analysis is carried out for the compressional mode and the resulting effective refractive index change is shown in Fig. 4.10. The effective refractive index

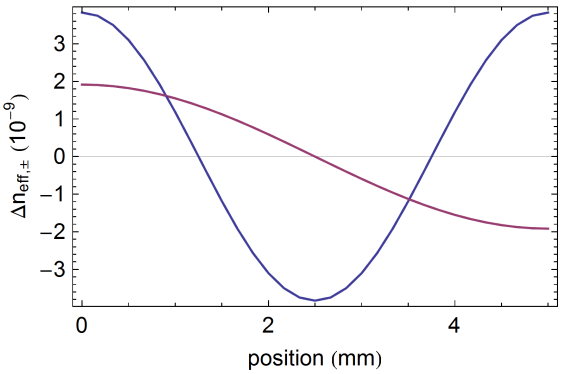

Figure 4.10: *Variation of the effective refractive index of both circularly polarized HE_{11}-modes caused by the fundamental (red) and second harmonic (blue) of the compressional modes. Amplitude: $\phi_0 = 1.7 \cdot 10^{-4}$ rad*

change is on the order of $\Delta n_{\text{eff}} \sim 10^{-9}$ but shows no polarization dependence. This is due to the fact that no birefringence occurs which breaks the symmetry in the two helical (circular polarization) or transversal (linear polarization) directions, as discussed above. Furthermore, the total optical path length change of the fiber adds up to zero. This is due to the symmetry of mode in which compressional and elongation, i.e. positive and negative axial strain, occur in equal measure. Note that, in a standing wave configuration, the maximum position variation of the antinodes occurs at the center of the fiber.

The additional phase caused by the fundamental compressional mode is independent of the polarization and amounts to

$$\Delta\gamma_{\text{comp,abs}} = \left| \int_0^{L/2} \Delta\beta_\pm \, \mathrm{d}z \right| = 36 \, \phi_{0,\omega,n}^{\max} \frac{1}{\mathrm{m}} =: \chi_{\text{comp,abs}} \, \phi_{0,\omega,n} \, . \tag{4.56}$$

Length scaling

In the following, the scaling of phase variations with the fiber length is discussed. An intuitive understanding can be reached by comparing the displacement amplitude scaling of the individual terms in $\delta\eta$ to that of the additional phase $\Delta\gamma$. Consider the torsional waves: Here $\Delta\gamma_{\text{tor,rel}} \propto \phi_{0,\omega,n}$ scales linearly with the mechanical amplitude and, therefore, originates from the terms in $\boldsymbol{\delta\eta}$ that scale as $\phi_{0,\omega,n}$, see Eq. (4.49). When integrating these linear terms along the fiber axis, one finds that they are independent of the length, as $\int \mathrm{d}z \, k_n \, \cos(k_n \, z) = \text{const.}$. It follows that $\Delta\gamma_{\text{tor,rel}}$ is independent of the length of the cylinder. This is in contrast to the terms that scale quadratic in $\phi_{0,\omega,n}$: They scale according to $\int \mathrm{d}z \, \cos(k_n \, z) \propto k_n^{-1} \propto L$. Note the exception of the components $\boldsymbol{\delta\eta}_{13}$ and $\boldsymbol{\delta\eta}_{23}$ where the second terms in the brackets scales quadratically but also contains the factor k_n which are, however, negligible for the small amplitudes considered here. This intuitively obtained result is substantiated by the relative magnitude of $\Delta\gamma_{\text{tor,rel}}/\Delta\gamma_{\text{tor,abs}} \sim 1/10$ that corresponds to the ratio of the terms that were related to them, compare Fig. 4.9 and the discussion of Eq. (4.46).

By using the same method, the following relations are found:

$$\begin{aligned} \Delta\gamma_{\mathrm{tor,rel}} &= \mathrm{const.} \\ \Delta\gamma_{\mathrm{tor,abs}} &\propto L \\ \Delta\gamma_{\mathrm{comp,abs}} &= \mathrm{const.} \end{aligned} \tag{4.57}$$

which where numerically confirmed.

4.6 Measurement results

In the following, the measurement results are presented. First, the optical setup is explained. Then, the spectrum of the optically active mechanical modes of tapered optical fibers with different waist lengths is determined. In the following section the influence of the probe laser polarization on the signal is discussed. Then, the amplitude profile of selected modes is determined from which the mechanical wave velocity is extracted. The last two sections are concerned with the measurement of the mechanical quality factors of several modes and the influence of the background gas pressure.

4.6.1 Experimental setup

In the previous sections it has been shown that the strain caused by the mechanical vibrations introduces anisotropy in the material. This anisotropy affects the optical modes guided by the nanofiber and in particular depends on the light polarization. The experimental techniques presented here, utilize this effect to study the mechanical motion either by changes in the optical path length of the fiber (method A) or by polarization fluctuations (method B).

In order to detect the optical path length change, the TOF-microresonator is used, compare Ch. 2.3). It is probed by a tunable diode laser (New Focus Velocity 6316) with a wavelength within the FBG stop-band. The laser beam is sent through polarization optics and then launched into a single-mode optical fiber using a fiber coupler (FC), see Fig. 4.11(a). The TOF-resonator is spliced to this fiber and placed inside a vacuum chamber in order to minimize the mechanical damping from the background gas where the pressure is set to $p \leq 10^{-6}$ mbar (a description of the vacuum system can be found in Ch. 3). At the output port of the fiber, the transmitted light is split by a 50/50 beam splitter (BS) and detected on two photodiodes (PD1 and PD2). The signal of PD2 is used to frequency stabilize the laser to an optical resonance. For this purpose, a side of fringe stabilization is used that is set to the half of the maximum transmission value, see Fig. 4.11(b). This way, the maximum dynamic range is available and, simultaneously, a high sensitivity to optical path length changes is achieved . The stabilization bandwidth is limited to 2 kHz so that it is much smaller than the mechanical frequencies and ensures that the stabilization does not compensate the signal from the mechanical motion. The signal from PD1 is then recorded by means of an oscilloscope or an electrical spectrum analyzer.

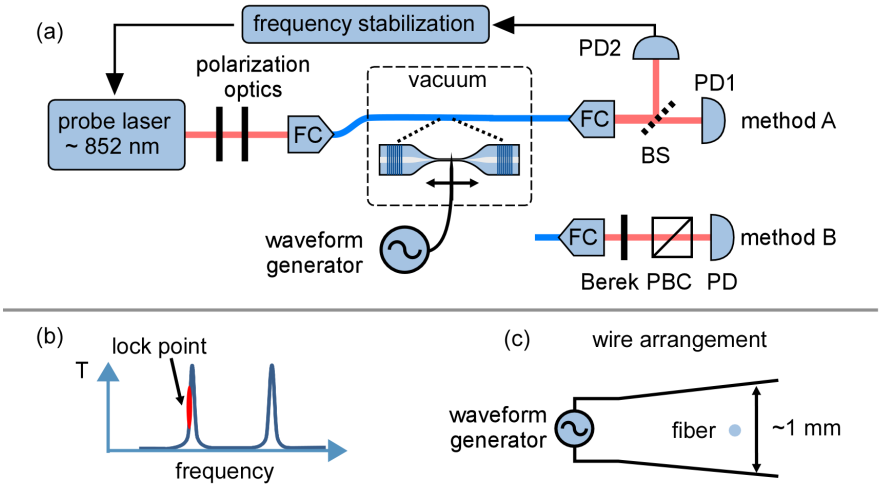

Figure 4.11: *(a) Schematical view of the experimental setup, see text for details. (b) Transmission signal of the Fabry-Pérot resonator with the lock-point indicated by the red point. (c) Schematical view of the electrode arrangement used to excite the mechanical modes that consists of two wires that are placed at the top and bottom of the nanofiber.*

When employing the cavity less method (method B) polarization fluctuations are detected. To this end, either a sample without FBGs is used or the laser is set to a wavelength in the transmission band of the FBGs. Furthermore, a different readout scheme is used, see Fig. 4.11(a). A polarizing beam-splitter (PBC) converts the polarization fluctuations to intensity variations that are then detected by a photodiode at the transmission port of the PBC. Prior to the PBC, an uniaxial birefringent crystal with its axis oriented along the beam propagation axis (Berek compensator) is used to optimize the signal via the light field polarization.

The mechanical modes can be actively excited by the force exerted by an external alternating electric field that acts on stray charges trapped on the insulating silica surface. This localized electric field is generated by two electrodes, see Fig. 4.11(c). They are made from tin-coated wires and are placed above and below the fiber oriented perpendicular to the fiber axis. An electrical waveform generator is used to produced the alternating electric field. The wires are tilted by a small angle with respect to each other in order to create an inhomogeneous field.

4.6.2 Spectrum of the optically active mechanical modes

First, the spectrum of the optically active mechanical modes is measured using the polarization sensitive method (method B) and thermal excitation. For this purpose, the peak detection mode of the electrical spectrum analyzer is used in which the peak value of the signal in each frequency bin is recorded instead of the average value. This method yields a higher sensitivity to narrow resonances at higher band-widths with the draw-back that the recorded signal may significantly overestimate the noise power spectral density. However, in order to identify the resonance frequencies, a large scanning range is required so

that this draw-back is acceptable in the interest of reasonably short measurement times.

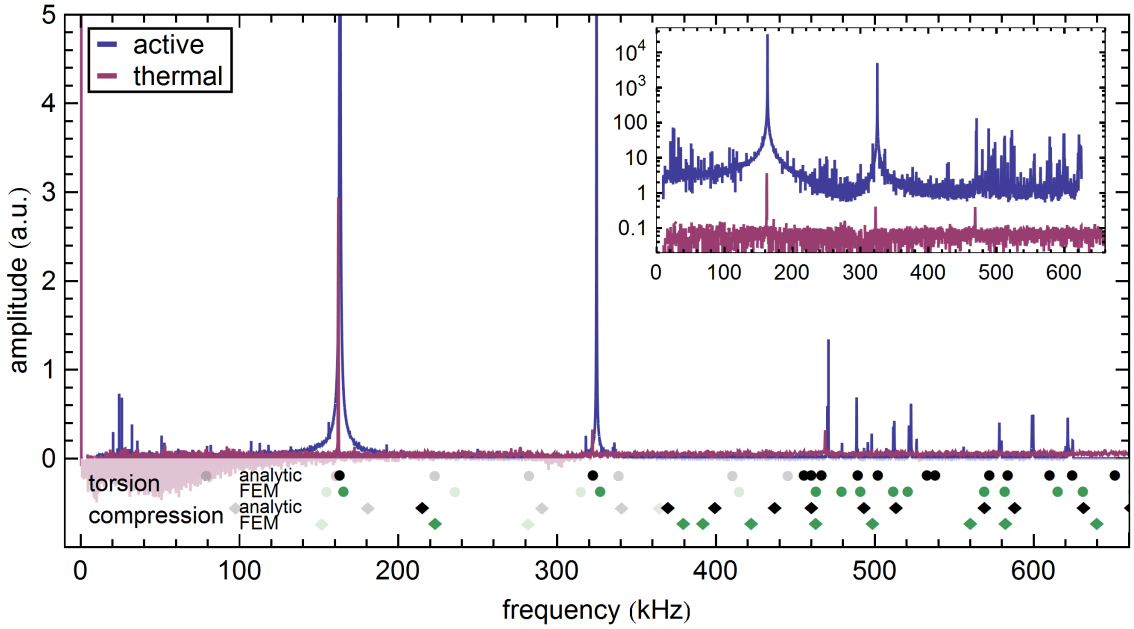

Figure 4.12: *Signal spectrum measured with the cavity-less method (method B) of two fibers with equal radius profiles. Red line: signal caused by thermal excitation (TOF-M1). Blue line: spectral response to active excitation (TOF-M3). Markers: theory predictions of the resonance frequencies by the analytic (FEM) model are shown in black (green). Inset: logarithmic plot of the same data sets which are scaled for better distinction.*

The purple line in Fig. 4.12 shows the thermally excited spectrum of TOF-M1 measured by the polarization sensitive method. The spectrum is corrected for the electronic noise by subtracting a spectrum recorded with blocked laser beam. It features three dominant peaks at frequencies of 162 kHz, 321 kHz and 469 kHz corresponding to three mechanical resonances. The frequencies are approximate multiples of the first resonance frequency which is a strong evidence that they are harmonics of the same mechanical mode and the lowest frequency corresponds to the fundamental mode. Furthermore, the frequency of the fundamental mode is in good agreement with the prediction for a standing torsional mode that extends over the length of the waist region $f = c_t/(2\,L_w) = 185$ kHz. The slightly lower resonance frequency comes as no surprise, since the shallow slope of the exponential profile near the waist allows the wave to extend into this region, thereby yielding a larger effective length of the standing wave.

This measurement is compared to that of a different sample with the same radius profile which is subject to external excitation at a fixed position. For this purpose, a sinusoidal voltage is applied to the electrodes the signal amplitude is monitored at the modulation frequency using a lock-in detection scheme. The spectral response, see blue line in Fig. 4.12, shows resonances at the same frequencies previously as the previous sample. This confirms the reproducibility of the fabrication method. Additionally, resonances in the frequency range beyond 470 kHz with a much smaller frequency spacing

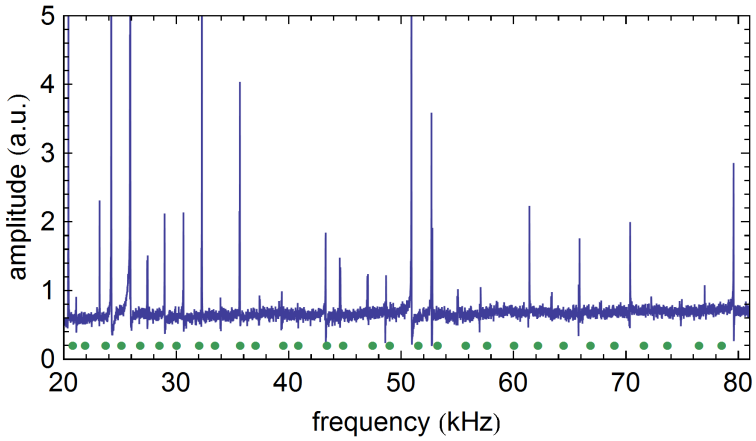

Figure 4.13: *Magnified view of measurement shown as blue trace in Fig. 4.12 around 50 kHz. Green dots: Frequency predictions of the string modes from the FEM model.*

are visible. This frequency is in good agreement with the theoretical cut-off frequency $\omega_t^{co} = 2\pi \cdot 450$ kHz for the exponential taper sections.

In order to compare the spectrum to the models, the predicted resonance frequencies are indicated by markers at the corresponding frequencies in Fig. 4.12. Here, taper modes are shown in pale coloring in order to distinguish them from the nanofiber modes. The resonance frequencies of the first two modes are in excellent quantitative agreement with the theory prediction for the torsional modes. At higher frequencies, a series of closely spaced modes appear in theory and measurement, which correspond to the modes beyond the cut-off frequency. Their precise frequencies are not reproduced by the model. Note that the two models also show discrepancies with respect to each other, although they use the same radius profile. However, they take the initial strain in the fiber differently into account (compare Ch. 4.3.1) which could cause such deviations. The discrepancies between model and measurement can be attributed to deviations of the assumed and actual radius and initial strain profiles.

In addition to the dominant resonances, a series of resonances is visible in the low frequency range which are shown in a magnified view around 50 kHz in Fig. 4.13. They occur regularly with varying visibility and are separated by $(1 \ldots 2)$ kHz. When compared with the string mode frequencies obtained from the FEM model, one finds a good agreement of the spacing as well as the pair-wise pattern around 50 kHz. The model predicts slightly higher frequency separations. This can be attributed to the shorter length of the TOF in the model (length ≈ 6 cm) in which the fiber pigtails that reach to the mounts are neglected (length ≈ 7.5 cm).

In order to check the general validity of the model, the same measurement was performed with two samples of different waist lengths and similar taper radius profiles. Figure 4.14 shows the measurement results obtained with samples with 5 mm (TOF-M4) and 3 mm (TOF-M5) waist lengths, respectively. The spectrum in Fig. 4.14(b) shows a series of peaks at frequencies ranging from 30 kHz to 200 kHz which have not been previously observed. When producing the sample TOF-M5, the fiber has been directly

(a) $L_w = 5\ mm$

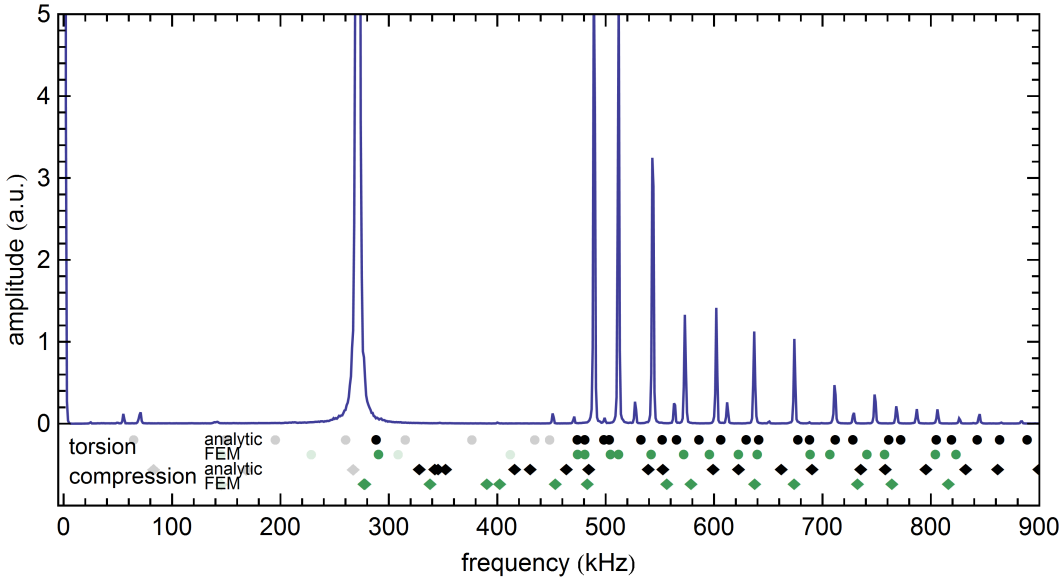

(b) $L_w = 3\ mm$

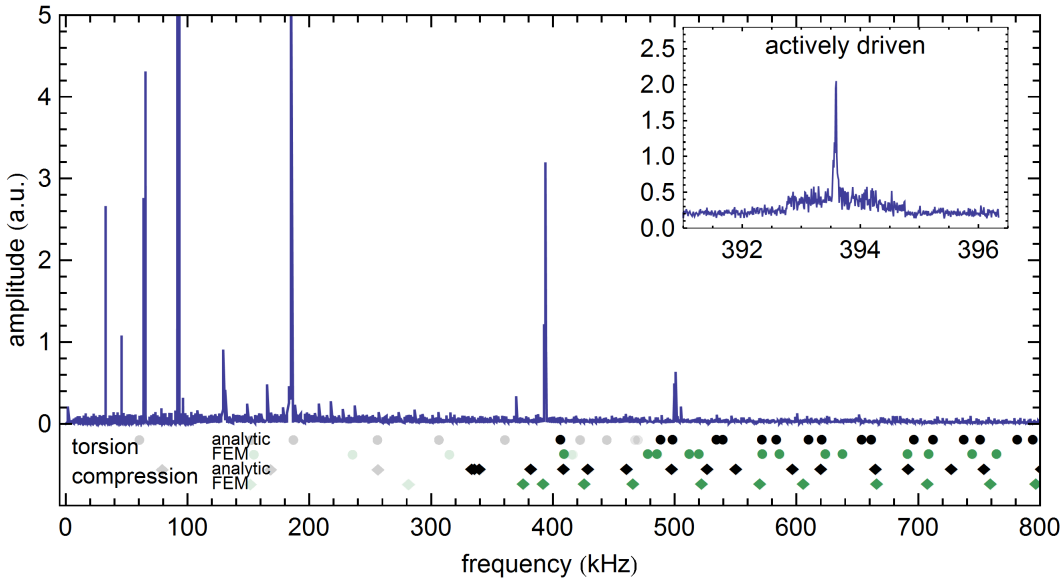

Figure 4.14: *(a) Noise spectral density of TOF-M4 with $L_w = 5$ mm taken from [168]. (b) Noise spectral density of TOF-M5 with $L_w = 3$ mm. Inset: Spectrum obtained by the measurement scheme based on active excitation (see above). In both graphs the theory predictions for the resonance frequencies by the analytic (FEM) model are shown by black (green) markers.*

attached to the aluminum holder and not, like all other samples, to the bending piezo (compare Fig. 1.12). For this reason, I attribute these resonances to vibrational modes of the mounts which were not visible in previous measurements due to the damping characteristics of the piezo and the teflon connector. These features were visible in spectra taken with different waist-lengths that also have been attached directly to the mount (not shown here). In particular, the first resonance matches in good approximation an FEM frequency prediction of the fundamental vibrational mode of the mount of 45 kHz [169].

The fundamental torsional modes are found at frequencies of 271 kHz and 394 kHz. These are ~ 20 % lower than the values one would naively expect by inversely scaling the previously measured resonance frequency with the waist length $f \propto L_w^{-1}$. However, as a simple approximation, one may take the shallow part of the taper sections by an additional effective length ΔL into account. Then, the resonance frequencies are given by $f = c_t/(2[L_w + \Delta L])$. A fit of this model to these three data points yields $\Delta L = (1.7 \pm 0.3)$ mm, which is in good agreement with previous measurements $\Delta L = 2.8^{+1.5}_{-1.1}$ mm that were carried out in our group with similar methods [168]. From the same fit, the phase velocity is be determined to be $c_t = (3720 \pm 210)\ \mathrm{m/s}$. It is in excellent agreement with the literature value $c_t = (3680 \pm 130)\ \mathrm{m/s}$ for the torsional phase velocity in a fused silica rod and clearly different from axial and string modes ($[5630 \pm 170]\ \mathrm{m/s}$ and $\leq 2200\ \mathrm{m/s}$ respectively).

Both spectra show a second harmonic at much lower frequencies than twice the frequency of the fundamental mode. This is due to the fact that ω_{co} is below the expected frequency of the second harmonic. The higher order modes are clearly visible in the spectrum of TOF-M4 while most of the modes do not appear in the spectrum of TOF-M5. The latter is most probably a result of a low signal to noise ratio. The theory prediction of frequency of the fundamental torsional modes is in good agreement with the measurement results for both samples and deviates by ≈ 5 %, a comparable value to the one previously observed. The higher order modes occur at a frequency beyond the predicted cut-off frequency of the torsional horn. Again, their exact frequencies are not reproduced by the theory. Summarizing, both models yield ab-initio predictions of the cut-off frequency of the exponential horn and the resonance frequencies below the cut-off frequency with an accuracy at the level of 5 % using only the design fiber profiles. They reproduce all spectral features for both, the torsional modes and the transversal modes (FEM-model).

4.6.3 Signal as function of the excitation amplitude

In order to verify that the signal is a result of a process that scales linearly with the mechanical displacement, the signal is studied as function of the excitation amplitude. This indirect method is required, since a direct observation of the displacement can not easily be achieved with nanofibers. However, the excitation process based on electrostatic forces is linear so that the observed scaling behavior is the same as for the displacement and signal amplitudes.

Figure Fig. 4.15 shows the signal caused by the fundamental mode as function of the electric excitation amplitude using the resonator based detection method. It clearly shows a linear response. For comparison, a similar measurement is performed with the

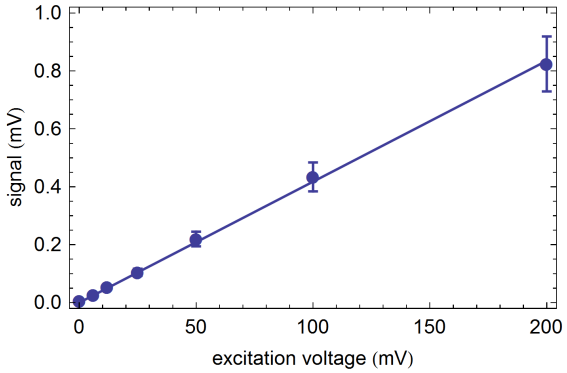

Figure 4.15: *Signal amplitude as function of the excitation voltage (peak to peak) measured with TOF-M2 employing the resonator based method at the frequency of the fundamental mode ($f = 148.028$ kHz)*

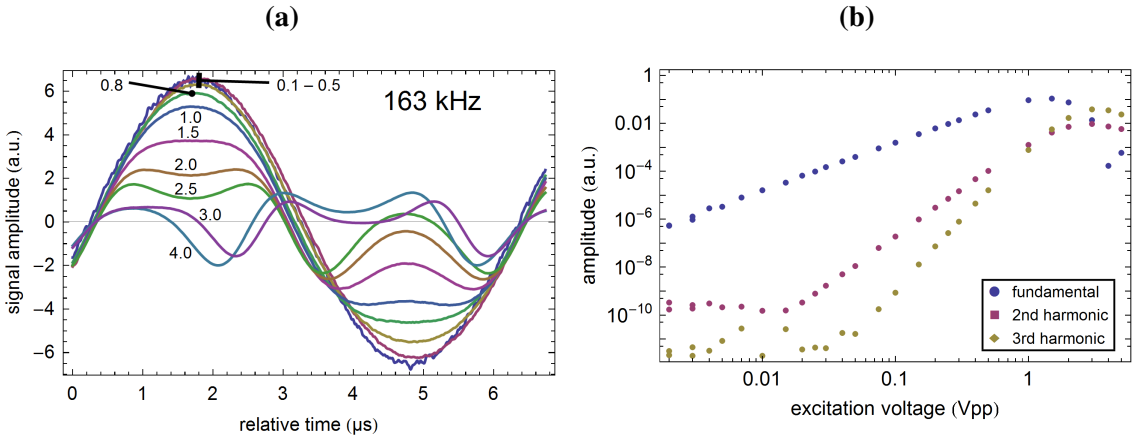

Figure 4.16: *(a) Time trace measured with TOF-M3 using the polarization sensitive method and several excitation amplitudes, see numbers in the plot in units of Volt. The traces are scaled to the excitation voltage, for a better comparison. (b) Signal amplitudes evaluated at 2-times and 3-times of the excitation frequency extracted from (a) as function of the excitation voltage.*

polarization sensitive method. Here, the time trace of the signal was recorded for several excitation voltages. Figure 4.16 shows these signal traces normalized to the excitation amplitude. At low driving amplitudes, the response follows a sinusoidal shape with a cycle time of ≈ 6 µs matching the excitation frequency of 163 kHz, thereby verifying the linear response of the system. When driving the resonance stronger, the signal becomes deformed and higher harmonics contribute to the signal. The amplitude at the first three harmonic frequencies are shown Fig. 4.16(b). Such a trace is in agreement with the previously made assumption that the fiber exhibits an intrinsic torsional strain from an small initial twist: If the resonance is driven sufficiently strong, the resulting strains can compensate the initial strain and thus cause a non-linear response. In addition the analyzer PBC yields a signal given by the sine of polarization angle and is thus only linear for small polarization variations.

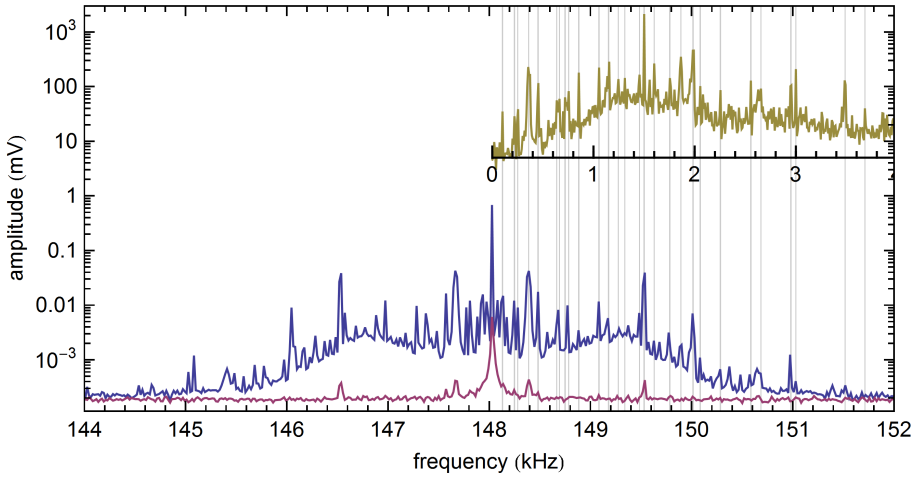

Figure 4.17: *Amplitude spectrum obtained with the resonator based method and TOF-M2 in the frequency range near the first resonance recorded with thermal (purple) and* 200 $\mathrm{mV_{pp}}$ *active excitation (blue). The yellow inset shows a low frequency spectrum measured without external excitation with the corresponding frequency axis. The spectrum is shifted to match its zero point with the first resonance frequency to compare the peak position to the side bands of the resonance (gray grid lines).*

When recording a spectrum with higher resolution in a frequency region around a resonance, the spectrum shows symmetric sidebands around the resonances. Figure 4.17 shows such a spectrum obtained with high driving amplitude (blue) and a thermal spectrum (red). The frequency difference between the sideband frequency and the resonance frequency matches the low frequency resonances of the system, see yellow inset in Fig. 4.17. Note, that these low frequency resonances are not actively driven but are most likely excited by environmental acoustic noise. This is a strong evidence that low-frequency vibrations of the TOF mechanically modulate sidebands onto the high frequency resonances. A likely interaction scheme is given by a modulation of the torsional phase velocity via axial strain modulations, compare Ch. 4.2.1.

4.6.4 Variations related to the probe laser polarization

By tuning the polarization of the probe-laser a second distinct set of resonances can be found. Figure Fig. 4.18 shows two of these resonances that were recorded using the resonator-based method at the frequencies of the first two torsional modes. For these measurements, the polarization was optimized for maximum visibility of each resonance. The separation of each resonance pair amounts to approximately 32 Hz, 55 Hz and 145 Hz for the first three modes, respectively. Furthermore, the probe laser polarization can be tuned such that no signal is visible, see yellow line in Fig. 4.18(a). This can occur when the probe light is circularly polarized in the waist region so that no polarization fluctuations occur.

The origin of these two sets of resonances is not clear. Such two distinguished sets of

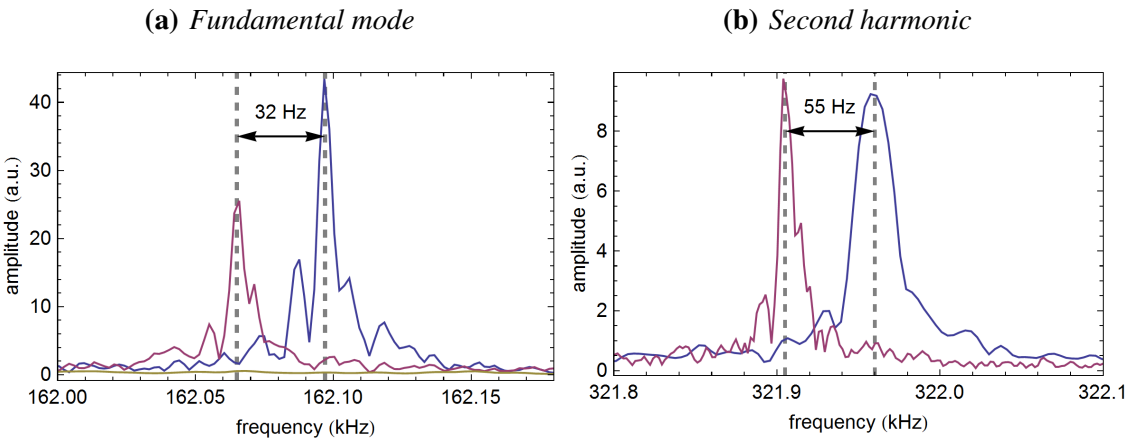

Figure 4.18: *Signal spectrum recorded using different polarization states of the probe laser. Each resonance yields two distinguishable peaks when tuning the polarization.*

polarization sensitive resonances have been observed in previous measurements [168]. In those measurements, a Mach-Zehnder interferometer with an integrated TOF was used. They found that the visibility varies periodically with the light field polarization angle every $90°$. In the following, effects are discussed that could cause such a feature. However, the analysis of the problem is complicated by the fact that the measurement setup offers no possibility to determine the light polarization in the nanofiber waist.

Interestingly, the separation of the peaks is neither constant nor a simple scaling law with the mode index. Typically, double peak structures originate from processes like an amplitude modulation of the signal, weak coupling of two degenerate modes or slightly different phase velocities which lifts a mode degeneracy. For torsional vibrations, however, no degenerate modes exist like for, e.g., string vibrations where the displacement can take place in two transversal directions. This eliminates mechanisms based on coupled modes and those that cancel a degeneracy.

A further explanation attempt is given by using a small polarization dependence of the TOF transmission. This would lead to slightly different waist temperatures when tuning the polarization caused by the variation of the intensity and thus the heating rate in the fiber. Due to the temperature dependence of the Young's modulus this gives rise to different phase velocities which could cause this $\sim 10^{-4}$ effect. Furthermore, a complex scaling behavior with the mode number can occur caused by inhomogeneous waist temperature and the different spatial widths of the modes. However, this would mean that the resonance frequency would be continuously tuned within the two extremal frequencies via the continuous change of the temperature. This, is contradictory to the observation of two distinct resonances with fixed frequencies which only can influenced in their amplitude (and not frequency) by the polarization.

Most likely the split resonances stem from the flexing of the fiber caused by low frequency vibrations. Those modes introduce a strain that may break the symmetry of the torsional strain profile in such a way that a net polarization rotation remains when the low frequency vibrations have a non-zero amplitude. This would cause an amplitude

modulation of the polarization signal, resulting in two peaks at the sum and difference signal. Unfortunately, this simplest case of a mode interaction scheme does not explain why one peak can be suppressed by choosing a certain polarization state. Furthermore, an amplitude modulation produces the same spacing independent of the carrier frequency. In other words one should observe the same frequency spacing of the peaks independent of the frequency of the torsional mode. However, the latter argument takes not the modal profiles of the two interacting modes into account. It is conceivable that only certain combinations of the torsional modes with other modes lead to a signal that differ for each harmonic. Then one could observe different frequency separations of the two peaks.

While these features are interesting and may lead to new physics, the current setup lacks the ability to determine the polarization in the waist region. Therefore, a systematic experimental investigation is left for future work. This also applies for the development of further ab-initio models. The main obstacles are the numerous free parameters that govern the effect of the TOF on the polarization of the guided light, e.g. intrinsic birefringence and birefringence by the flame brush technique, as well as the mounting imperfections, e.g., torsion or kinks. These induce unknown strain with arbitrary relative orientations in the different parts of the TOF. A promising approach for further studies would be to measure and control the polarization in the waist and to correlate the features with the known polarization states.

4.6.5 Modal amplitude profile

In the following, I present a measurement of the spatial form of the mechanical modes and compare its results with the theory predictions. This is achieved by exciting a single mode at a fixed frequency and recording the TOF's response while scanning the excitation position. The result of this measurement is shown in Fig. 4.19 for four selected modes of TOF-M1. The scan is split in two overlapping segments of $(-16 \ldots 2)$ mm and $(-7 \ldots 12)$ mm due to the limited traveling range of the translation stage. The center of the waist region is determined from the symmetry points of the modes. Each measurement consists of a profile recorded during the forward and backward motion of the stage. Their consistency confirms the reproducibility of the measurement method.

The modal amplitude profiles confirm that the resonances at 162 kHz, 321 kHz and 469 kHz correspond to the first three harmonics of a mechanical vibration. Furthermore, the cut-off behavior of the exponential horn manifests in their amplitude profiles: The first two modes have frequencies below ω^{co}, are confined to the waist region, and decay exponentially into the taper region. The two higher modes have frequencies beyond ω^{co} and extend much further into the taper region or, in case of the fourth mode ($f = 621.3$ kHz), exhibit clearly visible nodes along the taper region.

The measured amplitude profiles are slightly skewed which can be explained by a misalignment of the translation direction and the fiber axis. This leads to variations of the fiber position relative to the electrodes field configuration so that the driving force depends on the axial position. Furthermore, the effective excitation strength depends on the charge density on the fiber and the moment of inertia of the fiber. As a consequence, the measured response depends on the radius is only proportional to the modal amplitude

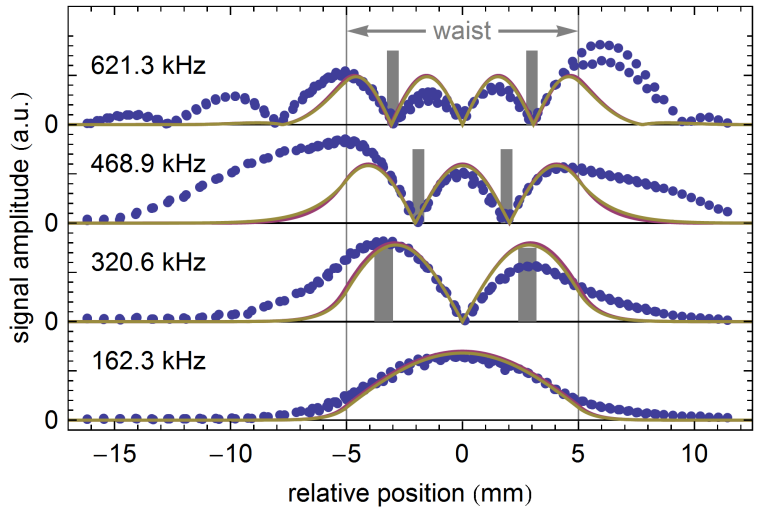

Figure 4.19: *Blue points: Absolute value of the signal amplitude as function electrode position for selected modes of TOF-M1. Lines: Theory prediction of the absolute amplitude profile (yellow: FEM, red: analytic model). For the theory predictions, the modes with the same symmetry and similar resonance frequencies are shown (166 kHz, 328 kHz, 463 kHz and 616 kHz in case of the FEM model and 163 kHz, 323 kHz, 467 kHz and 610 kHz in case of the analytical model).*

profile in the waist region where the radius is constant.

The mode profiles allow a direct measurement of the mechanical phase velocity from the simultaneous measurement of the frequency and the wavelength: $c = \lambda f$. The wavelength is measured from the separation of the nodes or antinodes of the mode in nanofiber region. The corresponding positions are marked by gray bars in Fig. 4.19. Their center indicate the position and their width the uncertainty range. The wavelength is given by their separation: $\lambda/2 = (6.2 \pm 0.4)$ mm at $f = (320.6 \pm 4.1)$ kHz, $\lambda/2 = (3.8 \pm 0.3)$ mm at $f = (468.9 \pm 1.9)$ kHz and $\lambda = (6.0 \pm 0.3)$ mm at $f = (621.3 \pm 0.2)$ kHz. From each pair of values, the torsional wave velocity is determined that is then used to compute the wave velocity by a weighed average of all measurements. This procedure yields

$$c_t = (3737 \pm 177)\frac{\mathrm{m}}{\mathrm{s}}\,, \tag{4.58}$$

which is in excellent agreement with the literature value $c_t = (3680 \pm 130)\,\mathrm{m/s}$ for the torsional phase velocity in a fused silica rod and, again, clearly different from axial and string modes ($[5630 \pm 170]\,\mathrm{m/s}$ and $\leq 2200\,\mathrm{m/s}$, respectively). Furthermore, it confirms the value obtained with the simple model based on an effective fiber length ($c_t = (3720 \pm 210)\,\mathrm{m/s}$) in Ch. 4.6.2.

The theory prediction of the absolute modal amplitude profiles obtained from the FEM-model and the analytical model are shown as yellow and purple lines in Fig. 4.19, respectively. They are in good qualitative agreement with the measurement. Especially, the amplitude profile in the waist region is accurately reproduced by the models. The taper regions, show higher signal than the predicted amplitude which is due to the above mentioned radius dependency of excitation strength.

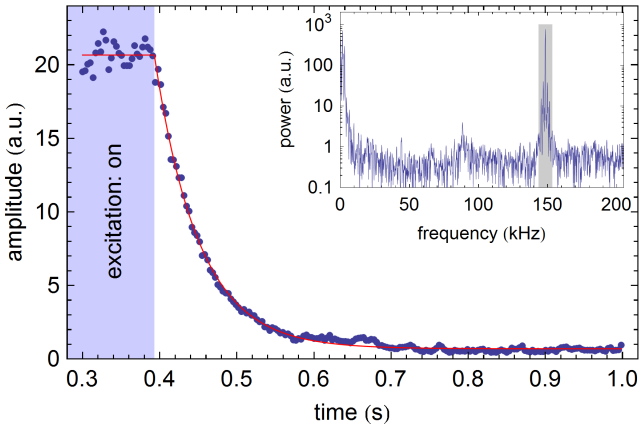

Figure 4.20: *Amplitude–time trace obtained from a ring-down measurement of the fundamental torsional mode (TOF-M2). The blue area marks the time interval during which the mode is actively driven at a frequency of* 148.2 *kHz. Red line: Exponential fit to the data with* $\tau_a = 57.5$ *ms. Inset: Spectral amplitude obtained by Fourier transformation. The grey area marks the integration region.*

f (kHz)	Q (10^4)	f (kHz)	Q (10^4)	f (kHz)	Q (10^4)
148	2.60 ± 0.05	502	0.71 ± 0.03	574	0.56 ± 0.03
302	2.30 ± 0.05	526	0.75 ± 0.03	778	0.31 ± 0.02
441	1.03 ± 0.03	529	0.11 ± 0.02	817	0.12 ± 0.01
453	0.17 ± 0.03	545	0.40 ± 0.03		
500	0.18 ± 0.05	556	0.33 ± 0.02		

Table 4.3: *Q-factor of selected mechanical modes.*

4.6.6 Mechanical quality factor

The Q-factors of the mechanical modes are measured using a ring-down technique: The mechanical motion is excited at its resonance frequency f_0 for long enough to reach an equilibrium situation. Then, the excitation is abruptly switched off while recording the signal amplitude using the resonator-based method. The signal is divided into consecutive time segments of equal length of 200 cycles, which are then Fourier-transformed individually. The resulting spectrum is shown in the inset of Fig. 4.20. In the next step, the spectral amplitude density is integrated over the frequency region $f_0 \pm 10$ kHz. The resulting amplitude time trace is shown in Fig. 4.20. It clearly shows an exponentially decaying profile which is fitted with the corresponding function $A(t) \propto exp(-t/\tau_\mathrm{a})$, where τ_a is the amplitude decay time constant. The Q-factor is computed from this decay constant by $Q = \pi\, \tau_\mathrm{a}\, f_0$ and listed for selected modes in Table 4.3. The first two harmonics feature a high value of $Q \approx 2.5 \cdot 10^4$. The Q-factor of the modes with resonance frequencies higher than ω_{co}, however, are substantially lower. This can be explained by the increasing energy fraction of the mode that is stored in the taper section which is accompanied with higher clamping losses.

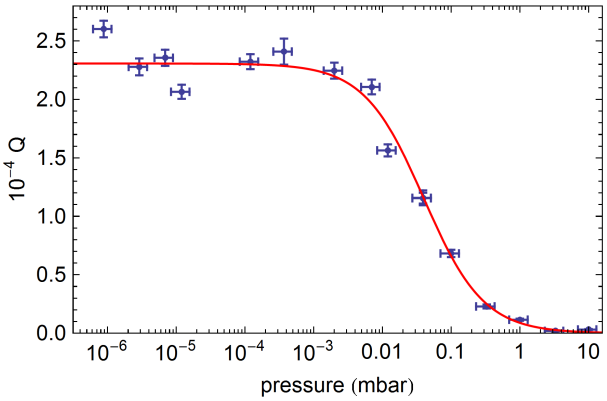

Figure 4.21: *Q-factor as function of the vacuum background pressure measured with sample TOF-M2. The red line shows the fit by an empiric model (see text).*

The mechanical material loss in fused silica has been studied extensively in literature [170, 171]. The losses originate from the coupling of the mechanical motion to the molecular vibrations of the SiO_2-molecules, i.e., the silicon atom tunneling through the potential barrier created by the two oxygen atoms or a breathing motion in which the molecular angle oscillates. However, for small structures such as nanofibers, the losses are dominated by surface effects [171]. They can be quantified by a loss angle $\xi = C\,S/V$ (compare Ch. 4.4), where $S/V \approx 8 \cdot 10^6\ 1/\mathrm{m}$ is the surface to volume ratio and $C = (9.6 \pm 3.3)$ pm is a material constant. Based on this loss angle the intrinsic Q-factor of mechanical modes in the nanofiber waist is predicted to be $Q_\mathrm{i} = \xi^{-1} = (1.5 \pm 0.5) \cdot 10^4$. The good agreement with the values obtained for the lower order modes shows that the resonator is limited by material losses. The fact that the measured Q-factors are even higher than the prediction for the nanofiber can be explained by the modal amplitude profile that extends into the taper profile where the surface to volume ratio is more favorable and the losses are smaller. As a result, the prediction for the intrinsic Q-factor is a lower limit for that of the TOF-modes. This improvement of the damping due to the larger extent of the high frequency modes is overcompensated by clamping losses. The Q-factors thus decrease with increasing resonance frequency.

4.6.7 Q-factor depending on the background gas pressure

In order to study the effect of the atmosphere surrounding the TOF on the mechanical damping, the Q-factor of the fundamental mechanical mode is measured as function of the vacuum background pressure. The result is shown in Fig. 4.21. The uncertainties originate from the fit of the decay constant and the accuracy of the pressure gauge which is 30 % of the measurement value. The Q-factor is approximately constant up to pressures of $p \sim 10^{-3}$ mbar, meaning that the losses are dominated by intrinsic losses, and then decreases due to the damping by the background gas. The damping of the torsional vibration by background gas most probably originates from the torque from gas collisions with nanoscopic deformations on the glass surface, e.g., bumps, cracks or the atomic lay-

ers. As a consequence, the damping constant is proportional to the particle density and, therefore, to the background gas pressure. The data can be accurately described by a model that considers the background gas damping to be proportional to the gas pressure $Q^{-1}(p) = Q_{\mathrm{i}}^{-1} + (\upsilon/p)^{-1}$. The parameters were determined by fitting the model to the data, see red line in Fig. 4.21, to be $Q_{\mathrm{i}} = (2.31 \pm 0.06) \cdot 10^4$ and $\upsilon = (923 \pm 89)$ mbar ($R^2 = 0.991$).

4.7 Summary

In this chapter, I studied optically active mechanical modes of tapered optical fibers in experiment and theory. The thermal excitation of these modes introduce high-frequency phase and polarization fluctuations of the fiber guided light. The spectrum of these fluctuations shows resonances with a high mechanical Q-factors of up to $Q = 2.6 \cdot 10^4$ at frequencies of several 100 kHz. These mechanical resonances were positively identified as torsional modes of the TOF by their frequencies and a measurement of their wave velocity of $c_t = (3737 \pm 177)\mathrm{m/s}$, which is in excellent agreement with the literature value $c_t = (3680 \pm 130)\ \mathrm{m/s}$ obtained from bulk silica elastic constants and clearly differentiated from that of compression waves $[5630 \pm 170]\ \mathrm{m/s}$ and string waves $\leq 2200\ \mathrm{m/s}$.

Two ab-initio theoretical models of torsional waves in tapered fibers have been developed following an analytical as well as a finite element method approach. From these models, it became clear that the mode structure of the TOF results from the cut-off behavior of the widely used exponential radius profile (exponential horn). The model prediction and a measurement of the modal amplitude profiles show consistently that the exponential section confines the mode to the nanofiber section below a cut-off frequency, thereby enabling high, material-limited Q-factors at low gas pressures. Furthermore, the model is capable of predicting the optical response of the fiber material to the mechanically introduced stress. This detailed understanding of optically active mechanical modes facilitates the optimization of the TOF radius profile when it comes to meeting experimental requirements.

These findings have important consequences for the use of tapered optical fibers in a high vacuum environment. As an example, first estimations show that the thermal polarization fluctuations may currently limit the storage time of nanofiber-based atom traps [18, 19]. Furthermore, they might also limit the ultimate ideality of tapered fiber coupling to photonic devices [22]. More generally, high-Q torsional resonances may also occur in other kinds of free-standing subwavelength-diameter waveguides and may influence the stability of the guided light fields. This applies in particular to the case of polarization maintaining structures where the torsional vibration directly translates into the polarization rotation. The exponential horn also provides a design option for nanostructures to isolate a certain part of a system from torsional or compressional vibrations. Other possible applications include sensing of nanoparticles deployed on the surface that introduce a localized impedance increase of the nanofiber.

Summary & Outlook

In the following I will give a summary of the key results that were obtained in the course of this work and provide an outlook for possible applications and further measurements.

The key device that was developed in this work is a Fabry-Pérot type resonator near the Cs D2-line wavelength that is based on a tapered optical fiber (TOF) with a subwavelength diameter nanofiber waist. For this purpose two Bragg mirrors are integrated into the fiber. These are either realized in the form of photonic structures in the nanofiber waist (NFBG-resonator) or as two laser-written fiber Bragg gratings in the untapered part of the fiber such that light passes the TOF twice per round-trip (TOF-microresonator). This way, resonators with nearly arbitrary lengths can be fabricated in order to meet experimental requirements. This resonator is easy to use and offers advantageous properties such as tunabilty and a monolithic design enabling alignment-free operation.

Thanks to the tight transverse confinement of the optical mode by the subwavelength nanofiber waist a large power fraction of the optical mode propagates outside the nanofiber in the form of a high intensity evanescent field. In combination with the low loss rate of the resonator, the field per photon near the surface of the nanofiber is high enough to reach the strong coupling regime of cavity quantum electrodynamics (CQED) for emitters that are placed in close proximity to the nanofiber. Even with its moderate finesse of $\mathcal{F} = 85.6(3)$ and corresponding free spectral range of $\Delta f_{\mathrm{FSR}} = 1.45084(45)$ GHz, it was shown from theoretical considerations that a high single-atom cooperativity parameter of $C = 56.5(4)$ can be reached for an emitter placed on the nanofiber surface. Furthermore, using the parameters for the π-polarized cesium D2 transition $|F = 4, m_F = 0\rangle \rightarrow |F' = 5, m_{F'} = 0\rangle$, one obtains an atom-cavity coupling rate of $g/2\pi = 38$ MHz which is much higher than the measured cavity decay rate $\kappa/2\pi = 8.6$ MHz and the free space decay rate of the atomic transition $\gamma_a/2\pi = 2.6$ MHz. This demonstrates that the TOF-microresonator is well-suited for CQED experiments in the regime of coherent dynamics ($g \gg \kappa, \gamma_a$).

The excellent benchmark parameters of the TOF microresonator are, unlike in free-space optical cavities, essentially constant over the full length of the nanofiber waist. As a consequence, the resonator provides a large volume in which a large number of emitters can be coupled to the resonator mode. This, in combination with its high transmission outside of the fiber Bragg grating stop band, makes this resonator a promising tool for, e.g., cavity quantum electrodynamics with fiber-coupled atomic ensembles [18, 64] and for the realization of quantum network node functionalities, such as, triggered single photon sources [104], quantum memories based on intra-cavity electromagnetically induced transparency [105], and entangled two photon sources [106].

The fact that a resonator with an integrated TOF is sensitive to temperature and strain changes in the latter is utilized in the course of this work to measure the far field heat radiation of a nanofiber and the mechanical modes of tapered optical fibers. These properties are highly relevant for experiments that employ nanofibers in a high-vacuum environment. In these experiments, no mechanical damping due to the background gas occurs and high frequency mechanical modes with high mechanical Q-factors can occur which may lead to fluctuations of the phase and polarization of the nanofiber mode. Furthermore, even small absorbed optical powers of $\sim 100\ \mu\mathrm{W}$ within the nanofiber can lead to very high temperatures due to its minuscule heat capacity of $\sim \mathrm{nJ/K}$. The dominant heat exchange process is given by heat radiation so that the latter determines the temperature and thermalization dynamics of the TOF for a given heating power.

The thermalization dynamics of a TOF was measured by detecting optical path length changes that occur in the tapered optical fiber. These are primarily due to temperature changes in the nanofiber waist which change the propagation constant in the latter mainly due to the thermo-optic effect. The total radiated heat was measured via the equilibrium temperature and the thermalization dynamics in dependence of the heating power. Thermalization time constants of ~ 100 ms were found for a 500 nm diameter optical nanofiber. From measurements at different background gas pressures and two nanofiber lengths, it was experimentally confirmed that the heat transport in gas and the heat conduction in silica yield a negligible contribution to the total heat transfer at pressures below 10^{-4} mbar.

The measured thermalization dynamics can be accurately described by an ab-initio thermodynamical model of a TOF that is based on its geometry and material constants and includes heat transport via heat radiation, heat conduction and heat diffusion in gas. This analysis confirms over a large temperature range that the total thermally radiated power in the far-field is accurately predicted by fluctuational electrodynamics which is based on first principles using only the optical properties and shape and size of the emitter.

While the heat exchange rate via thermal radiation of particles smaller than the thermal wavelength has been studied extensively before [47, 48], the samples employed in previous measurements have not been monodisperse, meaning that only statistical information of their morphology, size and material was available. In contrast to that, here a single object of predetermined shape and material has been studied, thereby enabling the direct comparison to an ab-initio model. Measuring and modeling the thermalization of microscopic particles with arbitrary shape from first principles is of fundamental interest and has important applications in the heat management of nano-devices, radiative forcing of aerosoles in the earth's atmosphere [49], or cavity opto-mechanics experiments [140]. Furthermore, the interferometric detection scheme that was devised in this work may prove to be useful for thermalization measurements in other experiments which provide no direct method for a temperature measurement, e.g., optically levitated microspheres [140–142]. Beyond that, a verification of the fluctuational dynamics model motivates to investigate other effects that are predicted at this size scale from this model, e.g., repulsive Casimir forces of parallel cylinders [143].

Using a technique that is similar to that employed in the thermalization measurements, optically active mechanical modes of tapered optical fibers were experimentally

investigated. The results show that the thermal excitation of these modes introduce high-frequency phase and polarization fluctuations of the fiber guided light. The spectrum of these fluctuations shows resonances with high mechanical Q-factors of up to $Q = 2.6 \cdot 10^4$ at frequencies of several 100 kHz. These mechanical resonances were identified as torsional modes of the TOF by measuring their wave velocity of $c_t = (3737 \pm 177)\mathrm{m/s}$. This value is in excellent agreement with the literature value $c_t = (3680 \pm 130)\ \mathrm{m/s}$ obtained from bulk silica elastic constants.

Two ab-initio theoretical models of the torsional motion of tapered optical fibers have been developed. They only use the design profile of the TOF and material constants and yield predictions for the resonance frequencies with a (relative) accuracy of $5\ \%$ compared to the measured frequencies. The analysis revealed that the mode structure of the torsional modes of a TOF results from the cut-off behavior of the widely used exponential radius profile, known as the exponential horn. The model prediction and a measurement of the modal amplitude profiles show consistently that the exponential section confines the mode to the nanofiber section below a cut-off frequency, thereby enabling high, material-limited Q-factors at low gas pressures.

These findings have important consequences for the use of tapered optical fibers in a high vacuum environment. As an example, first estimations show that the thermal polarization fluctuations may currently limit the storage time of nanofiber-based atom traps [18, 19]. Furthermore, they might also limit the ultimate ideality of tapered fiber coupling to photonic devices [22]. More generally, high-Q torsional resonances may also occur in other kinds of free-standing subwavelength-diameter waveguides and may influence the stability of the guided light fields. This applies in particular to the case of polarization maintaining structures where the torsional vibration directly translates into the polarization rotation. The detailed understanding of the mechanical spectrum and the effect of mechanical vibrations on the optical mode facilitates the design of radius profiles that exhibit an advantageous mode spectrum in view of experimental needs. In particular, the exponential profile provides a design option for nanostructures to isolate a certain part of a system from torsional or compressional vibrations.

In essence, this work has advanced the understanding of the widely used tapered optical fibers in view of their mechanical and thermal properties. The measurement and modelling of the heat radiation emitted by nanofibers deepens the fundamental understanding of thermal radiation at nanoscopic scales by contributing the first measurement of the total radiated power at the level of a single nanoscopic object. The resonator that was used for these measurements is in itself a promising tool for light–matter coupling experiments and can reach the strong-coupling regime of cavity quantum electrodynamics experiments with a single atom.

APPENDIX A

Appendix

A.1 Bessel's little helper

In this section selected relations for the Bessel functions are summarized [61, 172]

$$J_{-l}(x) = (-1)^l J_l(x) \tag{A.1}$$

$$J_{1/2}(x) = \sqrt{\frac{2}{\pi x}}\sin(x) \qquad J_{-1/2}(x) = \sqrt{\frac{2}{\pi x}}\cos(x) \tag{A.2}$$

$$J_l(z) = \frac{z}{2l}\left[J_{l-1}(z) + J_{l+1}(z)\right] \qquad J_l'(z) = \frac{1}{2}\left[J_{l-1}(z) - J_{l+1}(z)\right] \tag{A.3}$$

$$K_l(z) = \frac{z}{2l}\left[K_{l+1}(z) - K_{l-1}(z)\right] \qquad K_l'(z) = -\frac{1}{2}\left[K_{l+1}(z) + K_{l-1}(z)\right] \tag{A.4}$$

$$I_l(z) = \frac{z}{2l}\left[I_{l+1}(z) - I_{l-1}(z)\right] \qquad I_l'(z) = -\frac{1}{2}\left[I_{l+1}(z) + I_{l-1}(z)\right] \tag{A.5}$$

The functions can be approximated by the following relations in the limit $x \ll 1$

$$J_l(x) \to \frac{1}{l!}\left(\frac{x}{2}\right)^l, \qquad I_l(x) \to \frac{1}{l!}\left(\frac{x}{2}\right)^l, \tag{A.6}$$

$$Y_0(x) \to \frac{2}{\pi}\left[\ln\left(\frac{x}{2}\right) + 0.5772\ldots\right], \qquad Y_l(x) \to -\frac{(l-1)!}{\pi}\left(\frac{2}{x}\right)^l \quad l = 1, 2, \ldots, \tag{A.7}$$

$$K_0(x) \to -\left[\ln\left(\frac{x}{2}\right) + 0.5772\ldots\right], \qquad K_l(x) \to \frac{(l-1)!}{\pi}\left(\frac{2}{x}\right)^l \quad l = 1, 2, \ldots. \tag{A.8}$$

The functions can be approximated by the following relations in the limit $x \gg 1$

$$J_l(x) \to \sqrt{\frac{2}{\pi x}}\cos\left(x - \pi\frac{2l+1}{4}\right), \qquad I_l(x) = \sqrt{\frac{1}{2\pi x}}\exp(x) \tag{A.9}$$

$$Y_l(x) \to \sqrt{\frac{2}{\pi x}}\sin\left(x - \pi\frac{2l+1}{4}\right), \qquad K_l(x) = \sqrt{\frac{\pi}{2x}}\exp(-x) \tag{A.10}$$

A.2 Propagation constant of a mode in a medium with weakly anisotropic permittivity

In this section the response of a fiber guided mode to a small anisotropic permittivity change is derived. In particular, I derive an expression for the change of the mode's propagation constant ($\Delta\beta$) for the case in which the anisotropy is sufficiently small so that the fiber fields stay essentially unmodified. A similar expression for isotropic refractive index changes has been obtained in [62, Ch. 31-7] and I will parallel the derivation.

Therefore, we start with the vector function

$$\boldsymbol{F}_c = \boldsymbol{E} \times \bar{\boldsymbol{H}}^* + \bar{\boldsymbol{E}}^* \times \boldsymbol{H} \,, \tag{A.11}$$

and set the modal fields to be $\boldsymbol{E}$ and $\boldsymbol{H}$ for a known field and $\bar{\boldsymbol{E}}$ and $\bar{\boldsymbol{H}}$ for an unknown field distribution to be:

$$\boldsymbol{E} = \boldsymbol{E}_T \exp(\mathbb{i}\beta_j z) \,, \quad \boldsymbol{H} = \boldsymbol{H}_T \exp(\mathbb{i}\beta_j z) \,, \tag{A.12a}$$

$$\bar{\boldsymbol{E}} = \bar{\boldsymbol{E}}_T \exp(\mathbb{i}\bar{\beta}_k z) \,, \quad \bar{\boldsymbol{H}} = \bar{\boldsymbol{H}}_T \exp(\mathbb{i}\bar{\beta}_k z) \,, \tag{A.12b}$$

where fields $\boldsymbol{E}_T$, $\boldsymbol{H}_T$, $\bar{\boldsymbol{E}}_T$ and $\bar{\boldsymbol{H}}_T$ are the transversal electric and magnetic field distributions of the corresponding fields. The source-free Maxwell equations for the non-dissipative, anisotropic case with permittivity, $\epsilon_0\,\boldsymbol{\epsilon}$, for the barred and unbarred fields are given by:

$$\nabla \times \boldsymbol{E} = \mathbb{i} \left(\frac{\mu_0}{\epsilon_0}\right)^{1/2} k_0\, \boldsymbol{H} \,, \qquad \nabla \times \boldsymbol{H} = -\mathbb{i} \left(\frac{\epsilon_0}{\mu_0}\right)^{1/2} k_0\, \boldsymbol{\epsilon} \cdot \boldsymbol{E} \tag{A.13a}$$

$$\nabla \times \bar{\boldsymbol{E}}^* = -\mathbb{i} \left(\frac{\mu_0}{\epsilon_0}\right)^{1/2} k_0\, \bar{\boldsymbol{H}}^* \,, \qquad \nabla \times \bar{\boldsymbol{H}}^* = \mathbb{i} \left(\frac{\epsilon_0}{\mu_0}\right)^{1/2} k_0\, \bar{\boldsymbol{\epsilon}}^* \cdot \bar{\boldsymbol{E}}^* \,, \tag{A.13b}$$

where $k_0 = \omega/c_0$ is the vacuum wavenumber and $\boldsymbol{D} = \epsilon_0\,\boldsymbol{\epsilon} \cdot \boldsymbol{E}$ and $\boldsymbol{B} = \mu_0\,\boldsymbol{H}$ was ised. In the next step $\nabla \cdot \boldsymbol{F}_c$ is to be computed by using $\nabla \cdot (A \times B) = B \cdot (\nabla \times A) - A \cdot (\nabla \times B)$:

$$\nabla \cdot \boldsymbol{F}_c = \nabla \cdot (\boldsymbol{E} \times \bar{\boldsymbol{H}}^*) + \nabla \cdot (\bar{\boldsymbol{E}}^* \times \boldsymbol{H}) \tag{A.14a}$$

$$= \bar{\boldsymbol{H}}^* \cdot (\nabla \times \boldsymbol{E}) - \boldsymbol{E} \cdot (\nabla \times \bar{\boldsymbol{H}}^*) + \boldsymbol{H} \cdot (\nabla \times \bar{\boldsymbol{E}}^*) - \bar{\boldsymbol{E}}^* \cdot (\nabla \times \boldsymbol{H}) \tag{A.14b}$$

$$= \mathbb{i}\, k_0 \left(\frac{\epsilon_0}{\mu_0}\right)^{1/2} \left[\bar{\boldsymbol{H}}^* \cdot \boldsymbol{H} - \boldsymbol{H} \cdot \bar{\boldsymbol{H}}^* - \boldsymbol{E} \cdot \bar{\boldsymbol{\epsilon}}^* \cdot \bar{\boldsymbol{E}}^* + \bar{\boldsymbol{E}}^* \cdot \boldsymbol{\epsilon} \cdot \boldsymbol{E}\right] \,, \tag{A.14c}$$

$$= \mathbb{i}\, k_0 \left(\frac{\epsilon_0}{\mu_0}\right)^{1/2} \left[\bar{\boldsymbol{E}}^* \cdot \boldsymbol{\epsilon} \cdot \boldsymbol{E} - \boldsymbol{E} \cdot \bar{\boldsymbol{\epsilon}}^* \cdot \bar{\boldsymbol{E}}^*\right] \,. \tag{A.14d}$$

The a modified version of the divergence theorem is used

$$\frac{\partial}{\partial z} \int_{A_\infty} \boldsymbol{F}_c \cdot \hat{\boldsymbol{z}}\, \mathrm{d}A = \int_{A_\infty} \nabla \cdot \boldsymbol{F}_c\, \mathrm{d}A - \oint_L \boldsymbol{F}_c \cdot \hat{\boldsymbol{n}}\, \mathrm{d}l \,, \tag{A.15}$$

where A_∞ is an area perpendicular to the fiber axis, $\hat{\boldsymbol{z}}$ is the unit vector along the fiber axis, and $\hat{\boldsymbol{n}}$ is the unit vector parallel to the contour L that delimits the area A_∞. When using a

circular area for A_∞ one finds in the limit of an infinite radius that the last term vanishes because the fields decays to zero towards large radii for bound modes. Considering the z-dependence of the fields one finds

$$\mathbb{i}\,(\beta_j - \bar{\beta}_k) \int_{A_\infty} \left[\boldsymbol{E} \times \bar{\boldsymbol{H}}^* + \bar{\boldsymbol{E}}^* \times \boldsymbol{H}\right] \cdot \hat{\boldsymbol{z}}\,\mathrm{d}A = \int_{A_\infty} \mathbb{i}\,k_0 \left(\frac{\epsilon_0}{\mu_0}\right)^{1/2} \left[\bar{\boldsymbol{E}}^* \cdot \boldsymbol{\epsilon} \cdot \boldsymbol{E} - \boldsymbol{E} \cdot \bar{\boldsymbol{\epsilon}}^* \cdot \bar{\boldsymbol{E}}^*\right] \mathrm{d}A\,,$$

and, therefore,

$$\beta_j - \bar{\beta}_k = k_0 \left(\frac{\epsilon_0}{\mu_0}\right)^{1/2} \frac{\int_{A_\infty} \left[\bar{\boldsymbol{E}}^* \cdot \boldsymbol{\epsilon} \cdot \boldsymbol{E} - \boldsymbol{E} \cdot \bar{\boldsymbol{\epsilon}}^* \cdot \bar{\boldsymbol{E}}^*\right] \mathrm{d}A}{\int_{A_\infty} \left[\boldsymbol{E} \times \bar{\boldsymbol{H}}^* + \bar{\boldsymbol{E}}^* \times \boldsymbol{H}\right] \cdot \hat{\boldsymbol{z}}\,\mathrm{d}A}\,. \tag{A.16}$$

This result requires only that the waveguide is non-absorbing and is general otherwise.

Small anistropy and symmetric permittivity:

If the anisotropic contributions to the permittivity is sufficiently small so that the modifications to the transversal modal amplitudes are negligible one can set $\boldsymbol{E}_T = \bar{\boldsymbol{E}}_T$ and $\boldsymbol{H}_T = \bar{\boldsymbol{H}}_T$. Furthermore, the following treatment is restricted to non-dissipative waveguides, so that $\bar{\boldsymbol{\epsilon}}^* = \bar{\boldsymbol{\epsilon}}$ is real. Then, one finds:

$$\beta - \bar{\beta} = k_0 \left(\frac{\epsilon_0}{\mu_0}\right)^{1/2} \frac{\int_{A_\infty} [\boldsymbol{E}^* \cdot \boldsymbol{\epsilon} \cdot \boldsymbol{E} - \boldsymbol{E} \cdot \bar{\boldsymbol{\epsilon}} \cdot \boldsymbol{E}^*]\,\mathrm{d}A}{2\int_{A_\infty} \mathrm{Re}\,[\boldsymbol{E} \times \boldsymbol{H}^*] \cdot \hat{\boldsymbol{z}}\,\mathrm{d}A}\,. \tag{A.17}$$

Note that, for normalized fields the lower integral results to one. Consider the first term of the numerator which can be rewritten in the form

$$\boldsymbol{E}^* \cdot \boldsymbol{\epsilon} \cdot \boldsymbol{E} = \sum_{n,m} E_m^*\, \boldsymbol{\epsilon}_{mn}\, E_n = \sum_{n,m} E_n\, (\boldsymbol{\epsilon}^T)_{nm}\, E_m^* = \boldsymbol{E} \cdot \boldsymbol{\epsilon}^T \cdot \boldsymbol{E}^*\,.$$

The permittivity of the undisturbed fiber ϵ is diagonal and therefore symmetric which allows to simplify the result to:

$$\beta - \bar{\beta} = k_0 \left(\frac{\epsilon_0}{\mu_0}\right)^{1/2} \frac{\int_{A_\infty} [\boldsymbol{E}^* \cdot (\boldsymbol{\epsilon} - \bar{\boldsymbol{\epsilon}}) \cdot \boldsymbol{E}]\,\mathrm{d}A}{2\int_{A_\infty} \mathrm{Re}\,[\boldsymbol{E} \times \boldsymbol{H}^*] \cdot \hat{\boldsymbol{z}}\,\mathrm{d}A}\,. \tag{A.18}$$

Note that for a strain-induced anisotropy the permittivity remains symmetric. This can be seen by considering the impermittivity $\boldsymbol{\eta} = \boldsymbol{\eta}_0 + \boldsymbol{p} \cdot \boldsymbol{s}$ is symmetric as $\boldsymbol{p}$, $\boldsymbol{s}$ and $\boldsymbol{\eta}_0$ are symmetric so that

$$\boldsymbol{\epsilon}^T = (\boldsymbol{\eta}^{-1})^T = (\boldsymbol{\eta}^T)^{-1} = (\boldsymbol{\eta})^{-1} = \boldsymbol{\epsilon}\ \square \tag{A.19}$$

A.3 Transfer matrix of a slit in a fiber

The matrix of a slit can be computed from coupled mode theory and the corresponding derivation can be found in the literature [78]. Coupled mode theory is accurate since the modes, i.e. the guided and the radiative together, represent a complete basis set of modes. The basic idea of this formalism is that a coupling between modes exists that facilitates a power transfer. By decomposing the light field into the modes, expressions for the modal amplitude coefficients can be found in the form of coupled differential equations. For most practical purposes a subset of modes is used as an approximation to reduce the number of equations to a manageable amount. Here, the nanofibers are single-mode so that only one guided mode has to be taken into account. Furthermore, losses are neglegted in the following which is a good approximation for the quasi-linearly polarized mode in the photonic structures here when the polarization is oriented along the slits.

Consider an arbitrary optical field with frequency ω which can be decomposed into modes with electric (magnetic) field distributions $\boldsymbol{E}_i$ ($\boldsymbol{H}_i$) which are orthogonal with respect to the product:

$$\frac{1}{2}\int \mathrm{d}\boldsymbol{r}\,\mathrm{Re}\left[(\boldsymbol{E}_i \times \boldsymbol{H}_j^*)\cdot\hat{\boldsymbol{z}}\right] = P_i\,\delta_{ij}\;, \tag{A.20}$$

where $\hat{\boldsymbol{z}}$ is the unit vector along the fiber axis, P_i is the power stored in the mode with index i. The field components along the fiber axis $\boldsymbol{E}_\parallel$ and $\boldsymbol{H}_\parallel$ and perpendicular to the axis $\boldsymbol{E}_\perp$ and $\boldsymbol{H}_\perp$ are treated separately and the decomposition can be written as:

$$E_\perp = \sum_\alpha (a_\alpha^+ + a_\alpha^-)\,E_{\perp,\alpha}\;,\quad E_\parallel = \frac{\epsilon_0}{\epsilon}\sum_\alpha (a_\alpha^+ - a_\alpha^-)\,E_{\perp,\alpha}\;, \tag{A.21a}$$

$$H_\perp = \sum_\alpha (a_\alpha^+ - a_\alpha^-)\,H_{\perp,\alpha}\;,\quad H_\parallel = \frac{\epsilon_0}{\epsilon}\sum_\alpha (a_\alpha^+ + a_\alpha^-)\,H_{\perp,\alpha}\;, \tag{A.21b}$$

where a_α^+ and a_α^- are the corresponding coefficients for the forward and backward propagating mode with index α, respectively. These modes are coupled via the equations

$$\frac{\partial a_\alpha^+}{\partial z} = \mathbb{i}\,\beta_\alpha\,a_\alpha^+ + \mathbb{i}\sum_{\alpha'}\left(U_{\alpha,\alpha'}\,a_{\alpha'}^+ + V_{\alpha,\alpha'}\,a_{\alpha'}^-\right)\;, \tag{A.22a}$$

$$\frac{\partial a_\alpha^-}{\partial z} = \mathbb{i}\,\beta_\alpha\,a_\alpha^- - \mathbb{i}\sum_{\alpha'}\left(V_{\alpha,\alpha'}\,a_{\alpha'}^+ + U_{\alpha,\alpha'}\,a_{\alpha'}^-\right)\;, \tag{A.22b}$$

where the coupling coefficients are given by

$$U_{\alpha,\alpha'} = \frac{\omega\,\epsilon_0}{4\,P}\int \mathrm{d}\boldsymbol{r}\,(\epsilon-\epsilon_0)\left[\boldsymbol{E}_{\perp,\alpha}\,\boldsymbol{E}_{\perp,\alpha'}^* + \frac{\epsilon_0}{\epsilon}\,\boldsymbol{E}_{\parallel,\alpha}\,\boldsymbol{E}_{\parallel,\alpha'}^*\right] \tag{A.23a}$$

$$V_{\alpha,\alpha'} = \frac{\omega\,\epsilon_0}{4\,P}\int \mathrm{d}\boldsymbol{r}\,(\epsilon-\epsilon_0)\left[\boldsymbol{E}_{\perp,\alpha}\,\boldsymbol{E}_{\perp,\alpha'}^* - \frac{\epsilon_0}{\epsilon}\,\boldsymbol{E}_{\parallel,\alpha}\,\boldsymbol{E}_{\parallel,\alpha'}^*\right]\;. \tag{A.23b}$$

Here, only the coupling of four fundamental quasi-circular polarized nanofiber modes (including the two propagation directions) via the slit is considered. Then α takes only the values $\alpha = \{+1,-1\}$ for the right and left circular modes, respectively. It can be

shown that $U_{1,1} = U_{-1,-1} = U$, $U_{-1,1} = U_{1,-1} = U_c$, $V_{1,1} = V_{-1,-1} = V$ and $V_{-1,1} = V_{1,-1} = V_c$. The coupling equations (Eq. (A.22)) can be decoupled in the polarization by using the linear basis $a_x = (a_1 + a_{-1})/\sqrt{2}$ and $a_y = (a_1 - a_{-1})/\sqrt{2}$ corresponding to x- and y-polarization:

$$\frac{\partial a_x^+}{\partial z} = \mathrm{i}\,(\beta + U_x)\,a_x^+ + \mathrm{i}\,V_x\,a_x^- \;, \qquad \frac{\partial a_x^-}{\partial z} = -\mathrm{i}\,(\beta + U_x)\,a_x^- - \mathrm{i}\,V_x\,a_x^+ \;, \tag{A.24a}$$

$$\frac{\partial a_y^+}{\partial z} = \mathrm{i}\,(\beta + U_y)\,a_y^+ + \mathrm{i}\,V_y\,a_y^- \;, \qquad \frac{\partial a_y^-}{\partial z} = -\mathrm{i}\,(\beta + U_y)\,a_y^- - \mathrm{i}\,V_y\,a_y^+ \;, \tag{A.24b}$$

where $U_x = U + U_c$, $V_x = V + V_c$, $U_y = U - U_c$ and $V_y = V - V_c$. Now that the polarizations are decoupled, only the forward and backward propagating modes are coupled. The ratio of the coefficients correspond to transmission and reflection. This is in direct analogy to the transfer matrix formalism and the matrix follows after integration

$$M_{11}^{(x)} = \cos(K_x\,h) + \mathrm{i}\,\frac{\beta + U_x}{K_x}\,\sin(K_x\,h) \tag{A.25a}$$

$$M_{22}^{(x)} = \cos(K_x\,h) - \mathrm{i}\,\frac{\beta + U_x}{K_x}\,\sin(K_x\,h) \tag{A.25b}$$

$$M_{12}^{(x)} = -M_{21}^{(x)} = \mathrm{i}\frac{V_x}{K_x}\,\sin(K_x\,h)\;, \tag{A.25c}$$

where h is the length of the slit. Furthermore, the x-polarization of the mode is chosen and the expressions for the y-polarization is given by replacing the indices. This applies also for the following expressions. With that the single slit exhibits the (amplitude) transmission and reflection coefficients

$$r_x = \frac{\mathrm{i}\,V_x\,\sin(K_x\,h)}{K_x\,\cos(K_x\,h) - \mathrm{i}(\beta + U_x)\,\sin(K_x\,h)} \tag{A.26a}$$

$$t_x = \frac{K_x}{K_x\,\cos(K_x\,h) - \mathrm{i}(\beta + U_x)\,\sin(K_x\,h)}\;, \tag{A.26b}$$

where

$$K_x = \sqrt{(\beta + U_x)^2 - V_x^2}\;. \tag{A.27}$$

With that the transfer matrix of the stack is computed using Eq. (2.13) and Eq. (2.12). The (amplitude) reflection and transmission coefficients follow from the recursion formulas

$$r_x^{(N+1)} = r_x^{(N)} + \frac{t_x^{(N)\,2}\,r_x\,\exp(2\,\mathrm{i}\,\beta\,s)}{1 - r_x^{(N)}\,r_x\,\exp(2\,\mathrm{i}\,\beta\,s)}\;, \tag{A.28a}$$

$$t_x^{(N+1)} = \frac{t_x^{(N)}\,t_x\,\exp(\mathrm{i}\,\beta\,s)}{1 - r_x^{(N)}\,r_x\,\exp(2\,\mathrm{i}\,\beta\,s)}\;. \tag{A.28b}$$

where s is the length of the nanofiber segment between two slits and $r_x^{(1)} = r_x$ and $t_x^{(1)} = t_x$.

A.4 Refractive index of fused silica

The complex refractive index, $\hat{n} = n + i\kappa$, is the sole material property that enters the calculation of the spectral emissive power of thermal radiation. The uncertainty of the literature values are taken into account by using all four combinations of the maximum and minimum of each n (refractive index) and κ(extinction coefficient), respectively, in order to compute the total radiated power. Then, the maximum and minimum value of the latter are used for further calculations.

Optical fibers are made of high-quality synthetic fused silica, which is an amorphous glass, with a core with typically a few weight percent of dopants such as, e.g., germanium. Four types of fused silica are commercially available [70]: Type I and Type II are produced from crystal quartz by electric melting and from quartz powder by flame fusion, respectively, whereas Type III and Type IV glasses are synthetic glasses produced from $SiCl_4$ in a H_2–O_2 flame and in a water-vapor free plasma flame respectively. The synthetically produced glasses feature the lowest impurity content and, thereby, exhibit a higher transmission than the Type I and Type II glasses, in particular in the near-infrared and in the ultraviolet spectral ranges.

Since the TOF fabrication employs a H_2–O_2 flame for the tapering process, the glass in the TOF is considered to be a mixture of Type III and Type IV silica. Therefore, the minimum and maximum values of both n and κ, respectively, that are available for these two types of glass are extracted. For wavelength regions in which we did not encounter literature values for these particular types of glass, we also use data for other types of fused silica. The resulting minimum and maximum contributions of the complex refractive index that we employ for our calculations were derived from (34) and are shown in Fig. A.1 as function of the optical wavelength. We note that the values given for the extinction coefficient in the visible spectrum are at the lower limit of the parameter range that is experimentally accessible and therefore can be considered as maximum values. Since no further data is available and heat radiation in the visible spectrum contributes only marginally to the total heat transfer rate, we do not consider smaller values.

Fused silica is highly transparent in the visible and near infrared wavelength range which makes it an excellent medium for efficient light transport. However, it is strongly absorbing in the UV and infrared wavelength range around ≈100 nm and 10 µm respectively. These absorption bands can be related to energy bands of the lattice vibrational states (IR) and electronic absorption bands (UV) [173].

Linear approximation at low optical frequencies

For low optical frequencies, the permittivity of fused silica can be linearly approximated so that one can obtain an analytic expression for the heat radiation in the cryogenic temperature range. We fit a model of the form:

$$\epsilon = \epsilon_c + i\,\omega\,\lambda_{\text{in}}/c + O(\omega^2)\ . \tag{A.29}$$

We determined the material constants ϵ_c and λ_{in} from fits to the minimum and maximum traces ϵ in the range from $\omega = (0.8 - 10)$ THz, see Fig. (A.2). The data was weighted with a constant relative error, so that small and large values contribute equally to the fit result.

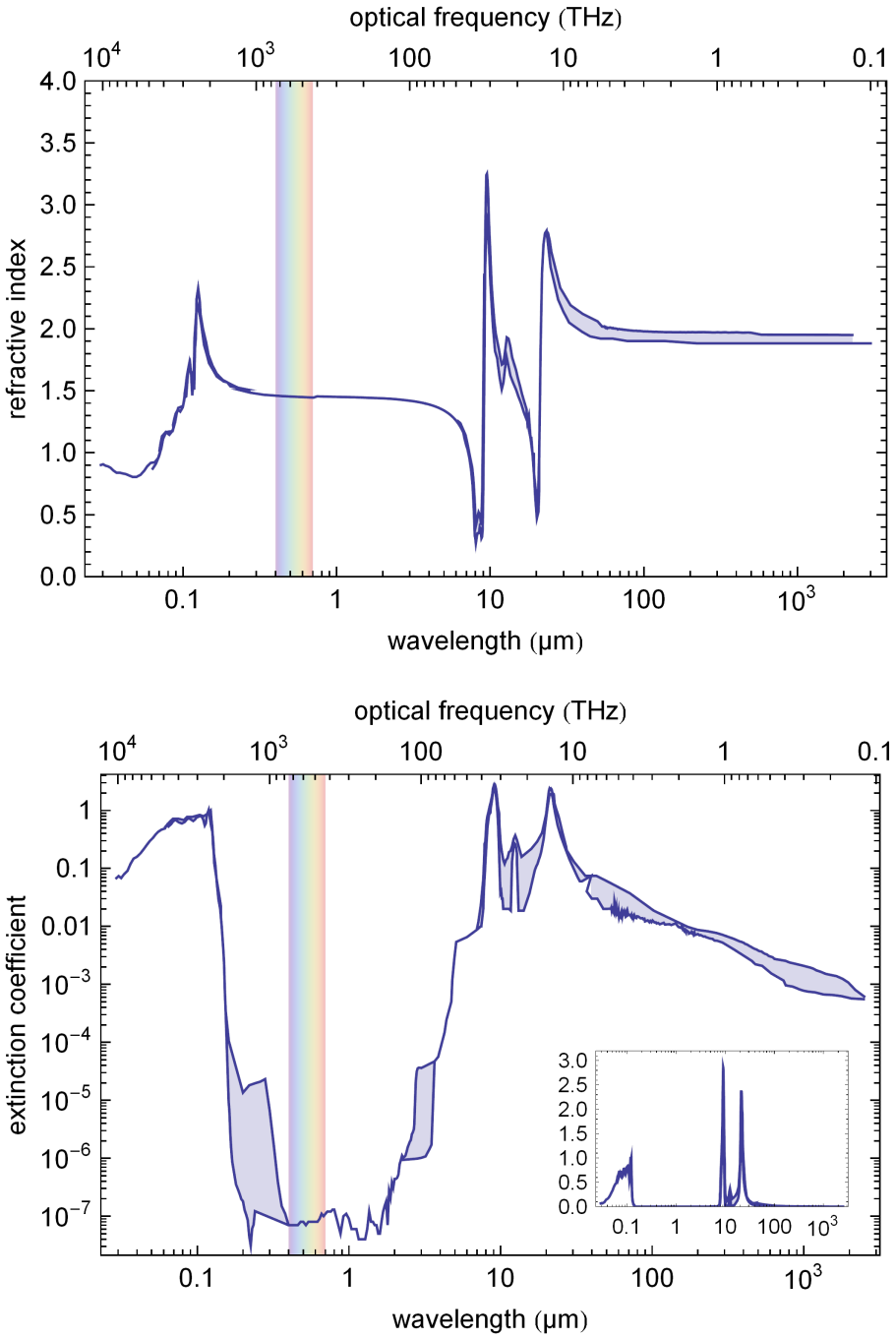

Figure A.1: *Refractive index and extinction coefficient of fused silica as function of the wavelength. The visible part of the spectrum,* $(400 - 700)$ *nm, is indicated by the rainbow bars.*

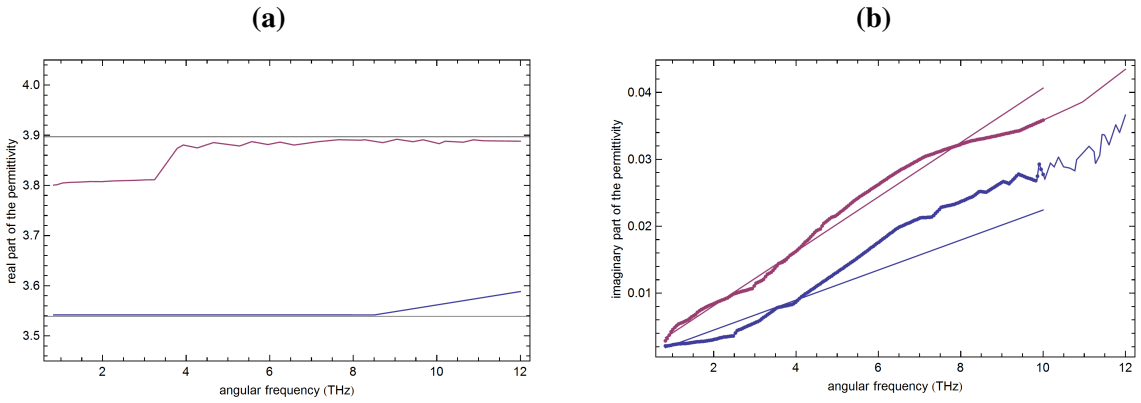

Figure A.2: *Minimum and maximum trace of the real part (a) and the imaginary part (b) of the spectral permittivity in the frequency range* $(0.1 - 10)$ *Thz. The lines indicate the minimum and maximum fit.*

By computing the average values and half their spacing we obtain $\lambda_{\text{in}} = (940 \pm 280)$ nm and $\epsilon_c = 3.7 \pm 0.2$.

A.5 Specific heat and heat conductivity of fused silica

The heat conductivity λ_{heat} and specific heat capacity c_{p} of silica can be found for a wide temperature range in literature as shown in Fig. A.3 [125, 174]. To obtain estimations of the thermalization time constants in the cryogenic temperature regime we fitted a power law to the values in the temperature range $(1 - 50)$ K:

$$f(T) = a_0 \cdot (T[K])^p \tag{A.30}$$

with the free parameters a_0 and p and T in units of Kelvin. We obtain values for the heat capacity of $a_0 = 2 \cdot 10^{-3}$ J/kg K and $p = 2.9$ and for the thermal conductivity $a_0 = 2 \cdot 10^{-2}$ W/K m and $p = 0.6$. The fits are shown in Fig. A.3 as lines in according colors as well as the relative deviation from the data points in the inset. We find that the fits reproduce the order of magnitude of the values and can be used as a rough estimation for the scaling behavior of the functions.

A.6 Thermal expansion coefficient of fused silica

The thermal expansion coefficient is defined as

$$\alpha_{\text{te}} = \frac{1}{L(T_0)} \frac{\partial L(T)}{\partial T} , \tag{A.31}$$

where T_0 typically corresponds to room temperature. Various works have studied the thermal expansion coefficient of fused silica in different temperature regimes and have obtained compatible results [122, 134–136]. It has been shown that the OH-content and

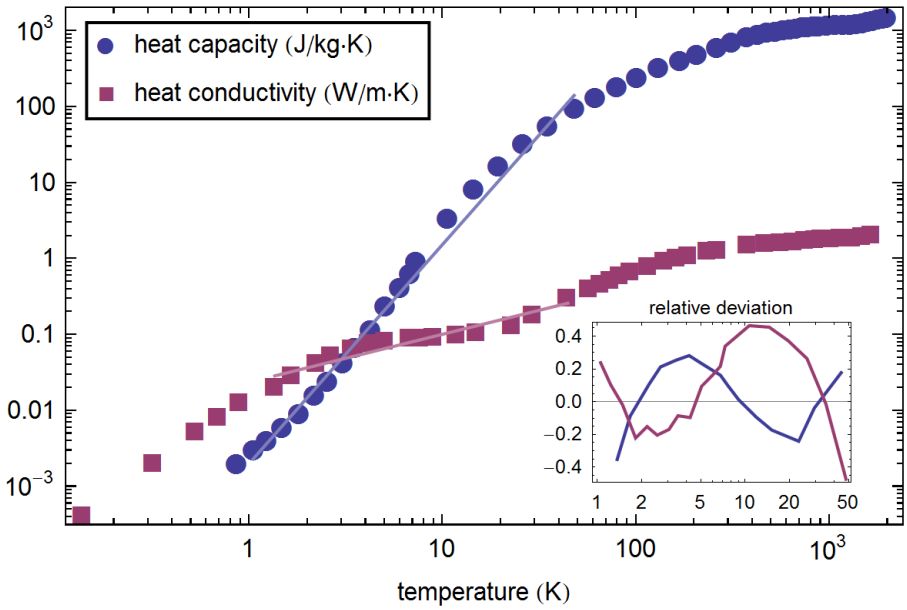

Figure A.3: *Thermal Conductivity and specific heat capacity of fused silica. Two power law functions have been fitted to the data in the temperature range* $(1-50)$ *K and are shown as transparent lines in the according colors. The inset shows their relative deviation from the literature values.*

the fictive temperature, T_f, of the glass has an influence on the thermal expansion. The latter is a material property that is determined by the glass composition as well as the cooling dynamics of the glass. In particular, the thermal expansion increases with higher fictive temperatures whereas a higher OH-content lowers α_{te} [135]:

$$\frac{L(981\,^{\circ}\mathrm{C}) - L(20\,^{\circ}\mathrm{C})}{L(20\,^{\circ}\mathrm{C})\,(981-20)^{\circ}\mathrm{C}} = (0.267 + 2.88\cdot 10^{-4}\cdot T_f[^{\circ}\mathrm{C}] - 3.26\cdot 10^{-5}\cdot \mathrm{OH[ppm]})\cdot 10^{-6}\frac{1}{\mathrm{K}}\,. \tag{A.32}$$

These effects can amount to a 10 % change of the thermal expansion coefficient. Since the OH-content and T_f are not known from the nanofiber production process, we use the values of α_{te} obtained from the NIST standard reference material SRM739 with an uncertainty of ± 10 % as shown in Fig. A.4 [122]. We have fitted the thermal expansion coefficient by a fourth order polynomial of the form

$$\begin{aligned}\alpha_{\mathrm{te}}(T) = -1.66(2)\cdot 10^{-6} + 1.40(2)\cdot 10^{-8}\,T - 3.02(7)\cdot 10^{-11}\,T^2 \\ + 2.71(9)\cdot 10^{-14}\,T^3 - 8.9(4)\cdot 10^{-18}\,T^4\end{aligned} \tag{A.33}$$

where the temperature T is in units of Kelvin.

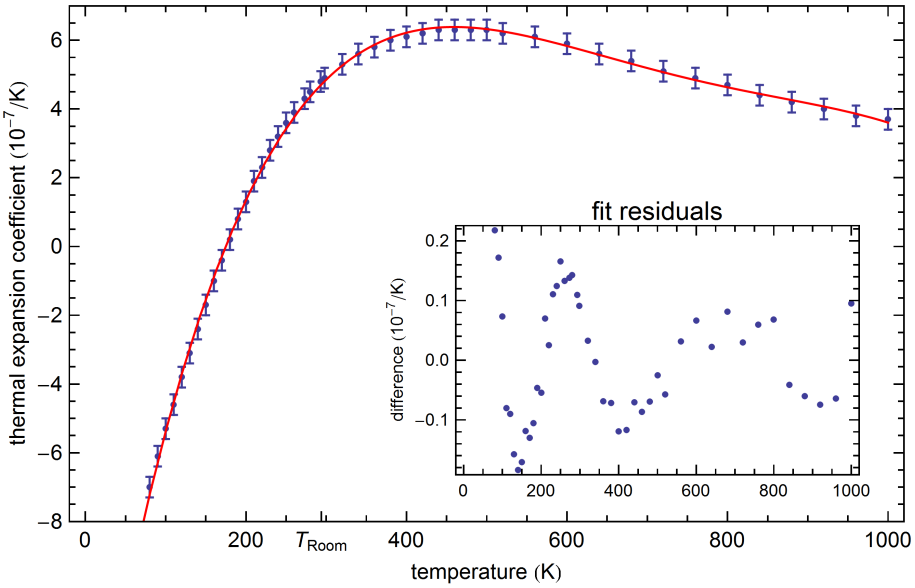

Figure A.4: *Thermal expansion coefficient of fused silica as a function of temperature from Ref. [122]. The red line is a fourth order polynomial fit and the inset shows the fit residuals. Inset: Residuals of the polynomial fit to the data* $\alpha_{\mathrm{te}}(T) - \alpha_{\mathrm{te}}^{\mathrm{fit}}(T)$ *in the same units as the main plot.*

A.7 Thermalization via heat radiation assuming volume heating

In the analysis of the thermalization measurements presented in Ch. 3, it was assumed that the heating of the TOF results form surface absorption. In this section, I study the influence of this heating model on the thermal model prediction by carrying out the analysis of the thermalization dynamics measurements for the other extreme case of heating by volume absorption on the example of TOF-resonator 3.

In the case of heating by volume absorption of laser light in the fiber, the heating power distribution is proportional to the power fraction of the mode that propagates inside the silica of the TOF:

$$\partial_z P_{\mathrm{abs}}^{\mathrm{vol}}(z) \propto \int_0^{2\pi} \mathrm{d}\phi \int_0^a r\,\mathrm{d}r\, |\boldsymbol{E}(r(z),\phi,z)|^2\,, \tag{A.34}$$

which is shown as the purple line in Fig. A.5(a). In this case, the heating power is higher in the taper regions because the fiber diameter increases and thereby the fraction of the model power that propagates inside the silica. Note that this heating distribution is not localized as in the surface absorption case but extents to the ends of the fiber. Nevertheless, it can be expected that the temperature of the nanofiber waist and its surroundings is much higher than the remaining parts of the TOF due its very small heat capacity when compared to the remaining fiber. It is, therefore, impractical to normalize the heating power to the full fiber length. I chose the section of the TOF that is simulated in the model to normalize

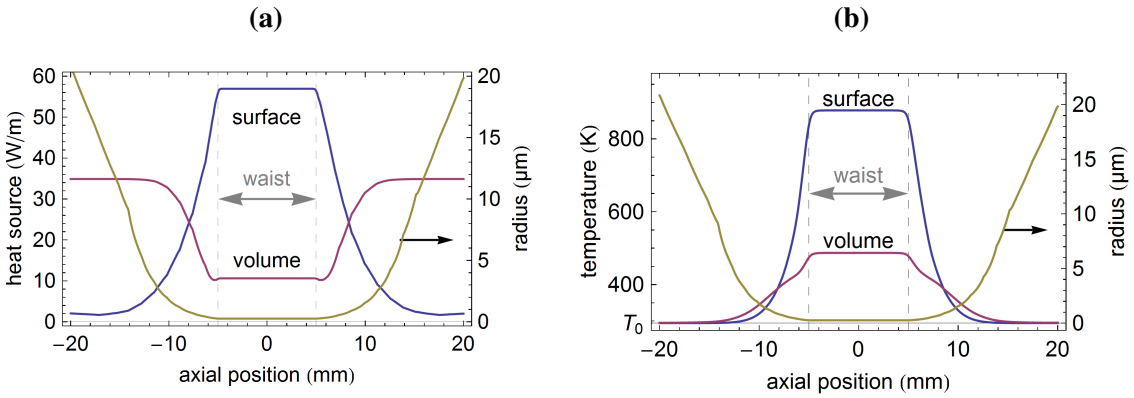

Figure A.5: *Heat source (a) and predicted equilibrium temperature distribution (b) as function of the axial position. The latter has been computed using the two heat source distribtuitions for* $P_{\mathrm{abs}} = 50$ μ*W and* $p = 10^{-7}$ *mbar.*

$\partial_z P_{\mathrm{abs}}^{\mathrm{vol}}(z)$ using again the integral along the fiber axis: $P_{\mathrm{abs}}^{\mathrm{vol}} = \int \mathrm{d}z\ \partial_z P_{\mathrm{abs}}^{\mathrm{vol}}$. Therefore, the simulated region has to be chosen sufficiently large, i.e. including the full region in which the temperature is raised, in order to obtain an accurate prediction for the optical path length change.

Figure A.5(b) shows the simulated temperature profiles which are obtained for each of the two heat sources in the equilibrium situation. In both cases, the region of high temperatures is found in the waist section and its close vicinity. On the first glance, this finding is surprising for volume heating because the heating power density exhibits its minimum in the waist section. However, the reason for this becomes clear when comparing the deposited heat energy with the heat capacity as function of the radius: While the heating power decreases by a factor of ≈ 3.5 from the taper region to the nanofiber, the heat capacity per unit length, scaling with the cross section of the fiber, decreases by a factor of ~ 100 in the same region. As a direct consequence, a much larger energy amount hast be stored in the taper section compared to the waist section in order to obtain the same temperature change. When comparing the two temperature profiles, the prediction for volume heating shows a broader temperature distribution with a lower equilibrium waist temperature. This is due to the fact that a larger fraction of the energy is deposited in the taper region.

The resulting maximum optical path length change is shown in Fig. A.6 as light shaded area with dotted delimiters together with the prediction for heating from surface absorption as dark shaded area with solid delimiters. The η-value is $\eta = (4.9 \pm 0.8) \cdot 10^{-3}$ and with that higher compared to the one obtained for surface absorption of $(1.3 \pm 0.4) \cdot 10^{-3}$. This is due to the previously discussed difference in the normalization routine of the heating power distribution. Furthermore, the predicted equilibrium temperatures are 25 % lower compared to those obtained assuming surface heating. This can be explained by the broader temperature profiles which cause a larger fraction of the TOF to contribute to ΔL_{opt} and thereby require lower temperatures to reproduce a given value. However, we observe little modification of the scaling behavior with respect to the heating power.

Figure A.7 shows the prediction for the thermalization times in the same color cod-

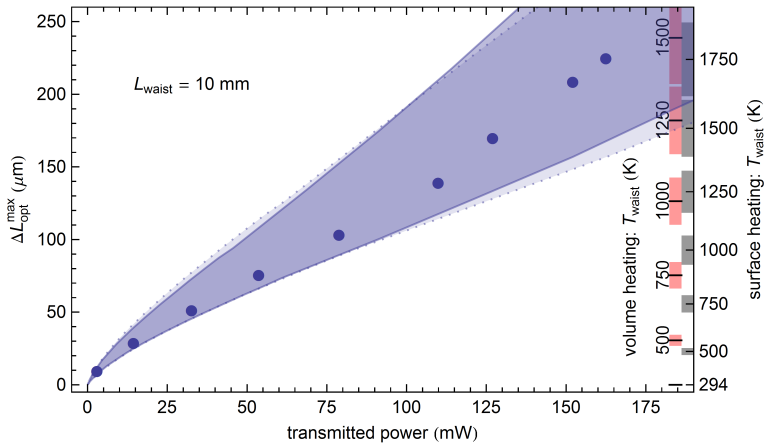

Figure A.6: *Maximum optical path length change as function of the heating laser power together with the model predictions using heating by volume absorption (dotted lines and light shaded region) and heating by surface absorption (solid lines and dark shaded region) for TOF-resonator 3 at $p \approx 10^{-6}$ mbar. Red temperature ticks: prediction for heating by volume absorption.*

ing. We find slightly higher predictions for the initial thermalization times which are still compatible with the measurement results. However, the final thermalization times are approximately 50 % longer compared to the predicitons based on heating by surface absorption and, comparing to the measurement results, largely overestimate the final thermalization time by approximately the same amount. This can be explained by the lower temperatures for a given ΔL_{opt} which in turn lead to a less efficient heat transport via heat radiation.

Summarizing, we have compared the model predictions for the two extreme cases of heating by pure surface and pure volume absorption. We find a good agreement of the predictions for the maximum optical path length change as function of the transmitted power and the initial thermalization times for both theories. The predicted equilibrium temperatures of the waist are ≈ 25 % lower than the values obtained by assuming heating by surface absorption, which are nevertheless nearly in agreement when considering their high uncertainty. The predictions of the final thermalization times are mostly ≈ 50 % higher compared to the data and the prediction based on heating by surface absorption which we attribute to the higher energy deposition in the taper regions and the corresponding lower temperatures.

The high transmission values of fused silica in the NIR spectral region in conjunction with the findings from other groups that the absorption is dominated by surface pollutants [127] leads us to the conclusion that the heating is dominated by absorption from pollutants on the fiber surface. This is supported by the excellent agreement of the theory predictions based on heating by surface absorption with the data and the disagreement of the measured final thermalization times with the theory prediction assuming heating by volume absorption.

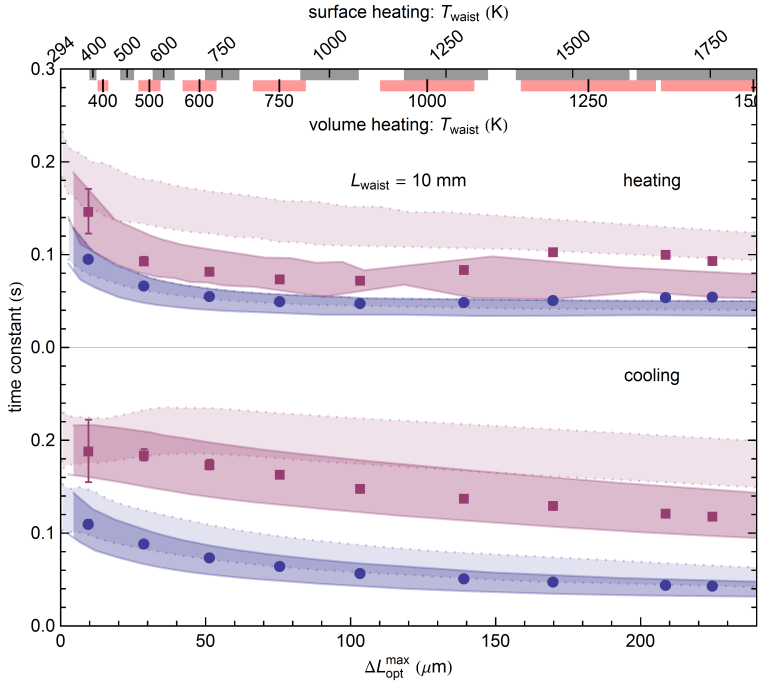

Figure A.7: *Thermalization time constants as function of the heating laser power together with the model prediction with a heating source from volume absorption (dotted lines and light shaded region) and that from surface absorption (solid lines and dark shaded region). Red temperature ticks: prediction for heating by volume absorption. (TOF-resonator 3 at $p = 10^{-7}$ mbar)*

A.8 Thermalization via heat radiation at cryogenic temperatures in a vacuum environment

The thermal radiation of a nanofiber at cryogenic temperatures is of special interest for studying near-field effects in heat radiation. At low temperatures around a few Kelvin, the thermal wavelength λ_T

$$\lambda_T = \frac{\hbar\, c}{k_\mathrm{B}\, T} \approx \frac{2.3\ \mathrm{mm}}{T[\mathrm{K}]}\ , \tag{A.35}$$

can easily reach values that are comparable to the distances involved in the experiment. In this case near field effects can modify or even dominated the radiation heat exchange [175]. Previous experiments have been limited towards extremely small separations by the surface roughness of the objects which prevents an exact measurement of the objects separation to the thermal bath. Measurements at cryogenic temperatures may provide a possibility to overcome this limitation: The near-field heat transfer is enhanced by the overlap of the evanescent fields of the bodies. These fields decay on the scale of the heat radiation wavelength. Therefore, the figure of merit for the heat transfer scaling is the ratio of the separation d and the thermally emitted wavelengths: d/λ_T. When increasing the wavelength of the thermally radiation by measuring at lower temperature one can perform measurements in the same regime of d/λ_T at higher separations and thereby overcome the current limitations. Here, the capabilities of nanofibers to investigate the

near-field thermal radiation heat transfer at cryogenic temperatures is studied. Therefore, I estimate the thermalization times of the TOF in a temperature range $T \geq 2$ K that is accessible with a helium cryostate that exists in our group [66].

Using a helium-cryostate, nanofibers can be cooled to a temperature of 2 K. Therefore, I here consider the temperature range of 1 K to 50 K for my estimations, corresponding to the thermal wavelength range 2.3 mm down to ≈ 50 µm. The cryostate mug in which the TOF is placed has a diameter of approximately 50 mm which is larger than the thermal wavelength in the temperature range that is considered here. It would, thereby, allow for reference measurements with reduced near-field effects. The most promising approach to probe near-field effects in this setup is to bring a plate or sphere near the fiber. For the second material we study the two cases of a metal at the example of gold and fused silica, i.e. a material with matched dielectric function.

Two cases regarding the distance of the fiber to the surroundings d are of special interest: First, $d \approx 100$ µm which is much smaller than the thermal wavelength at 4 K and can be implemented. Second, the closest possible distance which is limited to be approximately $d \approx 2$ µm by the restriction that the surroundings are not allowed to enter the evanescent field of the fiber and thereby spoil the fiber transmission.

For an unambiguous measurement of the radiated power, the latter has to be the dominating heat-exchange mechanism and the time scales have to be in an experimentally accessible region. Therefore, I study the time constants from each heat transfer mechanism individually. Starting from the heat transfer equation $\partial_t T = -\mathrm{d}H/(\rho\, c_\mathrm{p}\, \pi R^2\, \mathrm{d}L)$ (compare Eq. 3.19) I linearize the right side of the equation $\mathrm{d}H' := \mathrm{d}H/(\rho\, c_\mathrm{p}\, \pi R^2\, \mathrm{d}L)$ as function of T for small temperature changes $\delta T = T - T_1$ around an equilibrium temperature T_1 for each heat transfer mechanism:

$$\mathrm{d}H'(T) = \mathrm{d}H'(T_1) + \partial_T\, \mathrm{d}H'(T_1) \cdot (T - T_1)\,. \tag{A.36}$$

The expression $\mathrm{d}H'(T_1)$ vanishes since the system is in equilibrium at T_1 so that we find a differential equations with an exponential function as solution:

$$\partial_t\, \delta T = -\partial_T\, \mathrm{d}H'(T_1) \cdot \delta T \quad \Rightarrow \quad \delta T = A_1 \exp(-t \cdot \partial_T\, \mathrm{d}H'(T_1))\,, \tag{A.37}$$

with A_1 being an arbitrary constant. Here, the thermalization time is given by $\alpha(T_1) = (\partial_T\, \mathrm{d}H'\,(T_1))^{-1}$. Note that the heat capacity is temperature dependent and can be approximated by the power law $T^{2.9}$ at cryogenic temperatures, compare Ch. A.5. The total thermalization time constant can be obtained by inversely adding the individual time constants of the participating thermalization processes: $\alpha_\mathrm{tot}^{-1} = \alpha_1^{-1} + \alpha_2^{-1} + \ldots$.

The geometry of a silica cylinder that is mounted parallel to a metal (silica) plate has, has been, to the best of my knowledge, not been studied in literature. However, an estimate can be found from FED computations for a sphere-plate geometry which then is normalized to the sphere radius to obtain a heat transfer rate per unit length. This estimate was obtained based on the work of and in collaboration with M. Krüger and V. Golyk [176, 177]. In the following, the time constants of the individual heat transfer processes are estimated which are then compared as function of temperature in one figure in the end.

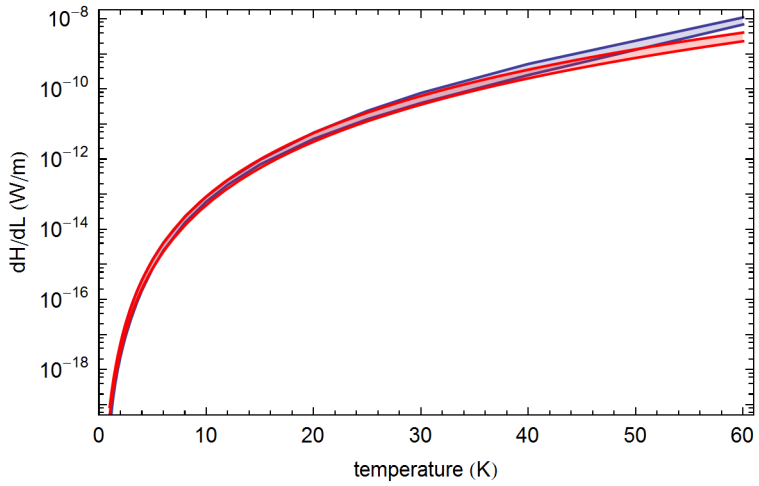

Figure A.8: *Total emitted power of a 500 nm diameter silica cylinder at cryogenic temperatures.*

Far-field heat radiation

For cryogenic temperatures where the optical frequency of the thermal radiation is much smaller than that of the lowest resonance of fused silica (~ 20 THz corresponding to a wavelength of ~ 20 µm) the permittivity can be approximated by

$$\epsilon = \epsilon_c + \mathbb{i}\,\omega\,\lambda_{\text{in}}/c + O(\omega^2)\,, \tag{A.38}$$

where ϵ_c and λ_{in} are material constants that are determined by a fit to literature values to be $\lambda_{\text{in}} = (940 \pm 280)$ nm and $\epsilon_c = 3.7 \pm 0.2$, see Ch. A.4. In this approximation, the radiated power of a silica cylinder with radius R simplifies to an analytic expression which reads [111]:

$$\frac{\mathrm{d}H}{\mathrm{d}x} = \frac{4\pi^4}{189}\,\frac{\hbar\,c^2\,\lambda_{\text{in}}\,R\,(2\pi\,R)}{\lambda_{\text{T}}^6}\left(1 + \frac{8}{(\epsilon_0+1)^2}\right) = (7 \pm 2)\cdot 10^{-20}\,T[K]^6 \cdot \frac{\text{W}}{\text{m}}\,, \tag{A.39}$$

where the value was computed for a fiber radius of $R = 250$ nm. For comparison the far-field radiated power per unit length is shown in Fig. A.8 either computed by this approximation or the full model. We find excellent agreement for temperatures below 30 K. The thermalization time constant takes the form

$$\alpha_{\text{ff}} = \left(\frac{6 - 2.9}{c_{\text{p}}\,\rho\,\pi R^2\,T}\cdot\frac{\mathrm{d}H}{\mathrm{d}L}\right)^{-1}\,. \tag{A.40}$$

Near field heat radiation

Analytic approximations for the radiative near-field heat exchange can be found for a silica sphere near a silica (metal) plate in two limiting cases. These concern the relation of the separation between the sphere and the plane d, the thermal wavelength and the sphere's radius R_{s}. We note, that the radius of the fiber has to be smaller than the minimum

absorption length in the spectrum (skin-depth). In the case of both, the sphere and the plate consisting of silica one obtains:

$$\lim_{d\gg\lambda_\mathrm{T}\gg R^\mathrm{sp}} \frac{\mathrm{d}H}{\mathrm{d}L} = \frac{\pi^3}{60}\,\frac{\hbar c^2\,\lambda_\mathrm{in}^\mathrm{sp}\,R^2\,\sqrt{\epsilon_\mathrm{c}^\mathrm{pl}-1}}{d^2\,\lambda_\mathrm{T}^4} = (1.7\pm0.5)\cdot10^{-14}\,\frac{T[\mathrm{K}]^4}{d[\mu\mathrm{m}]^2}\cdot\frac{\mathrm{W}}{\mathrm{m}}\,, \quad \text{(A.41)}$$

$$\lim_{\lambda_\mathrm{T}\gg d\gg R^\mathrm{sp}} \frac{\mathrm{d}H}{\mathrm{d}L} = \frac{\pi^3}{30}\,\frac{\hbar c^2\,\lambda_\mathrm{in}^\mathrm{pl}\,\lambda_\mathrm{in}^\mathrm{sp}\,R^2}{d^3\,\lambda_\mathrm{T}^4\,(\epsilon_\mathrm{c}^\mathrm{pl}+1)^2} = (9.3\pm4.5)\cdot10^{-16}\,\frac{T[\mathrm{K}]^4}{d[\mu\mathrm{m}]^3}\cdot\frac{\mathrm{W}}{\mathrm{m}}\,. \quad \text{(A.42)}$$

where the superscripts sp and pl indicate whether the quantity refers to the sphere or plate respectively, the values are give for a 500 nm diameter silica fiber taking the uncertainties of the complex refractive index into account.

Now, consider the other case of a silica sphere and a metallic plate. The dielectric function of a metal is given by the Drude model $\epsilon(\omega) = \epsilon_\infty - \omega_p^2/(\omega^2 + i\omega\,\omega_\tau)$, where $\omega_\mathrm{p} = 2\pi\,2.3\cdot10^{15}$ Hz is the plasma frequency and $\omega_\tau = 2\pi\,6.9\cdot10^{12}$ is the characteristic collision rate of gold [178]. Then, we find

$$\lim_{d\gg\lambda_\mathrm{T}\gg R^\mathrm{sp}} \frac{\mathrm{d}H}{\mathrm{d}L} = \frac{1}{\sqrt{2}\pi}\,\frac{\hbar c^{3/2}\,\omega_\mathrm{p}\,\lambda_\mathrm{in}^\mathrm{sp}\,R^2}{d^2\,\omega_\tau^{1/2}\,\lambda_\mathrm{T}^{7/2}} = (2.8\pm0.8)\cdot10^{-11}\,\frac{T[\mathrm{K}]^{7/2}}{d[\mu\mathrm{m}]^2}\cdot\frac{\mathrm{W}}{\mathrm{m}}\,, \quad \text{(A.43)}$$

$$\lim_{\lambda_\mathrm{T}\gg d\gg R^\mathrm{sp}} \frac{\mathrm{d}H}{\mathrm{d}L} = \frac{\pi^3}{30}\,\frac{\hbar c^3\,\omega_\tau\,\lambda_\mathrm{in}^\mathrm{sp}\,R^2}{d^3\,\omega_\mathrm{p}^2\,\lambda_\mathrm{T}^4} = (1.3\pm0.4)\cdot10^{-18}\,\frac{T[\mathrm{K}]^4}{d[\mu\mathrm{m}]^3}\cdot\frac{\mathrm{W}}{\mathrm{m}}\,, \quad \text{(A.44)}$$

Surprisingly, when comparing the heat exchange rates in the two assemblies we find an increase of three orders of magnitude for the silica–metal case in the limit of $d \gg \lambda_T$ and inverse situation for $d \ll \lambda_T$.

For a spacing of 100 µm both limiting cases have to be considered since it is comparable to the thermal wavelength, whereas for 2 µm spacing the distance is much smaller than the thermal wavelength. Taking the temperature scaling of the near-field radiated power into account one obtains for the thermalization time constants:

$$\alpha_\mathrm{nf} = \left(\frac{7/2-2.9}{c_\mathrm{p}\,\rho\,\pi R^2\,T}\cdot\frac{\mathrm{d}H}{\mathrm{d}L}\right)^{-1} \quad \text{for} \quad d \gg \lambda_T \gg R^\mathrm{sp} \quad \text{(A.45)}$$

$$\alpha_\mathrm{nf} = \left(\frac{4-2.9}{c_\mathrm{p}\,\rho\,\pi R^2\,T}\cdot\frac{\mathrm{d}H}{\mathrm{d}L}\right)^{-1} \quad \text{for} \quad \lambda_\mathrm{T} \gg d \gg R^\mathrm{sp}\,. \quad \text{(A.46)}$$

Heat conduction

In order to estimate the order of magnitude of the heat transfer by heat conduction, we use a simplified approach. For this purpose, the waist is modeled as a heat reservoir at an elevated temperature that transfers its heat to another heat reservoir given by a part of the taper of sufficiently large heat capacity. The spacing of these heat reservoirs is estimated from the results of the thermalization model, see Fig. 3.6, to be at least $\Delta x \geq 5$ mm, and at most the distance of the nanofiber to the fiber holder $\Delta x \leq 50$ mm.

The rate at which the heat energy flows through an area A into a volume is given by $\mathrm{d}H/\mathrm{d}t = -q_\mathrm{hc}\,A\,\partial_x T$, where q_hc is the heat conductivity [124]. The symmetry of

the TOF-profile results in a symmetric heat flow and, therefore, allows to consider half the TOF-profile with the center of the waist as the origin. Using the definition of the heat capacity and considering that the heat flow is directed out of the waist volume and therefore is negative we find the time evolution of the waist temperature T_w:

$$\frac{\mathrm{d}T_\mathrm{w}}{\mathrm{d}t} = \frac{q_\mathrm{hc}}{c_\mathrm{p}\,\rho\,L_\mathrm{waist}/2}\,\frac{\mathrm{d}T}{\mathrm{d}x} \approx \frac{2\,q_\mathrm{hc}}{c_\mathrm{p}\,\rho\,L_\mathrm{waist}}\,\frac{-(T_\mathrm{w}-T_0)}{\Delta x}\,, \tag{A.47}$$

where the temperature gradient is approximated by a linear decrease of T from the waist temperature to the temperature of the environment (T_0) within the length Δx and A is set to that of the nanofiber cross-section $A = \pi R^2$.

From this we find a time constant of the thermalization via heat conduction of

$$\alpha_\mathrm{cond.} = \left(\frac{2\,q_\mathrm{hc}}{c_\mathrm{p}\,\rho\,L_\mathrm{waist}\,\Delta x}\right)^{-1}\,. \tag{A.48}$$

Note that the temperature dependence of the heat conductivity is small and can, therefore, be neglected, compare Ch. A.5. As a cross-check one may estimate the corresponding thermalization time constant at room temperature and finds $\alpha_\mathrm{cond.} = 13$ s. This value is in good agreement with the FBG thermalization time, see Ch. 3.4.3, which substantiates this estimation.

Conclusions

The time constants that were obtained from the previous considerations are shown as function of the nanofiber temperature in Fig. A.9. We find a vast spread of thermalization constants covering 14 orders of magnitude. The heat conduction in the bulk material dominates the heat transport for small temperatures by orders of magnitude. This results from the relatively weak temperature dependence of the heat conductivity changing by about two orders of magnitude in the range from 1 K to 300 K. The decrease of the time constant is governed by heat capacity which changes 6 orders of magnitude in the same temperature range. While the latter influences the absolute value of the time constants, it enters in each one in the same way and, therefore, has no effect on their ratio.

Nevertheless, the estimations show that the heat transfer rate can be strongly increased by bringing a material with matched refractive index profile closer to the fiber than the thermal wavelength, whereas a metal plate yields no such increase compared to the far-field case. We note however, that this may only be qualitatively interpreted since the assumption that the $R \gg d$ is barely fulfilled at $d = 2$ µm.

When considering the case in which the separations are comparable to the thermal wavelength ($d \sim \lambda_T$), both approximations have to be taken into account so that the uncertainty covers several orders of magnitude. Based on the results presented here, no conclusion whether the near-field heat transfer rate exceeds that of the far-field can be reached. Still, for temperatures of few Kelvin the approximation $d \ll \lambda_\mathrm{T} \sim 1$ mm is more suitable than the opposite case.

While these estimations provied only a starting point for further investigations, we conclude that an experimental investigation of near-field effects in the cryogenic temperature region with the proposed geometry is not feasible. However, there may be other

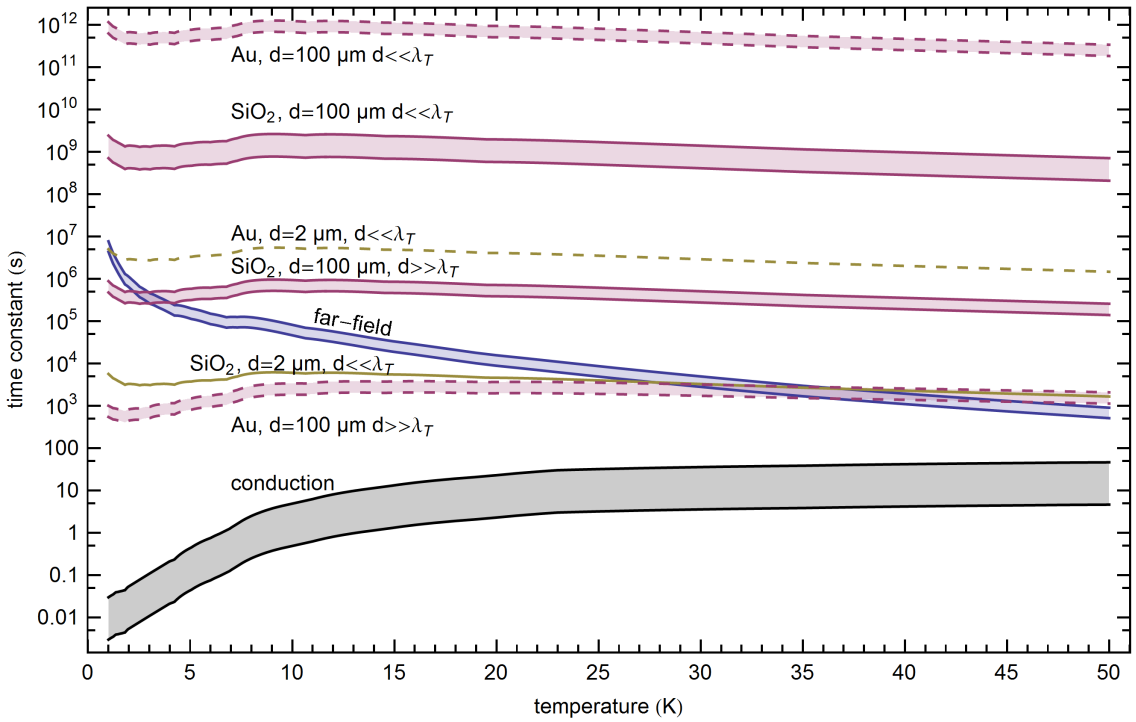

Figure A.9: *Time constants of the individial thermalization mechanisms as function of the nanofiber temperature. The two lines limiting each band are the minimum and maximum prediction including the uncertainties of λ_{in} and ϵ_{c} in case of the radiative terms or λ in case of the heat conduction. Black: Heat conduction in silica, blue: far-field heat radiation, red: near-field heat radiation at $d = 100$ µm, yellow: near-field heat radiation at $d = 2$ µm. The values for the setup based on a silica (gold) plate are shown as solid (dashed) lines in corresponding colors.*

geometries worth considering in which the thermal conductance of the material is not dominating. One major disadvantage of the fiber geometry in this context is the fixed ratio of heat capacity and cross section through which the heat is exchanged by conduction. This may be overcome by using a larger probe with a thin suspension so that the coupling to the heat bath is significantly smaller.

A.9 Blue print of the vacuum chamber

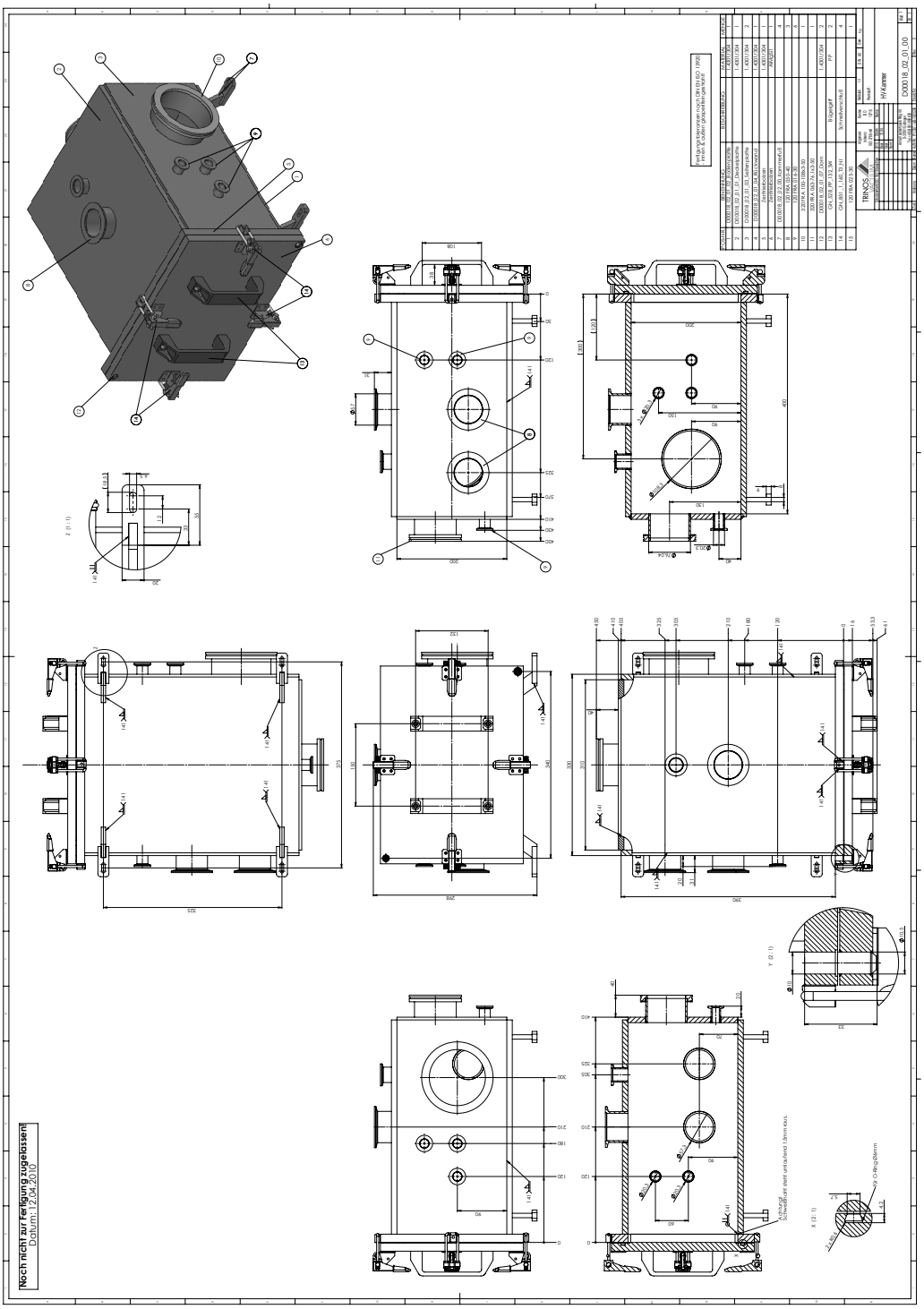

Bibliography

[1] M. Planck, "Zur Theorie des Gesetzes der Energieverteilung im Normalspectrum," Ann. Phys. **309**, 533 (1901).

[2] "http://www.nobelprize.org/nobel_prizes/physics/laureates/2012," (2013), accessed 2013-11-22.

[3] L. Tong, R. R. Gattass, J. B. Ashcom, S. He, J. Lou, M. Shen, I. Maxwell, and E. Mazur, "Subwavelength-diameter silica wires for low-loss optical wave guiding," Nature **426**, 816 (2003).

[4] J. Villatoro and D. Monzón-Hernández, "Fast detection of hydrogen with nano fiber tapers coated with ultra thin palladium layers," Opt. Express **13**, 5087 (2005).

[5] P. Polynkin, A. Polynkin, N. Peyghambarian, and M. Mansuripur, "Evanescent field-based optical fiber sensing device for measuring the refractive index of liquids in microfluidic channels," Opt. Lett. **30**, 1273 (2005).

[6] L. Zhang, F. Gu, J. Lou, X. Yin, and L. Tong, "Fast detection of humidity with a subwavelength-diameter fiber taper coated with gelatin film," Opt. Express **16**, 13349 (2008).

[7] J. Zhang, Q. Sun, R. Liang, J. Wo, D. Liu, and P. Shum, "Microfiber Fabry-Pérot interferometer fabricated by taper-drawing technique and its application as a radio frequency interrogated refractive index sensor," Opt. Lett. **37**, 2925 (2012).

[8] F. Warken, E. Vetsch, D. Meschede, M. Sokolowski, and A. Rauschenbeutel, "Ultra-sensitive surface absorption spectroscopy using sub-wavelength diameter optical fibers," Opt. Express **15**, 11952 (2007).

[9] A. Stiebeiner, O. Rehband, R. Garcia-Fernandez, and A. Rauschenbeutel, "Ultra-sensitive fluorescence spectroscopy of isolated surface-adsorbed molecules using an optical nanofiber," Opt. Express **17**, 21704 (2009).

[10] T. A. Birks, W. J. Wadsworth, and P. S. J. Russell, "Supercontinuum generation in tapered fibers," Opt. Lett. **25**, 1415 (2000).

[11] V. Grubsky and A. Savchenko, "Glass micro-fibers for efficient third harmonic generation," Opt. Express **13**, 6798 (2005).

[12] R. R. Gattass, G. T. Svacha, L. Tong, and E. Mazur, "Supercontinuum generation in submicrometer diameter silica fibers," Opt. Express **14**, 9408 (2006).

[13] U. Wiedemann, K. Karapetyan, C. Dan, D. Pritzkau, W. Alt, S. Irsen, and D. Meschede, "Measurement of submicrometre diameters of tapered optical fibres using harmonic generation," Opt. Express **18**, 7693 (2010).

[14] G. Sagué, E. Vetsch, W. Alt, D. Meschede, and A. Rauschenbeutel, "Cold-atom physics using ultrathin optical fibers: Light-induced dipole forces and surface interactions," Phys. Rev. Lett. **99**, 163602 (2007).

[15] K. P. Nayak, P. N. Melentiev, M. Morinaga, F. Le Kien, V. I. Balykin, and K. Hakuta, "Optical nanofiber as an efficient tool for manipulating and probing atomic fluorescence," Opt. Express **15**, 5431 (2007).

[16] K. P. Nayak and K. Hakuta, "Single atoms on an optical nanofibre," New J. Phys. **10**, 053003 (2008).

[17] M. J. Morrissey, K. Deasy, Y. Wu, S. Chakrabarti, and S. Nic Chormaic, "Tapered optical fibers as tools for probing magneto-optical trap characteristics," Rev. Sci. Instrum. **80**, 053102 (2009).

[18] E. Vetsch, D. Reitz, G. Sagué, R. Schmidt, S. T. Dawkins, and A. Rauschenbeutel, "Optical interface created by laser-cooled atoms trapped in the evanescent field surrounding an optical nanofiber," Phys. Rev. Lett. **104**, 203603 (2010).

[19] A. Goban, K. S. Choi, D. J. Alton, D. Ding, C. Lacroûte, M. Pototschnig, T. Thiele, N. P. Stern, and H. J. Kimble, "Demonstration of a state-insensitive, compensated nanofiber trap," Phys. Rev. Lett. **109**, 033603 (2012).

[20] M. J. Morrissey, K. Deasy, M. Frawley, R. Kumar, E. Prel, L. Russell, V. G. Truong, and S. Nic Chormaic, "Spectroscopy, manipulation and trapping of neutral atoms, molecules, and other particles using optical nanofibers: A review," Sensors **13**, 10449 (2013).

[21] S. Arnold, M. Khoshsima, I. Teraoka, S. Holler, and F. Vollmer, "Shift of whispering-gallery modes in microspheres by protein adsorption," Opt. Lett. **28**, 272 (2003).

[22] S. M. Spillane, T. J. Kippenberg, O. J. Painter, and K. J. Vahala, "Ideality in a fiber-taper-coupled microresonator system for application to cavity quantum electrodynamics," Phys. Rev. Lett. **91**, 043902 (2003).

[23] K. Srinivasan, P. E. Barclay, M. Borselli, and O. Painter, "Optical-fiber-based measurement of an ultrasmall volume high-q photonic crystal microcavity," Phys. Rev. B **70**, 081306 (2004).

[24] P. E. Barclay, K. Srinivasan, O. Painter, B. Lev, and H. Mabuchi, "Integration of fiber-coupled high-qsinx microdisks with atom chips," Appl. Phys. Lett. **89**, 131108 (2006).

[25] B. Min, S. Kim, K. Okamoto, L. Yang, A. Scherer, H. Atwater, and K. Vahala, "Ultralow threshold on-chip microcavity nanocrystal quantum dot lasers," Appl. Phys. Lett. **89**, 191124 (2006).

[26] K. Srinivasan and O. Painter, "Mode coupling and cavity–quantum-dot interactions in a fiber-coupled microdisk cavity," Phys. Rev. A **75**, 023814 (2007).

[27] K. Srinivasan, O. Painter, A. Stintz, and S. Krishna, "Single quantum dot spectroscopy using a fiber taper waveguide near-field optic," Appl. Phys. Lett. **91**, 091102 (2007).

[28] C. Junge, D. O'Shea, J. Volz, and A. Rauschenbeutel, "Strong coupling between single atoms and nontransversal photons," Phys. Rev. Lett. **110**, 213604 (2013).

[29] K. J. Vahala, "Optical microcavities," Nature **424**, 839 (2003).

[30] O. Benson, "Assembly of hybrid photonic architectures from nanophotonic constituents," Nature **480**, 193 (2011), and references therein.

[31] K. M. Birnbaum, A. Boca, R. Miller, A. D. Boozer, T. E. Northup, and H. J. Kimble, "Photon blockade in an optical cavity with one trapped atom," Nature **436**, 87 (2005).

[32] T. Aoki, B. Dayan, E. Wilcut, W. P. Bowen, A. S. Parkins, T. J. Kippenberg, K. J. Vahala, and H. J. Kimble, "Observation of strong coupling between one atom and a monolithic microresonator," Nature **443**, 671 (2006).

[33] T. Wilk, S. C. Webster, A. Kuhn, and G. Rempe, "Single-atom single-photon quantum interface," Science **317**, 488 (2007).

[34] M. L. Terraciano, R. Olson Knell, D. G. Norris, J. Jing, A. Fernandez, and L. A. Orozco, "Photon burst detection of single atoms in an optical cavity," Nat Phys **5**, 480 (2009).

[35] T. Kampschulte, W. Alt, S. Brakhane, M. Eckstein, R. Reimann, A. Widera, and D. Meschede, "Optical control of the refractive index of a single atom," Phys. Rev. Lett. **105**, 153603 (2010).

[36] C. Toninelli, Y. Delley, T. Stoferle, A. Renn, S. Gotzinger, and V. Sandoghdar, "A scanning microcavity for in situ control of single-molecule emission," Appl. Phys. Lett. **97**, 021107 (2010).

[37] C. Sayrin, I. Dotsenko, X. Zhou, B. Peaudecerf, T. Rybarczyk, S. Gleyzes, P. Rouchon, M. Mirrahimi, H. Amini, M. Brune, J.-M. Raimond, and S. Haroche, "Real-time quantum feedback prepares and stabilizes photon number states," Nature **477**, 73 (2011).

[38] J. Volz, R. Gehr, G. Dubois, J. Esteve, and J. Reichel, "Measurement of the internal state of a single atom without energy exchange," Nature **475**, 210 (2011).

[39] J. Goldwin, M. Trupke, J. Kenner, A. Ratnapala, and E. Hinds, "Fast cavity-enhanced atom detection with low noise and high fidelity," Nat. Commun. **2**, 418 (2011).

[40] J. D. Thompson, T. G. Tiecke, N. P. de Leon, J. Feist, A. V. Akimov, M. Gullans, A. S. Zibrov, V. Vuletić, and M. D. Lukin, "Coupling a single trapped atom to a nanoscale optical cavity," Science **340**, 1202 (2013).

[41] A. G. Worthing, "Deviation from lambert's law and polarization of light emitted by incandescent tungsten, tantalum and molybdenum and changes in the optical constants of tungsten with temperature," J. Opt. Soc. Am. **13**, 635 (1926), and references therein.

[42] Y. Ohman, "Polarized thermal emission from narrow tungsten filaments," Nature **192**, 254 (1961).

[43] G. Kirchhoff, "Über das Verhältniss zwischen dem Emissionsvermögen und dem Absorptionsvermögen der Körper für Wärme und Licht," Ann. Phys. **185**, 275 (1860).

[44] S. Shen, A. Narayanaswamy, and G. Chen, "Surface phonon polaritons mediated energy transfer between nanoscale gaps," Nano Lett. **9**, 2909 (2009), pMID: 19719110, http://pubs.acs.org/doi/pdf/10.1021/nl901208v .

[45] E. Rousseau, A. Siria, G. Jourdan, S. Volz, F. Comin, J. Chevrier, and J.-J. Greffet, "Radiative heat transfer at the nanoscale," Nat. Photon. **3**, 514 (2009).

[46] S. M. Rytov, Y. A. Kravtsov, and V. I. Tatarskii, *Principles of statistical radiophysics*, Vol. 3 (Springer, Berlin, 1978).

[47] C. F. Bohren and D. R. Huffmann, *Absorption and Scattering of Light by Small Particles* (Wiley, New York, 1998).

[48] T. C. Bond and R. W. Bergstrom, "Light absorption by carbonaceous particles: An investigative review," Aerosol Sci. Tech. **40**, 27 (2006).

[49] T. C. Bond, S. J. Doherty, D. W. Fahey, P. M. Forster, T. Berntsen, B. J. DeAngelo, M. G. Flanner, S. Ghan, B. Kärcher, D. Koch, S. Kinne, Y. Kondo, P. K. Quinn, M. C. Sarofim, M. G. Schultz, M. Schulz, C. Venkataraman, H. Zhang, S. Zhang, N. Bellouin, S. K. Guttikunda, P. K. Hopke, M. Z. Jacobson, J. W. Kaiser, Z. Klimont, U. Lohmann, J. P. Schwarz, D. Shindell, T. Storelvmo, S. G. Warren, and C. S. Zender, "Bounding the role of black carbon in the climate system: A scientific assessment," J. Geophys. Res-Atmos. **118**, 5380 (2013).

[50] J.-J. Greffet, R. Carminati, K. Joulain, J.-P. Mulet, S. Mainguy, and Y. Chen, "Coherent emission of light by thermal sources," Nature **416**, 61 (2002).

[51] X. Liu, T. Tyler, T. Starr, A. F. Starr, N. M. Jokerst, and W. J. Padilla, "Taming the blackbody with infrared metamaterials as selective thermal emitters," Phys. Rev. Lett. **107**, 045901 (2011).

[52] J. A. Schuller, T. Taubner, and M. L. Brongersma, "Optical antenna thermal emitters," Nat. Photonics **3**, 658 (2009).

[53] "`http://www.nobelprize.org/nobel_prizes/physics/laureates/2009`," (2013), accessed 2013-11-22.

[54] R. Garcia-Fernandez, W. Alt, F. Bruse, C. Dan, K. Karapetyan, O. Rehband, A. Stiebeiner, U. Wiedemann, D. Meschede, and A. Rauschenbeutel, "Optical nanofibers and spectroscopy," Appl. Phys. B **105**, 3 (2011).

[55] J. Chan, T. P. Mayer Alegre, A. H. Safavi-Naeini, J. T. Hill, A. Krause, S. Gröblacher, M. Aspelmeyer, and O. Painter, "Laser cooling of a nanomechanical oscillator into its quantum ground state," Nature **478**, 89 (2011).

[56] L. Russell, K. Deasy, M. J. Daly, M. J. Morrissey, and S. N. Chormaic, "Sub-doppler temperature measurements of laser-cooled atoms using optical nanofibres," Meas. Sci. Technol. **23**, 015201 (2012).

[57] H. Lee, T. Chen, J. Li, K. Y. Yang, S. Jeon, O. Painter, and K. J. Vahala, "Chemically etched ultrahigh-q wedge-resonator on a silicon chip," Nat. Photonics **6**, 369 (2012).

[58] R. Riviere, O. Arcizet, A. Schliesser, and T. J. Kippenberg, "Evanescent straight tapered-fiber coupling of ultra-high q optomechanical micro-resonators in a low-vibration helium-4 exchange-gas cryostat," Rev. Sci. Instrum. **84**, 043108 (2013).

[59] T. A. Birks and Y. W. Li, "The shape of fiber tapers," J. Lightwave Technol. **10**, 432 (1992).

[60] F. Warken, A. Rauschenbeutel, and T. Bartholomäus, "Fiber pulling profits from precise positioning," Photon. Spectra **42/3**, 73 (2008).

[61] A. Yariv, *Optical Electronics* (Saunders College Publishing, Philadelphia, 1991).

[62] A. W. Snyder and J. D. Love, *Optical Waveguide Theory* (Chapman and Hall, New York, 1983).

[63] B. E. A. Saleh and M. C. Teich, *Fundamentals of photoics*, 2nd ed. (Wiley, New York, 2007).

[64] F. Le Kien and K. Hakuta, "Cavity-enhanced channeling of emission from an atom into a nanofiber," Phys. Rev. A **80**, 053826 (2009).

[65] F. Warken, *Ultradünne Glasfasern als Werkzeug zur Kopplung von Licht und Materie*, Ph.D. thesis, Rheinische Friedrich-Wilhelm Universität, Bonn (2007).

[66] A. Stiebeiner, *Nanofiber-based Spectroscopy of Organic Molecules*, Ph.D. thesis, Johannes Gutenberg-Universität Mainz (2014).

[67] S. Ravets, J. E. Hoffman, L. A. Orozco, S. L. Rolston, G. Beadie, and F. K. Fatemi, "A low-loss photonic silica nanofiber for higher-order modes," Opt. Express **21**, 18325 (2013).

[68] S. Ravets, J. E. Hoffman, P. R. Kordell, J. D. Wong-Campos, S. L. Rolston, and L. A. Orozco, "Intermodal energy transfer in a tapered optical fiber: optimizing transmission," J. Opt. Soc. Am. A **30**, 2361 (2013).

[69] A. Stiebeiner, R. Garcia-Fernandez, and A. Rauschenbeutel, "Design and optimization of broadband tapered optical fibers with a nanofiber waist," Opt. Express **18**, 22677 (2010).

[70] R. Kitamura, L. Pilon, and M. Jonasz, "Optical constants of silica glass from extreme ultraviolet to far infrared at near room temperature," Appl. Opt. **46**, 8118 (2007).

[71] J. Canning, "Fibre gratings and devices for sensors and lasers," Laser Photonics Rev. **2**, 275 (2008).

[72] J.-L. Kou, M. Ding, J. Feng, Y.-Q. Lu, F. Xu, and G. Brambilla, "Microfiber-based Bragg gratings for sensing applications: A review," Sensors **12**, 8861 (2012).

[73] B.-O. Guan, J. Li, L. Jin, and Y. Ran, "Fiber Bragg gratings in optical microfibers," Opti. Fiber Technol. , Accepted (2013).

[74] V. Hodzic, J. Orloff, and C. C. Davis, "Periodic structures on biconically tapered optical fibers using ion beam milling and boron implantation," J. Lightwave Technol. **22**, 1610 (2004).

[75] W. Liang, L. Yang, J. K. Poon, Y. Huang, K. J. Vahala, and A. Yariv, "Transmission characteristics of a Fabry-Perot etalon-microtoroid resonator coupled system," Opt. Lett. **31**, 510 (2006).

[76] Y. Liu, C. Meng, A. P. Zhang, Y. Xiao, H. Yu, and L. Tong, "Compact microfiber Bragg gratings with high-index contrast," Opt. Lett. **36**, 3115 (2011).

[77] M. Ding, P. Wang, T. Lee, and G. Brambilla, "A microfiber cavity with minimal-volume confinement," Appl. Phys. Lett. **99**, 051105 (2011).

[78] F. Le Kien, K. Nayak, and K. Hakuta, "Nanofibers with Bragg gratings from equidistant holes," J. Mod. Opt. **59**, 274 (2012).

[79] W. Liang, Y. Huang, Y. Xu, R. K. Lee, and A. Yariv, "Highly sensitive fiber Bragg grating refractive index sensors," Appl. Phys. Lett. **86**, 151122 (2005).

[80] K. P. Nayak and K. Hakuta, "Photonic crystal formation on optical nanofibers using femtosecond laser ablation technique," Opt. Express **21**, 2480 (2013).

[81] J. Li, X. Shen, L.-P. Sun, and B.-O. Guan, "Characteristics of microfiber Fabry-Perot resonators fabricated by uv exposure," Opt. Express **21**, 12111 (2013).

[82] M. Sadgrove, R. Yalla, K. P. Nayak, and K. Hakuta, "Photonic crystal nanofiber using an external grating," Opt. Lett. **38**, 2542 (2013).

[83] P. Berman, *Cavity quantum electrodynamics* (Academic Press, Inc., Boston, MA (United States), 2008).

[84] A. Zeilinger, "General properties of lossless beam splitters in interferometry," Am. J. Phys. **49**, 882 (1981).

[85] H. Walther, B. T. H. Varcoe, B.-G. Englert, and T. Becker, "Cavity quantum electrodynamics," Rep. Prog. Phys. **69**, 1325 (2006).

[86] C. Gerry and P. Knight, *Introductory Quantum Optics* (Cambridge Press, 2005).

[87] E. Jaynes and F. W. Cummings, "Comparison of quantum and semiclassical radiation theories with application to the beam maser," P. IEEE **51**, 89 (1963).

[88] D. A. Steck, "Cesium D–Line Data (rev. 1.6)," (2003), http://steck.us/alkalidata.

[89] L. Reimer, *Scanning Electron Microscopy - Physics of Image Formation and Microanalysis*, edited by P. W. Hawkes, Optical Sciences, Vol. 45 (Springer Berlin / Heidelberg, 1998).

[90] Y. Fu and N. Bryan, "Investigation of physical properties of quartz after focused ion beam bombardment," Appl. Phys. B **80**, 581 (2005).

[91] H. Karge and R. Mühle, "High dose ion implantation effects in glasses," Nucl. Instrum. Methods B **B65**, 390 (1992).

[92] V. Schneider and R. Syms, "Gallium-doped sol-gel glass waveguides on si substrates by sc-rta," Electron. Lett. **34**, 1849 (1998).

[93] G. S. Cassany, *Cold atom physics using ultra-thin optical fibres*, Ph.D. thesis, Universität Bonn (2008).

[94] D. Hole, P. Townsend, J. Barton, L. Nistor, and J. Van Landuyt, "Gallium cholloid formation during ion implantation of glass," J. Non-Cryst. Sol. **180**, 266 (1995).

[95] S. Mizutani, I. Ohdomari, T. Miyazawa, T. Iwamori, I. Kimura, and K. Yoneda, "Diffusion of gallium in quartz and bulk-fused silica," J. Appl. Phys. **53**, 1470 (1982).

[96] A. van Ommen, "Diffusion of ion-implanted ga in SiO_2," J. Appl. Phys. **57**, 1872 (1985).

[97] A. Mikkelsen, E. Hilner, J. Andersen, S. Ghatnekar-Nilsson, L. Montelius, and A. Zakharov, "Low temperature ga surface diffusion from focused ion beam milled grooves," Nanotechnology **20**, 325304 (2009).

[98] E. Lindner, C. Chojetzki, S. Brückner, M. Becker, M. Rothhardt, and H. Bartelt, "Thermal regeneration of fiber Bragg gratings in photosensitive fibers," Opt. Express **17**, 12523 (2009).

[99] G. Brambilla, F. Xu, P. Horak, Y. Jung, F. Koizumi, N. P. Sessions, E. Koukharenko, X. Feng, G. S. Murugan, J. S. Wilkinson, and D. J. Richardson, "Optical fiber nanowires and microwires: fabrication and applications," Adv. Opt. Photon. **1**, 107 (2009).

[100] D. O'Shea, A. Rettenmaier, and A. Rauschenbeutel, "Active frequency stabilization of an ultra-high q whispering-gallery-mode microresonator," Appl. Phys. B **99**, 623 (2010).

[101] E. Vetsch, S. Dawkins, R. Mitsch, D. Reitz, P. Schneeweiss, and A. Rauschenbeutel, "Nanofiber-based optical trapping of cold neutral atoms," IEEE J. Sel. Top. Quant. **18**, 1763 (2012).

[102] Fibercore Homepage, "http://fibercore.com/product/sm-fiber-for-visible-through-to-near-ir," Accessed 2013-11-06.

[103] Y. Colombe, T. Steinmetz, G. Dubois, F. Linke, D. Hunger, and J. Reichel, "Strong atom-field coupling for Bose-Einstein condensates in an optical cavity on a chip," Nature **450**, 272 (2007).

[104] F. Le Kien and K. Hakuta, "Triggered generation of single guided photons from a single atom in a nanofiber cavity," Phys. Rev. A **83**, 043801 (2011).

[105] F. Le Kien and K. Hakuta, "Intracavity electromagnetically induced transparency in atoms around a nanofiber with a pair of Bragg grating mirrors," Phys. Rev. A **79**, 043813 (2009).

[106] F. Le Kien and K. Hakuta, "Deterministic generation of a pair of entangled guided photons from a single atom in a nanofiber cavity," Phys. Rev. A **84**, 053801 (2011).

[107] A. H. Safavi-Naeini, J. Chan, J. T. Hill, T. P. M. Alegre, A. Krause, and O. Painter, "Observation of quantum motion of a nanomechanical resonator," Phys. Rev. Lett. **108**, 033602 (2012).

[108] R. Siegel and J. R. Howell, *Thermal radiation heat transfer* (McGraw-Hill, 1972).

[109] K. Joulain, J.-P. Mulet, F. Marquier, R. Carminati, and J.-J. Greffet, "Surface electromagnetic waves thermally excited: Radiative heat transfer, coherence properties and casimir forces revisited in the near field," Surf. Sci. Rep. **57**, 59 (2005).

[110] V. P. Carey, G. Chen, C. Grigoropoulos, M. Kaviany, and A. Majumdar, "A review of heat transfer physics," Nanosc. Microsc. Therm. **12**, 1 (2008).

[111] V. A. Golyk, M. Krüger, and M. Kardar, "Heat radiation from long cylindrical objects," Phys. Rev. E **85**, 046603 (2012), arXiv:1109.1769 [quant-ph] .

[112] M. Krüger, T. Emig, and M. Kardar, "Nonequilibrium electromagnetic fluctuations: Heat transfer and interactions," Phys. Rev. Lett. **106**, 210404 (2011).

[113] Y. Fan, S. B. Singer, R. Bergstrom, and B. C. Regan, "Probing planck's law with incandescent light emission from a single carbon nanotube," Phys. Rev. Lett. **102**, 187402 (2009).

[114] J. H. I. Lienhard and J. H. V. Lienhard, *A Heat Transfer Text Book*, 4th ed. (Phlogiston Press, 2011).

[115] H. Tanaka, S. Sawai, K. Morimoto, and K. Hisano, "Evaluation of hemispherical total emissivity for thermal radiation calorimetry," Int. J. Thermophys. **21**, 927 (2000).

[116] M. Reid, A. Rodriguez, and S. Johnson, "Fluctuation-induced phenomena in nanoscale systems: Harnessing the power of noise," P. IEEE **101**, 531 (2013).

[117] J. D. Jackson, *Classical Electrodynamics*, 3rd ed. (Wiley, New York, 1999).

[118] H. B. Callen and T. A. Welton, "Irreversibility and generalized noise," Phys. Rev. **83**, 34 (1951).

[119] H. B. Callen and R. F. Greene, "On a theorem of irreversible thermodynamics," Phys. Rev. **86**, 702 (1952).

[120] G. S. Agarwal, "Quantum electrodynamics in the presence of dielectrics and conductors. i. electromagnetic-field response functions and black-body fluctuations in finite geometries," Phys. Rev. A **11**, 230 (1975).

[121] S. R. de Groot and P. Mazur, *Non-equilibrium Thermodynamics* (Dover New York, 1984).

[122] N. I. of Standards and Technology, "Certificate for standard reference material 739: Fused-silica thermal expansion," (1991), `https://www-s.nist.gov/srmors/certificates/archive/739.pdf`.

[123] E. Palik, *Handbook of thermo-optic coefficients of optical materials with applications*, edited by G. Ghosh, Vol. 3 (Academic Press, London, 1998).

[124] W. Demtröder, *Experimentalphysik 1*, 3rd ed., Vol. 1 (Springer Berlin / Heidelberg, 2003).

[125] J. J. Freeman and A. C. Anderson, "Thermal conductivity of amorphous solids," Phys. Rev. B **34**, 5684 (1986).

[126] J. Horbach, W. Kob, and K. Binder, "Specific heat of amorphous silica within the harmonic approximation," J. Phys. Chem. B **103**, 4104 (1999).

[127] M. Fujiwara, K. Toubaru, and S. Takeuchi, "Optical transmittance degradation in tapered fibers," Opt. Express **19**, 8596 (2011).

[128] S. Pal, T. Sun, K. T. Grattan, S. A. Wade, S. F. Collins, G. W. Baxter, B. Dussardier, and G. Monnom, "Non-linear temperature dependence of Bragg gratings written in different fibres, optimised for sensor applications over a wide range of temperatures," Sensor. Actuator. **112**, 211 (2004).

[129] C. Tan and J. Arndt, "Temperature dependence of refractive index of glassy sio2 in the infrared wavelength range," J. Phys. Chem. Solids **61**, 1315 (2000).

[130] J. H. Wray and J. T. Neu, "Refractive index of several glasses as a function of wavelength and temperature," J. Opt. Soc. Am. **59**, 774 (1969).

[131] C. Liao, D.-n. Wang, Y. Li, T. Sun, and K. T. V. Grattan, "Temporal thermal response of type II-IR fiber Bragg gratings," Appl. Opt. **48**, 3001 (2009).

[132] A. Kersey, M. Davis, H. Patrick, M. Leblanc, K. Koo, C. Askins, M. Putnam, and E. Friebele, "Fiber grating sensors," J. Lightwave Technol. **15**, 1442 (1997).

[133] N. F. Borrelli and R. A. Miller, "Determination of the individual strain-optic coefficients of glass by an ultrasonic technique," Appl. Opt. **7**, 745 (1968).

[134] Y. Kikuchi, H. Sudo, and N. Kuzuua, "Thermal expansion of vitreous silica: Correspondence between dilatation curve and phase transitions in crystalline silica," J. Appl. Phys. **82**, 4121 (1997).

[135] B. Kühn and R. Schadrack, "Thermal expansion of synthetic fused silica as a function of oh content and fictive temperature," J. Non-Cryst. Sol. **355**, 323 (2009).

[136] J. W. Berthold III and S. F. Jacobs, "Ultraprecise thermal expansion measurement of seven low expansion materials," Appl. Opt. **15**, 2344 (1976).

[137] A. J. Barlow and D. N. Payne, "The stress-optic effect in optical fibers," IEEE J. Quantum Elect. **QE-19**, 834 (1983).

[138] R. H. Doremus, "Viscosity of silica," J. Appl. Phys. **92**, 7619 (2002).

[139] J. P. Koulakis, C. D. Mitescu, F. Brochard-Wyart, P.-G. De Gennes, and E. Guyon, "The viscous catenary revisited: experiments and theory," J. Fluid Mech. **609**, 87 (2008).

[140] D. E. Chang, C. A. Regal, S. B. Papp, D. J. Wilson, J. Ye, O. Painter, H. J. Kimble, and P. Zoller, "Cavity opto-mechanics using an optically levitated nanosphere," P. Natl. Acad. Sci. USA **107**, 1005 (2010).

[141] J. Gieseler, B. Deutsch, R. Quidant, and L. Novotny, "Subkelvin parametric feedback cooling of a laser-trapped nanoparticle," Phys. Rev. Lett. **109**, 103603 (2012).

[142] N. Kiesel, F. Blaser, U. Delić, D. Grass, R. Kaltenbaek, and M. Aspelmeyer, "Cavity cooling of an optically levitated submicron particle," P. Natl. Acad. Sci. USA **110**, 14180 (2013).

[143] V. A. Golyk, M. Krüger, M. T. H. Reid, and M. Kardar, "Casimir forces between cylinders at different temperatures," Phys. Rev. D **85**, 065011 (2012), arXiv:1202.1167 [quant-ph] .

[144] K. Eom, H. S. Park, D. S. Yoon, and T. Kwon, "Nanomechanical resonators and their applications in biological/chemical detection: Nanomechanics principles," Physics Reports **503**, 115 (2011).

[145] D. J. Alton, N. P. Stern, T. Aoki, H. Lee, E. Ostby, K. J. Vahala, and H. J. Kimble, "Strong interactions of single atoms and photons near a dielectric boundary," Nat. Phys. **7**, 159 (2011).

[146] D. E. Chang, A. S. Sorensen, E. A. Demler, and M. D. Lukin, "A single-photon transistor using nanoscale surface plasmons," Nat. Phys. **3**, 807 (2007).

[147] L. D. Landau and E. M. Lifshitz, *Course of Theoretical Physics – Theory of Elasticity*, 2nd ed., Vol. 7 (Pergamon Press, 1970).

[148] A. E. H. Love, *A Treatise on the Mathematical Theory of Elasticity*, 4th ed. (Dover New York, 1926).

[149] S. Timoshenko and J. N. Goodier, *Theory of Elasticity*, 2nd ed. (McGraw-Hill, 1951).

[150] S. Timoshenko, *Vibration Problems in Engineering*, 2nd ed. (D. Van Nostrand Comp. Inc., 1937).

[151] S. Spinner, "Temperature dependence of elastic constants of vitreous silica," J. Am. Ceram. Soc. **45**, 394 (1962).

[152] H. G. Pfaender and H. Schröder, *Schott-Glaslexikon* (Moderne Verlags GmbH, 1983).

[153] H. Ni, X. Li, and H. Gao, "Elastic modulus of amorphous SiO_2 nanowires," Appl. Phys. Lett. **88**, 043108 (2006).

[154] E. Silva, L. Tong, S. Yip, and K. Van Vliet, "Size effects on the stiffness of silica nanowires," Small **2**, 239 (2006).

[155] W. C. Elmore and M. A. Heald, *Physics of Waves* (Dover New York, 1985).

[156] H. Engan, Y. Byong, and J. Blake, "Propagation and optical interaction of guided acoustic waves in two-mode optical fibers," J. Lightwave Technol. **6**, 428 (1988).

[157] R. W. Pyle, *Solid Torsional Horns*, Ph.D. thesis, Harvard University, Cambridge (1963).

[158] V. I. Erofeev, V. V. Kazhaev, and N. P. Semerikova, "Torsional waves of finite amplitude in elastic rod," Mech. Sol. **42**, 974 (2007).

[159] M. Chi, B. G. Dennis Jr., and J. Vossoughi, "Transverse and torsional vibrations of an axially-loaded beam with elastically constrained ends," J. Sound Vib. **96**, 235 (1984).

[160] A. G. Webster, "Acoustical impedance and the theory of horns and of the phonograph," P. Natl. Acad. Sci. USA **5**, 275 (1919).

[161] *COMSOL ver. 4.3 Manual* (2013).

[162] P. R. Saulson, "Thermal noise in mechanical experiments," Phys. Rev. D **42**, 2437 (1990).

[163] G. I. González and P. R. Saulson, "Brownian motion of a torsion pendulum with internal friction," Phys. Lett. A **201**, 12 (1995).

[164] C. Wuttke and A. Rauschenbeutel, "Thermalization via heat radiation of an individual object thinner than the thermal wavelength," Phys. Rev. Lett. **111**, 024301 (2013).

[165] D. F. Nelson and M. Lax, "Theory of the photoelastic interaction," Phys. Rev. B **3**, 2778 (1971).

[166] C. Holmes, *Direct UV written planar devices for sensing and telecommunication applications*, Ph.D. thesis, University of Southampton (2009).

[167] J.-C. Beugnot and V. Laude, "Electrostriction and guidance of acoustic phonons in optical fibers," Phys. Rev. B **86**, 224304 (2012), arXiv:1207.2998 [physics.optics] .

[168] P. Eiswirt, *Untersuchung der Speicherzeitlimitierung einer nanofaserbasierten Dipolfalle*, Diplomarbeit, Johannes Gutenberg-Universität Mainz (2011).

[169] C. Wagner, *Experimentelle Untersuchung von lichtinduzierten Kräften zwischen zwei optischen Nanofasern*, Master's thesis, Universität Mainz (2010).

[170] R. O. Pohl, X. Liu, and E. Thompson, "Low-temperature thermal conductivity and acoustic attenuation in amorphous solids," Rev. Mod. Phys. **74**, 991 (2002).

[171] S. D. Penn, A. Ageev, D. Busby, G. M. Harry, A. M. Gretarsson, K. Numata, and P. Willems, "Frequency and surface dependence of the mechanical loss in fused silica," Phys. Lett. A **352**, 3 (2006).

[172] I. Bronstein, K. Semendjajew, G. Musiol, and H. Mühlig, *Taschenbuch der Mathematik*, 5th ed. (Verlag Harri Deutsch, 2000).

[173] G. Ghosh, "Model for the thermo-optic coefficients of some standard optical glasses," J. Non-Cryst. Sol. **189**, 191 (1995).

[174] R. C. Zeller and R. O. Pohl, "Thermal conductivity and specific heat of noncrystaline solids," Phys. Rev. B **4**, 2029 (1971).

[175] A. I. Volokitin and B. N. J. Persson, "Near-field radiative heat transfer and noncontact friction," Rev. Mod. Phys. **79**, 1291 (2007).

[176] M. Krüger, G. Bimonte, T. Emig, and M. Kardar, "Trace formulas for nonequilibrium casimir interactions, heat radiation, and heat transfer for arbitrary objects," Phys. Rev. B **86**, 115423 (2012).

[177] V. A. Golyk and M. Krüger, "Estimate of the heat transfer between a cylinder and a plate," Priv. Comm. (2013).

[178] P. B. Johnson and R. W. Christy, "Optical constants of the noble metals," Phys. Rev. B **6**, 4370 (1972).

Acknowledgements / Danksagung

A project like a PhD-thesis in experimental physics is not feasible without the help and support of colleagues and friends. I would like to take the opportunity and thank at least some of them at this point.

First, I thank my group leader for giving me the opportunity to work on this project and for his ideas, advice, and support during the thesis.

I thank the former and current members of my work group for their help, advice, support, and simply having a great time inside and outside the institute.

I thank my collaborators for their contributions:

- Fiber optics group at the IPHT Jena for the development and fabrication of the FBGs.
- The FIB teams for their support giving me the opportunity to use the machines:
  - ZMNS in Vienna
  - MPIP in Mainz
  - USTEM in Vienna
  - CESAR in Bonn
- The groups concerned with non-equilibrium statistical physics at the MIT and MPI Stuttgart for fruitful discussions and their FED implementation
- The nanotechnology group at the Laserzentrum Hannover for microstructuring the first copper substrate for the FIB-milling and trying to realize plastic structures on the nanofibers.

I thank the diploma and bachelor students that were involved in this work.

I acknowledge financial support by the Volkswagen Foundation (Lichtenberg Professorship), the ESF (EURYI Award), NanoSci-E+ (NOIs project), and the Austrian Science Fund (FWF; SFB FoQus Project No. F4017).

And last but not least, danke ich meiner Freundin, die im Verlauf dieser Arbeit einiges ertragen musste und mich trotzdem immer unterstützt hat. Das ist meiner Ansicht nach nicht selbstverständlich und ich bin sehr dankbar dafür.